Development of Near Infrared Emitting Ag_2X (X: S and Te) Quantum Dots and Hybrid Nanoparticles

by

İbrahim Hocaoğlu

A Thesis Submitted to the
Graduate School of Sciences and Engineering
in Partial Fulfillment of the Requirements for
the Degree of

Doctor of Philosophy
in
Material Science and Engineering

Koc University
September 2014

Koc University

Graduate School of Sciences and Engineering

This is to certify that I have examined this copy of a Ph.D. thesis by

İbrahim Hocaoğlu

and have found that it is complete and satisfactory in all respects,

and that any and all revisions required by the final

examining committee have been made.

Committee Members:

_____

Havva F. Yağcı Acar, Ph. D. (Advisor)

_____

Alphan Sennaroğlu, Ph. D.

_____

Mehmet Somer, Ph. D.

_____

Uğur Ünal, Ph. D.

_____

Dönüş Tuncel, Ph. D.

Date: _____

ABSTRACT

Near Infrared Emitting Quantum dots (NIRQDs) has gained great interest recently for biotechnology and energy applications. Silver chalcogenides, especially Ag_2S, with low band gap energies offer a great potential for both of these applications. However, Ag_2S NIRQDs are usually synthesized in organic solvents and are hydrophobic in nature which is not suitable for bio-applications. There are few studies in the literature towards their synthesis in water but these are quite complicated synthesis methods. Besides, Quantum yield of Ag_2S QDs reported until now are below 3%.

In this thesis work, Ag_2S NIRQDs have been synthesized in a very simple one step aqueous synthetic route with thiolated capping agents. Colloidally stable and highly luminescent Ag_2S QDs emitting in the Near infrared window I (NIR-I) have been prepared with 2-mercaptopropionic acid (2-MPA) as a coating. Particles showed near band-edge emission. The emission maximum of these Ag_2S-2MPA NIRQDs are tunable between 780-950nm. They have the highest photoluminescence quantum yields (PLQY) in the literature which are 7-39% with respect to LDS 798 NIR dye. An important improvement need of this system is the ability to tune emission in a broader range within NIR-I window with high PLQY for all practical purposes.

A second set of Ag_2S NIRQDs were synthesized through decomposition of *Meso*-2,3-dimercapto succinic acid (DMSA) in water. Slow decomposition of DMSA in water allowed better tuning of emission in the 730-920 nm range with PLQYs around 7%. This is not as high as the values obtained from Ag_2S-2MPA NIRQDs but the advantage is the fact that particles emitting within this range all has PLQY high enough to be used as optical probes.

Potential as optical agents and in vitro cytotoxicity of both 2-MPA and DMSA coated Ag_2S-NIRQDs have been eveluated. They both showed almost no cytotoxicity in MCF-7 and HeLa cancer cell lines and even in more vulnerable NIH/3T3 cells (with quite high doses up to 0.84 mg/ml). In addition, interaction of the NIRQDs with cells and the blood components showed excellent hemocompatibility of these particles. These particles showed internalization by these cell lines and endosomal compartmentalization. These results indicate that both of these Ag_2S NIRQDs are highly promising QDs for medical and biotechnology applications satisfying the NIR emission, high quantum yield and excellent cyto- and hemocompatibility.

Another novel material developed in this work is the hybrid nanoparticle with both optical and superparamagnetic properties. Here, hybrid nanoparticles composed of biocompatible and MRI active superparamagnetic iron oxide nanoparticles (SPIONs) and biocompatible NIR-luminescent Ag_2S-2MPA Quantum dots were prepared in a simple, one step, biphasic ligand exchange method. An array of colloidally stable and NIR-I emitting hybrids with magnetic response have been prepared. Magnetic component of hybrids allow magnetic targeting of these particles, increasing cellular interaction and uptake as proven by the in vitro cell uptake and cytotoxicity experiments. These hybrids were also shown as effective imaging agents in confocal laser microscopy images of HeLa cells. These particles demonstrate a great potential for in vivo application of QDs with great cytocompatibility, high luminescence properties and magnetic response.

Lastly, in an effort to develope silver chalcogenide QDs with emission tuned in a much broader range within NIR window, alloyed silver sulfides with a lower band gap material, Ag_2Te were attempted. In an aqueous synthesis of 2-MPA coated Ag_2Te and $Ag_2Te_xS_{1-x}$ NIRQDs, the influence of Te/S, coating/Ag as well as different sources of chalcogens and chalcogen addition sequences on particle properties were studied. All synthesized Ag_2Te-

2MPA and $Ag_2Te_xS_{1-x}$-NIRQDs emit in the NIR-I range (900-1100 nm) with bimodal emission profile where, the first and the second emission maxima were tunable between 920-950nm and 1000-1050nm, respectively. Origin of such bimodal emission profile has been investigated and discussed yet, further studies are also proposed. These quantum dots were also shown as non-toxic in the in vitro cell studies and showed a great potential as optical labels in the in vitro studies performed with HeLa cells. Confocal Laser Microscopy images indicated cytoplasmic distribution of QDs with strong optical signal.

Overall, different silver chalcogenide quantum dots emitting in the 700-1000 nm biological window with highest quantum yields in the literature and their hybrids with SPIONs were developed and shown as non-toxic and hemocompatible optical probes in the in vitro studies.

ÖZET

Yakın Kızılötesi Bölgesinde Işıyan Kuantum Noktacıkları (YKBIKN) biyoteknoloji ve enerji uygulamaları için son zamanlarda büyük önem kazanmıştır. Gümüş kalkogenitler, özellikle Ag_2S, düşük bant aralık enerjileri ile her iki uygulama için de büyük bir potansiyele sahiptir. Bununla birlikte, genellikle organik çözücülerde sentezlenen ve doğası hidrofobik olan Ag_2S YKBIKN, biyo - uygulamalar için uygun değildir. Litaratürde suda sentezlenmiş birkaç çalışma vardır ama bu yöntemler oldukça karmaşıktır. Bunun yanında, Ag_2S YKBIKN `nın bugüne kadar rapor edilen kuantum ışıma verimleri % 3 altındadır.

Bu tez çalışmasında, Ag_2S YKBIKN sulu sentetik yoldan tek aşamada tiyol bağlı kaplamalar kullanılarak sentezlenmiştir. Yakın Kızılötesi I. Bölgede (YKB-I) ışıyan, kolloidal açıdan kararlı ve son derece ışıma verimi yüksek olan Ag_2S KN ları 2-merkaptopropionik asit kaplaması ile hazırlanmıştır. Parçacıklar yakın bant-kenar emisyonu göstermiştir. Bu Ag_2S-2MPA YKBIKN 780-950 nm aralığında dalgaboyu ayarlanabilir emisyon maximumuna sahiptirler. Bunlar, YK boyası olan LDS 798 e göre ışıma verimleri % 7-39 arasında değişen, literatürdeki en yüksek FotoLüminesans Kuantum Verimlerine (FLKV) sahiptirler. Bu sistemdeki en önemli gelişme ihtiyacı, tüm pratik amaçlar için YKB-I içersinde daha geniş aralalıkta ayarlanabilir emisyona ve yüksek FLKV ne sahip parçacıklar hazırlamaktır.

Ag_2S YKBIKN ikinci seti, suda *Mezo*- 2,3- dimerkapto süksinik asit (DMSA) ayrışması ile sentezlenmiştir. Su içinde DMSA 'nın yavaş ayrışması, FLKV yaklaşık %7 civarında olan parçacıkların emisyonunun 730-920 nm dalgaboyu aralığında daha iyi ayarlanmasını sağlamıştır. Bu FLKV değerleri Ag_2S–2MPA YKBIKN için elde edilen değerler kadar

yüksek değildir fakat yine de bu aralıkta ışıyan parçacıkların FLKV optik prob olarak kullanılmaları için yeterince yüksektir.

Potansiyel optik ajanlar olarak 2-MPA ve DMSA kaplı Ag_2S - YKBIKN in vitro sitotoksisiteleri tespit edilmiştir. Her ikisi de , MCF - 7 ve HeLa kanser hücreleri ve hatta daha hassas olan NIH / 3T3 hücrelerinde (0.84 mg / ml seviyesinde ki oldukça yüksek dozlarda dahi) hemen hemen hiç bir toksisite göstermemiştir. Buna ek olarak, YKBIKN nın hücre ve kan bileşenleri ile etkileşimi bu taneciklerin kan ile çok uyumlu olduğunu göstermiştir. Bu parçacıkların, bu hücre hatlarında internalizasyonu ve endozomal bölmelere dağılımı mikroskopik yöntemlerle görülmüştür. Bu sonuçlar, Ag_2S YKBIKN nın YKB ışımaları, yüksek kuantum verimine sahip olmaları ve mükemmel sito ve hemo uyumlu olmaları, tıbbi alanda ve biyoteknolojik uygulamalar için oldukça ümit verici KN olduklarını göstermektedir.

Bu çalışmada geliştirilen bir diğer yeni malzeme , optik ve süperparamanyetik özelliklere sahip olan hibrit nanoparçacıklardır. Burada, biyo-uyumlu ve MR aktif SüperParamanyetik Demir Oksit Nanopartiküllerinden (SPDONs) ve biyo-uyumlu YKB lüminesan Ag_2S-2MPA kuantum noktacıklarından oluşan hibrit nanoparçacıklar basit, tek aşamalı, iki fazlı ligand değiştirme yöntemiyle hazırlandı. Bir dizi, kolloidal olarak kararlı, YKB-I `de ışıyan ve manyetik tepkiye sahip hibrit nanoparçacıklar hazırlanmıştır. In vitro hücre alımı ve sitotoksisite deneyleri , bu parçacıkların hücresel etkileşim ve alımının, manyetik hedeflenmesi ile arttığını göstermiştir. Bu hibritler HeLa kanser hücrelerinin konfokal lazer mikroskopisi ile etkili bir şekilde görüntülenmesinde kullanılmıştır. Bu parçacıkların sito-uyumlu olmaları, yüksek lüminesan özelliklerine ve manyetik tepkiye sahip olmaları, in vivo uygulamaları için büyük bir potansiyelleri olduğunu göstermektedir.

Son olarak ,YKB`de ışıyan ve çok daha geniş bir aralıkta emisyonu ayarlanabilir gümüş kalkojenit KN geliştirmek için, Te alaşımlı Ag_2S ve daha düşük band aralığına sahip Ag_2Te

sentezlendi. 2-MPA kaplı Ag_2Te ve $Ag_2Te_xS_{1-x}$ YKBIKN nın suda sentezinde, Te/S, kaplama/Ag, farklı kalkojen kaynaklarının ve kalkojen ekleme sırasının parçacık özellikleri üzerine etkisi incelenmiştir. Ag_2Te-2MPA ve $Ag_2Te_xS_{1-x}$-2MPA YKBIKN`ler YKB-I içerisinde 900-1100 nm arasında, ilki 920-950 nm ve ikincisi 1000-1050 nm arasında ayarlanabilen iki-modlu (iki tepeciğe sahip) ışımaya sahiptirler. Böyle iki modlu emisyon profillerinin kökeni araştırılmış ve tartışılmıştır. Ayrıca konunun daha iyi anlaşılması için başka çalışmalar da önerilmiştir. Bu kuantum noktacıklarının da in vitro hücre çalışmalarında toksik olmadığı görülmüş ve HeLa hücrelerinde sitoplazmaya alınımları ve dağılımları, optik etiket olarak büyük bir potansiyele sahip oldukları gösterilmiştir.

Genel olarak, 700-1000 nm biyolojik penceresinde, literatürdeki en yüksek kuantum verimiyle ışıyan farklı gümüş kalkojenit kuantum noktacıkları ve bunların SPDONs ile hibritleri geliştirilmiş ve in vitro çalışmalarda , toksik olmadıkları ve kan ile uyumlu, güçlü optik problar oldukları gösterilmiştir.

Dedicated to
my beloved uncle

VEHBİ HOCAOĞLU

for his great contributions
throughout my life

ACKNOWLEDGEMENTS

First of all, I would like to express my gratitude to my friend Pınar Conger and Assoc.Prof Özgür Birer for their guidance to enroll KU for Ph.D. Especially, I would like to thank Dr. Birer for his sincerity, encouragement, motivation and directing me to Funda Hoca at the beginning of my Ph.D, whom I worked with.

I am deeply indebted to my supervisor Assoc. Funda Yağcı Acar for her guidance, trust, motivation and encouragement not only for my thesis but also in many aspects of life. Her positive and friendly attitude, endless energy and sincerity led me go ahead despite of encountering difficulties and struggling challenges. Trust was the important driving force to overcome difficulties. I would like to thank her once more for everything, for her great contributions to my research, to improve myself academically and personally.

I would like to express my gratitude to my thesis committee members Prof. Alphan Sennaroğlu, Prof. Mehmet Somer, Assoc. Prof. Uğur Ünal and Prof. Dönüş Tuncel for their time, invaluable contributions and suggestions to my thesis. I am also grateful to them for not only being in my committee, but also for their help, advices and collaborations when I needed their assistance and guidance throughout my Ph.D.

Beside the chemistry department in BiIkent University, I would like to express my appreciation to Prof. Dönüş Tuncel for her contributions to my senior project that I performed in her laboratory as a requirement of my BS degree. I gained enthusiasm for science and skills for scientific research in her laboratory.

I would like to express my appreciation to many valuable collaborators, as well. I am deeply grateful to Prof. Alphan Sennaroğlu, Dr. Natali Çizmeciyan and Prof. Adnan Kurt for the optimization of Near IR based photoluminescence measurement and for their great

contribution to this field. It wouldn`t be possible to publish our initial results, which made us the pioneer of this field, without them. I am very grateful to Assoc. Prof Özgür Birer and Assoc. Prof. Uğur Ünal for establishing a home-made, unique photoluminescence measurement set up which is being used for many students now. It would be extremely difficult to conduct this research without them. I am deeply indebted to Prof. Alper Kiraz for establishing home-made confocal laser scanning microscope for the fluorescence imaging in the Near IR range which is not available in the markets. We would not able to characterize our optical probes without him.Many thanks for their great contributions.

I would like thank also Prof. Can Özen and Rengin Erdem from METU for the initial cytotoxicity tests and in vitro images, which was very difficult with the conventional microscopes. I want to express my thanks to Dr. Gülen Ulusoy, Fatma Demir and Didar Aşık for their significant support and contribution to biological evaluation of my QDs. Many thanks to Prof. Christian Grandfils and Chantal Servin (Belgium) for the hemocompatibility measurements. I would like to thank Prof. Francois Rossi and Dr. Isaac Jimenez (JRC, ITALY) and Prof Mehmet Ali Gülgün and Melike Yıldızhan (Sabancı University) for the characterization of the particles by TEM and EDX.

I would like to express my gratitude to Prof. Mehmet Somer for the synthesis of Na_2Te which is a very important chalcogenide source for my research and many other studies on going in Polymers and Nanomaterials Research Laboratory. He is the unique producer of the Sodium Telluride all over the world. He also conducts solid state synthesis of silver chalcogenides which will be used in further studies. I would also thank the former and present members of his research group especially Selçuk Acar, Ali Baş and Ali Bateni for their support, XRD analyses, glove box, annealing etc. Overall, I would like to thank all of them once more for their worthy collaborations, significant support and contributions to my studies.

I would like to thank Koc University Surface Technology Research Center (KUYTAM) for their help in characterization of QDs. I deeply appreciate the assistance and support of the KUTAM team, Dr. Barış Yağcı, Cansu Yıldırım, Assoc. Prof. Özgür Birer and Assoc.Prof. Uğur Ünal.

I would like to express my thanks to KU, TUBITAK and KUTEM for funding.

I am deeply grateful to all faculty members of the Material Science and Engineering Program for their assistance.

I am deeply grateful to Buğra Mert Aytekin, Harun Aybars Şimşek, Mehmet Burak Sevinç, Fatih Çınar and Osman Çelik who were the presents of my teaching assistantship in CHEM 103, for their friendship, motivation, support and for their invisible contributions in the last two years of my Ph.D. career. I had great pleasure from the times that I have spent with them. Especially, my special thanks to Buğra Mert Aytekin for his invaluable attempt to establish this friendship. I would also thank Yasin Atagün and Muhammed İkbal Aksakal who were the members of this close friend group.

I would like to express my thanks to former and present members of "Polymers and Nanomaterials Research group": Dr. Pınar Dağtepe, Dr. Yurdanur Türker, Dr. Rouhullah Khodadust, Dr. Aydın Can, Yasemin Yar, Özlem Ünal, Emek Durmuşoğlu, Hande Öztürk, Neslihan Hancıoğlu, Zeynep Yurtsever, Sinem Ertaş; my undergraduate students, Funda Kar and especially Enes Buz and Emre Köken for their support, for the harmony and created synergy in the group. Many thanks to all of my colleagues and friends in the Chemistry department and in other Colleges: Erhan Atcı, İlknur Erucar, Ahmet Topçu, Dr. Emre Heves, Dr. Fehmi Çivitçi, Dr. Özlem Yalçın, Başarbatu Can, Zeynep Gizem Narin, Dr. Kamil Kiraz, Meltem İpekçi, İsmail Yorulmaz, Ersen Beyatlı, Feriha Eylül Saraç, Mustafa Ertürk, Kerem Karakuş, Yasin Kılınç, Orkun Önal, Çağla Koşak, Melis Peniç,

Armen Yıldırım, Özgün Önder, Mehmet Akif Yalçınkaya, Ece Aytan and Mine Toker. I would like to raise special thanks to Dr. Pınar Tatar, Dr. Ceren Yılmaz and Cansu Yıldırım for always being positive, for their motivation and support.

I am deeply indebted to staff of Science College: Nuran Şimşekel, Nesrin Atağ, Ayşe Çağ Ruçoğlu, Şehnaz Martens, Pınar Akgüneş and Melek Şimşek for their significant support, logistics and contributions in the department and laboratory. I would like to also thank Muharrem Güler for not only the technical support and supply he provided, but also for his motivation and friendship.

Finally, I would like to express my sincere thanks to my huge family. Special thanks to Özyanık family as they became part of my life in the year of 2011 and brought me luck, finally I was able to complete my thesis. I am very grateful to my mother Esen Hocaoğlu and my father Nurettin Hocaoğlu for their everlasting support, trust, guadiance, encouragement, motivation, financial and spiritual support. Many thanks to my sister Zeynep Hocaoğlu and my brothers Mehmet Hocaoğlu, Ramazan Hocaoğlu and Macit Hocaoğlu for their trust and love in every single step of my life. I would like to also thank the other members of my family for their support: my cousins, my nephews, my nieces, my uncles and my aunts. I would like to express my gratitudes to my aunt Fatma Hocaoğlu and my uncle Vehbi Hocaoğlu to whom I have dedicated my thesis, for his invaluable contributions throughout my life.

TABLE OF CONTENTS

LIST OF TABLES ..... **xvii**

LIST OF FIGURES ..... **xix**

LIST OF SCHEME ..... **xxvii**

NOMENCLATURE ..... **xxviii**

CHAPTER 1: INTRODUCTION **1**

1.1 Quantum Dots 1
1.1.1 Exciton, Quantum Confinement and Brus equation 3
1.1.2 Optical properties of QDs 7
1.1.3 Synthesis of QDs 9
1.1.4 Medical and Biotechnology Applications of the QDs 15
1.1.5 Comparison of QDs with Organic Dyes 16
1.1.6 Limitation of Cd-Chalcogenide QDs in biomedicine 19
1.2 Near Infra-Red Emitting Quantum Dots (NIRQDs) 20
1.2.1 Advantages of NIRQDs 20
1.2.2 NIRQDs in Literature 23
1.3 Hybrid Nanoparticles 24
1.4 Proposal and Aim of this Thesis Work 27

CHAPTER 2: SYNTHESIS AND CHARECTERIZATION OF AQUEOUS 2-MPA COATED Ag_2S NEAR IR EMITTING QUANTUM DOTS **32**

2.1 Introduction 32
2.2 Experimental 34
2.2.1 Materials 34
2.2.2 Preparation of Ag_2S-2MPA NIRQDs 34
2.2.3 Cell Culture 35
2.2.4 Evaluation of cytotoxicity 35
2.2.5 Cell Imaging 36
2.3 Characterization Methods 36
2.4 Results and Discussions 38
2.4.1 Synthesis and Characterization of Ag_2S-2MPA NIRQDs 38
2.4.2 Influence of the reaction variables on particle properties 42
2.4.3 In-Vitro Cell Studies 51

2.5 Conclusions 54

CHAPTER 3: SYNTHESIS AND CHARECTERIZATION OF AQUEOUS DMSA COATED Ag_2S NEAR IR EMITTING QUANTUM DOTS 56

3.1 Introduction 56
3.2 Materials and Methods 57
3.2.1 Materials 57
3.2.2 Preparation of Ag_2S-DMSA Nanoparticles 58
3.2.3 Cell Culture 58
3.2.4 Determination of Cytotoxicity 59
3.2.5 Cell Imaging 59
3.2.6 Hemocompatibility Studies 60
3.3 Characterization Methods 62
3.4 Results and Discussion 64
3.4.1 Effect of the reaction parameters on optical properties 64
3.4.2 Characterization by TEM, XPS and XRD 73
3.4.3 Assessment of *In Vitro* Cytotoxicity 76
3.4.4 Hemocompatibility Assessment 77
3.4.5 In vitro Cell Imaging 81
3.5 Conclusions 83

CHAPTER 4: AQUEOUS NIR EMITTING HYBRID NANOPARTICLES (Ag_2S-Fe_3O_4) FOR BIOMEDICAL APPLICATIONS 85

4.1 Introduction 85
4.2 Materials and Method 88
4.2.1 Materials 88
4.2.2 Preparation of Ag_2S-2MPA NIRQDs 89
4.2.3 Preparation of Ag2S-Fe3O4 Hybrid nanoparticles 89
4.2.4 Cell culture 90
4.2.5 Cell viability via MTT assay 90
4.2.6 Cell Imaging 91
4.3 Characterization Methods 92
4.4 Results and Discussion 93
4.4.1 Hybrid magnetic and luminescent particles (Ag_2S-2MPA/ Fe_3O_4) 93
4.4.2 In Vitro Studies 102
4.5 Conclusions 109

CHAPTER 5: SYNTHESIS AND CHARECTERIZATION OF AQUEOUS Ag_2Te and $Ag_2Te_xS_{1-x}$ NEAR IR EMITTING QUANTUM DOTS..... 111

5.1 Introduction..... 111
5.2 Materials and Methods..... 113
5.2.1 Materials..... 113
5.2.2 Synthesis of Ag_2X-2MPA..... 114
5.2.3 In Vitro cytotoxicity studies..... 115
5.2.4 Cell Imaging..... 116
5.3 Characterization of Ag_2X..... 116
5.4 Results and Discussion..... 117
5.4.1 Photoluminescence measurement system..... 117
5.4.2 Synthesis and Characterization of 2-MPA coated Ag_2Te..... 119
5.4.3 Synthesis and Characterization of $Ag_2Te_xS_{1-x}$..... 129
5.4.4 In Vitro Studies..... 146
5.5 Conclusion..... 148

CHAPTER 6: CONCLUSION..... 151

6.1 Publications & Conferences..... 157

APPENDIX A: CALCULATION OF PARTICLE SIZE FOR Ag2S QDs BY BRUS EQUATION..... 159

A.1 Band gap determination from absorption Spectra..... 159
A.2 Matlab code for size output by Brus equation..... 160

BIBLIOGRAPHY..... 170

VITA..... 180

LIST OF TABLES

Table 1.1 Semiconductors with their band gap energies[1] 2
Table 2.1 Binding Energies of Ag and S core levels 42
Table 2.2 Atomic ratios of Ag and S by XPS analysis. 42
Table 2.3 Influence of Ag/S, 2-MPA/Ag and reaction temperature on the properties of Ag_2S-2MPA NIRQDs. 47
Table 2.4 Changes in the particle properties with time. 50
Table 3.1 Influence of DMSA/Ag ratio and reaction time on the properties of Ag_2S-DMSA NIRQDs 66
Table 3.2 Properties of Ag2S-DMSA NIRQDS at different DMSA/Ag 67
Table 3.3 Influence of the temperature on DMSA decomposition and NIRQD properties. 69
Table 3.4 Properties of RT synthesized DMSA and 2MPA capped Ag_2S particles. 72
Table 3.5 Percentage of hemolysis, complement activation, and hemostasis activation (Quick and TCA) after incubation at 37°C of the QDs in whole blood. 80
Table 4.1 Properties of Ag_2S NIRQDs and corresponding hybrid nanoparticles. 96
Table 4.2 Binding Energies of the XPS signals with the compositions 98
Table 5.1 Recipe of Ag2Te-2-MPA synthesis 119
Table 5.2 Hydrodynamic size and Zeta-Potential of IH90 and IH82 codded QDs 125
Table 5.3 BEs of Ag, Te and S atoms calculated by XPS analysis. 128
Table 5.4 Ag, Te and S amounts detected in Ag_2Te-2MPA NIRQDs by ICP. 129
Table 5.5 Formulation of $Ag_2Te_xS_{1-x}$ NIRQDs Syntheses to study the influence of S/Te ratio 130
Table 5.6 Size calculation and colloidal stability of $Ag_2Te_xS_{1-x}$ NIRQDs 131

Table 5.7 Effect of S sources mixed with Te for the synthesis of $Ag_2Te_xS_{1-x}$ NIRQDs in simultaneous addition of chalcogens 135
Table 5.8A) Reaction parameters of IH98 and IH120, BEs and ratios of Ag, Te and S atoms B) for IH98 C) for IH120 and D) compositions of IH98 and IH120 determined by XPS analyses. 140
Table 5.9 Ag, Te and S amount in $Ag_2Te_xS_{1-x}$ NIRQDs analyzed by ICP OES 141
Table 5.10 Synthesis parameters of $Ag_2Te_xS_{1-x}$ NIRQDs by Sequential addition of chalcogens 141
Table 5.11 Calculated particle sizes for $Ag_2Te_xS_{1-x}$ NIRQDs 144
Table 5.12 Cell viability of the HeLa cell lines exposed to QDs. 147
Table A.1 Particle size of Ag_2S NIRQDs with respect to absorbance edges**.** 163

LIST OF FIGURES

Figure 1.1 Wavelengths corresponding to bulk Band Gap Energies of the semiconductors.3
Figure 1.2 Comparison of electron density and DOS in bulk semiconductor, quantum well, quantum wire and quantum dot.[1] 4
Figure 1.3 Quantum confinement, continuous and discrete energy levels in bulk material and molecules.[1] 5
Figure 1.4 Band gap energy relation with the size reduction due to the confinement and emission spectra of the different size particles in visible region.[14] 7
Figure 1.5 Four levels of energy transitions for excitation and emission mechanism. 8
Figure 1.6 Absorbance and PL spectra of the CdTe QDs. Stoke shift (30nm) and FWHM (50nm).[17] 8
Figure 1.7 (A) Structure of a generic core/shell QD[20], (B) Structure of a TOPO coated hydrophobic (a) and (b) thioglycolic acid coated hydrophilic quantum dot. 10
Figure 1.8 Schematic representation of CdS/ZnS core/shell structure and the PL spectra of CdS, ZnS and CdS/ZnS QDs.[27] 12
Figure 1.9 Three major methods to transfer hydrophobic particles into water[28, 29] 13
Figure 1.10 Chemical structures of the water soluble organic coatings. 14
Figure 1.11 Absorbance and Emission spectra of organic dyes and CdSe Quantum Dots. Picture of the CdSe QDs stimulated at the same wavelengths corresponding their spectra above.[25] 18
Figure 1.12 Photostability of QDs versus organic fluorophores. Top row: Nuclear antigens were labelled with QD 630–streptavidin (red), and microtubules were labelled with AlexaFluor 488(green) simultaneously in a 3T3 cell. Bottom row: Microtubules were

labelled with QD 630–streptavidin (red), and nuclear antigens were labelled with AlexaFluor 488(green).[51] 19
Figure 1.13 Absorption coefficients of the hemoglobin deoxyhemoglobin and water molecule with respect to wavelengths. 22
Figure 1.14 Potential application areas of NIRQDs 22
Figure 1.15 Different methods for the preparation of SPION hybrid nanoparticles.[96] ... 26
Figure 1.16 Four binding structure models of 2-MPA (I-III) and 3-MPA (II-IV) to CdS. 29
Figure 2.1 XRD patterns of Ag_2S QDs (a) at room temperature and (b) after 180 ^oC heat treatment. 39
Figure 2.2 IR spectrum of 2-MPA coated Ag_2S NIRQDs**.** 40
Figure 2.3 (a) Ag3d and (b) S2p XPS spectra of Ag_2S-2MPA QDs before plasma etching. Comparison of (c) Ag3d and (d) S2p peaks before (level 0) and after (level 1) plasma etching. 41
Figure 2.4 Absorbance and photoluminescence spectrum of Ag_2S QD (Ag/S=4 2-MPA/Ag=5 T=50 ^oC 7h reaction.) 43
Figure 2.5 TEM image of Ag_2S-2MPA NIRQDs (Ag/S=4, 2-MPA/Ag=5, T=30^oC) 44
Figure 2.6 Absorbance and photoluminescence spectra of the Ag_2S-2MPA particles prepared different reaction temperatures (Ag/S=4, 2-MPA/Ag=5) 45
Figure 2.7 Time dependent evolution of absorbance and photoluminescence bands for the reactions A) at 30 °C B) 50 °C C) 90 °C (Ag/S =4 and 2-MPA/Ag =5) 46
Figure 2.8 Absorbance spectra of Ag_2S QDs synthesized at for different 2-MPA/Ag ratios (a) 90 ^oC. at (b) 30 ^oC. and for different Ag/S ratios at (c) 90 ^oC and (d) 30 ^oC. 48
Figure 2.9 . PL spectra of Ag_2S QDs prepared at different 2-MPA/Ag ratios at (a) 90 ^oC and (b) 30 ^oC, and at different Ag/S ratios at (c) 90 ^oC and (d) 30 ^oC. 49
Figure 2.10 Absorbance and PL spectra of Ag_2S-2MPA NIRQDs (synthesized at room temperature) recorded after the synthesis. 50

Figure 2.11 Change in the metabolic activity of NIH/3T3 mouse fibroblast cells after 24 h exposure to Ag_2S quantum dots as determined by XTT Assay. Reported values are mean ± SEM (n=6). No significant difference was observed between control (ctrl) and QD treated cells (One-way ANOVA with Tukey`s multiple comparison at $p < 0.05$) 51
Figure 2.12 Change in the metabolic activity of HeLa and MCF-7 cancer cells after 24 h exposure to Ag_2S NIRQDs as determined by MTT Assay. 53
Figure 2.13 Cellular uptake and localization of Ag_2S QDs by NIH/3T3 mouse fibroblast cells (200 µg/mL QD, 24 h incubation). (A) Fluorescence, (B) Transmission and (C) Overlay channels of confocal micrograph. The scale bar represents 20 µm. 54
Figure 3.1 Absorbance spectra of a) Ag^+-DMSA complex b) Ag_2S-DMSA NIRQDs prepared at 90 ^oC at DMSA/Ag= 2.5. 65
Figure 3.2 Absorbance and corresponding photoluminescence spectra of Ag_2S-DMSA NIRQDs at different time points during the synthesis performed at 70 ^oC and DMSA/Ag ratios of a) 1.5 b) 2.5 c) 3.5. 68
Figure 3.3 Comparison of the Photoluminescence spectra of the Ag_2S-DMSA NIRQDs at different SH/Ag ratio at the same reaction time (4h) and the temperature (90 ^oC). 69
Figure 3.4 Absorbance a) and PL b) spectra of the samples taken from the synthesis of Ag_2S NIRQDs at 90^oC. 70
Figure 3.5 Comparison of the Photoluminescence spectra of the Ag_2S-DMSA NIRQDs synthesized at different temperature. 70
Figure 3.6 Absorbance a) and Photoluminescence b) spectra of DMSA and 2MPA coated Ag_2S NIRQDs. 72
Figure 3.7 TEM and EDX Analyses of the Ag_2S-DMSA NIRQDs. TEM of the nanoparticles at a) 10 nm b) 20 nm scale, c) focused lattice planes for defining d-spacing parameter corresponding plane. d) Bright field image of the Ag_2S-DMSA NIRQDs, e) Ag

and f) S elemental mapping and g) their merged image showing composition of the particles, h) Ag and S transitions by EDX acquisition. 73
Figure 3.8 Size of the Ag_2S-DMSA NIRQDs (9nm) by DLS (TEM SAMPLE). 74
Figure 3.9 XPS spectra of Ag_2S-DMSA NIRQDs a) Ag 3d region b) S 2p region..... 75
Figure 3.10 XRD patterns of the Ag_2S-DMSA QDs as is (RT) and annealed at 180 ^oC.... 76
Figure 3.11 Dose dependent cell viability of HeLa cancer cells and NIH/3T3 mouse fibroblast cells after 24 incubation with Ag_2S-DMSA quantum dots..... 77
Figure 3.12 Comparison of the blood cell distributions (Red blood cells (RBC's), Platelets (PT) and White Blood Cells (WBC) of the blood control to the blood incubated with Ag_2S NIRQD (100 µg/mL). 79
Figure 3.13 Fluorescence image of HeLa cells a) without and b) with internalized Ag_2S-DMSA NIRQDs obtained by confocal laser scanning microscope. 82
Figure 3.14 Cellular uptake and localization of Ag_2S-DMSA NIRQDs by HeLa cells (150 µg/mL QDs, 6h incubation).(A) Fluorescence, (B) Transmission and (C) Overlay channels of confocal micrograph. Scale bar represents 5µm..... 82
Figure 4.1 Preparation of hybrid nanoparticles by ligand exchange method..... 90
Figure 4.2 Picture of hybrid nanoparticles showing a ferrofluid behavior against an external magnet. 93
Figure 4.3 Absorbance and photoluminescence spectra (λ_{exc}=532 nm) of Hybrid nanoparticles (H1) and Ag_2S-2MPA NIRQDS (QD1). 95
Figure 4.4 Normalized absorbance spectra of SPION and Hybrid nanoparticles..... 95
Figure 4.5 Hydrodynamic sizes of Ag_2S QDs, SPIONs and Hybrid nanoparticles (H4). . 96
Figure 4.6 PL spectra of both Ag_2S-2MPA NIRQDs and Hybrid nanoparticles excited at 532 nm. 97

Figure 4.7 XPS spectra of Hybrid nanoparticles. a) Fe 2p region in Hybrid (H4), b) Fe 2p region in SPION, c) Ag 3d region at level 0 and level 1 (plasma etching) and d) S 2p region at level 0 and level 1. 98
Figure 4.8 Infrared spectra of hybrid nanoparticles and Ag_2S-2MPA NIRQDs. 99
Figure 4.9 a and b) TEM images of hybrid nanoparticles at different magnification. EDX analyses of hybrid nanoparticles showing distribution of c) Ag and Fe, d) Ag, S, Fe and O in STEM images, e) EDX energy transitions for the elements between 0-8 keV. 100
Figure 4.10 TEM images of hybrid nanoparticles indicating presence of different size particles. 101
Figure 4.11 Changes in the metabolic activity of HeLa cells after 24 h exposure to Ag_2S quantum dots and Hybrids as determined by MTT Assay. 103
Figure 4.12 Cellular uptake of hybrid nanoparticles, Ag_2S-2MPA NIRQDs and Ag^+ determined by ICPOES for HeLa cell lines. 103
Figure 4.13 Change in the metabolic activity of NIH/3T3 mouse fibroblast cells after 24 h exposure to Ag_2S quantum dots and Hybrids as determined by XTT Assay. 104
Figure 4.14 Cellular uptake of hybrid nanoparticles, Ag_2S-2MPA NIRQDs and Ag^+ determined by ICPOES for 3T3 cell lines. 106
Figure 4.15 Viability of HeLa and NIH-3T3 cells treated with H4 and H2 hybrid nanoparticles at 25 μg Ag/ml for 24h in the presence or absence of external magnetic field. 107
Figure 4.16 A) Autofluorescence of HeLa cells B) Florescence image of internalized hybrid nanoparticles in HeLa cells by confocal Laser Scanning Microscopy. The scale bars represent 5μm. Excitation wavelength is 532nm. 108
Figure 4.17 Confocal Laser Scanning micrographs of hybrid nanoparticles localized in HeLa cells (50 μg/ml hybrids incubated for 6h.) A) Fluorescence B) Transmission C) Overlay images. The scale bar represents 5μm. 108

Figure 4.18 Confocal Laser Scanning micrographs of hybrid nanoparticles localized in cytoplasm of HeLa cells (50 µg/ml hybrid incubated for 6h. and nuclei was stained by DAPI A) Florescence B) Transmission C) Overlay images. The scale bar represents 5µm. Exc: 420 nm. 108
Figure 5.1 Preparation of NaHTe solution. 115
Figure 5.2 Responsivity values of Si and InGaAs detectors with respect to wavelengths 118
Figure 5.3 PL spectra of IH98 recorded by Si and InGaAs detectors. Excitation wavelength is 532 nm. 119
Figure 5.4 a) Absorbance and Photoluminescence spectra taken with b) Si detector (λexc:532nm) c) InGaAs detector (λexc:532nm) and d) InGaAs detector (λexc:605nm) of the reaction IH82 (samples taken at different time intervals). 120
Figure 5.5 a) Absorbance and b) Photoluminescence spectra of the reaction IH90 taken with Si detector (λexc:532nm). 121
Figure 5.6 a) Absorbance and b) Photoluminescence spectra of the reaction IH135 taken with Si detector (λexc:532nm). 121
Figure 5.7 a) Absorbance and b) Photoluminescence spectra of the reaction IH137 taken with Si detector (λexc:532nm). 123
Figure 5.8 Comparison of the luminescence intensities of the samples of the four different reactions (IH82, IH90, IH135 and IH137) taken at 30m. And 1h (only for IH82)..... 123
Figure 5.9 Infra-red spectrum of the IH90 codded Ag_2Te-2MPA NIRQDs. 124
Figure 5.10 a) TEM image, b) size distribution and c) EDX analyses of the IH90 codded Ag_2S-2MPA NIRQDs. 126
Figure 5.11 A) XPS spectra of Ag_2Te NIRQDs a) Ag 3d b) S 2p before plasma etching c) Ag 3d d) S 2p peaks before and after plasma etching. B) BE spectrum of Te atom. 127
Figure 5.12 a) Absorbance and b) Photoluminescence spectra of the reaction IH84 taken with Si detector (λexc:532nm). 132

Figure 5.13 a) Absorbance and b) Photoluminescence spectra of the reaction IH96 taken with InGaAs detector (λexc:532nm). 132
Figure 5.14 a) Absorbance and b-c Photoluminescence spectra of the reaction IH97 taken with InGaAs detector (λexc:532nm) and Si detector (λexc:532nm) respectively. 133
Figure 5.15 a) Absorbance and b) Photoluminescence spectra of the reaction IH98 taken with Si detector (λexc:532nm). 134
Figure 5.16 Photoluminescence intensity comparison of the samples of the different reaction. 134
Figure 5.17 a) Absorbance and b) Photoluminescence spectra of the reaction IH120 taken with Si detector (λexc: 532nm). 136
Figure 5.18 a) Absorbance and b) Photoluminescence spectra of the reaction IH122 taken by Si detector (λexc:532nm). 136
Figure 5.19 a) Absorbance and b) Photoluminescence spectra of the 5^{th} hour of the reactions IH98, IH120 and IH122 taken by Si detector (λexc:532nm). 137
Figure 5.20 IR spectra of $Ag_2Te_xS_{1-x}$ NIRQDs obtained from reactions a) IH120 b) IH122. 138
Figure 5.21 a) Absorbance and b) Photoluminescence spectra of the reaction IH132 taken with Si detector (λexc:532nm). 142
Figure 5.22 a) Absorbance and b) Photoluminescence spectra of the reaction IH133 taken with Si detector (λexc:532nm). 143
Figure 5.23 a) Absorbance and b) Photoluminescence spectra of the reaction IH134 taken with Si detector (λexc:532nm). 143
Figure 5.24 PL spectra of the samples a) 10 min. b) 3h after the addition of S source. ... 145
Figure 5.25 PL spectra of the IH90 and IH98 taken at different time points. 146

Figure 5.26 Viability of HeLa cancer cells after 24 h exposure to Ag_2Te (IH 90 and IH82) and $Ag_2Te_xS_{1-x}$ (IH 97)NIRQDs. Indicated doses are Ag concentration within the applied dose of QDs..... 147
Figure 5.27 Confocal Laser Scanning Micrographs of Ag_2Te NIRQDs localized to HeLa cells a) Fluorescence b) Transmission c) overlay images. Excitation at 532 nm. 148
Figure A.1 Absorbance spectrum of Ag_2S NIRQDs for band gap determination. 159

LIST OF SCHEME

Scheme 2.1 Aqueous synthesis of 2-MPA coated Ag_2S NIRQDs. 35
Scheme 3.1 Synthesis of both DMSA and 2MPA coated Ag_2S NIRQDs at 25 ^oC..... 71

NOMENCLATURE

$AgNO_3$	Silver(I)nitrate
Ag_2S	Silver(I)sulfide
Ag_2Te	Silver(I)telluride
Ag_2Se	Silver(I)selenide
CB	Conduction Band
DAPI	4',6-diamidino-2-phenylindole
DOS	Density of States
Dh	Average hydrodynamic size
DLS	Dynamic Light Scattering
DMSA	*Meso*-2,3-DimercaptoSuccinicAcid
EBR	Electron Bohr Radius
E_g	Band gap energy
EDX	Electron Dispersive X-ray
$FeCl_3.6H_2O$	Iron(III)chloride hexahydrate
$FeCl_2.4H_2O$	Iron(II)chloride tetrahydrate
α-Fe_2O_3	Iron Oxide (maghemite)
Fe_3O_4	Iron Oxide (magnetite)

FTIR	Fourier Transform Infrared Spectra
FWHM	Full Width at Half Maximum
GSH	Gluthathione
h	Planck's constant
ICPOES	Inductively Coupled Plasma Optical Emission Spectrometer
IR	InfraRed
InGaAs	Indium Galium Arsenide
LA	Lauric acid
LED	Light Emitting Diodes
m_e	Effective mass of electron
m_h	Effective mass of hole
MNP	Magnetic NanoParticle
MRI	Magnetic Resonance Imaging
MTT	Thiazolyl blue tetrazolium bromide
NaOH	Sodium hydroxide
Na_2S	Sodium sulfide
Na_2Te	Sodium telluride
Na_2Se	Sodium selenide
$NaBH_4$	Sodium borohydrate

NC	Nano-Crystal
NIR	Near InfraRed
NIRQDs	Near Infrared Emitting Quantum Dots
OA	Oleic Acid
PAA	Poly(acrylic acid)
PBS	Phosphated Buffer Salline
PL	PhotoLuminescence
PLQY	PhotoLuminescence Quantum Yield
PMT	PhotoMultiplier Tube
QD	Quantum Dot
QY	Quantum Yield
–SH	Thiol
SPIONs	Super Paramagnetic Iron Oxide Nano Particles
TAA	ThioAcetAmide
TGA	ThioGlycolicAcid
1-TGL	1-ThioGlycerol
TEM	Transmission Electron Microscopy
TOP	n-Tri-Octyl Phosphine
TOPO	n-Tri-Octyl Phosphine Oxide

UV	Ultra Violet
VB	Valence Band
Vis	Visible
XPS	X-ray Photoelectron Spectroscopy
XRD	Xray Diffraction
XTT	Sodium 3′-[1-(phenylaminocarbonyl)-3,4-tetrazolium]-bis (4-methoxy-6-nitro) benzene sulfonic acid hydrate

Chapter 1

1 INTRODUCTION

1.1 Quantum Dots

Physical, optical and electronic properties of the bulk semiconductors effectively change as their sizes are reduced to nanometer range. Quantum Dots (QDs) are the luminescent semiconductor nanomaterials in the size range of 2-10 nm. Optical and electronic properties of QDs are highly dependent on size due to effective quantum confinement obtained within this size regime and they are most popular with their size tunable emission.

Inorganic solids are categorized as metals, semiconductors and insulators. Metals have continuous energy band whereas semiconductors and insulators have forbidden energy levels or band gap between the filled valence band (VB) and empty conduction band (CB). This band gap determines the materials characteristics (Semiconductor or Insulators).[1] In general, materials with band gap energy higher than 3 eV are defined as insulators without any generalization.

Band gap energy of the semiconductors is critical for the development of QDs to obtain nanoparticles with desired optical properties in a defined electromagnetic radiation (EMR) region (Figure 1.1). Most quantum dots are prepared from the element groups

II –VI (CdS, CdTe CdSe ZnS)[2-5], III-V (InP InAs)[6, 7] and IV-VI (PbS, PbTe, SnSe)[8-11] forming semiconductor solids. Bulk band gap energies of some popular Semiconductors utilized as QDs emitting in the Vis-NIR region are listed in Table 1.1. Band gap energies (Eg in eV) of these semiconductors are converted into wavelength (nanometer) to better visualize the emission window that can be targeted with these QDs (Figure 1.1). The Eg of the nanocrystal must be higher than the Eg of a bulk semiconductor to fall into quantum confined regime. Thus, Eg is the bounding factor for the preparation of QDs (This part will be explained in detail in the quantum confinement section).

Table 1.1 Semiconductors with their band gap energies[1]

Semiconductors	Band Gap (eV)
CdS	2.42
CdSe	1.75
CdTe	1.5
InP	1.35
InAs	0.36
Ag_2S	0.9
Ag_2Te	0.65
PbS	0.41
PbTe	0.35

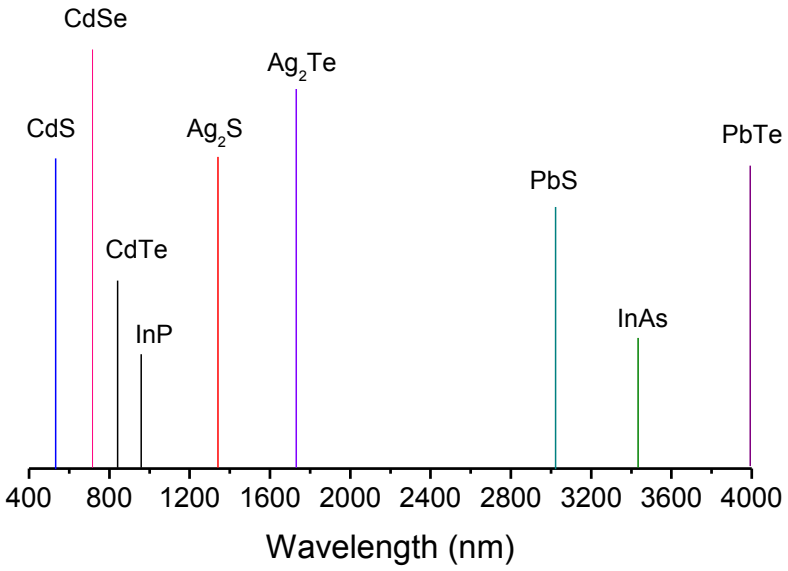

Figure 1.1 Wavelengths corresponding to bulk Band Gap Energies of the semiconductors.

1.1.1 Exciton, Quantum Confinement and Brus equation

Electrons in the VB of the semiconductors can only be excited to CB by the photons with the energy equal or greater than the band gap energy. Excitation of the electrons in this process creates a negatively charged electron and a positively charged hole pair. This pair is called as an *exciton*.

$$h\upsilon \leftrightarrow e^{-}(CB) + h^{+}(VB)$$

There is a specific separation between the electron and hole of an exciton. This distance is known as Exciton Bohr Radius (EBR). This distance is different for each material. In semiconductors, size of the particles are bigger than EBR thus there is a weak confinement in the material. On the other hand, strong confinement is achieved as the

diameter of QD get equal or smaller than the EBR. In a bulk semiconductor there is no confinement and electrons are free to move in all directions. In quantum wells, only one dimension and in quantum wires two dimensions are confined. These systems have at least one dimension for electrons to move. Thus, they show partial confinement. In quantum dots, confinement is achieved in all three dimensions so; they exhibit total confinement (Figure 1.2). Electronic properties or number of free electrons per unit volume, become more quantized as the dimensions are constricted. Density of states becomes discrete with the confinement to atomic level.

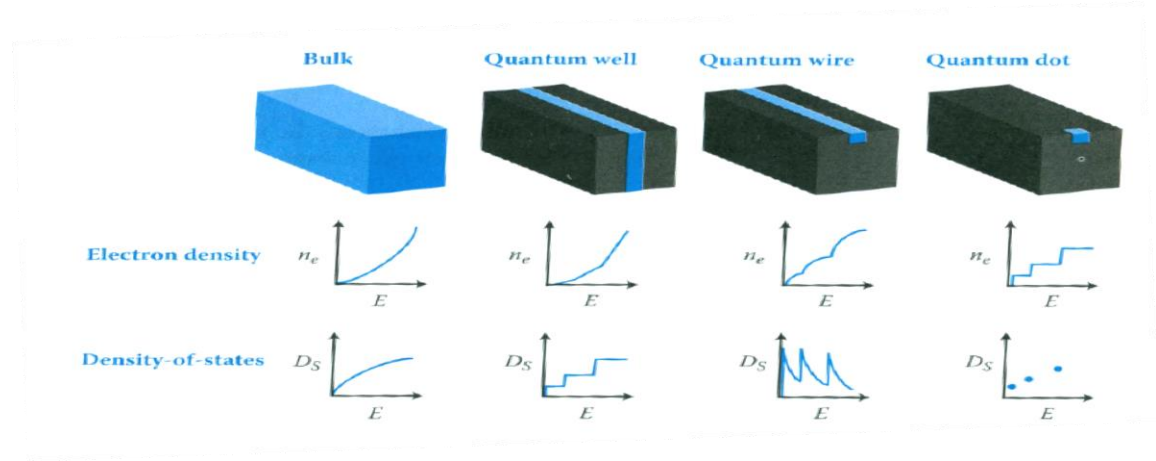

Figure 1.2 Comparison of electron density and DOS in bulk semiconductor, quantum well, quantum wire and quantum dot.[1]

Bulk materials consist of many atoms and energy levels have many splits without differentiating sublevels (All electrons in billions of atoms overlap and form a band) meaning a continuous band structure (Figure 1.3). In the confinement regime, the energy levels become rather discrete when the volume of the solid is reduced. This phenomenon is shown in Figure 1.3. Energy levels ceased to be continuous in quantized atomic levels. Hence, as the size of the material is decreased, confinement and band gap energy increase. This results in size dependent energy or emission tunability concept in QDs.

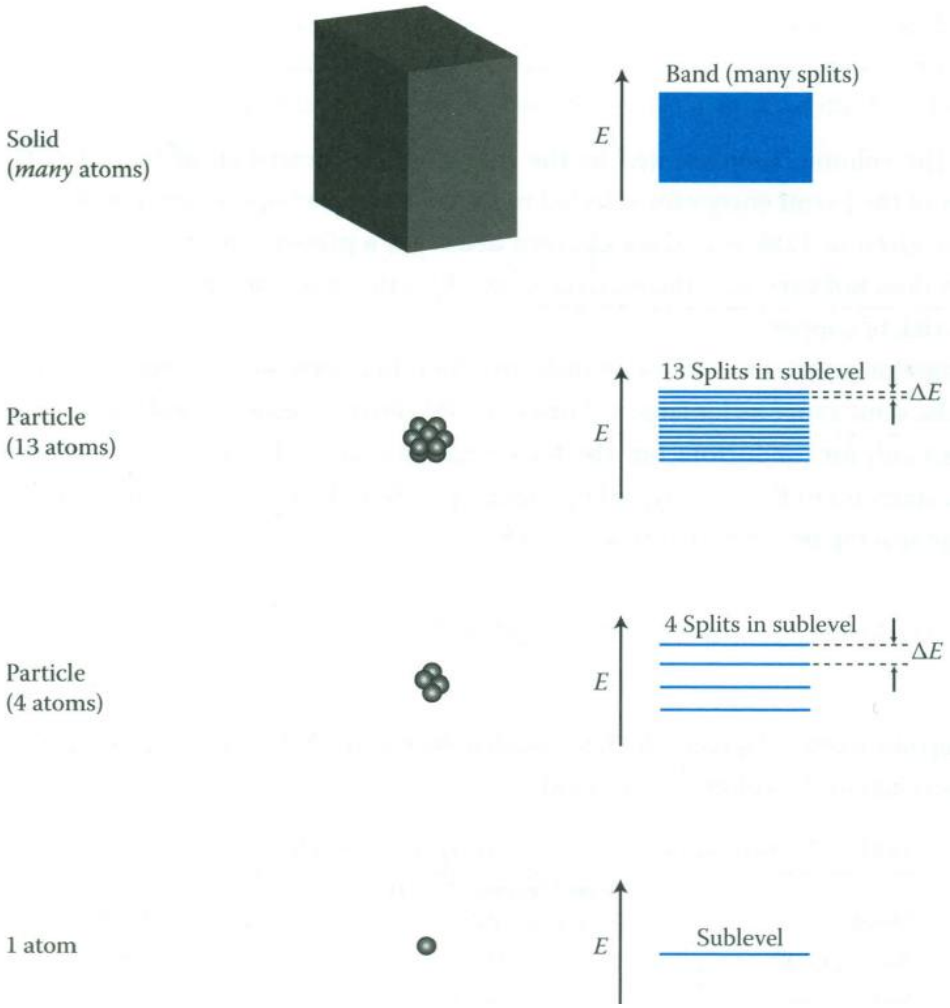

Figure 1.3 Quantum confinement, continuous and discrete energy levels in bulk material and molecules.[1]

Exciton (electron-hole pair) formation and quantum confinement effect have urged the studies on relating the particle size to band gap energy of the small nanoparticles (QDs).[1] Louis Brus was the pioneer who first studied size dependent band gap energy change in the nanocrystals by modifying the Schrödinger's equation.[12, 13] Brus equation (equation 1.1) is the most popular model used for the empirical size

calculations for the QDs . *Eg(QD)* and *Eg(Bulk)* are the band gap energies of the quantum dot and the bulk semiconductor respectively, *R* is the radius of the QD, *h* is the Planck's constant, *e* is the charge of an electron, ε is the dielectric constant for the nanocrystal solid, m_e and m_h are the electron and hole masses in the solid, respectively. The second term in the equation is a particle in a box model for electron-hole pair. The third term represents columbic attraction between electron and the hole. As a result, as the size of the particles decreases, the energy of the particles increases.

$$Eg(QD) = Eg(Bulk) + \frac{h^2}{8R^2}\left[\frac{1}{m_e} + \frac{1}{m_h}\right] - 1.8\frac{e^2}{4\pi\varepsilon\varepsilon_0 R} \qquad (1.1)$$

Emission wavelength of the QDs can be tuned by controlling the particle size.[14] The band gap energy in QDs increases with decreasing size of the nanocrystals (Figure 1.4). Cd-based QDs (CdX X: S, Te, Se) emit in the visible region (from red to blue). Different sized particles emit at different wavelength corresponding to different Eg. Smaller particles with less number of atoms have larger band gap requiring higher energies for excitation and emit photons at shorter wavelengths with respect to the larger particles.

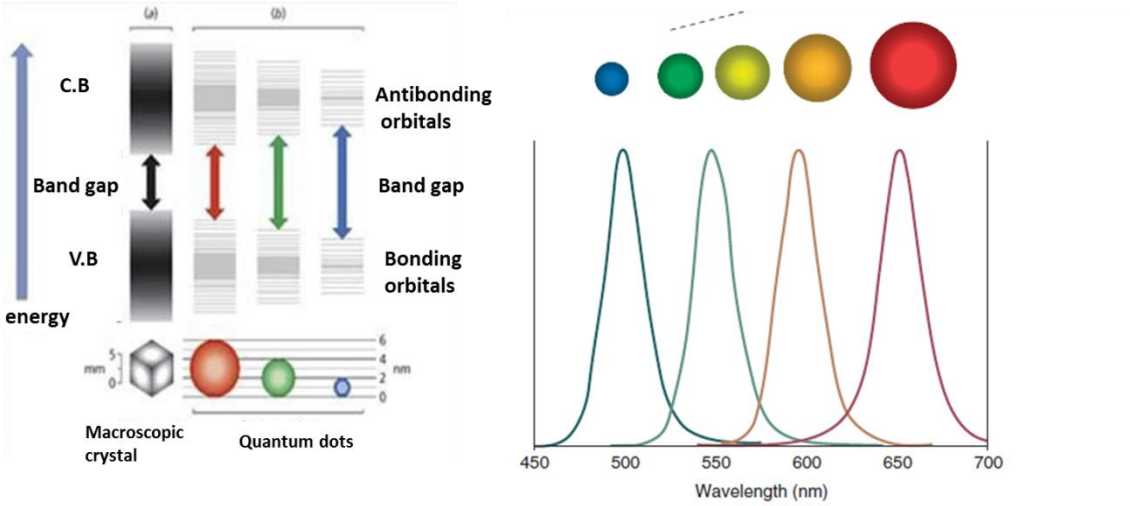

Figure 1.4 Band gap energy relation with the size reduction due to the confinement and emission spectra of the different size particles in visible region.[14]

1.1.2 Optical properties of QDs

Required minimum energy to excite QDs is band gap dependent, therefore, size dependent. Electrons are promoted to excited state from ground state as semiconductor nanoparticles or QDs irradiated with light having the energy equal or bigger than the band gap energy of the QD. This phenomenon is known as absorption of photons at the irradiation wavelength by the electrons. These electrons are not stable at excited states and relax back to ground state with radiative and non-radiative decay. Radiative decay is emission of the photon by the energy loss upon relaxation, called as fluorescence. These transitions are shown in Figure 1.5. First, excitation from |g> to |3> occurs by photon absorption at the wavelength λ_p. Second, very rapid non-radiative decay is observed from |3> to |2>. Third, spontaneous or stimulated emission is seen between |2> to |1> at the wavelength $\lambda_{emission}$. Last, very rapid non-radiative decay can be observed from |1> to |g>. Non radiative events are faster than radiative decay and occur due to loss of heat and phonon scattering. However, energy loss is lower in QDs due to quantized energy levels.[15, 16] Energy loss during the non-radiative decay causes energy difference between absorbance and emission spectra. Thus, energy of the

emitted photons is lower than excitation energy. As a result, a red shift on the emission maxima of the QDs with respect to their absorption maxima is seen and this is known as Stokes shift (Figure 1.6).

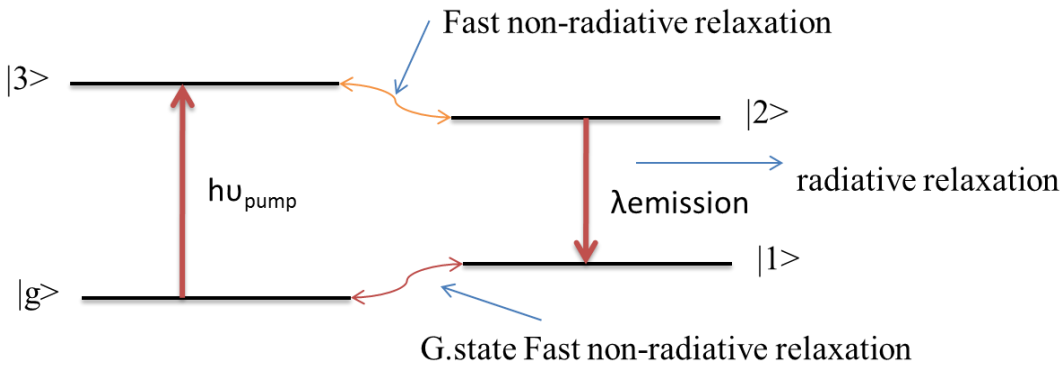

Figure 1.5 Four levels of energy transitions for excitation and emission mechanism.

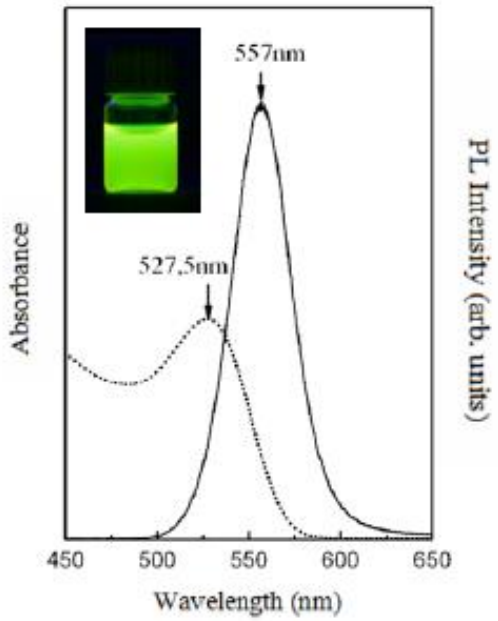

Figure 1.6 Absorbance and PL spectra of the CdTe QDs. Stoke shift (30nm) and FWHM (50nm).[17]

Emission profile of QDs is usually very narrow and symmetric Gaussian peak. The band width of emission curve is determined at the half intensity of the maximum and defined as Full Width Half Maximum (FWHM) (Figure 1.6). Band width is one of the important characteristics that indicates a level of size distribution of particles. Narrow FWHM indicates narrow size distribution. The sharper and the narrower the peak, the more monochromatic emission signals with high resolution are obtained due to better crystallization of the inorganic core and mono-disperse size distribution.

Figure 1.4 demonstrates emission spectra of different sized particles of the same material. FWHM of the spectra are very narrow to observe different colors or signal without any overlap. These properties make QDs extremely valuable for simultaneous emission of different QDs at a given time, such as in barcodes, sensors and displays.[18, 19]

1.1.3 Synthesis of QDs

Structure of a Quantum Dot: Quantum Dots mainly compose of two parts: inorganic core and organic coating. The inner part (core) of the QD is the inorganic semiconductor nanocrystal responsible form size-tunned emission. The organic coating bound on the inorganic crystalline core is responsible from passivization of the nanocrystal surface for the sake of controlling crystal growth, functionalization, enhancing the colloidal and PL (reducing defects) stability, and protection of the core from oxidation. Sometimes, an inorganic shell composed of another metal chalcogenide is grown on the initial core, enhancing particle quality in terms of PLQY and stability as well as oxidation stability. However, an organic cap (coating) is a must to achieve colloidal solutions of particles, which is necessary for bio-applications. Capping molecule is chosen according to the application as water or oil soluble, biocompatible or not, functional or not. This capping molecule further can be responsible from attaching ions, molecules such as drugs or genes and ligands such as antibodies or

peptides for targeting of QDs to specific sites such as tumor in bio-applications. Figure 1.7A shows a typical onion like core/shell/coating structure of a generic QD.

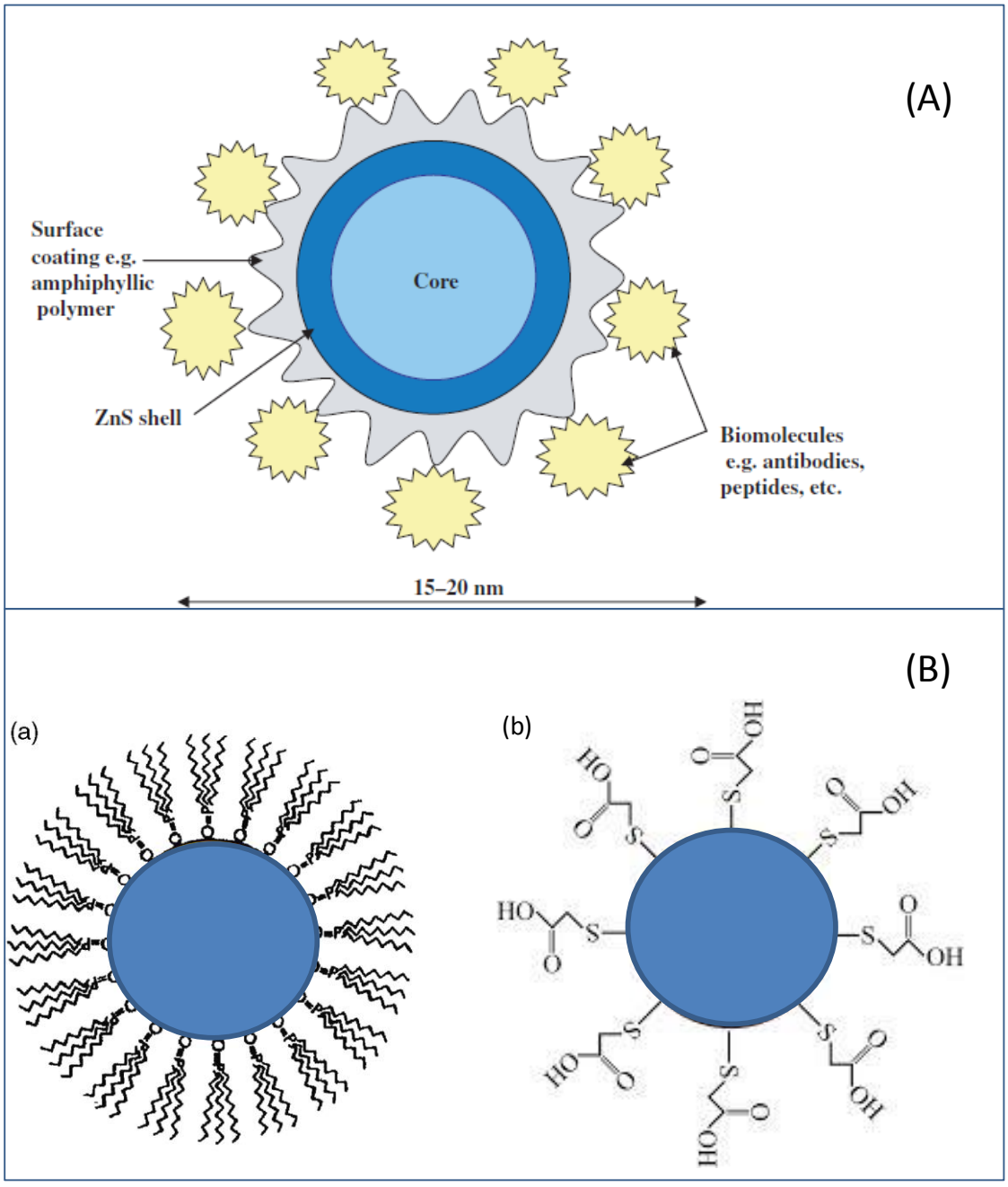

Figure 1.7 (A) Structure of a generic core/shell QD[20], (B) Structure of a TOPO coated hydrophobic (a) and (b) thioglycolic acid coated hydrophilic quantum dot.

Synthesis of Quantum Dots: Most of the QDs have been synthesized in organic media. First colloidal Cd-based QDs (CdX X:S, Se,Te) emitting in the visible region were developed by the Bawendi's group and high crystallinity and monodispersity of the particles with a moderate PLQY were reported.[2] In their reaction method, CdX QDs were synthesized by the decomposition of organometallic precursors (dimethylcadmium ($Cd(Me)_2$)) at a high temperature (300 ^oC) in the presence of solvent (n-trioctylphosphine (TOP)) and n-trioctylphosphine-oxide (TOPO) as a capping ligand (Figure 1.7 B). Chalcogenide solutions were also prepared in TOP from elemental S, Se or Te. After these reports, many QDs have been prepared like ZnS, CdS, ZnSe, CdTe and PbSe emitting in the UV to NIR, based on this method with some modifications.[21-25] However, $Cd(Me)_2$ is a highly toxic, expensive and unstable material at room temperature. Thus, later, alternative Cd precursors (CdO, $Cd(CH_3COO)_2$ and $CdCl_2$) have been used successfully in the syntheses of the Cd based QDs. Capping agents are also important in the syntheses for passivating the surface and maintaining the stable particles in colloidal systems. Hydrophobic molecules with polar end groups having high affinity to the QD surface such as thiols, phosphines, carboxylates or amines have been utilized in the organic media. These molecules adsorb/bind on to the surface of QDs and their hydrophobic chains extent into the solvent providing colloidal suspension of QDs in non-polar solvents (like TOP, chloroform, toluene, etc.) (Figure 1.7 B). Nowadays, TOP/TOPO free QD preparation are preferred as TOP/TOPO are extremely toxic, air-sensitive and not environmentally friendly. Most frequently used alternative capping agents are hexylphosphonic acid (HPA), hexadecylamine (HDA), octadecylamine (ODA), dodecanethiol (1-DT) and oleicacid (OA).

Epitaxial growth of a second material with a wider band gap, which has a higher conduction and lower valance band than the core, was also one of the routine methods in obtaining stable QDs such as CdS/ZnS QDs (Figure 1. 7 A). Such a structure ensures effective confinement of electron and hole within the core also passivates the surface

(Figure 1.8). This prevents oxidation and surface defect related non-radiative events, hence increases the photostability and luminescence quantum yield of the QD. Besides, biocompatible ZnS shell prevents Cd release and improves the biocompatibility of QDs as well.[3, 21, 25, 26]

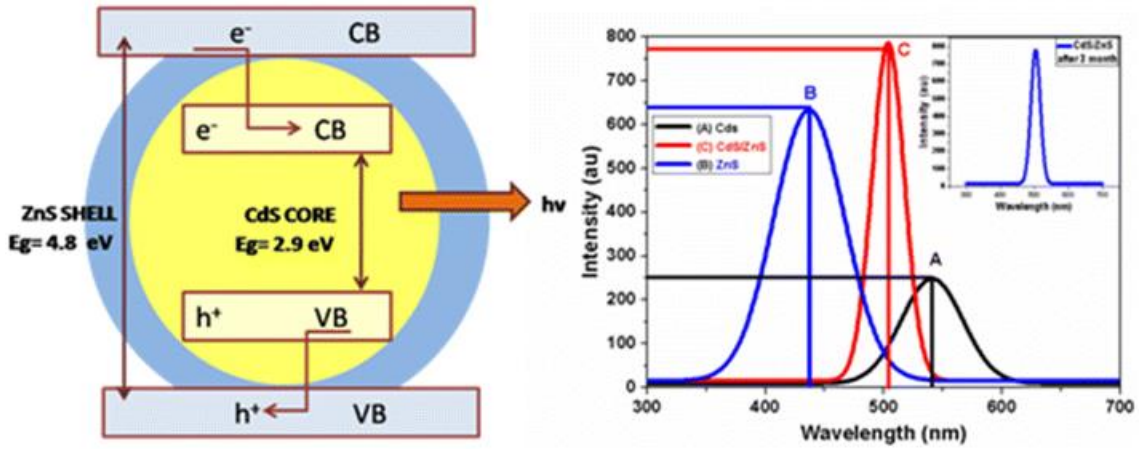

Figure 1.8 Schematic representation of CdS/ZnS core/shell structure and the PL spectra of CdS, ZnS and CdS/ZnS QDs.[27]

For biology and medical use, QDs should be in aqueous environment. Either QDs synthesized in organic medium can be transferred to aqueous medium or QDs can be directly synthesized in an aqueous medium. Three general methods have been used to transfer QDs into the aqueous phase (Figure 1.9):

1. Ligand Exchange: The hydrophobic capping agent (TOP/TOPO) on the surface of the QD can be changed with a water soluble ligand such as a thio-acid (HS-R-COOH) which has two polar ends (or functional groups) by the ligand exchange method. One end binds to the crystal surface and the second polar end interacts favorably with the aq. medium.
2. Silica Shell: QDs can be covered by a silica shell utilizing two types of silane, one hydrophobic to encapsulate the original hydrophobic cap, one hydrophilic to reside on the periphery and provide aq. suspension. Alternatively, two different silanes can be used in a ligand exchange followed by sol-gel reaction.

3. Interdigitating Bilayer via hydrophobic interaction: QDs can be coated by amphiphilic copolymers or phospholipids forming an interdigitated bilayer with the hydrophobic original coating of the QD with the hydrophobic component of the polymer or phospholipid, and exposing the hydrophilic component to the aq. medium.

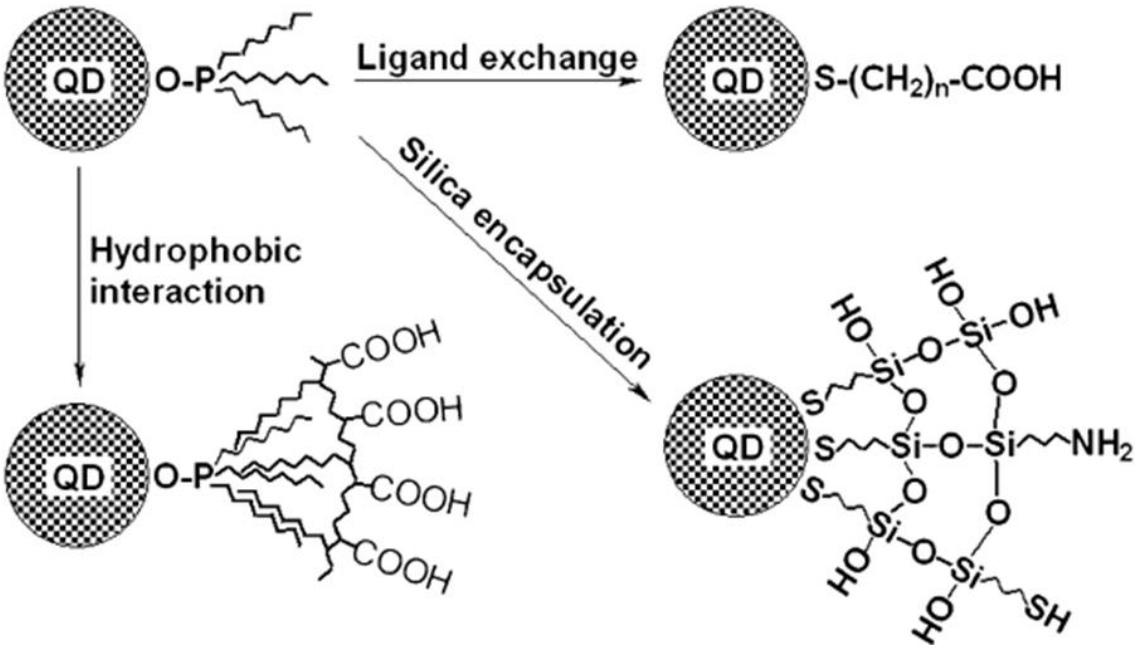

Figure 1.9 Three major methods to transfer hydrophobic particles into water[28, 29]

Each and every one of these methods has their own limitations. Some of them are very tedious procedures, and some cause a dramatic loss in the emission intensity of the particles with significant red shift of the emission peak due to surface perturbation.

Alternatively, QDs can be prepared in an aqueous medium by using water soluble precursors and capping agents. In a typical synthesis, Cd salts are dissolved in water and sodium salts of the chalcogenides are added in the presence of at least one type of difunctional capping agents. One of the functional groups should have high affinity for the crystal surface such as thiols for strong binding. The second functional group should

ave a favorable interaction with water, keeping particles suspended in an aq. medium (Figure 1.7 B).

In the aqueous preparation methods, many different water soluble coatings in the form of small molecules or as polymers can be used. [30-32] Most common coating materials studied in our laboratory are thioglycolic acid (TGA), 2-mercaptopropionic acid (2-MPA), 3-mercaptopropionic acid (3-MPA), 1-thioglycerol (1-TGL), L-cysteine (L-Cys), glutathione (GSH), meso-2,3-dimercaptosuccinic acid (DMSA) and polyacrylic acid (PAA). Structures of these organic coatings are seen Figure 1.10. Selection of the coating molecule influences the crystal growth and particle properties as will be discussed later. [31-34]

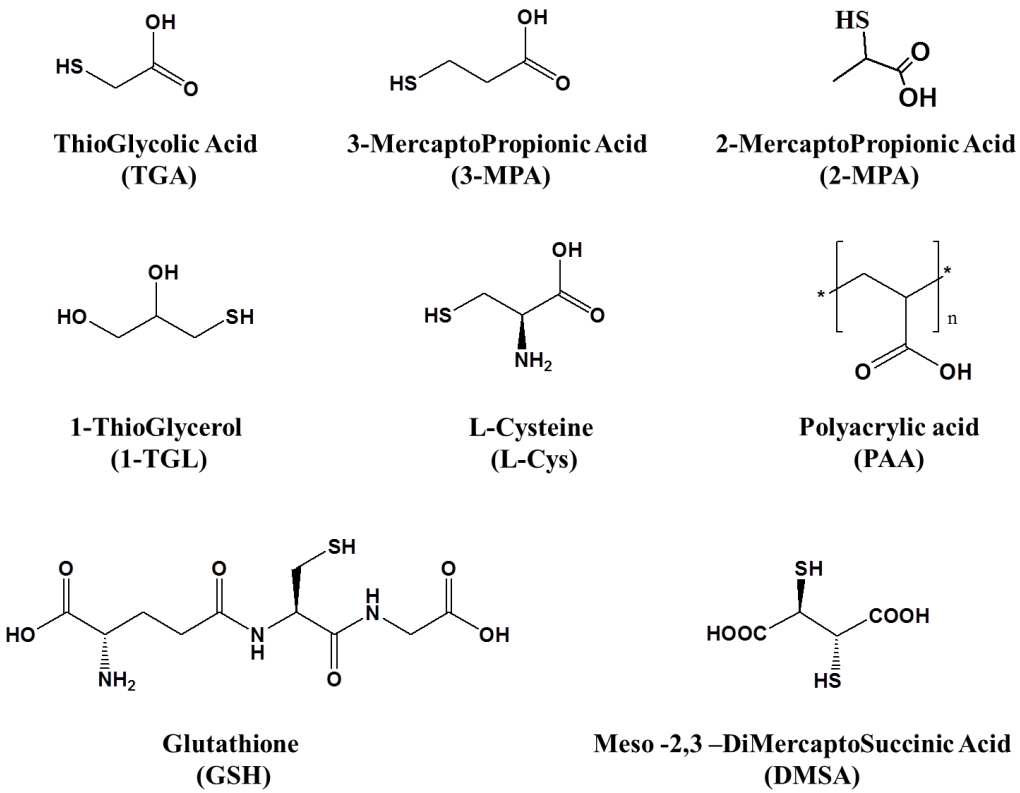

Figure 1.10 Chemical structures of the water soluble organic coatings.

In terms of chalcogen sources available for aq. synthesis of QDs, Na_2X (X:S, Se,Te), NaHX (X: Se, Te), thiourea and thioacetamide are the most widely used ones. Na_2X and NaHX are air sensitive. NaHX can be freshly prepared by the reduction of the elemental form of Te and Se.[35-38] Cadmium, zinc or silver mostly used as their acetate or nitrate salts.

Reaction temperature of an aq. synthesis varies from ambient temperature to 100 ^oC (reflux) affecting the nucleation, growth and the quality of the particles. As the reaction temperature increases, larger crystals obtained. Syntheses cannot be done above 100 ^oC thus crystallinity of the particles are lower and broader size distributions are usually seen with respect to hydrophobic QDs obtained at high temperatures in shorter times. However, transfer of these hydrophobic particles into water causes quite a loss in luminescence that, the lower quantum yields of the QDs obtained in aq. medium cease to be a problem. Therefore, direct preparation of QDs in water is more practical for the bioapplications, however, monodisperse particles with high PLQY is highly desirable within aq. method.

pH is usually an important factor affecting crystal growth and quality, possibly due to different complexes formed by the capping molecule and the cation (Cd^{2+}, Ag^{+}, etc.).[39, 40] Besides, stoichiometry between M and X, as well as the concentration of the capping molecule affects the crystal growth and particle quality which intern allows particle size tuning and luminescence quality. These will be discussed in detail in the fallowing chapters.

1.1.4 Medical and Biotechnology Applications of the QDs

Small size and luminescent properties of QDs are very attractive for bio-applications and medicine. One popular application of QDs is optical imaging both in the form of labeling and diagnostics. In addition, they can be used as a vehicle to transport active materials such as drugs and genes to cells and/or tissues, hence act as means for therapy. Since, the surface of QDs can be decorated with functional groups for

attachment of biologically significant molecules, they can be used as targeted delivery vehicles. Their bio/medical applications can be summarized as follows:[20, 35, 41-45]

- Diagnostics
  - In vivo optical imaging
    - Cell tracking
    - Vascular imaging
    - Cancer localization
  - In vitro optical imaging
    - Labelling live cells/organelles
    - Pathology
    - Nucleic acid sensing
- Therapy
  - Drug/gene delivery
  - Photo Dynamic Therapy

QDs have been also utilized in electronic and optical applications. Solar Cells[46, 47], Light Emitting Diodes (LEDs)[48], Photovoltaics[46, 49] and Lasers[50] are the main application areas for device technologies.

1.1.5 Comparison of QDs with Organic Dyes

QDs have strong light absorbance and may luminesce anywhere from visible to NIR based on their composition and size with usually a large Stoke`s shift. The surface of the QD can be engineered in such a way that it can be easily modified or conjugated with other molecules. QDs have broad absorbance and narrow symmetric emission

spectra. However, organic fluorophores have narrow absorbance range, asymmetric emission bands and small Stoke`s shift (Figure 1.11)[25]. A material specific excitation source must be used for the organic dyes and this makes excitation of different dyes impossible with a single excitation source. However, multiple wavelengths can be used to excite QDs and/or a single excitation source is sufficient to excite many different QDs simultaneously which is extremely advantageous for practical purposes. In addition, QDs have better color and signal resolution with the longer lifetime with respect to dyes. QDs have minimum interactions with the surroundings hence they are more photostable. Organic dyes photo-bleach in minutes, on the other hand, QDs retain their photostability over hours under continuous illumination.

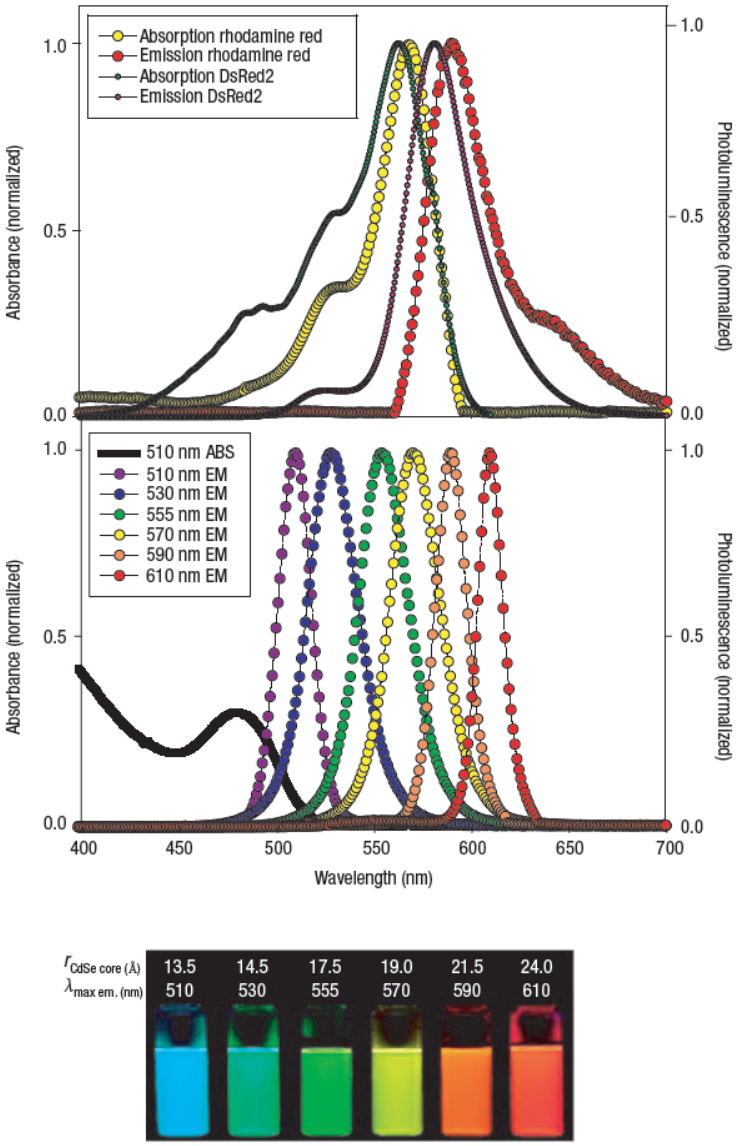

Figure 1.11 Absorbance and Emission spectra of organic dyes and CdSe Quantum Dots. Picture of the CdSe QDs stimulated at the same wavelengths corresponding their spectra above.[25]

Wu and Liu et al. have shown the difference between the photostabiliy of QDs and organic fluorophores.[51] They have labeled the nuclear antigen and microtubules of 3T3 cells with Alexa-488 dye and QD-630 simultaneously and followed the change in the fluorescence intensity over the course of 3 min. under continuous illumination. In the top row of the Figure 1.12, nuclear antigens were labelled with the QD and the

microtubules were labelled with the dye. In the bottom row, labeling was done in the reverse order. It was seen that emission of the dye bleached in 3 min. but, luminescence intensity of the QD was stable over 3 min.

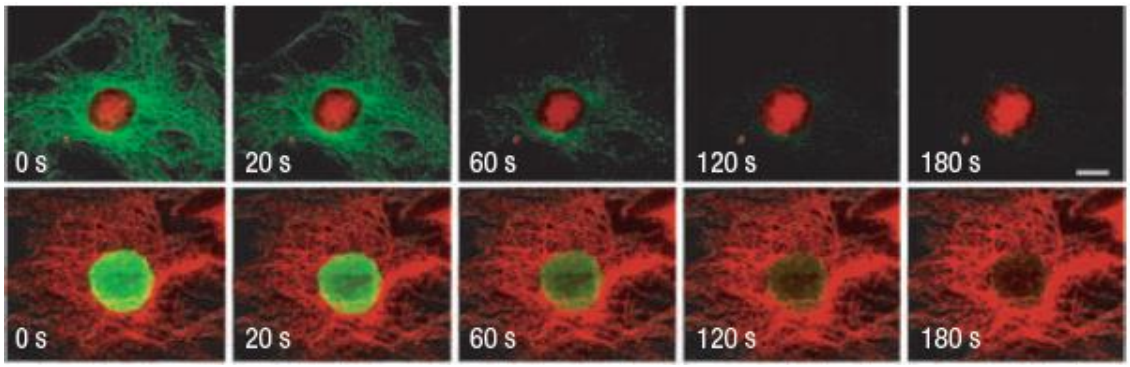

Figure 1.12 Photostability of QDs versus organic fluorophores. Top row: Nuclear antigens were labelled with QD 630–streptavidin (red), and microtubules were labelled with AlexaFluor 488(green) simultaneously in a 3T3 cell. Bottom row: Microtubules were labelled with QD 630–streptavidin (red), and nuclear antigens were labelled with AlexaFluor 488(green).[51]

1.1.6 Limitation of Cd-Chalcogenide QDs in biomedicine

One of the important concerns in the application of the QDs in biomedicine is the toxicity. Cd as a heavy metal has an intrinsic toxicity and most of the Cd-chalcogenides releases Cd^{2+}. In addition, these QDs emit in the visible region and are excited with UV pump. UV lights are harmful for living organelles and tissue as well as causing autofluorescence due to absorption of the body components such as hemoglobin, deoxyhemoglobin, collagens, in addition to scattering. As a result, penetration of UV and Visible lights through tissue are restricted. Therefore, Cd-chalcogenides are practical neither for deep tissue imaging nor for other in vivo applications.[25, 42, 52]

There are several methods to make Cd based QDs biocompatible. The simplest method is to coat the Cd-chalcogenides with PEG (polyethylene glycol). PEGylation decrease the toxicity and increase the blood circulation time of the QDs. Therefore, many times it

should be conjugated with a targeting ligand in order to increase the contact of particles with the target cell or tissue. The second method is the silanization or forming a silica shell around the QD. But, hydrolysis of silica shell may occur in time and mostly this is followed with PEGylation as well. Also, the method is tedious. Third, QDs can be coated with an amphiphilic polymer composed of both hydrophobic and hydrophilic parts. This might increase the size of the particles restricting the use of the QDs. Both of the methods are very laborious. Lastly, core-shell structures can be adopted. Coating the surface of QDs with ZnS layer enhance particle quality and minimize Cd release, rendering particles more stable and biocompatible.[14, 25, 42, 53]

Cd-free structures have been also developed to obtain non-toxic QDs utilized in bioapplications. InP[6], InAs/InP/ZnSe[54], $CuInS_2$/ZnS[55] and $CuInSe_2$[56] have been reported structures in the literature. They can be effectively used in biological application. However, preparation of those QDs is very laborious and expensive.

1.2 Near Infra-Red Emitting Quantum Dots (NIRQDs)

1.2.1 Advantages of NIRQDs

NIRQDs are highly popular in the recent years due to strong absorbance of the visible range and emission in the NIR window.

In photovoltaic solar cells, expanding the absorbance range into NIR is highly desirable in order to prevent heating of the device and to capture a broader range of the solar spectrum.[57] This can be best achieved with NIRQDs since most organic materials do not absorb in the NIR region.[57, 58]

In the biological applications, QDs offer enormous advantages over organic fluorophores with unmatched luminescence lifetime, higher sensitivity and broad absorbance-narrow luminescence emission band which enables excitation of multiple QDs at a single wavelength and multiplexing. However, QDs that are excited in the UV and emitting in the visible region are not that practical. Firstly, biological constituents like water, hemoglobin, deoxy-hemoglobin and lipids absorb and scatter light in the visible region (400-700 nm) (Figure 1.13). Thus, the light does not penetrate into deep tissue below 700 nm. [52, 59, 60] Secondly, the living tissues like collagen [58] has a significant autofluoresence in the visible region. [61] Thirdly, the penetration depth of visible light is limited.[61, 62] NIR light having less interaction with the tissues and body fluids is advantageous over organic and inorganic florescent components. The near infrared range (700-900 nm) defined as Near IR window I (NIR-I) is considered as an appropriate diagnostic window for biological applications especially for [44] [20] *in vitro* and *in vivo* imaging/labeling[43] and deep tissue imaging.[52] Some of the potential application areas of NIRQDs are stated in the chart in Figure 1.14. In addition to these, Lim et al, formerly also studied behaviors of the body fluids and constituents in the Near IR region (1200-1600).[63] They have shown that beside the NIR-I window, second Near IR region (NIR-II) is also safe for the deep tissue imaging in vivo without any background autofluoresence. However, NIR-II window is not practical due to the lack of cheap or routine instrumentation for imaging.

Some of the potential application areas of NIRQDs are stated in the chart in Figure 1.14. In addition to these, Lim et al, formerly also studied behaviors of the body fluids and constituents in the Near IR region (1200-1600).[63] They have shown that beside the NIR-I window, second Near IR region (NIR-II) is also safe for the deep tissue imaging in vivo without any background autofluoresence. However, NIR-II window is not practical due to the lack of cheap or routine instrumentation for imaging.

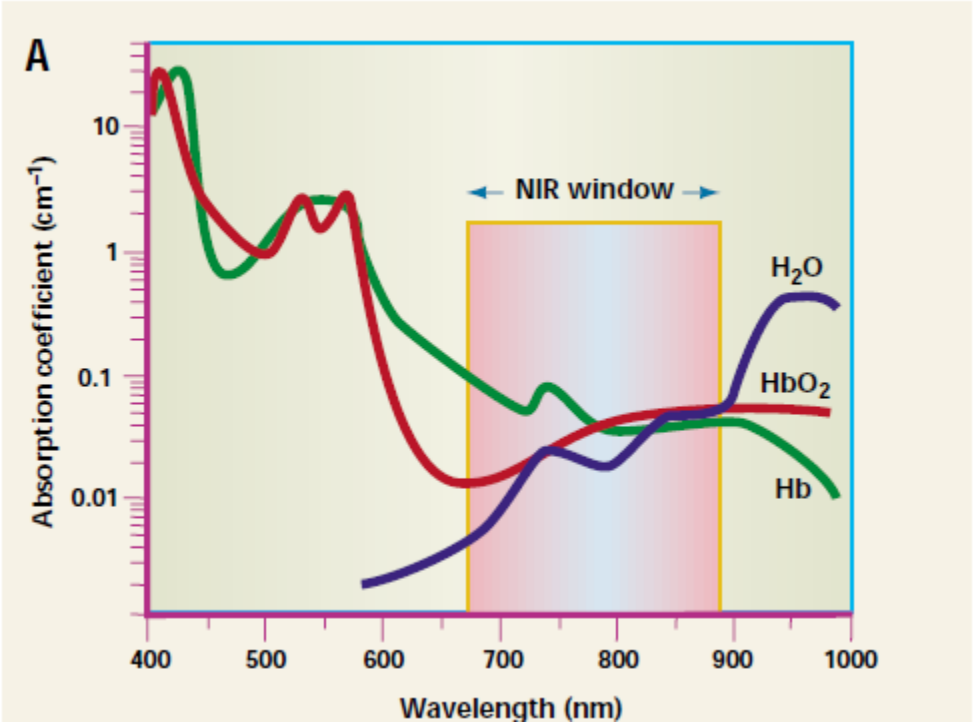

Figure 1.13 Absorption coefficients of the hemoglobin deoxyhemoglobin and water molecule with respect to wavelengths.

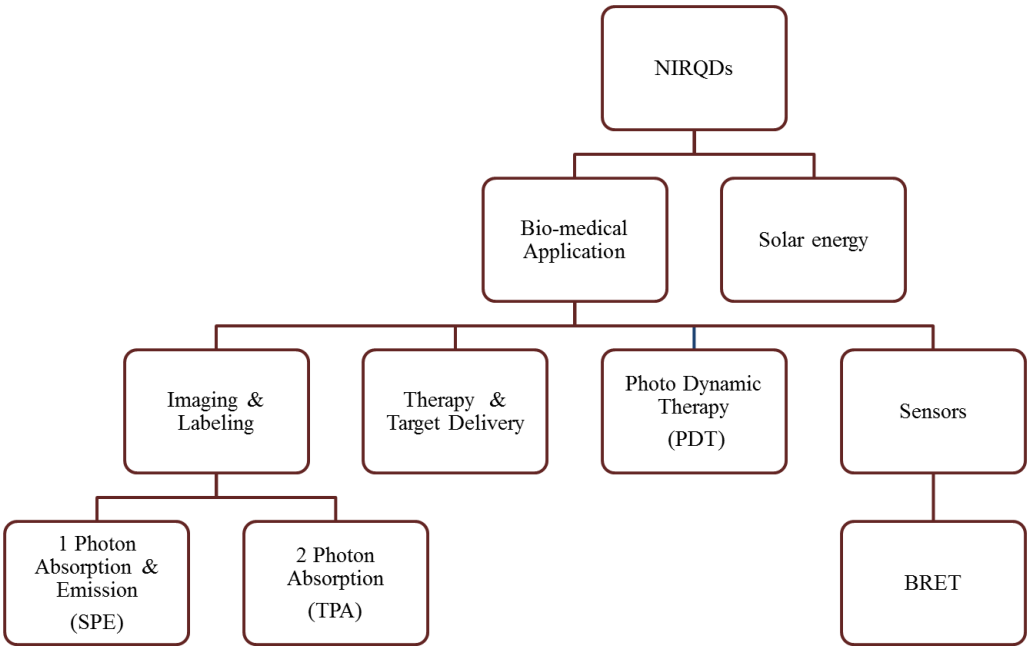

Figure 1.14 Potential application areas of NIRQDs

1.2.2 NIRQDs in Literature

Some typical examples of NIRQDs reported in the literature are CdSeTe,[35] CdSeTe/Cd, CdHgTe/CdS,[64] CdTe/CdSe/ZnSe[65] and PbS[52]. There are few NIRQDs that have been successfully used in the *in vivo* imaging: Morgan at al.[66] used CdMnTe/Hg QD as an angiographic contrast agent, Kim at al.[67] demonstrated imaging of sentinel lymph nodes in mouse with CdTe/CdSe QDs and Prasad et al.[68] used CdTe/ZnS QDs in imaging of Panc-1-tumor. However, apart from the imaging window consideration, toxicity is another important road-block in front of the practical use of QDs, especially for the *in vivo* applications. Elemental forms of cadmium, lead and mercury as well as their chalcogens are quite toxic.[54, 69] Although significant improvement in toxicity is achieved through core/shell structures and PEGylation of Cd-based QDs, there is a growing demand for Cd-free QDs for biotechnology and medical use.[68]

Nontoxic (reported by Hirsch et al.[70]) bulk Ag_2S have a band gap energy of 0.9 eV and is stable in α phase with a monoclinic crystal structure (α-Ag_2S).[71, 72] Therefore, Ag_2S QDs have great potential as biocompatible NIRQDs. Until 2013, there has been only couple of reports on Ag_2S synthesis and applications in medicine and biotechnology. Majority of the work on silver chalcogenides and their bioapplications appeared in the literature during the duration of this thesis work. Most of the Ag_2X (X: S, Se, Te) NIRQDs in the literature have been prepared in organic medium using organic soluble coating materials. [69, 73-75] Those quantum dots have emission characteristics in the 650-1200 nm range with very low photoluminescence quantum yield (below 2%).[74, 75] Alternatively, Zhu et al synthesized Ag_2S nanoparticles in ethyleneglycol at above 140 ^{o}C by the decomposition of 3-mercaptopropionic acid and transferred resulting particles into water phase without any ligand exchange procedure.[76] This is an important aspect since for medical or biological applications, QDs have to be suspended in aqueous medium. Usually this is done through ligand exchange or overcoat.[53, 77] Ligand exchange often cause decrease in the

luminescence intensity which is not desirable. Therefore, aqueous preparation of Ag_2X NIRQDs is more practical for biological studies. There are few examples of Ag_2X NIRQDs prepared in aqueous media. In one of the earlier reports, Castanon et al. demonstrated aqueous synthesis of Ag_2S nanoparticles larger than 30 nm without any emission data.[78] More recently, Remya et al prepared aqueous Ag_2S nano-clusters in two steps through hydrothermal decomposition of the gluthathione complex of Ag nanoparticles at low temperature over 24h.[79]

Although it was very limited until last year or so, reports indicated high biocompatibility of Ag_2S QDs making them superior to Cd and Pb based systems.[80-83] Until recently, only toxicity (almost nontoxic up to 50μg/ml) of Ag_2Se NIRQDs have been reported and used for *in vivo* imaging.[73] Two of the most recent studies on Ag_2S QDs involve the evaluation of cytotoxicity, cell proliferation, ROS (reactive oxygen species) generation, apoptosis, necrosis and DNA damages related to Ag_2S QDs and both of them reported high biocompatibility.[84, 85] They also showed effective optical imaging both in vivo and in vitro utilizing Ag_2S NIRQDs emitting in NIR I and NIR II windows.

1.3 Hybrid Nanoparticles

Multifunctional nanoparticles capable of different functions are of great interest especially in biotechnology and medicine where dose is a concern and multiple actions are desired. One very valuable hybrid composition is Superparamagnetic Iron Oxide Nanoparticles (SPIONs)) and luminescent QDs which are responsive to magnetic field and light, simultaneously. Such hybrid materials allow great opportunity in multiplexed sensors but mostly in medicine with potential for dual sensing (magnetic and optical) and dual action like sensing-separation or sensing and magnetic dragging and combined action of therapy-imaging.

Magnetite (Fe_3O_4) and maghemite (γ-Fe_2O_3) demonstrate a superparamagnetic behavior in very small size regime (less than 10nm) as a single crystal. They achieve high

magnetization in an external magnetic field with a complete loss of magnetization upon removal of the external magnetic field, therefore can be safely used in medicine. Besides, superparamagnetic iron oxide nanoparticles (SPIONs) are relatively safe and non-toxic. SPIONs are proven as effective contrast agents in MRI which utilizes changes in the relaxation of protons in the vicinity of SPIONs.[86] Also, they have been commercially used in magnetic separation of cells, proteins etc.[87] Ability to respond to magnetic field are also exploited in magnetic targeting, where SPIONs tagged with therapeutic agents were targeted to the tissue or cells with a magnetic field localized around the target site. [88, 89] This is further extended to therapy called hyperthermia where the target tissue, usually the cancerous tissue, is heated up by SPIONs in alternating field.[87, 90] Therefore, such hybrid nanoparticles offer great potential for MRI and optical imaging for medical diagnosis combined with therapy and targeting abilities.[91] In a way, they are good theranostic materials.

Hybrid nanoparticles have been prepared by different methods in the literature (Figure 1.15). Mostly, co-encapsulation of magnetic and luminescent nanoparticles within silica or polymeric matrices is used.[92, 93] They can be also prepared by epitaxial growth of the second particle on the first one.[94, 95]

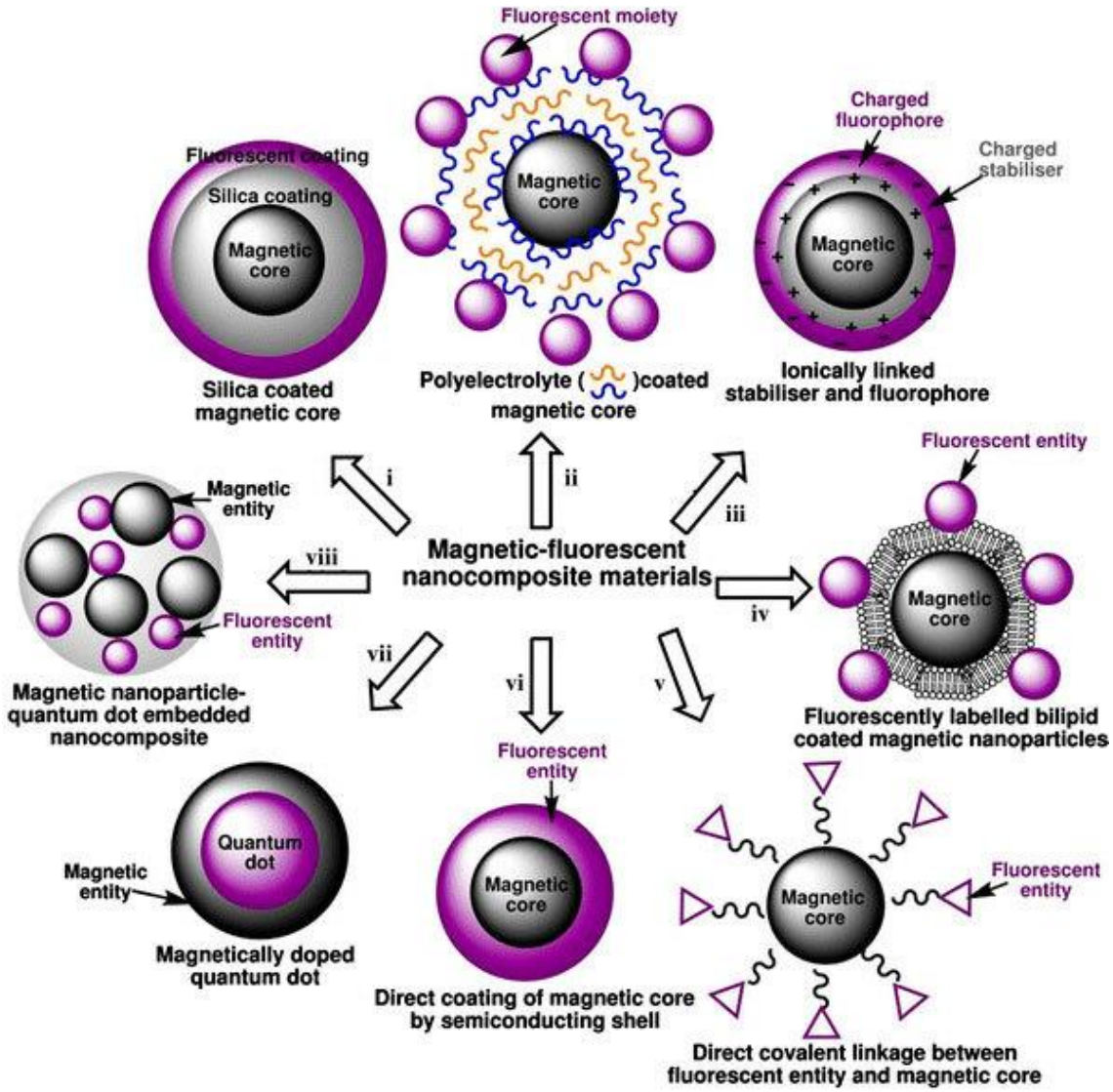

Figure 1.15 Different methods for the preparation of SPION hybrid nanoparticles.[96]

Formerly reported hybrid nanoparticles have been prepared from magnetic nanoparticle and QDs (Cd based) emitting in the visible region. They were used for the purpose of dual imaging in bioapplications and magnetic separation with optical imaging etc. In more recent studies hybrid nanoparticles (from CdTe and SPION) have been prepared and successfully used the in vivo and in vitro drug delivery enhanced with magnetic targeting. [97] Also, most recently, Cd-free structures like C-dots have been combined with SPION to minimize toxicity effects.[98]

QDs (Cd-chalcogenides) emitting in the visible region is not practical for the bioapplications concerning toxicity, autofluorescence and deep tissue imaging. Beside these, SPIONs have strong absorption in the visible region so some of the emitted photons are absorbed by SPIONs, decreasing the overall emission intensity of the hybrid.. As SPIONs do not absorb NIR light and NIRQDs can be excited with lower energy with respect to visible QDs, emitted photons should not be affected by the presence of SPIONs. In addition, IR lights penetrate deeper and autofluorescence of the living tissue is lower at NIR region. Thus, NIRQDs are the best candidates to prepare multifunctional hybrid nanoparticles with SPIONs for bio-medical applications.

1.4 Proposal and Aim of this Thesis Work

Despite of great potential and promise of quantum dots in medicine and biotechnology, practical and clinical applications of QDs are limited due to mentioned limitations. Therefore, there is a tremendous need for the development of safe and strongly luminescent Quantum Dots working in the NIR-window to eliminate autofluoresence of tissue and provide deep tissue imaging with excitation in the visible wavelengths. Functional surfaces for the attachment of biologically significant species such as targeting ligand, drugs or genes are necessary for advanced utilization of QDs. Colloidal stability and long term luminescence stability are critical for practical applications of these QDs as well. Last but not least, an economic and simple preparation method utilizing safe starting materials are highly desirable from industrial

perspective for the commercialization of QDs. To address these limitations and needs, all the studies performed in this thesis work, aimed to develop size and emission tunable aqueous silver chalcogenide QDs emitting in the NIR-I window, directly in aqueous medium from safe starting materials at relatively low temperatures and perform physical/chemical characterization and evaluate their potential as imaging agents and theranostic materials. One additional goal of this thesis is to develop multifunctional hybrid nanoparticles from silver chalcogenides and superparamagnetic iron oxide nanoparticles in a simple way to provide unique nanostructures that can be addressed and detected both optically and magnetically, providing opportunity for dual imaging (MRI and optical), combined action of sensing and dragging (optical magnetic sensing and magnetic dragging), diagnosis and therapy (drug delivery and hyperthermia) as well as multiplexed sensing.

Three different approaches have been adapted to achieve size tunable synthesis of silver chalcogenides, mainly silver sulfide:

1. Investigation of reaction variables such as Ag/S ratio, coating amount, temperature and length of the reaction in a standard aqueous synthesis utilizing silver nitrate, sodium sulphide and 2-mercaptopropionic acid as a coating. This represents the most conservative approach.

2. Use of slow sulphur releasing reagent, *meso*-2,3-dimercaptosuccinic acid (DMSA). This method has been discovered in Dr. Acar`s laboratory previously. The uniqueness of this approach comes from the fact that DMSA acts both as a biocompatible coating and a S-source.

3. Development of alloys : $Ag_2Te_xS_y$. This is one of the most unique approaches of this study and this is the first report of such particles.

In the aqueous preparation methods, many different water soluble coatings can be used.

Acar et al.[31] synthesized 2-MPA and 3-MPA coated CdS QDs and found out that 2-

MPA coated CdS QDs have remarkably higher photoluminescence quantum yield (54% vs 19%) and stability (over years) compared to 3-MPA coated CdS.

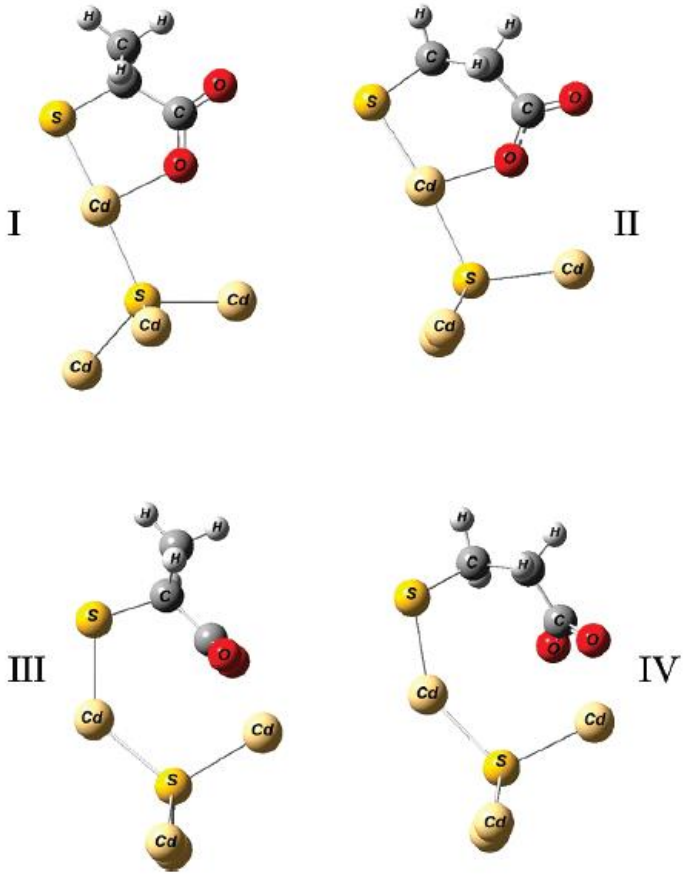

Figure 1.16 Four binding structure models of 2-MPA (I-III) and 3-MPA (II-IV) to CdS.

Ab initio calculations of four possible structures mimicking interaction/binding of 2MPA molecules with the CdS surface (Figure 1.16) indicated that 2-MPA binds to the surface via carboxylate as well (structure I, Figure 1.16),possibly causing the observed improved luminescence and stability. For the purpose of size and emission tuning of the Ag_2S QDs, typical variables such as Ag/S ratio, coating amount, temperature and length of the reaction were studied in a routine aq. preparation technique.

Another approach in controlling particle size, hence emission wavelength, involves use of DMSA which acts both as a coating and a slow S-releasing agent as demonstrated before by Sevinc et al. in the size tunable synthesis of CdS QDs. [34] DMSA is a FDA approved drug used as metal chelating agent, especially in heavy metal poisoning. Sevinc et al. discovered that it is not only a strong binding ligand for CdS but also a S-source if appropriate temperature and pH is used. Therefore, this dual function of DMSA was investigated in the synthesis of Ag_2S NIRQDs.

As the third approach to size tunable Ag_2S NIRQDs alloys alloyed with Te was attempted. Ag_2Te has lower band gap energy (0.65 eV [71]) than Ag_2S. Therefore, alloys composed of different ratios of Te/S may provide size and emission tunability in a broader range. For this purpose, aqueous synthesis of 2-MPA coated Ag_2Te and $Ag_2Te_xS_{1-x}$ has performed. Influence of different S-sources on the composition and optical properties was studied utilizing Na_2S, thioacetamide (TAA) and DMSA as a sulfur source in two different ways: 1) simultaneous addition of chalcogens, 2) sequential addition of chalcogens. Na_2S was used as a fast and DMSA and TAA were used as slow S-releasing agents which would impact the crystal growth and composition. Compositional changes as a result of chalcogen source and addition sequence was investigated.

Lastly, superparamagnetic and NIR luminescing hybrid nanoparticles were prepared in a simple ligand exchange method from SPIONs (Fe_3O_4) and Ag_2S-2MPA NIRQDs where two particles were bound together through 2-MPA: Carboxylates binding to SPION and thiols binding to QD surface. Response of SPIONs to external magnetic field has been widely utilized to target nanoparticles to the site of interest such as tumors and enhance internalization of nanoparticles increasing the therapeutic effect and decreasing potential side effects.[88, 89] A hybrid nanoparticle therefore can be targeted via magnetic manipulation. Also, combinations of imaging modalities are desirable. Optical imaging has a benefit of sensitivity but lack resolution and has depth limitation, whereas MRI offers high resolution at any depth but lack sensitivity.[91]

Combination of the two in a single entity may provide a synergistic effect and provide both sensitivity and high resolution in medical imaging. Functional surfaces are effective in conjugating targeting ligands which would enhance the targeting ability. Furthermore, functional groups of the hybrid nanoparticles can be utilized to load drugs to the hybrids and therefore create highly functional theranostic nanoparticles.

For the evaluation of these new silver chalcogenide quantum dots and their hybrids with SPIONs as biomedical materials, a series of in vitro studies were planned: cytotoxicity and hemocompatability studies for biocompatability and confocal laser microscopy for the optical detection of QDs in cells in vitro and evaluation of potential as an optical probe.

Chapter 2

2 SYNTHESIS AND CHARECTERIZATION OF AQUEOUS 2-MPA COATED Ag_2S NEAR IR EMITTING QUANTUM DOTS

2.1 Introduction

Quantum dots with their unique optical and electrical properties initiated many developments in a variety of technology areas. Group II-VI semiconductors, CdS, CdTe and CdSe, are the most studied ones and they emit in the visible region.[14, 42, 99] Lately, there is a tremendous demand for near infrared (NIR) emitting quantum dots (NIRQD), especially in biological applications and in efficient solar energy conversion.[100]

Quantum Dots emitting in the Near-Infrared region (NIRQD) has emerged as a response to increasing demand for more suitable QDs in biotechnology and medicine. Biological molecules or natural constituents such as hemoglobin, deoxyhemoglobin and water have intense interactions with visible monochromatic light.[52] Living tissues also have autoflorescence in the visible region. Near-Infrared (NIR-I) region between 700-900 nm where absorption and scattering activities are lower in the living tissues, defined as the therapeutic window.[44, 52]

The most frequently used NIRQDs are Cd-based, such as CdTeS, CdHgTe/CdS[64] and CdSe/CdTe[65] and there are few examples to their bio-applications.[20, 57] For example, Prasad et al. showed imaging of panc-1-tumor using functionalized CdTe/ZnS QDs.[68] CdMnTe/Hg QDs were used as an angiographic contrast agent by Morgan et al.[66] and CdTe/CdS QDs were used in the in vitro cell and in vivo tumor imaging.[99] However, heavy metal toxicity is an important concern for both *in vitro* and *in vivo* studies.[54] Recent efforts are directed towards development of Cd, Pb and Hg free, biocompatible QDs. Therefore, there is an urgent demand and a tremendous effort to decrease the cytotoxicity of QDs and/or to develop non-cytotoxic QDs.[101]

Ag_2S have a band gap energy of 0.9 eV and is stable in α phase with a monoclinic crystal structure (α-Ag_2S).[71, 72] Previously, Hirsch reported no significant toxicity of bulk Ag_2S.[70] Non-aqueous preparation of silver chalcogenide NIRQDs and their properties for potential applications have been recently documented in the literature. [69, 74, 75, 102] These Ag_2X-NIRQDs (X:S, Se, Te) emit in the range of 690-1127 nm, but exhibit low photoluminescence quantum yields (PLQY below 2%). Aqueous preparation methods for colloidal Ag_2S nanoparticles, relevant for biological applications, are quite rare in the literature. Castanon et al prepared Ag_2S in aqueous media but particles were at least 30 nm and no data on optical properties were available.[78] Considering the low band gap and potential for cytocompatibility, aqueous Ag_2S nanoparticles especially with improved luminescence are one of the best candidates for NIRQDs for biological applications.[74, 75]

Here, one-step synthesis of 2-mercaptopropionic acid (2-MPA) coated aqueous Ag_2S NIRQDs were demonstrated. Influence of reaction variables such as Ag/S, 2-MPA/Ag ratios and reaction temperature on the optical properties of nanoparticles were investigated. For potential biological uses, cytocompatibility of particles were investigated and an *in vitro* imaging using NIH/3T3 cell lines were demonstrated.

2.2 Experimental

2.2.1 Materials

All reagents were analytical grade or highest purity. Silver nitrate (AgNO3) was purchased from Sigma-Aldrich. Sodium sulfide (Na_2S) was purchased from Alfa-Aesar. 2-Mercaptopropionic acid (2-MPA), aceticacid (CH_3COOH), sodium hydroxide (NaOH), and 4% paraformaldehyde were purchased from Merck. LDS 798 Near-IR laser dye was purchased from Exciton Inc. Milli-Q water (18 mOhm) was used as solvent. DMEM medium (with 1.0 g/L glucose, stable L-glutamine, 3.7 g/L $NaHCO_3$, and phenol red), 10% fetal bovine serum and Trypsin-EDTA were purchased from Biochrom AG, Germany. 1% penicillin-streptomycin antibiotic solution was purchased from HyClone, USA. Sodium 3′-[1-(phenylaminocarbonyl)-3,4-tetrazolium]-bis (4-methoxy-6-nitro) benzene sulfonic acid hydrate (XTT) assay was purchased from Biological Industries, Israel. Thiazolyl blue tetrazolium bromide (MTT) *Biochemica* was purchased from AppliChem, Germany. 96-well plates were purchased from Greiner Bio-One, Germany. 6-well plates were purchased from Orange Scientific, Belgium.

2.2.2 Preparation of Ag_2S-2MPA NIRQDs

As an example, 2-MPA was dissolved in 75 ml of deoxygenated deionized water. pH of the solution was adjusted to 7.5 by using NaOH and CH_3COOH solutions (2M). Then, 42.5 mg of $AgNO_3$ was added, pH was readjusted to 7.5 and solution was brought to the desired temperature (30, 50 or 90 ^oC). 25 ml of deoxygenated aqueous Na_2S solution was then added slowly to the reaction mixture under vigorous mechanical stirring at 5000 rpm. During the reaction, samples were taken at different time points to follow the particle growth. Prepared quantum dot solutions were washed with DI water using Amicon-Ultra centrifugal filters (3000 Da cut off) and stored in dark at 4 ^oC.

Influence of reaction variables were studied in different reactions keeping the Ag concentration fixed at 2.5mM and varying the sodium sulfide and 2-MPA concentrations to achieve Ag/S ratio of 2.5, 4, 6 and 2-MPA/Ag ratio of 5 and 10.

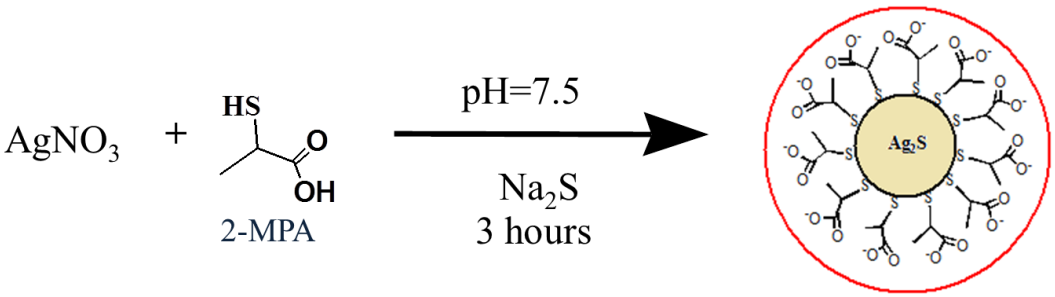

Scheme 2.1 Aqueous synthesis of 2-MPA coated Ag_2S NIRQDs.

2.2.3 Cell Culture

Culturing of mouse fibroblast cells (NIH-3T3) was done according to ATCC recommendations. Cells were cultured in DMEM medium with 1.0 g/L glucose, stable L-glutamine, 3.7 g/L $NaHCO_3$, and phenol red. Full medium also contained 10% fetal bovine serum and 1% penicillin-streptomycin antibiotic solution. Trypsin-EDTA was used for cell detachment. Cells were incubated 37 ^oC under 5% CO_2.

2.2.4 Evaluation of cytotoxicity

XTT assay was used for the evaluation of cytotoxicity. 10,000 cells/well in 96-well plates were seeded. Following overnight incubation, medium was replenished; cells were treated with QDs (10 to 600 µg/ml) and incubated for 24 h. After washing, XTT reaction solution was added and incubated for 2 h. Spectrophotometric readings were taken at 500 and 650 nm. Absorbance at 650nm was subtracted from the absorbance at 500nm which corrects the results for the QD absorbance. For each sample, six replicates were used from two independent experiments. Statistical significance of the observed differences was determined using one-way ANOVA with Tukey's multiple comparison test of GraphPad Prism software package from GraphPad Software, Inc., USA.

2.2.5 Cell Imaging

50,000 cells/well in 6-well plates containing cover glasses were seeded. After overnight incubation, cells were treated with 200 ug/mL QDs in full medium for 24 h. Following the wash step, cells were fixed with 4% paraformaldehyde. Zeiss LSM 510 confocal laser scanning microscope equipped with a Plan-Neofluar 40X (NA: 1.3) objective was used for image acquisition. Excitation wavelength was 543 nm. LP605 filter was used to collect QD emission.

2.3 Characterization Methods

Absorbance spectra were taken with a Shimadzu 3101 PC UV-vis-NIR spectrometer in the 300-1000 nm range. Particle sizes were calculated from experimentally measured absorption edge by using the Brus equation[12, 13](eqn.1)(Appendix A)

$$\Delta E = \frac{\hbar^2 \pi^2}{8R^2}\left[\frac{1}{m_e}+\frac{1}{m_h}\right]-1.8\frac{e^2}{\varepsilon_{Ag_2S}\,4\pi\varepsilon_0 R} \quad (1)$$

where ΔE is the band gap energy difference between the bulk semiconductor and the nanocrystal, R is the radius of the nanocrystal, m_e (0.286 m_0) and m_h (1.096) are the respective effective electron and hole masses for Ag_2S,[72] and ε_{Ag2S}(5.95) is the dielectric constant.[72]

In the photoluminescence (PL) measurements, Ag_2S-2MPA samples were excited with a continuous-wave, frequency-doubled Nd:vanadate laser operating at 532 nm. The excitation beam was chopped at 24 Hz to provide reference for lock-in detection. The emitted luminescence was then collected with a concave gold reflector and imaged into a 0.5-meter Czerny-Turner monochromator. An amplified silicon detector sensitive over the wavelength range of 400-1100 nm was used together with a lock-in amplifier. The excess pump light was blocked by using a long-pass filter that had a transmission of 90% from 550 to 1100 nm. In the determination of the luminescence bands, the spectral response of the detection system was also taken into account. For Quantum

Yield (QY) calculations, samples were prepared at five different concentrations and LDS 798 NIR dye in methanol (quantum yield reported as 14% by the producer) was used as a reference. QY calculations were done based on the procedures detailed in the literature.[30, 32, 103]

A few ml of the Ag_2S-2MPA solutions were freeze-dried for X-PS, X-RD and ATR-FTIR analysis. Thermo Scientific K-Alpha XPS with Al K-alpha monochromatic radiation (1486.3 eV) was used for the XPS analysis of Ag_2S nanoparticles. Powdered samples were placed on an aluminum adhesive tape. 50.0 eV pass energy was used for the scans with flood gun. A 400 μm spot size was used. A base pressure of better than 3×10^{-9} mbar and experimental pressure of 1×10^{-7} mbar were achieved. C1s peak at 285.0 eV was used as a reference. For XRD measurements, the powdered sample was placed on a piece of glass with a double sided sticky tape. Tape was attached to sample holder with dough. D8 advance Bruker instrument with Cu K-α radiation (λ=1.5406 A^o) was used for the crystal pattern analysis between 2θ angles of 10^o and 80^o. Infrared Spectra were taken with a Thermoscientific Nicolet iS10 instrument (ATR-FTIR) in the wavenumber range of 400-4000 cm^{-1}.

TEM images were taken on a Tecnai G2 Spirit BioTwin Transmission Electron Microscope with single-tilt specimen holder (FEI Company) operated at 120kV. Samples were prepared by dropping a dilute Ag_2S-2MPA colloidal solution on a carbon coated copper grid and letting to dry.

Malvern zetasizer nano S (red badge) ZEN 1600 was used for the measurement of hydrodynamic size of aqueous nanoparticles. The zeta potential of colloidal solutions was measured with Brookhaven zetapals, Zetapotential analyzer instrument by using the Smoluchowsky model.

Spectro Genesis FEE Inductively Coupled Plasma Optical Emission Spectrometer (ICP OES) was used for determination of Ag concentration in solutions. QDs were digested with acids and diluted to certain volumes. Ag^+ ion concentrations in solutions were determined by correlating regressed standard curve.

2.4 Results and Discussions

2.4.1 Synthesis and Characterization of Ag_2S-2MPA NIRQDs

2-MPA coated Ag_2S QDs were prepared in water with slow addition of sulfide to 2-MPA-silver salt mixture. Color of the solution turns into yellow with the addition of sulfide ion and the resulting colloidal QD solution has a dark brown color.

The crystal structure of the formed nanoparticles was investigated by powder XRD. A broad XRD spectrum was recorded for the as-made Ag_2S-2MPA nanoparticles as seen in Figure 2.1, similar to those reported by Jiang et al.[74] The nano size of the particles causes peak broadening and the amorphous coating hides the crystal peaks. After samples were heated up to 180 ^oC over 1h under Ar atmosphere, sharp identifiable peaks were obtained in the XRD spectrum (Figure 2.1 b). Coating material may decompose or detach from the nanoparticle surface and particles may grow at 180 ^oC providing a well resolved pattern. The obtained pattern corresponds to monoclinic α-Ag_2S XRD pattern (stable crystal form at ambient atmosphere) having JCPDS No: 14-72 (according to STOE WinXPOW software) which is in agreement with previous reports.[74, 78]

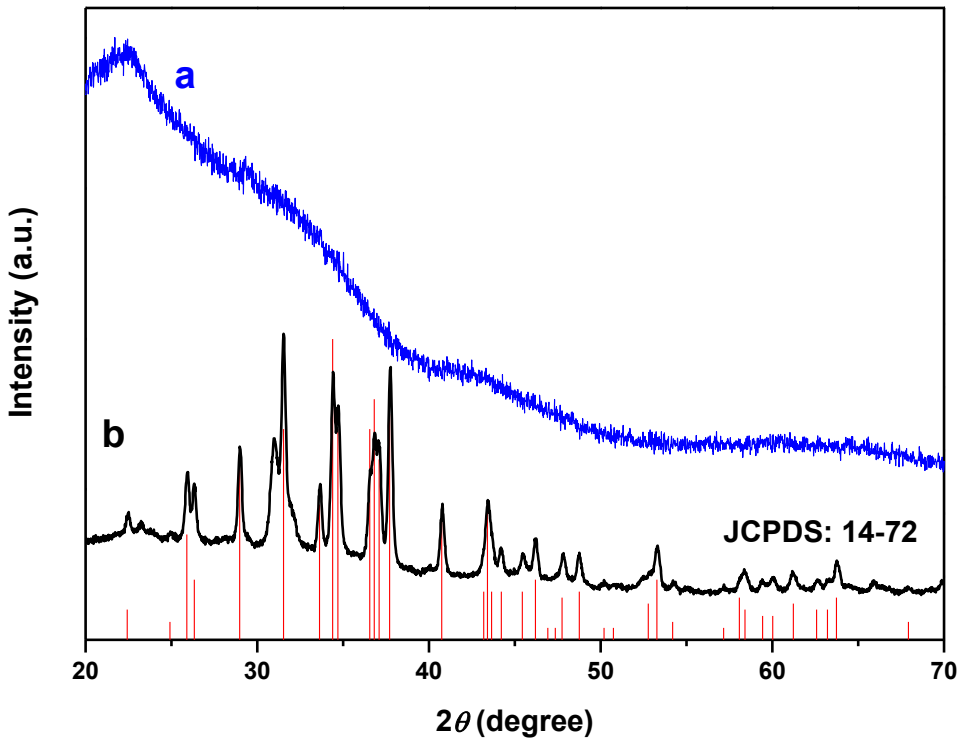

Figure 2.1 XRD patterns of Ag_2S QDs (a) at room temperature and (b) after 180 ^oC heat treatment.

The IR spectrum of Ag_2S-2MPA confirms binding of 2-MPA from the thiol since there is no S-H stretching band around 2560 cm^{-1} but confirms the presence of 2-MPA (Figure 2.2). Strong bands at 1560 and 1390 cm^{-1} are typical for asymmetric and symmetric stretching modes of carboxylate and peaks at 2968 cm^{-1} and 2928 cm^{-1} are assigned to asymmetric and symmetric C-H stretching of 2-MPA.

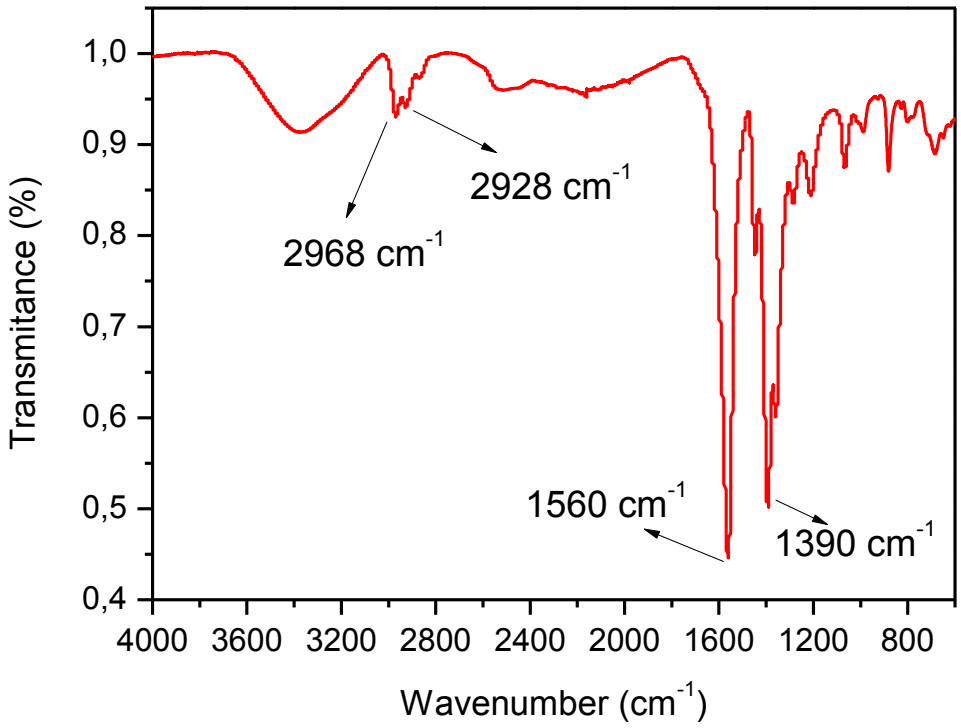

Figure 2.2 IR spectrum of 2-MPA coated Ag_2S NIRQDs.

XPS of Ag_2S-2MPA NIRQDs confirmed the chemical structure. Figure 2.3 shows the Ag3d and S2p core level peaks of Ag_2S. Binding energies (BE) of Ag $3d_{5/2}$ and $3d_{3/2}$ spin-orbit pair shows up at 367.5 eV and 373.5 eV (Level 0: no etching)) (Table 2.1 and Figure 2.3) which agrees well with the literature values for Ag_2S.[104, 105] These signals shifted to 367.7 eV and 373.7 eV when the surface was etched by Ar^+ plasma (Level 1). The difference between the levels can be seen in Figure 2.3 c. The S2p core level could be fitted to two different spin-orbit coupling pairs (Figure 2.3 b). The $S2p_{3/2}$ peak at 161 eV is indicative of Ag-S-Ag bond and the second $S2p_{3/2}$ peak at 163 eV is due to the thiol of the capping agent (2-MPA).[104, 106] Depth analysis through plasma etching supports such a peak assignment. As can be seen in figure 2.3 d, the peak around 163 eV diminished and two peaks at 160.41 and 161.58 eV dominated the S2p core level spectrum after etching. Both of these peaks are due to core Ag_2S but upon

etching, slight differences in the chemical environment may occur, causing such a slight shift in the peak position. Area analysis of the peaks indicates a sulfur rich surface and a major contribution from 2-MPA (Tables 2.1and 2.2). Upon etching, the Ag/S ratio reaches the theoretical value of 2 and the ratio of sulfur from Ag-S to sulfur from 2-MPA increases (Table 2.2).

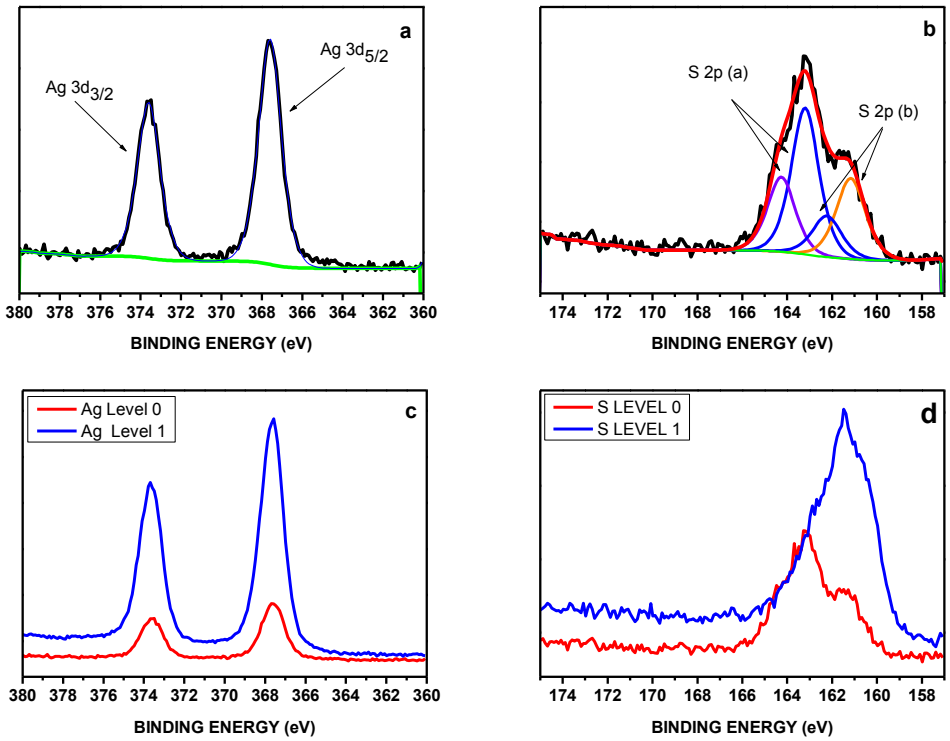

Figure 2.3 (a) Ag3d and (b) S2p XPS spectra of Ag_2S-2MPA QDs before plasma etching. Comparison of (c) Ag3d and (d) S2p peaks before (level 0) and after (level 1) plasma etching.

Table 2.1 Binding Energies of Ag and S core levels

	Peak	BE (eV)	FWHM	% Area
LEVEL 0				
	$Ag3d_{5/2}$	367,49	1,44	20,93
	$Ag3d_{3/2}$	373,51	1,44	
	$S2p_{3/2}$	161,00	1,69	33,1
	$S2p_{1/2}$	162,06	1,69	
	$S2p_{3/2}$	162,93	1,31	45,98
	$S2p_{1/2}$	164,13	1.31	
LEVEL 1				
	$Ag3d_{5/2}$	367,66	1,34	20,07
	$Ag3d_{3/2}$	373,66	1,34	
	$S2p_{3/2}$	160,41	1,25	9,25
	$S2p_{1/2}$	161,47	1,25	
	$S2p_{3/2}$	161,58	2,4	20,63
	$S2p_{1/2}$	162,84	2,4	

Table 2.2 Atomic ratios of Ag and S by XPS analysis.

	Ag/S_{Ag-S}	Ag/S_{total}	S_{Ag-S}/S_{2-MPA}
LEVEL 0	0,632	0,265	1,39
LEVEL 1	2,170	0,672	2,23

2.4.2 Influence of the reaction variables on particle properties

Ag_2S-2MPA quantum dots have a near band-edge emission (Figure 2.4). Particle size and properties can be tuned with reaction temperature, ligand/Ag, and Ag/S ratio. Changing such parameters changed the crystal size of particles between 2.3-3.05 nm with hydrodynamic sizes up to 4.7 nm (Table 2.3, Figure 2.5). Hydrodynamic sizes

measured by DLS are larger than the calculated crystal sizes due to the presence of thin organic coating (2-MPA) on the nanocrystals. All the colloidal particles have a negative surface potential at and above -30eV as expected from carboxylate groups on the surface, which supports colloidal stability. Luminescence peaks are rather broad with FWHM around 160 nm but this is usual for aqueous preparations.[31, 74, 75]

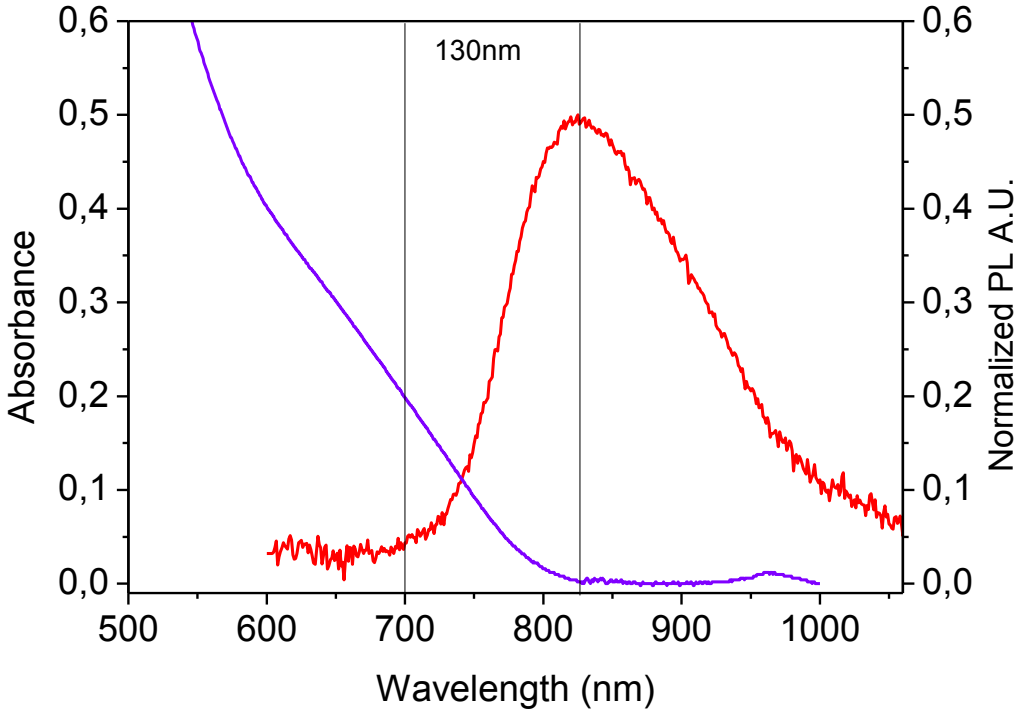

Figure 2.4 Absorbance and photoluminescence spectrum of Ag_2S QD (Ag/S=4 2-MPA/Ag=5 T=50 ^oC 7h reaction.)

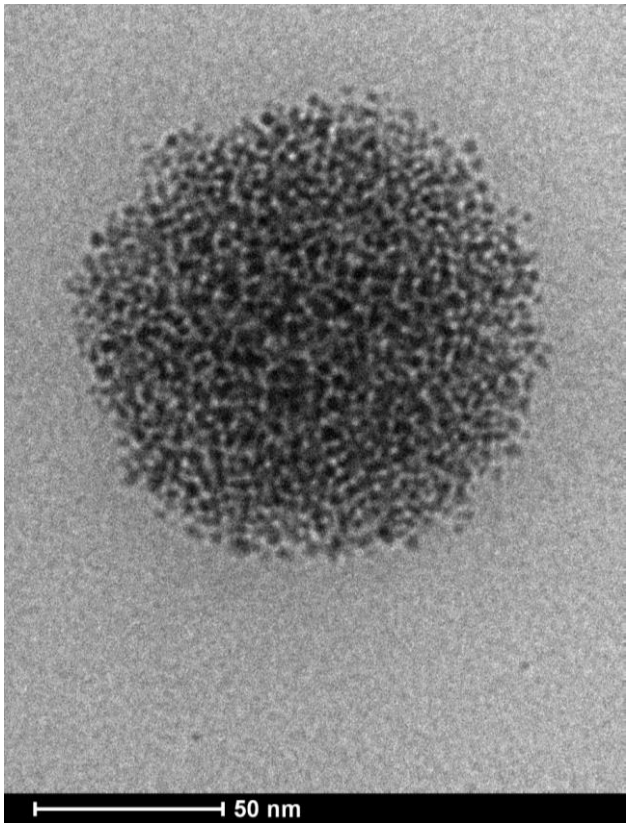

Figure 2.5 TEM image of Ag_2S-2MPA NIRQDs (Ag/S=4, 2-MPA/Ag=5, T=30^oC)

2.4.2.1 Influence of the reaction temperature

One of the most significant parameters affecting crystal growth and hence properties is the reaction temperature.

Quantum confined Ag_2S particles could be easily synthesized at 30, 50, and 90 ^oC (Table 2.3). Typical absorbance and PL spectra of the Ag_2S, synthesized at different temperatures are shown in Figure 2.6. Increasing temperature causes a red shift in the absorption onset, indicating an increase in crystal size with increasing temperature from 2.38 to 2.7 nm, which is in agreement with the literature.[74, 99] Usually, the critical size for stable particles increases with temperature, causing formation of larger crystals at higher temperatures. In this case, the most significant change is seen at 90°C. Besides, more than a dramatic difference in the particle size, a significant improvement (30%) in the luminescence was observed with increasing reaction temperature from 30

to 50°C (Figure 2.6). This might be due to better crystallization of the particles at 50°C.

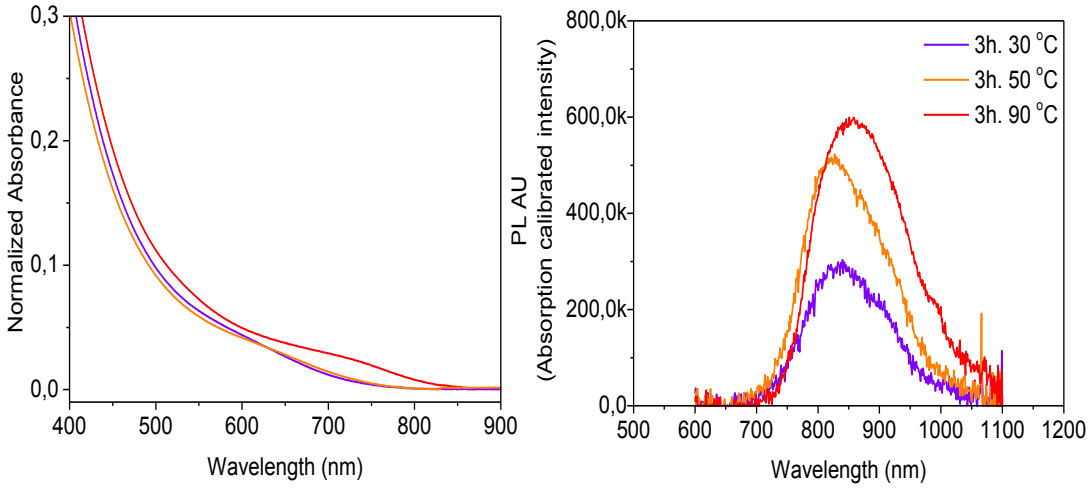

Figure 2.6 Absorbance and photoluminescence spectra of the Ag_2S-2MPA particles prepared different reaction temperatures (Ag/S=4, 2-MPA/Ag=5)

The growth of particles with time was monitored at these three temperatures. For the highest possible luminescence intensity, the optimum reaction duration was determined as 3 h at 90°C, 7 h at 50°C and 24 h at 30°C (Figure 2.7). Absorbance and PL spectra of the aliquots taken from the reaction at 50°C from the first hour of the reaction until 22h are shown in Figure 2.6. The photoluminescence quantum yield (PLQY) of the NIRQD at 7h is 27%. At longer reaction times, significant peak broadening was observed. As can be seen in Figure 2.7 B, there is a clear red shift in the absorbance onset with time. On the other hand, the emission peak did not show any shift at the high energy end, but a broadening and a slight shift at the low energy tail. The red shift in both of these spectra confirms the increase in particle size with time. However, it appears to be more like an increase with size distribution as opposed to a complete growth of all particles. This observation can be investigated further in future.

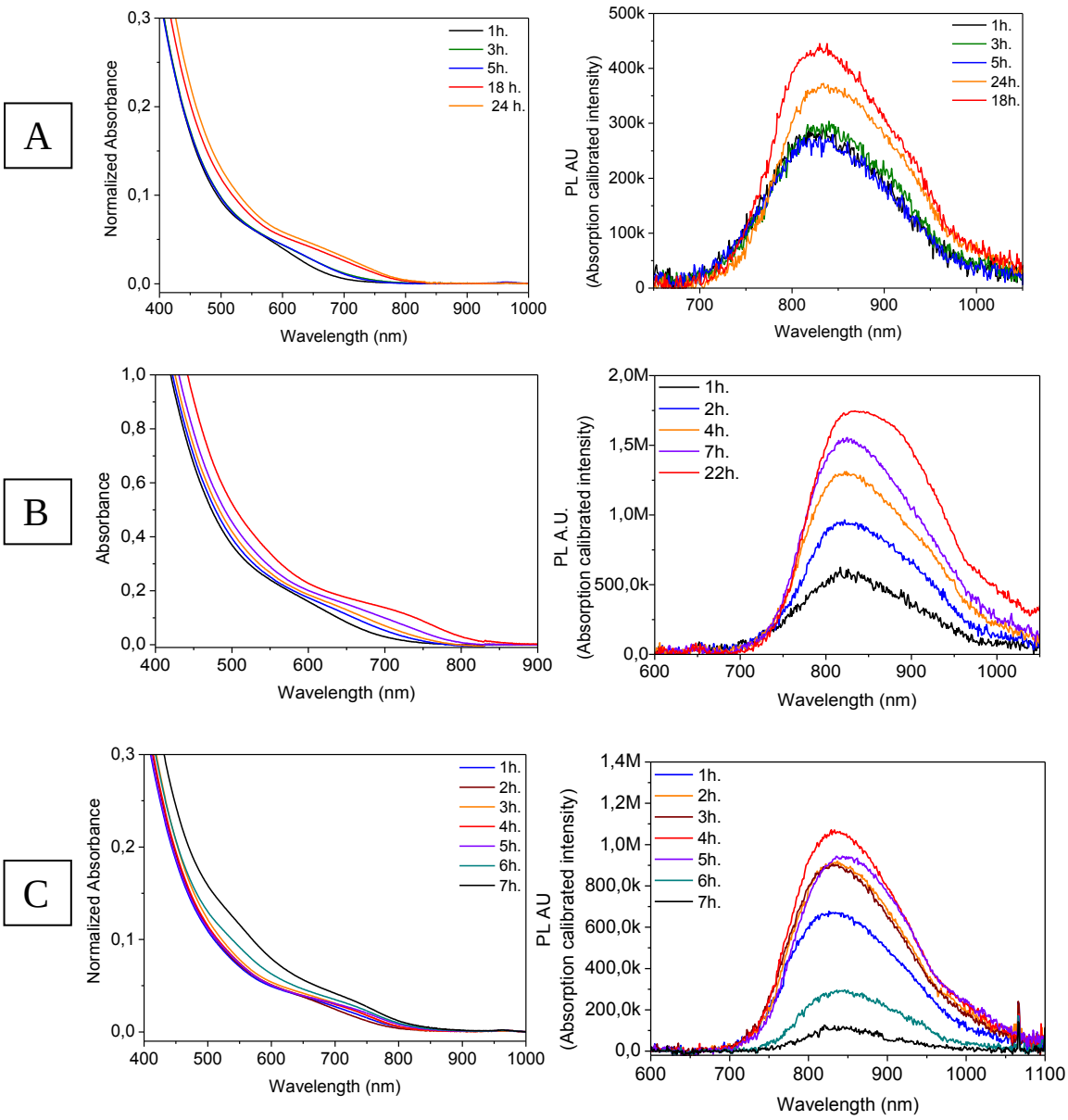

Figure 2.7 Time dependent evolution of absorbance and photoluminescence bands for the reactions A) at 30 °C B) 50 °C C) 90 °C (Ag/S =4 and 2-MPA/Ag =5)

2.4.2.2 Influence of coating amount

Changing 2-MPA/Ag ratio may influence colloidal stability, particle size and luminescence efficiency. Usually, increasing coating/cation ratio leads to a decrease in the particle size. However, in the Ag_2S-2MPA system, a different trend was seen. 2-

MPA/Ag molar ratios of 5 and 10 were studied in reactions performed at 90 and 30 ^oC.

Table 2.3 Influence of Ag/S, 2-MPA/Ag and reaction temperature on the properties of Ag_2S-2MPA NIRQDs.

Ag/S	2MPA/ Ag	Temp. (^oC)	Rxn time (h)	λ_{cutoff} [a] (nm)	Size[b] (nm)	Band Gap (eV)	$\lambda_{m,max}$ (nm)	FWHM (nm)	Dh[c] (nm)	Zeta pot. (mV)	QY (%)[d]
4	5	30	3	727	2.38	1.71	837	157	3.3	-30	-
4	5	30	1	695	2.29	1.79	827	157	2.8	-55	-
4	5	50	3	757	2.46	1.64	827	173	3.1	-39	-
4	5	90	3	834	2.70	1.49	851	181	3.1	-57	17
4	10	90	3	935	3.05	1.33	950	-	3.9	-46	-
4	10	30	1	711	2.33	1.75	815	162	3.0	-42.3	7
2.5	5	90	3	950-990	>3.1	<1.3	-	-	4.7	-58	-
6	5	90	3	763	2.48	1.63	828	168	3.1	-77.5	14
6	5	30	1	655	2.20	1.9	786	220	3.0	-55	-

[a] Absorbance onset, [b] Calculated by Brus equation, [c] Hydrodynamic diameter measured by DLS and reported as the number average, [d] Quantum yield calculated with respect to LDS 798 near-IR dye.

At 90 ^oC, doubling the 2-MPA/Ag ratio increased the particle size from 2.70 to 3.05 nm with about a 100 nm red shift in the emission peak which was also accompanied with a dramatic decrease in the luminescence intensity (Table 2.3, Figure 2.9 a). Since the band edge of the Si detector used restricts the measurements beyond 1000 nm, it is difficult to discuss the PL properties of the larger particles (3nm). On the other hand, increasing 2-MPA/Ag ratio at 30 ^oC did not change particle properties as much. Major influence of increasing amount of 2-MPA at 30 ^oC is actually better luminescence which is centered around 820 nm (Figure 2.9 b) without any shift on the absorbance spectra (Figure 2.8 b). More coating may provide better surface passivation and less surface defects. This may reduce non-radiative coupling events and therefore, increase the luminescence efficiency. The major difference in properties originating from the reaction temperature actually does depend on the stability of 2-MPA. When 2-MPA

was heated above 50 ^oC in water under conditions identical to the QD synthesis, a yellow-brown color appears after 4h, indicating decomposition and sulphur release. This has two consequences: (1) As the 2-MPA amount increases, there will be more sulphur release, decreasing the Ag/S ratio, and therefore increasing the particle size (Figure 2.8 a and 2.9 a); (2) 2-MPA decomposition would decrease the effective thiol binding and interfere with the surface passivation. This may cause surface trap related non-radiative couplings and hence poorer luminescence. Less effective surface passivation may also lead into formation of larger particles. The reactions at 90 ^oC are not reproducible above 3h due to excessive 2-MPA decomposition.

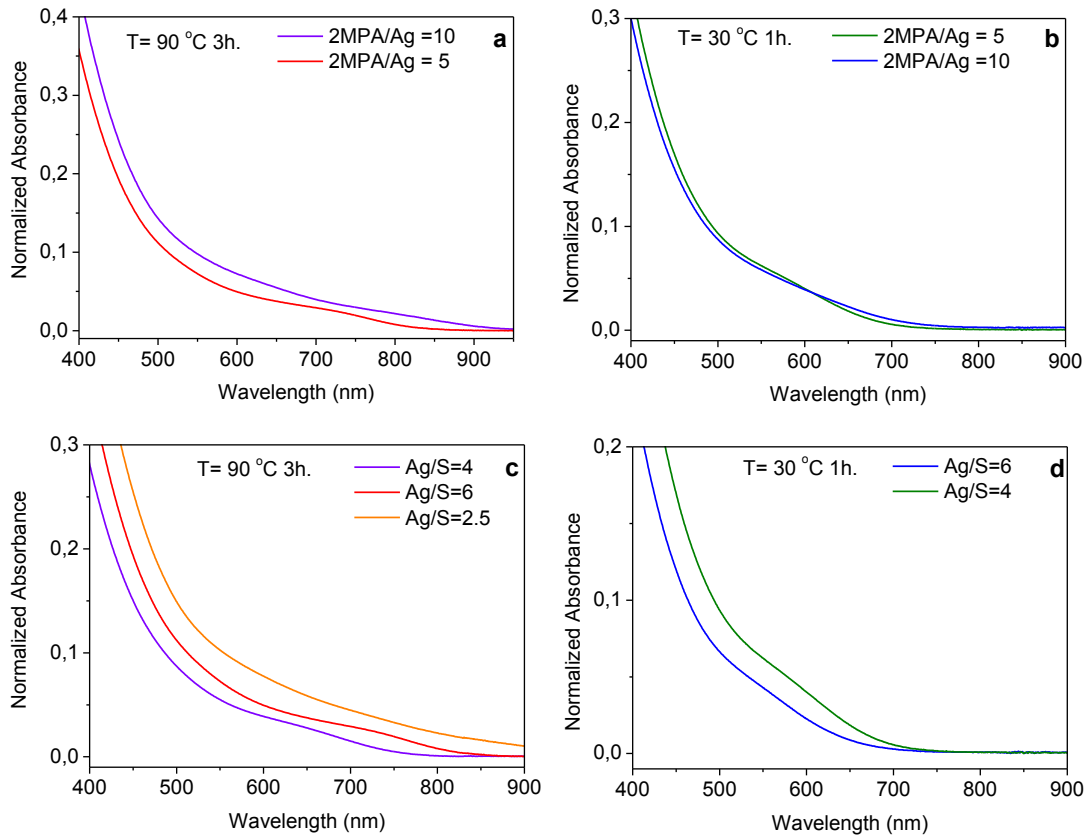

Figure 2.8 Absorbance spectra of Ag_2S QDs synthesized at for different 2-MPA/Ag ratios (a) 90 ^oC. at (b) 30 ^oC. and for different Ag/S ratios at (c) 90 ^oC and (d) 30 ^oC.

2.4.2.3 Influence of Ag/S Ratio

Stoichiometry of silver to sulphide ions influences the optoelectronic properties (emission tunability) and particle sizes of the Ag_2S-2MPA QDs dramatically. Three different Ag/S ratios (2.5, 4, 6) were studied at 90 ^oC (Table 2.3) keeping the other variables constant. Decreasing Ag/S ratio from 6 to 2.5 causes a red shift in the absorbance and luminescence spectra, indicating formation of larger particles (Figure 2.8 c and 2.9 c). At the ratio of 2.5, QDs with only very poor luminescence signal with a peak maximum over 1000 nm (which was the limit of our detector) (Figure 2.9 c) was obtained. In such a result, as much as the stoichiometry, some decomposition of 2-MPA may have played a role, as well.

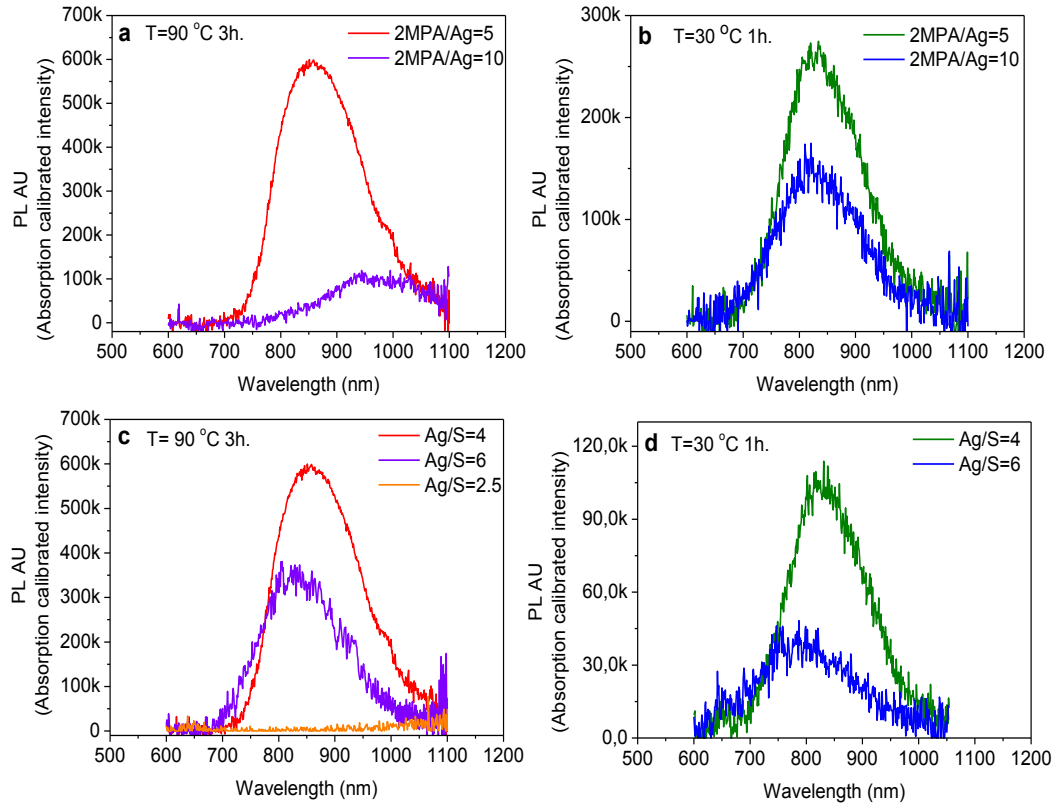

Figure 2.9 . PL spectra of Ag_2S QDs prepared at different 2-MPA/Ag ratios at (a) 90 ^oC and (b) 30 ^oC, and at different Ag/S ratios at (c) 90 ^oC and (d) 30 ^oC.

Particles prepared at 90°C are larger than those synthesized at lower temperatures as

discussed before (Table 2.3). Increasing Ag/S ratio decreased the particle size at 30°C as well (Figure 2.9 d and Table 2.3). Best quality particles are obtained at the Ag/S ratio of 4.

2.4.2.4 Influence of aging on particle properties

Table 2.4 Changes in the particle properties with time.

Analysis time*	Ag/S	2-MPA/ Ag	λ_{cutoff} [a] (nm)	Size[b] (nm)	Band Gap (eV)	$\lambda_{em,max}$ (nm)	FWHM (nm)	Dh[c] (nm)	Zeta Pot. (mV)	QY[d] %
1 day	4	5	695	2.29	1.79	827	157	2.8	-55	<5
1 month	4	5	822	2.66	1.51	863	165	3.5	-38	39
6 months	4	5	855	2.77	1.45	843	141	4.3	-28	29

[a] Absorbance onset, [b] Calculated by Brus equation, [c] Hydrodynamic diameter measured by DLS and reported as the number average. [d] Quantum yield calculation with respect to LDS 798 near IR dye. 1h. reaction. *Time passes after synthesis.

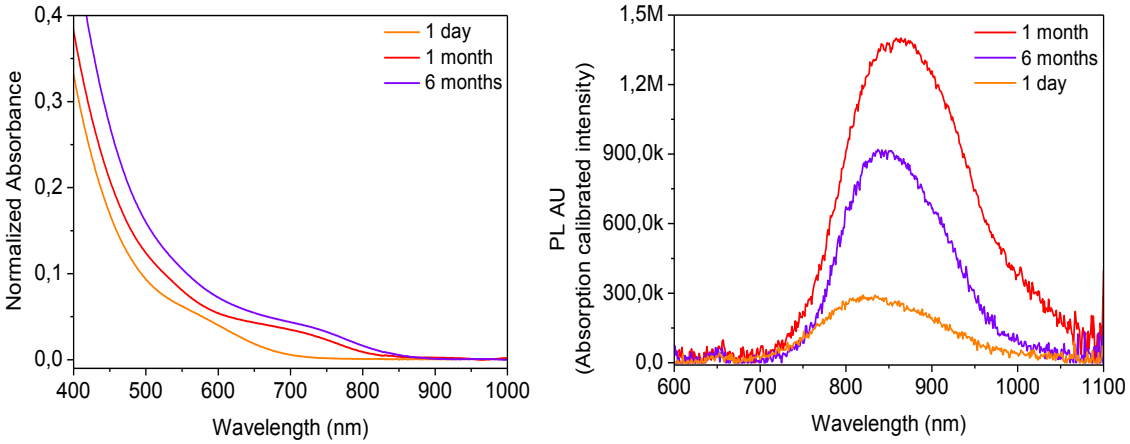

Figure 2.10 Absorbance and PL spectra of Ag_2S-2MPA NIRQDs (synthesized at room temperature) recorded after the synthesis.

Interestingly for the particles prepared at room temperature, a substantial increase in the PLQY was observed over time which was not seen in case of 2-MPA coated CdS.[31] Figure 2.10 shows the red shift in absorbance edge from the first day to 6-months after the synthesis. Luminescence intensity increased dramatically within the first month up to 39% and then decreased. These changes brought about a decrease in the zeta

potential as well. Particle properties are given in Table 2.4. This event is under investigation but slow decomposition of 2-MPA may deposit more sulphur to the surface and cause a slight particle growth and improve luminescence by pacifying surface traps. However, this may eventually cause more traps on the surface as well which would have a negative impact on PLQY.

2.4.3 In-Vitro Cell Studies

2.4.3.1 Evaluation of cytotoxicity of Ag_2S-2MPA NIRQDs

Cytotoxicity of Ag_2S-2MPA NIRQDs were tested on NIH-3T3 mouse fibroblast cells using XTT assay[107], which is based on mitochondrial reductase enzyme activity.

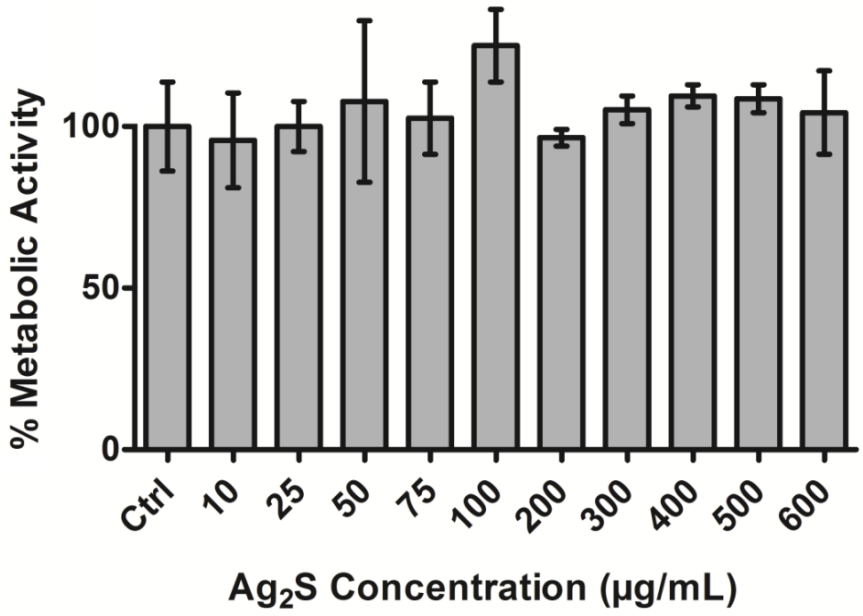

Figure 2.11 Change in the metabolic activity of NIH/3T3 mouse fibroblast cells after 24 h exposure to Ag_2S quantum dots as determined by XTT Assay. Reported values are mean ± SEM (n=6). No significant difference was observed between control (ctrl) and QD treated cells (One-way ANOVA with Tukey`s multiple comparison at $p < 0.05$)

Aqueous Ag_2S-2MPA NIRQDs used for these studies had 2.5 mg particle/mL

concentration which corresponds to 1.3 mg silver/mL (measured by ICP OES) and had 10% PLQY six months after preparation at the time of cell studies. Figure 2.11 shows the percent metabolic activity change of control and Ag_2S treated cells as a function of QD concentration between 10 to 600 µg particle/mL after 24 hr incubation. Statistical analysis of the results indicates no significant difference in the vitality of untreated and Ag_2S treated samples. This result is in line with previous reports stating low or no toxicity for silver complexes unlike free silver ions.[108-110] Biocompatibility of silver sulfide quantum dots is also supported by others studies.[108] What was not seen before was cytocompatibility at such high doses of Ag_2S. Suresh and Pelletier et al biofabricated Ag_2S nanoparticles using metal-reducing bacterium *S. oneidensis* and observed no cytotoxicity at 150 µg/mL and below, on epithelial and macrophage cells after 12 h treatment. Silver sulfide nanoworms prepared in BSA have also been shown to have low toxicity on HeLa cervical cancer cells upto 50 µg/ml dose. However, cells did proliferate at higher doses (0.2-1g/ml) since protein BSA act as a nutrient for many cells.[111]

There are no nanoparticles in the literature which are cytocompatible at such high doses (600 µg particle/mL or 312 µg Ag/mL), to the best of our knowledge. Also, considering that NIH-3T3 is usually more vulnerable than cancer cell lines, this is an extremely valuable finding. They have also showed no toxicity in HeLa and MCF-7 cell lines up to 300 µg/ml (Figure 2.12).

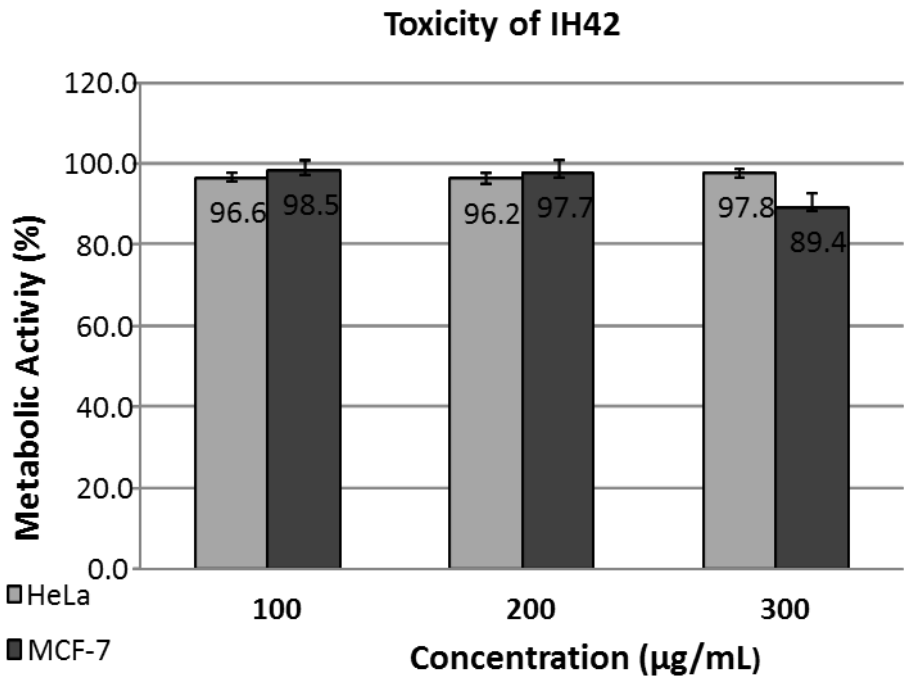

Figure 2.12 Change in the metabolic activity of HeLa and MCF-7 cancer cells after 24 h exposure to Ag_2S NIRQDs as determined by MTT Assay.

2.4.3.2 Evaluation of Ag_2S-2MPA NIRQDs as optical probes in vitro

Cellular uptake and intracellular localization of Ag_2S-2MPA NIRQDs were studied using confocal laser scanning microscopy. To the best of our knowledge, this is the first fluorescence microscopy study of a mammalian cell imaged with a Ag_2S QD. NIH-3T3 cells treated with 200 µg particle/mL QD for 24 hr and fixed with paraformaldehyde before image acquisition. Ag_2S-2MPA NIRQDs are effectively internalized and exhibit a punctuated cytoplasmic distribution indicating localization to endosomes and lysosomes as typical for QD nanoparticles (Figure 2.13). As expected for a particle of this size, no nuclear localization is observed.

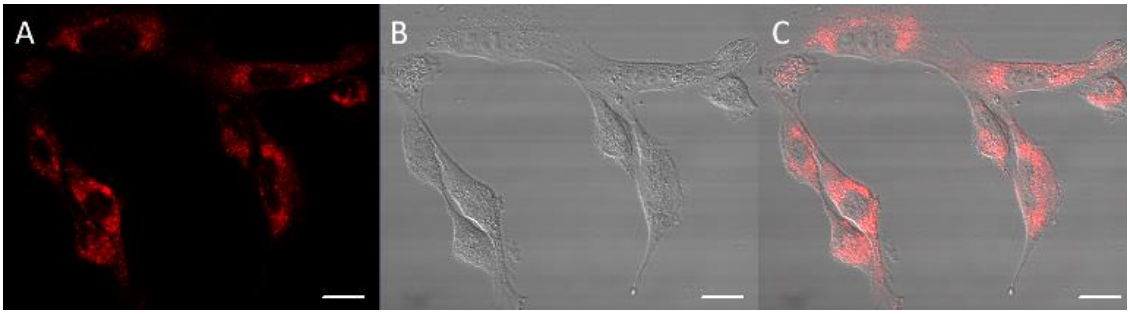

Figure 2.13 Cellular uptake and localization of Ag_2S QDs by NIH/3T3 mouse fibroblast cells (200 µg/mL QD, 24 h incubation). (A) Fluorescence, (B) Transmission and (C) Overlay channels of confocal micrograph. The scale bar represents 20 µm.

Infra-red emission of the particles provides a major advantage in the cell imaging studies. Autofluorescence of cells is particularly strong in the green region of the electromagnetic spectrum. Therefore, infra-red fluorescence imaging is ideal since there is minimal or no background signal from the cells in this region. However, typical confocal fluorescence Photo Multiplier Tube (PMT) detectors have low sensitivity in this region, resulting in reduced photon collection. To overcome this difficulty, we increased the laser power and detector sensitivity to the maximum allowed level in our system. Using these settings, we could obtain high quality confocal images with a clean background.

2.5 Conclusions

Colloidally stable, highly cytocompatible and highly luminescent aqueous Ag_2S NIR emitting QDs were successfully synthesized in water with 2-MPA coating. Size and therefore emission wavelength of these NIRQDs can be tuned by varying the Ag/S, 2MPA/Ag ratios and the reaction temperature. Decomposition of 2-MPA at 90°C at extended reaction times impacts the crystal size. Particle size can be tuned between 2.3-3.1 nm with emission maximum between 780-950 nm. Particles demonstrate a strong negative zeta potential due to carboxylate groups on the surface and exhibit excellent colloidal stable for over a year now. These particles poses significantly better PLQY in the range of 7-39% compared to reported values in the literature which is less than 1% for Ag_2S.[73-75]

In addition, these Ag_2S-2MPA NIRQDs showed dramatically improved cytocompatibility in NIH/3T3 cell lines and have been demonstrated as effective imaging agents for first time in the literature. Excellent cyctocompatibility, improved QY and colloidal stability make these nanoparticles an exciting candidate for bioapplications, specifically for in vivo imaging. These NIRQDs are also invaluable for solar energy conversion with strong absorption and emission characteristics.

Chapter 3

3 SYNTHESIS AND CHARECTERIZATION OF AQUEOUS DMSA COATED Ag_2S NEAR IR EMITTING QUANTUM DOTS

3.1 Introduction

In previous chapter we have demonstrated a simple, single-step synthesis of cytocompatible Ag_2S-2MPA NIRQDs via direct addition of sulphur source to silver salt in water.[112] These NIRQDs have high QYs compared to those reported in the literature but failed to produce particles luminescing at significantly different wavelengths and maintain high QY. Common approach towards manipulating size is the adjustment of reaction time, ligand/Ag or Ag/S ratio which usually failed in case of Ag_2S.[85, 112]

We have previously demonstrated that meso-2,3-dimercaptosuccinic acid (DMSA) can be used as a slow sulphur releasing agent between pH 7-10 and at temperatures between 50-90 ºC.[34] Size tunable CdS QDs were synthesized by the decomposition of DMSA and the best condition for effective size tuning was determined as pH 7.5 and 70 °C.[34] In such reactions, DMSA acted both as a sulphur source and a coating material. Furthermore, DMSA is a metal chelating agent[113] and an FDA approved drug used in heavy metal poisoning.[114] DMSA coating improved the cytocompatibility of CdS QDs significantly.

In this chapter, DMSA is evaluated as a slow S-releasing reagent and a biocompatible coating material in an effort to synthesize biocompatible, size tunable Ag_2S NIR QDs in a very simple procedure. Resulting particles were evaluated for cyto and hemocompatability as well as as optical probes in the in vitro studies involving HeLA and NIH 3T3 cells . In vitro assessment of cytocompatibility and hemocompatibility were performed for these Ag_2S/DMSA NIRQDs. Cytotoxicity of QDs are frequently determined, however, till now, very few studies have examined the hemocompatibility of QDs.[115-117] Indeed, when diluted in the blood stream, nanomaterials will be able to elicit several toxicological reactions, in particular: embolisation, hemolysis, cellular activation, but also several well-known biological cascades such as coagulation, complement activation, kinin/kininogen, fibrinolysis. Moreover, it is important to stress that the first barrier that nanoparticles encounter is the blood itself and the Reticulo-Endothelial System (RES). Because of the high efficiency of this clearance system in eliminating foreign bodies from the blood circulation, blood life-time of nanopartices does not exceed typically seconds/minutes. Therefore, in addition to cytocompatibility, assessment of hemocompatibility is essential before considering any preclinical studies. Compared to macroscopic particles, hemoreactivity of nanoparticles may be expected to be significantly enhanced due to very high surface/volume ratio. Therefore, a significant interaction of nanoparticles with humoral and cellular blood components of the blood is highly expectable.

3.2 Materials and Methods

3.2.1 Materials

All reagents were analytical grade or highest purity. Meso-2,3- dimercaptosuccinic acid (DMSA) and silver nitrate ($AgNO_3$) were purchased from Sigma-Aldrich. Sodium sulfide (Na_2S) was purchased from Alfa-Aesar. Sodium hydroxide (NaOH), 2-Mercaptopropionic acid (2-MPA), ethanol and aceticacid (CH_3COOH) were purchased from Merck. LDS 798 Near-IR laser dye was purchased from Exciton Inc. Only Milli-Q

water (18.2 MOhm) was used when needed. For biological applications, DMEM medium (with 4500 mg/L glucose, 4.0 mM L-glutamine, and 110 mg/L sodium pyruvate), trypsin-EDTA, penicillin-streptomycin and fetal bovine serum were purchased from HyClone, USA. Thiazolyl blue tetrazolium bromide (MTT) *Biochemica* was purchased from AppliChem, Germany. Paraformaldehyde solution 4 % in PBS and UltraCruz™ 96 well plates were purchased from Santa Cruz Biotechnology, Inc., USA. Glass bottom dishes were purchased from MadTek, USA. Dimethyl sulfoxide Hybri-Max™ and phosphate buffered saline (pH 7.4) were purchased from Sigma, USA.

3.2.2 Preparation of Ag_2S-DMSA Nanoparticles

As an example, 42.5 mg of $AgNO_3$ was dissolved in 75 ml of deoxygenated deionized water. 25 ml of deoxygenated aqueous DMSA solution prepared at pH 7.5 was then added to the reaction mixture. pH of the solution was adjusted to 7.5 by using NaOH and CH_3COOH solutions (2M). Under vigorous mechanical stirring at 5000 rpm, reaction mixture was brought to the desired temperature (70 or 90 ^oC). During the reaction, samples were taken at different time points to follow the particle growth. Prepared quantum dot solutions were washed with DI water using Amicon-Ultra centrifugal filters (3000 Da cut off) and stored in dark at 4 ^oC.

Influence of reaction variables were studied in different reactions keeping the Ag concentration fixed at 2.5mM and varying DMSA concentrations to achieve DMSA/Ag ratio of 1.5, 2.5 and 3.5 (Table 1&2).

3.2.3 Cell Culture

Human cervical carcinoma (HeLa) and mouse fibroblast cells (NIH-3T3) were cultured according to ATCC recommendations. Cells were cultured in DMEM medium with 4500 mg/L glucose, 4.0 mM L-glutamine, and 110 mg/L sodium pyruvate. Complete medium also contained 10% fetal bovine serum and 1% penicillin-streptomycin antibiotic solution. Trypsin-EDTA was used for cell detachment and cells were incubated 37 ^oC under 5% CO_2.

3.2.4 Determination of Cytotoxicity

Cytotoxicity was evaluated by performing thiazolyl blue tetrazolium bromide (3-(4,5-dimethyl-thiazol-2yl)-2,5-diphenyltetrazolium bromide, MTT) assay on HeLa and NIH-3T3 cells. 96-well culture plates were seeded with 10^4 cells in culture medium and incubated at 37 ^oC and 5% CO_2 for 24 h. Following incubation, medium was replenished; cells were treated with QDs (10 to 150 μg/mL) and incubated for 24 h. After washing, MTT reaction solution was added on the cells and incubated for 4 h. DMSO:Ethanol (1:1) solution (100 μL) was added with gentle shaking for 15 min to dissolve the purple formazan. Absorbance at 600 and 630 nm was measured with an ELISA analyzer and reference absorbance at 630 nm was subtracted from the absorbance at 600 nm. Experiments were repeated for four times. Absorbance values of the QDs were substracted from the formazan values. Statistical significance of the observed differences was determined using one-way ANOVA with Tukey's multiple comparison test of GraphPad Prism software package from GraphPad Software, Inc., USA.

3.2.5 Cell Imaging

50,000 HeLa cells were seeded in glass bottom dishes. After 18 h incubation, cells were treated with 150 μg/mL QDs in full medium for 6 h. After being washed with PBS (pH 7.4), cells were fixed with 4% paraformaldehyde for 15 min and wash step was repeated.

A home-built sample scanning confocal microscope based on an inverted microscope frame (Nikon TE 2000U) equipped with a 60X (Nikon, NA=1.49) oil immersion objective was used for image acquisition. Excitation wavelength was 532 nm. A broadband 10/90 dichroic beam splitter was used for excitation. A long pass glass filter (RG665) was placed before Silicon APD based photon counting modules to detect the QD emission.

3.2.6 Hemocompatibility Studies

Hemocompatibility tests were performed with a Ag_2S NIRQD which was synthesized at DMSA/Ag ratio of 2.5, 70°C in 4h. Hemocompatibility tests were performed according to ISO standards (10993–4). Normal human blood from healthy volunteer donors was collected in Terumo Venosafe citrated tubes (Terumo Europe N. V., Belgium). Experiments were done within 2 h after blood collection. All tests were performed with the agreement of the local ethical committee of the Medicine Faculty of the University of Liège. Hemocompatibility of Ag_2S/DMSA NIRQDs was evaluated by studying hemolysis, morphology of blood cells, complement activation (C3a), and coagulation activation, both through the extrinsic pathway (PT assay) and the intrinsic pathway (APTT assay). QDs dispersed in PBS were diluted in whole blood in order to obtain final nanoparticle concentrations of 100, 10, and 1 μg/mL. Samples were incubated for 15 min at 37 °C under lateral agitation (250 rpm).

3.2.6.1 Micrographs of blood smear

After blood incubation, 5 μL of the blood was withdrawn and spread on a microscopy glass slide. Blood cells were observed with an Olympus Provis microscope at 20× and 50× magnification in transmission mode.

3.2.6.2 Haemolysis

The haemolytic test was performed following Standard Practice for Assessment of Haemolytic Properties of Materials (ASTM designation F 756-00). Briefly, after QD incubation in whole blood, the samples were centrifuged at 600g for 5 min at room temperature, and supernatants were collected and mixed with the cyanmethemoglobin reagent. The hemoglobin released was measured by reading the absorbance of 100-fold dilution of whole blood in Drabkin's reagent at 540 nm in a microplate reader (Anthos HT III, type 12600, Anthos, Salzburg, AU). A calibration curve was established using bovine hemoglobin as the standard. Saponine (0.8 mg mL^{-1}) and PBS were used as

positive and negative controls, respectively. Hemolysis was expressed as the percentage of hemoglobin released to total hemoglobin content, taking the positive control as 100% of hemolysis. The tests were done in triplicate.

3.2.6.3 Count and size distribution of RBCs, platelets and white blood cells

QD dispersions and blood were prepared and incubated as described before. After 15 min of incubation, blood cells were counted and their size distribution was determined with CELL-DYN 18 Emerald (Abbott Diagnostics). Three analyses were conducted per sample.

3.2.6.4 Complement Activation

Complement activation was assessed using the Human C3a ELISA kit for quantification of Human C3a-des-Arg (Becton Dickinson). After a 15 min incubation of blood and QD mixtures, EDTA (1 mM final) was added to block any future complement activation. Samples were centrifuged at 2000g for 5 min at RT, and supernatants were used for the analysis of complement activation following the kit protocol (BD OptEIA, Human C3a ELISA, Cat. No.550499). Absorbance was measured at 450 nm with a microplate reader (Anthos HT III, type 12600). Plasma containing 2 mg mL^{-1} of Zymosan was taken as a positive control and plasma without additives as a negative control. The concentration of C3a was expressed as a percentage of activation by reference to the negative control set at a value of 100% of complement activation. Measurements were done in duplicate.

3.2.6.5 Coagulation Experiments

Whole blood and QD dispersions were mixed and incubated as described before. Samples were centrifuged at 2000g for 5 min at RT, and the supernatants were collected, recalcified to reverse the effect of citrate anticoagulant, and supplied with the specific activators of coagulation (thromboplastin). Prothrombin time (PT) to evaluate the extrinsic pathway, and activated partial thromboplastin time (APTT) to evaluate the

intrinsic pathway, were measured directly with a Dade Behring Coagulation Timer analyzer (BCT) (Siemens Healthcare Diagnostics NV/SA, Belgium) using commercial reagents (Thromborel® S, Dade Behring/Siemens, for PT determination and C.K. PREST kit, Roche Diagnostics, France, for a PTT). Kaolin reagent was used as a positive control and PBS as a negative control. Clotting time was measured for each sample, and coagulation capacity was expressed as a percentage, taking the value of standard human plasma (Dade Behring/Siemens) as 100%. Measurements were done in duplicate.

3.3 Characterization Methods

A Shimadzu 3101 PC UV-Vis-NIR spectrometer was utilized for the absorbance spectroscopy in the 300-1000 nm range. The Brus equation[12, 13](eqn.1) was used for the particle size calculation from experimentally determined absorption onset (Appendix A).

$$\Delta E = \frac{\hbar^2 \pi^2}{8R^2}\left[\frac{1}{m_e} + \frac{1}{m_h}\right] - 1.8\frac{e^2}{\varepsilon_{Ag_2S} 4\pi\varepsilon_0 R} \quad (1)$$

ΔE is the band gap energy difference between the bulk semiconductor and the quantum dot, R is the radius of quantum dot, m_e (0.286 m_0) and m_h (1.096) are the respective effective electron and hole masses for Ag_2S,[72] and ε_{Ag2S}(5.95) is the dielectric constant of bulk Ag_2S.[72]

Photoluminescence spectra were recorded with a homemade setup. The system was built around a 1/8 monochromator (Newport Cornerstone 130) equipped with a 600 l/mm grating working in 400-1000 nm range. The excitation source was the frequency doubled output of a DPSS laser at 532 nm. The luminescence signal was filtered by a 590 nm long pass filter before it was wavelength selected and detected with a Si detector with femtowatt sensitivity (Thorlabs PDF10A, 1.4 x 10^{-15} $W/Hz^{1/2}$). The power of the excitation source was monitored with a powermeter and the reported spectra are

normalized for excitation power.

QY calculations were done based on the procedures detailed in the literature.[30, 32, 103] As a reference LDS 798 NIR dye (QY is 14% was reported by the producer) was used. Typically, five different concentrations of the dye (in MeOH) and sample (in water) were prepared, all with absorption below 0.15 at excitation wavelength and the PL spectra of each was obtained. Proportion of the areas under the emission peaks were used in the calculations. Area values of the different concentrations were plotted for both samples and the reference dye (standard). Typical QY is the ratio of the slope of the sample (m_{slope}) and the slope of the dye ($m_{standard}$). The equation below is used for QY calculation (eqn 2).

$$\Phi_{yield} = \frac{m_{sample}}{m_{standard}} \left(\frac{\eta_{water}^2}{\eta_{MeOH}^2} \right) \qquad (2)$$

Refractive indices of sample (η_{water}) and the reference dye (η_{MeOH}) solutions are important for the calculation.

Samples were dried into powder form using freeze-drier for X-PS and XRD analysis. XPS analyses were performed with a Thermo Scientific K-Alpha XPS with Al K-alpha monochromatic radiation (1486.3 eV). Ag_2S powders were placed on adhesive aluminum tape and 400 μm x-ray spot size was used. The pass energy of 50.0 eV corresponds to a resolution of roughly 0.5 eV. The base pressure was below 3×10^{-9} mbar and experimental pressure was about 1×10^{-7} mbar due to charge neutralization with flood gun. C1s peak at 285.0 eV was assigned as the reference signal for evaluations.

D8 advance Bruker instrument was used for the XRD. Solid samples were put on a piece of a glass with a double sided tape. The glass was placed into sample holder with dough. Crystal peaks were recorded between 2θ angles of 10^o-80^o with Cu K-α radiation (λ=1.5406).

For TEM analysis, JEOL ARM 200 CFEG Cs-corrected STEM operated at 200 kV was used. EDS was done with JEOL Centurion detector with 100 mm^2 detector area.
Hydrodynamic size and the zeta potential of the aqueous colloidal Ag_2S/DMSA were measured by the Malvern zetasizer nano ZS.
Ag^+ ion concentration of the quantum dot solutions were determined by Spectro Genesis FEE Inductively Coupled Plasma Optical Emission Spectrometer (ICP OES) using appropriate regression curves created with standard solutions. QDs were etched with nitric acid and sulfuric acid mixture and diluted with DI water for the ICP analysis. Experiments were done in triplicate and the average was reported.

3.4 Results and Discussion

3.4.1 Effect of the reaction parameters on optical properties

In a typical reaction, Ag^+ and DMSA forms a complex with a strong absorbance at around 255 nm (Figure 3.1 a). Absorbance maximum of the initial complex vanishes slowly with time as the reaction mixture was heated indicating the decomposition of the complex and formation of the Ag_2S crystals. As Ag_2S nanocrystals form and grow, the absorbance onset shifts to longer wavelengths (Figure 3.1 b).
Primary purpose of using DMSA here is to benefit from slow sulphur release from DMSA to tune the crystal size and therefore the emission wavelength of Ag_2S QDs. Therefore, DMSA/Ag ratio and the reaction temperature which influence the decomposition rate were studied as variables and their influence on the particle size, emission wavelength and quantum yield were analyzed. Three different DMSA/Ag ratios were used at fixed temperature of 70 ºC and pH 7.5.

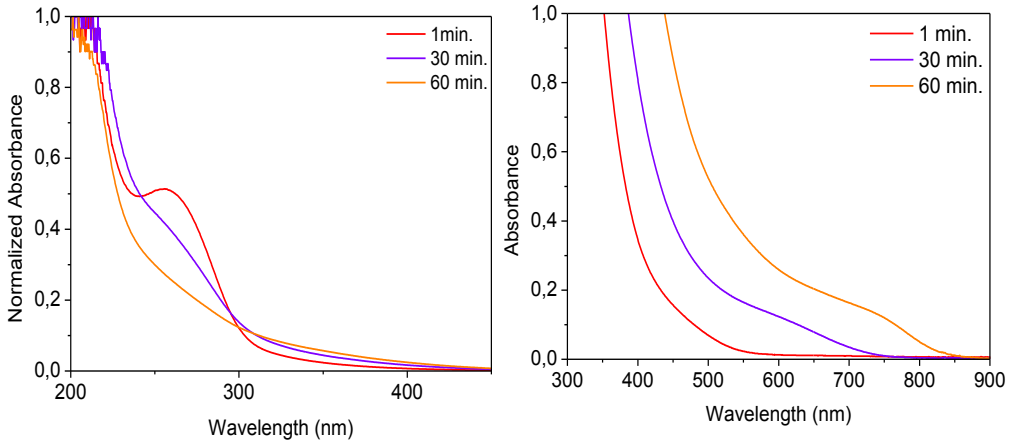

Figure 3.1 Absorbance spectra of a) Ag^+-DMSA complex b) Ag_2S-DMSA NIRQDs prepared at 90 ^oC at DMSA/Ag= 2.5.

Initial reaction at DMSA/Ag ratio of 1.5 was monitored for 19h by the UV-Vis spectrophotometer and spectrofluorometer (Figure 3.2 a). Red shift of the absorbance onset implies crystal growth with time as DMSA decomposes slowly and releases sulphur. This profile is completely different than those obtained with 2-MPA coating and Na_2S as a sulphur source, where only intensity changed with time. Crystal sizes of Ag_2S/DMSA QDs were increased from 2.20 to 2.95 nm with time as calculated by the Brus equation using the absorbance onsets (Table 3.1). The increase in crystal sizes were accompanied by the red shift in emission maximum of the particles from ca. 780 to 920 nm. Luminescence intensity of the particles continuously increased up to 4h (emission maximum at 828nm) and then decreased with further increase in particle size. Major drop in the luminescence intensity was observed at the 5^{th} h. Yet, DMSA decomposition provided size tunable Ag_2S NIRQDs luminescing between 780-920 nm in a one pot reaction.

Table 3.1 Influence of DMSA/Ag ratio and reaction time on the properties of Ag_2S-DMSA NIRQDs

DMSA/Ag	Time	λ_{cutoff}[a] (nm)	Size[b] (nm)	Band Gap (eV)	$\lambda_{em,max}$ (nm)	FWHM (nm)	QY[c] %
1.5	1h.	662	2.20	1.88	782	195	
1.5	3h	792	2.57	1.57	800	173	
1.5	4h	844	2.73	1.47	828	158	
1.5	5h	870	2.82	1.43	858	150	
1.5	19h	907	2.95	1.37	923	-	
2.5	1h.	677	2.24	1.83	730	170	
2.5	3h	791	2.60	1.57	789	129	
2.5	4h	810	2.62	1.53	810	139	6.5
2.5	5h	833	2.70	1.49	829	137	6.3
3.5	30min.	625	2.10	1.99	730	-	
3.5	2h	807	2.61	1.54	794	142	
3.5	4h	837	2.71	1.48	834	134	6.4
3.5	9h	890	2.89	1.40	910	>180	

T=70 °C pH=7.5, [a]Determined from absorbance spectrum, [b]Diameters of the particles calculated by Brus equation, [c] Quantum yield. LDS 798 NIR dye was used as a reference.

Reactions were performed at higher DMSA/Ag ratio as well to evaluate its impact on the rate of crystal growth, size tunability and luminescence efficiency. Increasing the DMSA amount impacts the reaction in two counteracting ways: Larger amounts of DMSA can reduce the particle size as it can passify the surface of the growing crystals at an earlier stage.

On the other hand, increasing the DMSA amount introduces more S^{2-} to the medium through decomposition which decreases the Ag/S ratio and increases the particle size. Absorbance and photoluminescence spectra of Ag_2S synthesized at DMSA/Ag ratio of 2.5 and 3.5 are shown in Figure 3.2b and 3.2c. As particles grow with time, a distinctive

absorption feature appeared in 3h and luminescence maxima starting around 750 nm shifted towards 850 nm in 5 h. Any further reaction caused a dramatic drop in the luminescence intensity although emission maximum shifted to ca 920 nm. As the DMSA/Ag ratio increased the major impact was seen in the full with at half maximum (FWHM) as it got narrower at high ratios. Increasing DMSA amount from 1.5 to 2.5 caused a small decrease in size and slight blue shift in emission peak and increasing further to 3.5 increased the size and caused a slight red shift in the emission (Figure 3.3). These refer to early passivation of the growing crystal with increasing coating amount, and increasing crystal size with decreasing Ag/S ratio at higher concentration of DMSA, as proposed earlier. But overall, increasing DMSA/Ag ratio did not cause a dramatic increase in particle size/emission maximum but a narrowing in the emission peak with a slight increase in luminescence intensity at the ratio of 3.5 (Figure 3.3, Table 3.2). These indicate that at these ratios (2.5 and 3.5) excess DMSA was most influential in stabilizing the surface. At all DMSA/Ag ratios QDs produced in 4h have the highest luminescence intensity within 810-834 nm peak emission range with a QY around 6.4% with respect to LDS 798 NIR dye (14% QY in DMSO) (Table 3.1, Table 3.2) which is quite good compared to most NIR emitting QDs in the literature[82] and good enough to evaluate these particles for bio-imaging purposes as will be demonstrated later in this article.

Table 3.2 Properties of Ag2S-DMSA NIRQDS at different DMSA/Ag

DMSA/Ag.	λ_{cutoff} [a] (nm)	Size [b] (nm)	Band Gap (eV)	$\lambda_{em,max}$ (nm)	FWHM (nm)	Zeta potential (mV)	QY [c] %
1.5	844	2.73	1.47	828	158	-57	-
2.5	810	2.62	1.53	810	139	-54	6.5
3.5	837	2.70	1.48	834	134	-56	6.4*

T= 70 ^{0}C pH=7.5, reaction time =4h. [a] Absorbance onset, [b] Calculated by Brus equation, [c] Quantum yield is calculated with respect to LDS 798 NIR dye, * QY is calculated from the 7h. Sample.

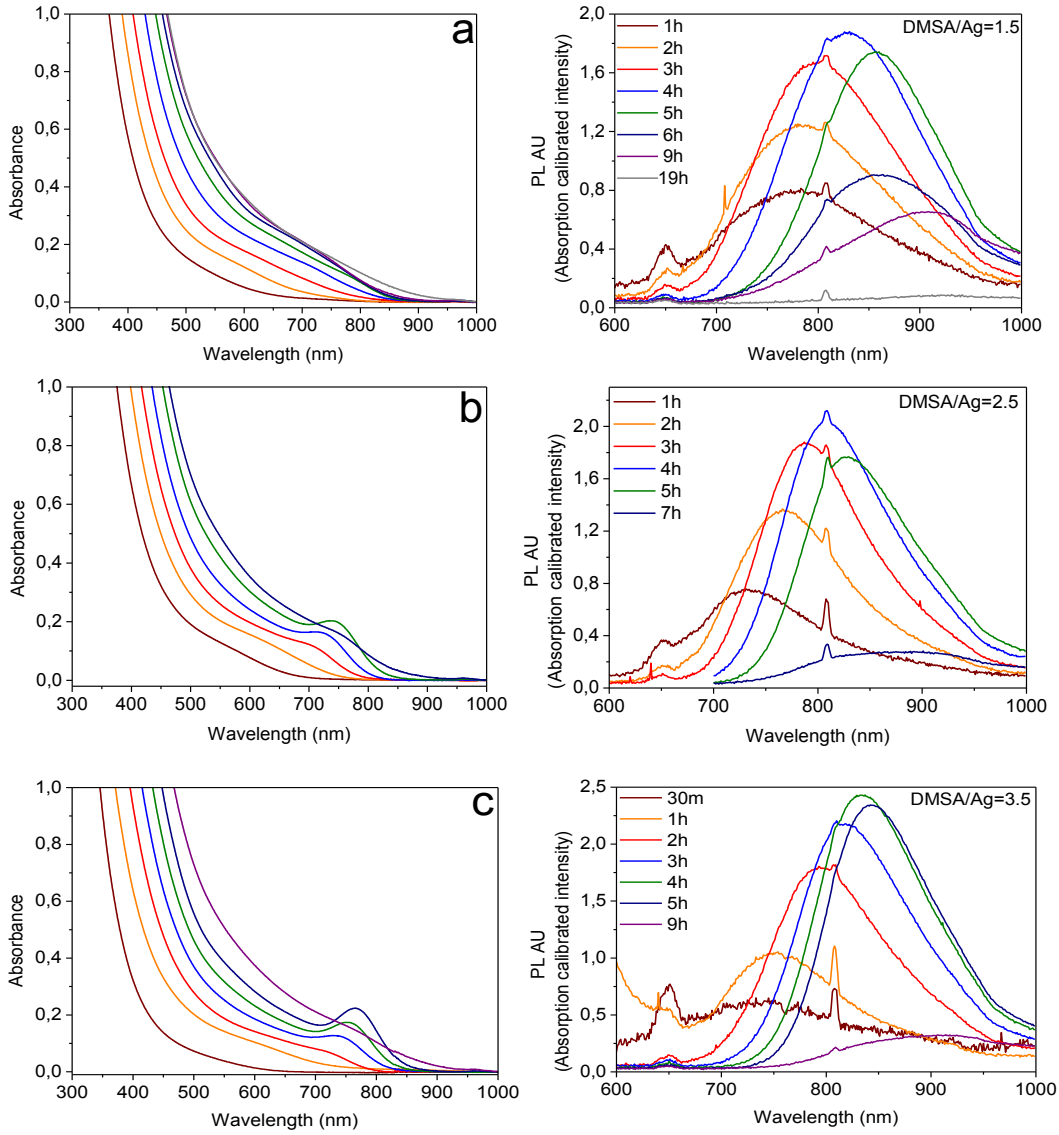

Figure 3.2 Absorbance and corresponding photoluminescence spectra of Ag_2S-DMSA NIRQDs at different time points during the synthesis performed at 70 ^{o}C and DMSA/Ag ratios of a) 1.5 b) 2.5 c) 3.5.

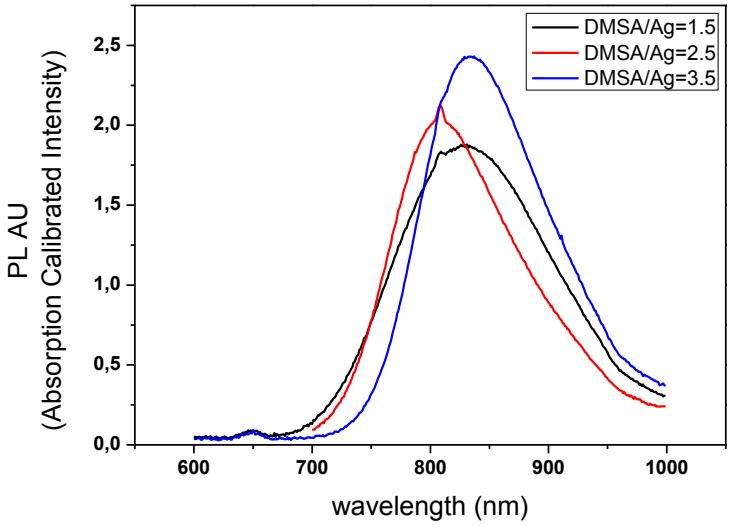

Figure 3.3 Comparison of the Photoluminescence spectra of the Ag_2S-DMSA NIRQDs at different SH/Ag ratio at the same reaction time (4h) and the temperature (90 ^oC).

Table 3.3 Influence of the temperature on DMSA decomposition and NIRQD properties.

Time (min)	λ_{cutoff} [a] (nm)	Size [b] (nm)	Band Gap (eV)	$\lambda_{em,max}$ (nm)	FWHM (nm)
30	739	2.41	1.68	760	150
60	837	2.70	1.48	840	165
90	886	2.87	1.40	875	168
120	886	2.87	1.40	926	>170

T=90 ^oC, DMSA/Ag=2.5, [a]Determined from absorbance spectrum, [b]Diameters of the particles calculated by Brus Equation.

One of the important parameters affecting decomposition of DMSA and particle growth is the temperature. Synthesis of Ag_2S-DMSA NIRQDs (DMSA/Ag = 2.5) at 90 ^oC speeded up the sulphur release and the crystal growth. As can be seen in the absorbance spectra in Figure 3.4 a, particle growth stopped at the 3rd hour. A distinct red shift in emission maximum was observed in every 30 min from 750 to 900 nm (Figure 3.4 b).

Other properties were also reported for each sample at different temperature on Table 3.3. Particles with emission maximum at 830-840nm were achieved in after 5h at 70°C but in 1h at 90°C. However, photoluminescence intensity of these particles are about four times lower than the particles synthesized at 70°C (Figure 3.5).

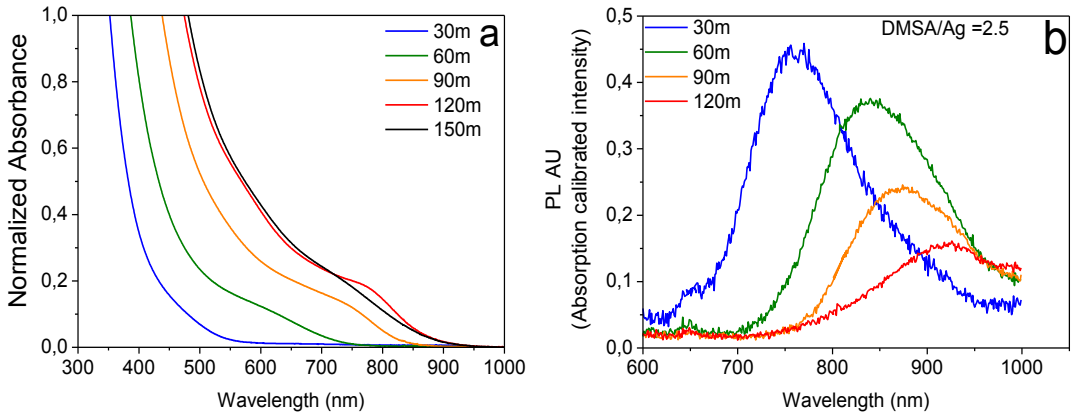

Figure 3.4 Absorbance a) and PL b) spectra of the samples taken from the synthesis of Ag_2S NIRQDs at 90°C.

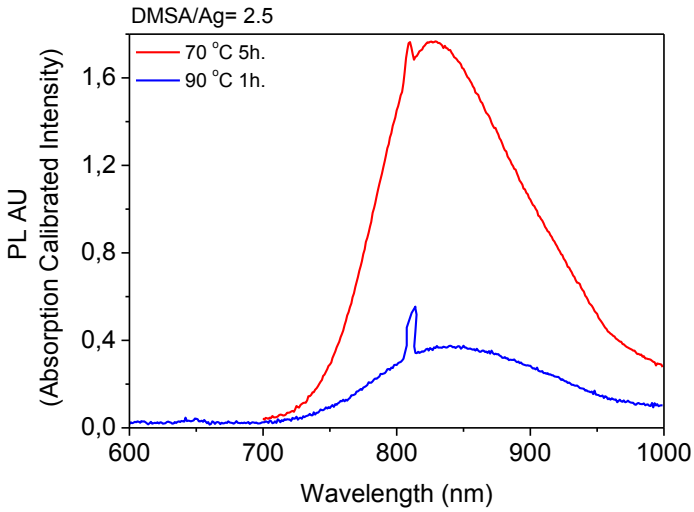

Figure 3.5 Comparison of the Photoluminescence spectra of the Ag_2S-DMSA NIRQDs synthesized at different temperature.

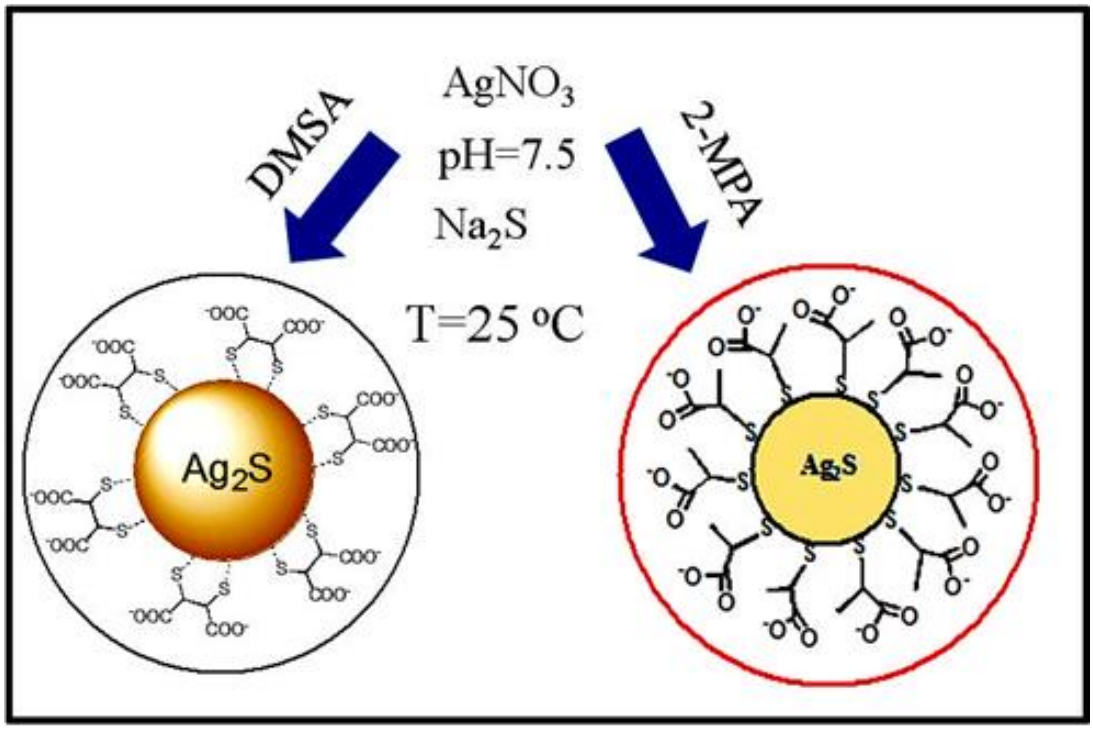

Scheme 3.1 Synthesis of both DMSA and 2MPA coated Ag_2S NIRQDs at 25 °C.

DMSA as an FDA approved biocompatible drug is actually a very valuable coating material for QDs designed for biological applications. Therefore, using it only as a coating material without any decomposition is an alternative method for the Ag_2S/DMSA nanoparticles. Therefore, DMSA coated aqueous Ag_2S NIRQDS (pH:7.5, Ag/Na_2S=4, DMSA/Ag=5 were also prepared at 25 °C using Na_2S as an external sulphur source similar to 2-MPA coated Ag_2S NIRQDS (Scheme 3.1)[112] Both synthesized particles have absorbance profile up to 1000nm in the Vis-NIR range (Figure 3.6 a). Ag_2S-DMSA QDs have smaller particle sizes when the absorbance edges compared. DMSA coated Ag_2S QDs emit at lower wavelength (750 nm) with respect to 2MPA coated Ag_2S QDs (around 850 nm). Nonetheless, 2MPA coated Ag_2S QDs have 30 times better luminescence intensity (Figure 3.6 b). However, luminescence of Ag_2S-DMSA NIRQDs synthesized at room temperature was dramatically inferior to those prepared at 70°C. This may relate to better quality and crystallinity of later particles.

Both of the particles have negative zeta potential below -30 mV indicating the particles are colloidally stable (Table 3.4).

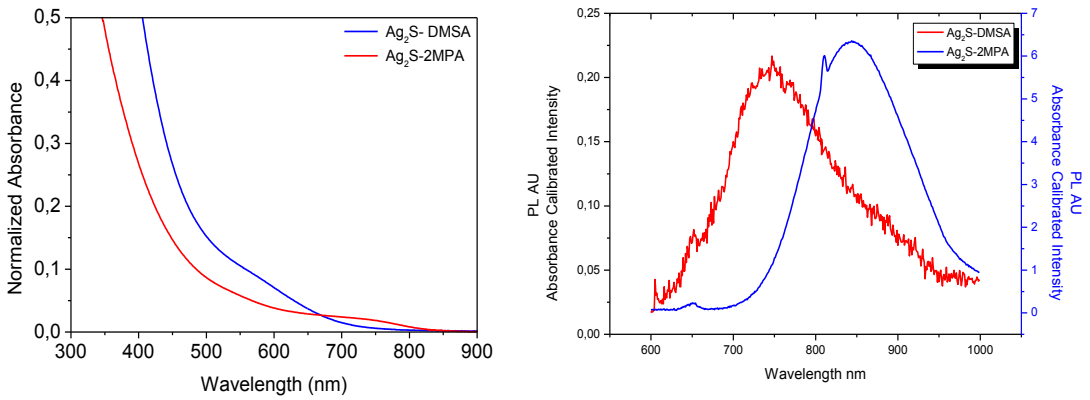

Figure 3.6 Absorbance a) and Photoluminescence b) spectra of DMSA and 2MPA coated Ag_2S NIRQDs.

Table 3.4 Properties of RT synthesized DMSA and 2MPA capped Ag_2S particles.

Reaction ID	Ag/S	λ_{cutoff} [a] (nm)	Size[b] (nm)	Band Gap (eV)	$\lambda_{em,max}$ (nm)	FWHM (nm)	Dh[c] (nm)	Zeta potential (mV)
DMSA	4	709	2.33	1.75	745	186	3.36	-55
2MPA	4	701	2.31	1.77	840	150	3.1	-38

T= 25 °C, pH=7.5, reaction time =1h. [a]Absorbance onset, [b]Calculated by Brus equation, [c] Hydrodynamic size calculated by DLS.

3.4.2 Characterization by TEM, XPS and XRD

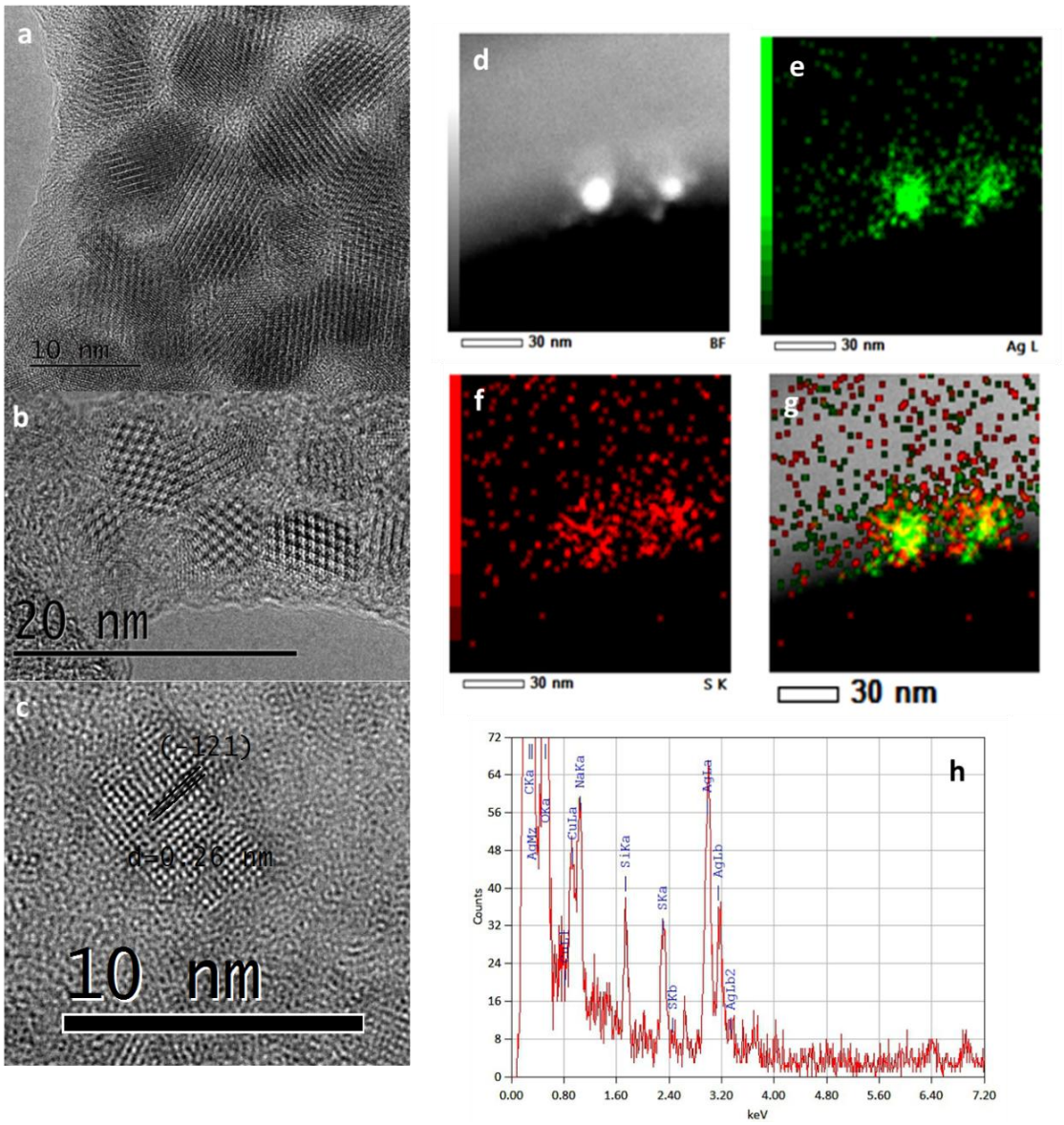

Figure 3.7 TEM and EDX Analyses of the Ag_2S-DMSA NIRQDs. TEM of the nanoparticles at a) 10 nm b) 20 nm scale, c) focused lattice planes for defining d-spacing parameter corresponding plane. d) Bright field image of the Ag_2S-DMSA NIRQDs, e) Ag and f) S elemental mapping and g) their merged image showing composition of the particles, h) Ag and S transitions by EDX acquisition.

TEM images of Ag_2S-DMSA NIRQDs show mostly spherical and highly crystalline structure with particle sizes between 5-8 nm (Figure 3.7 a and 3.7 b). Interplanar distance of the crystallite was measured as 0.26 nm (Figure 3.7 c) which is correlated with the -121 plane of the monoclinic Ag_2S in alpha phase (JCPDS: 14-0072).[71, 118] Significant movement and aggregation were observed during the measurement possibly due to the presence of organic coating. Crystal sizes measured by TEM do not correlate well with the sizes calculated by the Brus equation, but sure are more reliable. Sizes obtained from TEM are slightly smaller than sizes measured by DLS as expected which is due to the presence of the coating material (Figure 3.8).

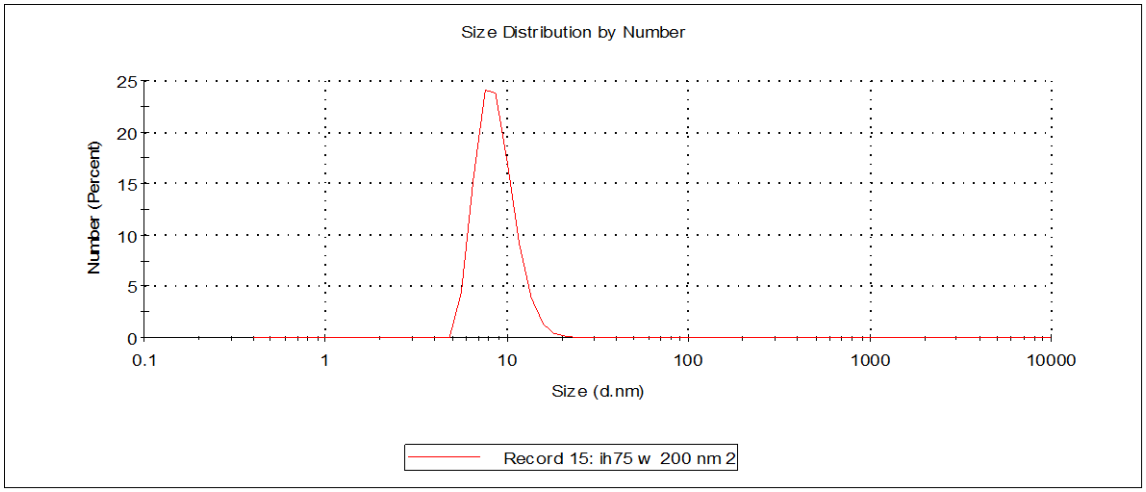

Figure 3.8 Size of the Ag_2S-DMSA NIRQDs (9nm) by DLS (TEM SAMPLE).

Yet, sizes calculated by the Brus equation and reported in Table 3.1 and 3.3 can be used to determine the influence of reaction variables on the particle size and hence the luminescence wavelength. Although, Brus equation is used frequently for size calculation of quantum dots, there are no reports in the literature where both the size measured by TEM and calculated by the Brus equation are present for Ag_2S quantum dots. This is probably due to the significant differences in results as we observed here. None of the m_e, m_h values reported for Ag_2S provided diameters matching with those obtained from TEM. Recently, Zhang et al. reported size tunable synthesis of Ag_2S QDs through decomposition of Ag-diethyldithiocarbamate at high temperatures and

measured sizes of QDs by TEM.[119] Smallest particles they have prepared have a broad luminescence centered at 975 nm with an average diameter of 2.4 nm. This is close to our largest particle diameter and luminescence peak. Although not reported directly, from the available UV-absorbance data, it seems like their TEM based size analysis will not match to diameters calculated by the Brus equation either.

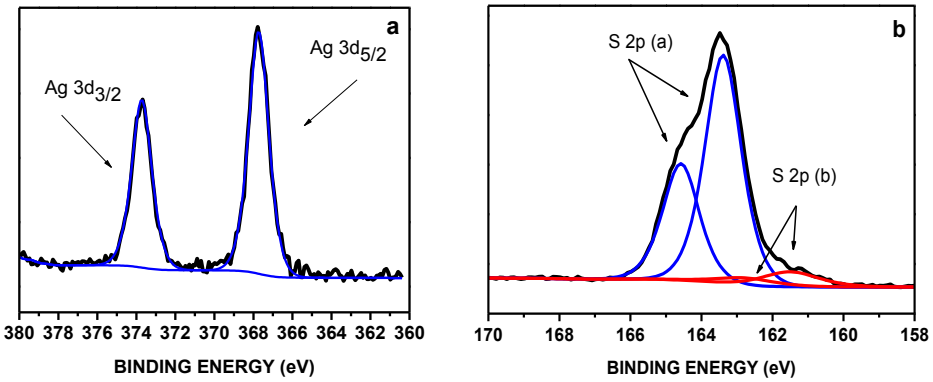

Figure 3.9 XPS spectra of Ag_2S-DMSA NIRQDs a) Ag 3d region b) S 2p region.

XPS analysis confirmed the chemical composition of the Ag_2S-DMSA NIRQDs. Binding energies (BE) and corresponding signals of Ag 3d and S 2p core level are shown on Figure 3.9. Ag has peaks at the BEs of 367.73 ($3d_{5/2}$) and 373.72 ($3d_{3/2}$) eV consistent with +1 oxidation state in bulk Ag_2S.[105, 106] The sulphur 2p region is fitted to two doublet sets; the intense pair ($2p_{3/2}$ at 163.39 eV) belong to S of the coating material (DMSA). The weak pair ($2p_{3/2}$ at 161.51 eV) corresponds to the bond of Ag-S-Ag originating from the inorganic core.

DMSA coated Ag_2S QDs have a typical XRD pattern seen on Figure 3.10. Bulk form of Ag_2S is in alpha phase having the monoclinic crystal structure at room temperature.[71] However, Ag_2S QDs in nanoparticle form exhibits an amorphous pattern possibly due to the small size and organic coating around the inorganic core. Crystalline peaks are hidden under the amorphous peak. Annealing of QDs at 180 ^oC provided the typical XRD pattern matching with the monoclinic phase (JCPDS: 14-72).[74]

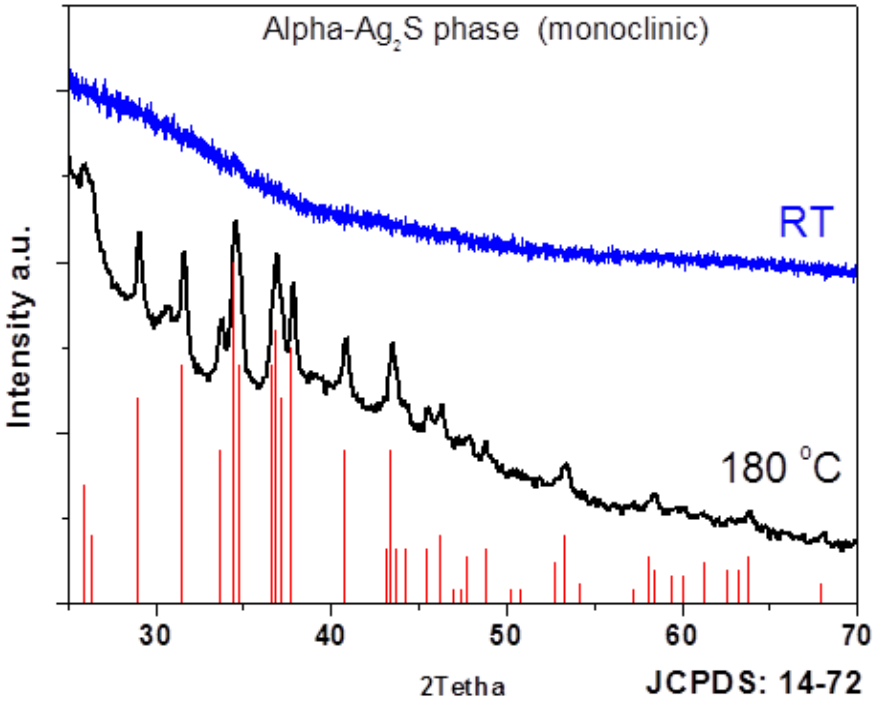

Figure 3.10 XRD patterns of the Ag_2S-DMSA QDs as is (RT) and annealed at 180 ^{o}C.

3.4.3 Assessment of *In Vitro* Cytotoxicity

Toxicity of quantum dots is very critical for biological applications. Ag-chalcogenites reported to exhibit almost no toxicity in different cancer cell lines.[73, 82] In case of BSA coated Ag_2S, cell proliferation was observed and this was attributed to BSA which may act as a nutrient.[111] We have shown excellent biocompatibility of 2MPA coated Ag_2S not only in cancer cell lines but also in more susceptible NIH-3T3 cells.[112] Very recently, glutathione coated Ag_2S NIR QDs were reported to have negligible cytotoxicity in HepG2 and L929 cells.[80, 83]Analysis of apoptosis and necrosis studies of Ag_2S coated with a multidentate polymer also indicated negligible cytotoxicity.[81] Toxicity of DMSA coated Ag_2S quantum dots to HeLa and NIH-3T3 cells were

evaluated using MTT assay. In 24 h incubation, HeLa cells were not affected up to 150 µg/ml of Ag (corresponding to QD concentration of 0.84 mg/ml) (Figure 3.11). Similar to our previous results with Ag_2S-2MPA NIRQDs and literature[111], an increase in the cell viability, possibly indicating proliferation was observed in HeLa cells. Causes of such behavior are still not clear. NIH-3T3 fibroblast cells are more vulnerable than the cancer cell lines, thus, cell viability decreased by about 20% at 100 µg Ag/mL corresponding to 0.56 mg/ml incubation of the Ag_2S QDs which is an extremely high dose for these studies (Figure 3.11). Most studies would stop at about 100µg QD/ml dose. Overall, DMSA coated Ag_2S NIRQDs are cytocompatible nanoparticles.

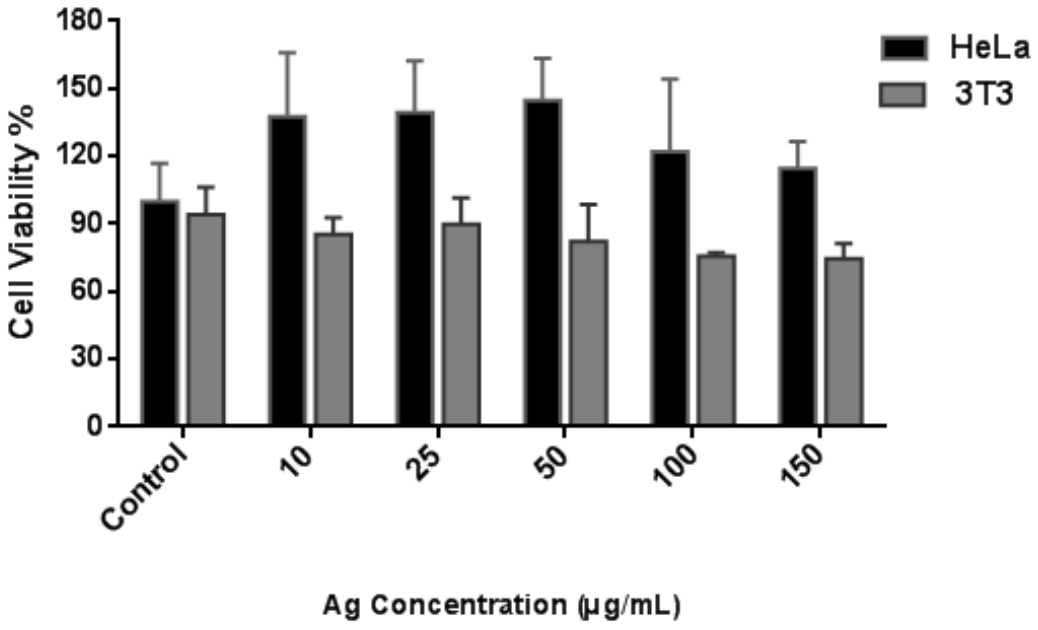

Figure 3.11 Dose dependent cell viability of HeLa cancer cells and NIH/3T3 mouse fibroblast cells after 24 incubation with Ag_2S-DMSA quantum dots.

3.4.4 Hemocompatibility Assessment

Quantum dots` hemocompatibility was evaluated by studying hemolysis, the morphology of blood cells, complement activation (C3a), and coagulation activation,

through the extrinsic and intrinsic pathways.

3.4.4.1 RBC integrity in the presence of QD's

The main cell populations of the blood, erythrocytes, are the first to be evaluated in any hemocompatibility studies.

Hemagglutination (erythrocyte aggregation), plasma membrane rupture or changes in cell morphology are amongst the possible reactions which can occur when a foreign nanomaterial is in contact with the whole blood. All these phenomenon can induce severe circulatory disorders and even lethal toxicity. In view to exclude any possible change in RBC's, we have characterized them by adopting complementary techniques. Following blood incubation with QD's, hemolytic test was conducted according to the ASTM (Standard Practice for Assessment of Haemolytic Properties of Materials). The hemolysis rates determined in the presence of the formulations did not exceed 2% (see Table 3.5). Therefore these QD's may be considered non-hemolytic within the concentrations tested. This is in agreement with the hemolysis rates reported for BSA coated Ag_2S QDs at similar concentrations.[82] As a confirmation QD's under study did not affect RBC size distribution profile and cell counts (Figure 3.12). The microscopic analysis of blood smear (results not showed) also demonstrates the absence of any morphology changes after blood contact with the samples. Therefore, we may conclude that these nanoparticles do not affect the integrity of erythrocytes, the blood major cellular component. This observation is not really surprising taking into account that our QD's have a relatively strong negative Zeta potential. These surface characteristics are therefore counteracting any possible ionic interaction with erythrocytes which have negative surface charges as well.[120]

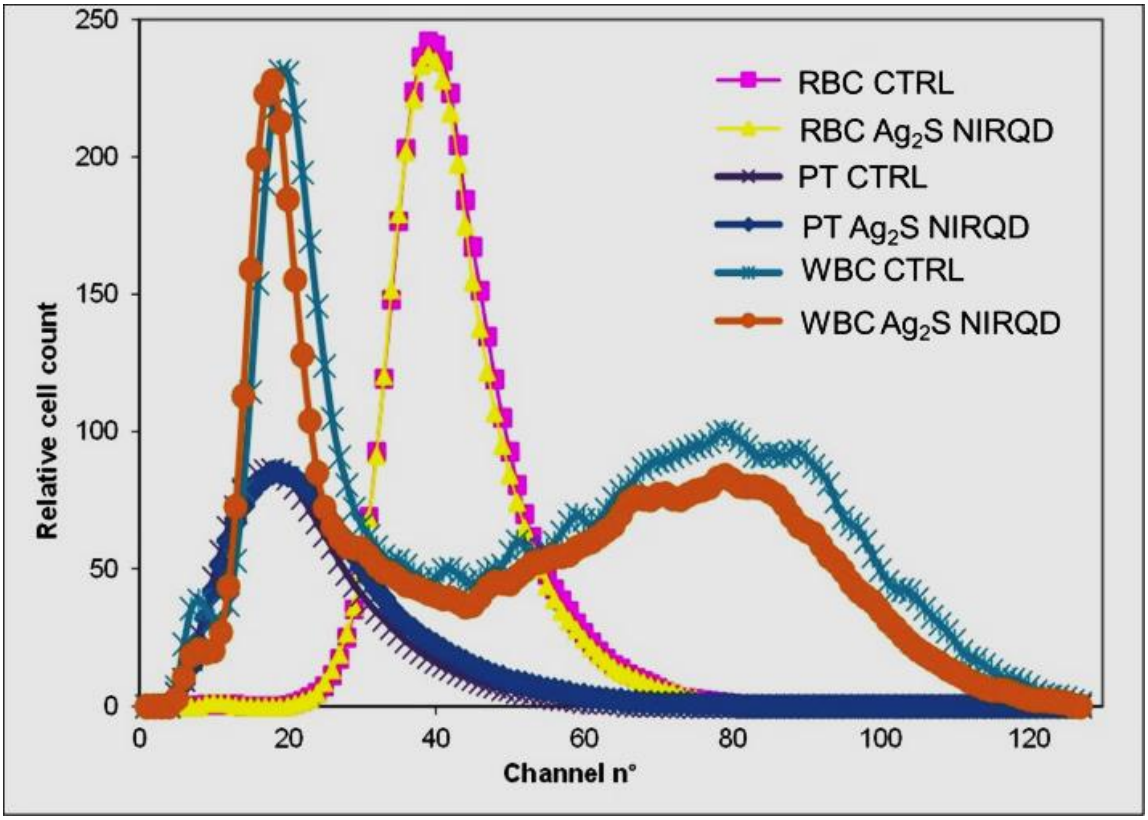

Figure 3.12 Comparison of the blood cell distributions (Red blood cells (RBC's), Platelets (PT) and White Blood Cells (WBC) of the blood control to the blood incubated with Ag_2S NIRQD (100 µg/mL).

3.4.4.2 Platelets and White Blood Cells (WBC's) behavior in the presence of QDs

Platelets, the second main cell population of the blood, are by far more reactive to the presence of foreign surfaces compared to RBC's. Indeed one of their primary functions in hemostasis relies upon their rapid adhesion to the foreign surface exposed by an injured vessel in order to limit any bleeding. Platelet plasma membrane is particularly rich in various biological receptors and are also well-known to interact with various synthetic surfaces, including those in nano-size range.[121] As part of our immune system, some of our WBC's, in particular neutrophils and monocytes have to interact quickly with foreign materials in order to clear them from the blood compartment.

Table 3.5 Percentage of hemolysis, complement activation, and hemostasis activation (Quick and TCA) after incubation at 37°C of the QDs in whole blood.

QD's (µg/mL)	Hemolysis[a] (%)	Complement activation[b] (%)	Quick activation[c] (%)	TCA activation[c] (%)
1	0.08 ± 0.00	102.2 ± 6.6	93.4 ± 7.6	102.0 ± 5.2
10	0.22 ± 0.07	135.1 ± 6.3	98.4 ± 3.3	88.1 ± 6.1
100	0.22 ± 0.07	116.2 ± 1.1	100 ± 4.1	68.6 ± 4.5
Ctrl +	39.66 ± 0.07	158.9 ± 3.6	123.2 ± 3.2	-
Ctrl -	0.37 ± 0.09	100.0 ± 3.9	100 ± 4.3	100.6 ± 5.0

[a] Hemolysis percent represent free plasma hemoglobin released as a result of contact with the test material divided by the total blood hemoglobin multiplied by 100. Ctrl +: Saponin, Ctrl -: PBS. [b] Complement activation is expressed as a % of C3a concentration, adopting normal blood incubated in the same conditions as 100%. Ctrl +: blood incubated with Zymosan, Ctrl -: Plasma with no additives. [c] Quick and TCA hemostasis assays are reported in % of the clotting ability of the sample compared to the clotting ability of a standard human plasma normalized to 100. Ctrl +: Kaolin, Ctrl - : PBS.

The comparison of the platelet and leucocyte size distribution of the blood control to the blood contacted with QDs (Figure 3.12) clearly highlights that at the highest concentration of nanoparticles assessed, 100 µg/mL, no significant alteration is observed for any cell type. It is also the case for the global counting of these cells (results not shown). At a level of our pre-screening hemocompatibility study, these data are therefore supporting the fact that Ag_2S-DMSA NIRQDs do not interact significantly with the various blood cell elements. This observation is of particular interest regarding platelets which are well-known to react when in contact with foreign body surfaces.

The complement system is also part of our immune response to facilitate the elimination of certain pathogens from the body. But its chronic activation throughout the alternative pathway, via the nonspecific adsorption to foreign surface and cleavage of the C3 protein to produce C3a, can be responsible for hypersensitivity and anaphylaxis reactions.[122] Complement activation mediated by nanoparticles can also result in their rapid removal from systemic circulation by mononuclear cells via a receptor-mediated phagocytosis of complement. Based on the data provided on Table 3.5, only a

slight activation of the complement system, which is not dose dependent in the range of QD concentrations tested, was detected.

3.4.4.3 Assessment of hemostasis in the presence of Ag_2S-DMSA NIRQDs

The effect on hemostasis control was determined by coagulation assays, both through the extrinsic pathway (PT assay) and the intrinsic pathway (APTT assay). Clot formation was determined after blood incubation with QDs. Clotting ability of the standard plasma is assumed to be 100%. The longer it takes plasma to clot, the lower is its clotting ability, and the lower is the resulting test value expressed in percent to the standard plasma. It is also worth mentioning that these two coagulation pathways are intrinsically linked. For example, tissue factor–factor VIIa complex initiating the extrinsic pathway is also capable of activation of factor IX of the intrinsic pathway; in turn, the intrinsic tenase complex influences the tissue factor-dependent pathway.[123] The extrinsic coagulation pathway was not affected by Ag_2S-DMSA NIRQDs, while the intrinsic pathway was significantly inhibited at the highest concentrations of the QDs (100 μg/mL) (Table 3.5). As reported recently, inhibition of intrinsic and extrinsic pathways of coagulation can be explained by the non-specific adsorption of proteins involved in the coagulation cascades onto the surface of materials involved.[124] Among these proteins, fibrinogen, factor IX, prothrombin, factor X, and antithrombin III deserve particular interest as key factors in the activation of all humoral blood reactions. The fact that the intrinsic pathway is specifically altered in contrast to the extrinsic mode is not really surprising keeping in mind that more protein factors are involved in the former one. Although it would be valuable to identify the exact nature of the factor(s) involved in the QDs-mediated coagulation inhibition, this mechanistic study was outside of the main focus of our work.

3.4.5 In vitro Cell Imaging

Use of Ag_2S-DMSA NIRQDs as optical imaging agents was evaluated as well since such bio-applications are the major motivation behind such particles.

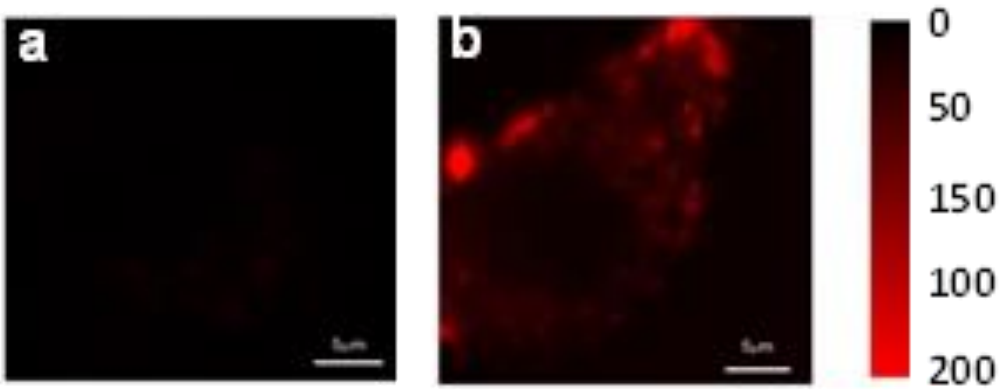

Figure 3.13 Fluorescence image of HeLa cells a) without and b) with internalized Ag_2S-DMSA NIRQDs obtained by confocal laser scanning microscope.

Couple of examples found in the literature demonstrated in vitro imaging of cancer cells with Ag_2S NIRQDs emitting in the NIR-I[112] and NIR-II window[85]. Also, in vivo imaging of nude mouse with Ag_2Se NIRQDs[73] and Ag_2S NIRQDs[76] were recently reported.

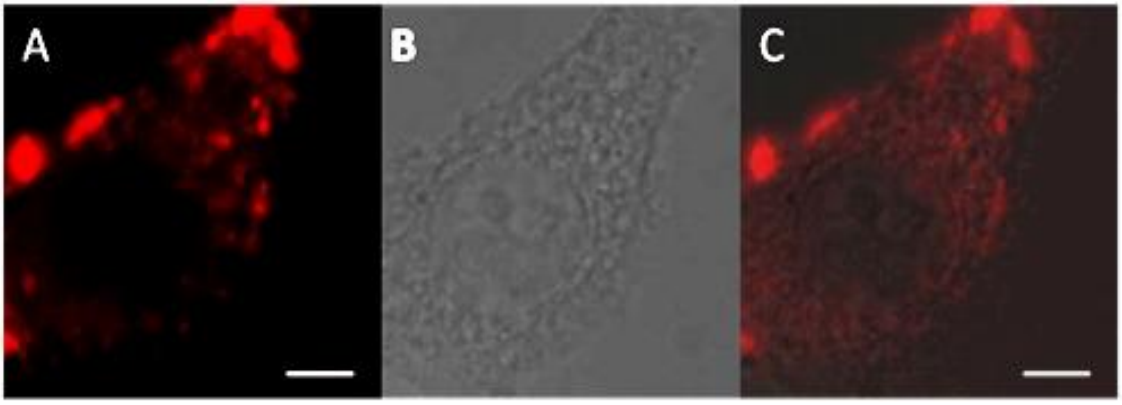

Figure 3.14 Cellular uptake and localization of Ag_2S-DMSA NIRQDs by HeLa cells (150 µg/mL QDs, 6h incubation).(A) Fluorescence, (B) Transmission and (C) Overlay channels of confocal micrograph. Scale bar represents 5µm.

Here, HeLa cells incubated with Ag_2S-DMSA NIRQDs 6h was imaged under fluoresence microscope. These QDs are easily excited at 532 nm which causes a minimal autofluoresence from the cells (Figure 3.13 a) but allows visualization of a

very bright cellular image with a high intensity from QD internalized HeLa cells (Figure 3.13 b). Confocal laser scanning microscope image in Figure 3.14 shows strong fluorescence of Ag_2S-DMSA NIRQDs in HeLa cells. These QDs have typical cytoplasmic distribution to endosomes and lysosomes with no nuclear uptake.

3.5 Conclusions

In vivo utilization of QDs as imaging agents and/or delivery vehicles require a delicate balance of toxicity, biocompatibility, stability, luminescence quality, size and excitation/emission wavelengths. Considering all these Ag_2S NIRQDs present a great potential. Utilization of DMSA, FDA approved heavy metal chelating drug, as a coating and slow sulphur releasing agent under appropriate conditions (pH 7.5 and 70°C and above) at mole ratios of DMSA/Ag of 1.5, 2.5 and 3.5, provided Ag_2S QDs with tunable emission between 730-900 nm with the best quality particles around 800-860 nm range which is the desired window for medical purposes. QY of these particles are as high as 6.5% and high enough for effective optical imaging. They are demonstrated as effective cytoplasmic imaging agents in HeLa cells. Recently, aqueous Ag_2S QDs coated with BSA were prepared with tunable sizes (within a range of 150 nm) in the second NIR region with the best particles emitting at around 1150 nm with 1.8% QY[82]. Considering the imaging devices and routine instrumentation, working in the second NIR window is difficult since it is beyond the limits of most widely used Si and PMT detectors.

DMSA coated Ag_2S NIRQDs showed good cytocompatibility and hemocompatibility in the *in vitro* experiments without any PEGylation or protein shell such as BSA. This achievement is significant and very valuable for *in vivo* experiments where long blood circulation time and high level of cytocompatibility is necessary. These Ag_2S-DMSA NIRQDs are non-toxic up to 840 μg/ml (200 μg/ml Ag^+)in HeLa cancer cell lines and showed only 20% reduction in cell viability of 3T3 NIH cells in 24h. Hemocompatibility testing has also highlighted that they do not elicit any major

reaction within the blood up to a concentration of 100 μg/mL. These QDs do not affect the integrity of erythrocytes, do not interact with platelets and show only a slight alteration on the complement system and on the intrinsic pathway of coagulation. To the best of our knowledge this is the first report assessing the hemocompatibility of Ag_2S QDs in such detail. Drugs and targeting moieties can be conjugated to the surface carboxylates of these QDs. These NIR QDs hold great potential as new theranostic nanoparticles.

Chapter 4

4 AQUEOUS NIR EMITTING HYBRID NANOPARTICLES (Ag_2S-Fe_3O_4) FOR BIOMEDICAL APPLICATIONS

4.1 Introduction

Multifunctional colloidal nanoparticles are of special interest for medicine and biotechnology. Superparamagnetic Iron Oxide Nanoparticles (SPIONs)[125-127] and luminescent semiconductor Quantum Dots (QDs)[31, 42, 44] have been widely studied for medical and biological applications for diagnostics, therapy and labeling. SPIONs have been particularly utilized as contrast agents in MRI for both vascular and organ imaging, especially for liver.[126, 127] Magnetic separation is another application reached commercialization in biotechnology.[87, 128] Cell tracking[129], magnetic drug delivery, hyperthermia[87, 128], detoxification[90] etc. are the other applications of SPIONs which are in the research or clinical phase.

QDs are mostly being utilized in electronic, energy and biological applications.[41, 46, 57, 59, 130, 131] They possess broad absorption and narrow emission profiles allowing excitation of different QDs at a single wavelength with minimal overlap of emission.[44, 89] In addition, high extinction coefficient and photo-stability makes them superior optical probes in labeling and diagnosis compared to organic fluorophores.[42, 132] Cd chalcogenides such as CdS, CdSe, CdTe, were the most

studied semiconductors and emit in the visible range (400-700 nm).[35, 100] However, they pose significant toxicity in biological applications.[54] Attempts to reduce cytotoxicity related to Cd^{2+} release involves ZnS overcoat, silica shell etc.[77, 133-135] However, there are additional problems. Excitation in the UV and emission in the visible region is far from being ideal for the imaging of biological systems due to intrinsic absorption, autofluoresence and scattering of the tissues and the limitation in the penetration depth. Therefore, QDs emitting in the Near-Infra Red region (NIRQDs) is a better option as optical probes in biotechnology and medicine. Most of the NIRQDs reported in the literature are prepared from binary or ternary alloys of Cd chalcogenides and/or core/shell systems. CdTeSe/CdS,[100] CdMnTe/Hg[66], CdTe/ZnS[136] and PbS[9] are some of the examples of NIRQDs utilized in biological imaging. However, elemental form of Pb, Cd, and Hg are quite toxic.[54, 62] Most recently, silver chalcogenides[69, 74] have gained significant importance due to NIR emission[71] and excellent cytocompatibility.[70] Ag_2S NIRQDs both emitting in the NIR-I and NIR-II window are highly bio/cytocompatible reported in recent studies.[82, 84, 85, 112] These Ag_2S NIRQDs have been effectively utilized in both *in Vitro* cellular and *in Vivo* imaging.[76, 85, 112]

Magnetic-luminescent hybrid nanoparticles are highly attractive multifunctional materials since they offer opportunity for dual imaging, sensing-separation, imaging-therapy and multiplexed sensors. Response of SPIONs to external magnetic field has been widely utilized to target nanoparticles to the site of interest such as tumors and enhance internalization of nanoparticles increasing the therapeutic effect and decreasing potential side effects.[88, 89] A hybrid nanoparticle therefore can be targeted via magnetic manipulation. Also, combinations of imaging modalities are desirable. Optical imaging has a benefit of sensitivity but lack resolution and has depth limitation, whereas MRI offers high resolution at any depth but lack sensitivity.[91] Combination of the two in a single entity may provide a synergistic effect and provide both sensitivity and high resolution in medical imaging. Also, real time imaging of the theranostic nanoparticle and imaging the outcome of the therapy via optical means are

valuable in the therapy. In one of the most recent studies, Shen et al. prepared a hybrid material from CdTe and SPION via entrapment of these particles in a gelled Chitosan matrix and tagged with folic acid. These particles were biocompatible and successful in the in vivo and in vitro drug delivery. [97] Alternatively, C-dots (Cd free), have been used along with SPION to eliminate Cd based toxicity.[98]

In addition strong absorption of SPIONs in the visible region is another important problem related to hybrids composed of SPION and visible QDs. This causes absorption of photons emitted from QDs by SPIONs, hence reduce the overall QY of the hybrid nanoparticles significantly. Use of Gd-species (T1 agents in the MRI) instead of SPIONs is one of the most recent solutions to the problem. Abdukayum et al, prepared a hybrid from Gd-species and persistent luminescent particles ($Zn_{2.94}Ga_{1.96}Ge_2O_{10}:Cr^{3+},Pr^{3+}$)[91] This complex was nontoxic to MCF-7 and 3T3 cells, and shown as effective T1 agent in MRI and optical imaging agent in the *in vivo* studies. For deeper penetration and minimization of autofluorescence, upconverting materials such as $NaYF_4$ and $NaYF_4$: Yb/Er have been combined with Gd/SPION.[137] These particles were further coated with PEG to decrease cytotoxicity.

Here, we demonstrate an alternative solution with utilization of SPIONs and Ag_2S NIRQDs. A magnetic-luminescent hybrid nanoparticle composed of SPIONs and Ag_2S NIRQDs would provide many advantages for medical/biotechnology applications: 1. Excitation at longer wavelengths (in the visible region) which is safer than UV, 2. No absorption of the emitted photons by SPIONs since they have no absorption in the NIR, 3. No autofluoresence from the natural biological components in the NIR, 4. Increased penetration depth, 5. None or less decrease in the QY, 6. No significant toxicity related to QD without a need for PEGylation, 7. Multimodality: optical and magnetic resonance imaging where neither modality (magnetic and optical providing both resolution and sensitivity) pose ionizing radiation, combined action of imaging and magnetic targeting, combined action of imaging and therapy (hyperthermia). With this motivation, here we demonstrate the synthesis of Fe_3O_4-Ag_2S super-paramagnetic-luminescent hybrid nanoparticles and discuss their properties.

Briefly, 2-MPA coated aqueous Ag_2S NIRQDs were directly prepared in a single step in aqueous medium with QY up to 30%.[112] To the best of our knowledge, this is the best QY reported for Ag_2S QDs until now and possesses a great advantage in deep tissue imaging. As reported by Won et al, improvement of QY is much more efficient than increased concentration in enhancing the CNR and the imaging depth[138]. Ag_2S-2MPA NIRQDs have been successfully used for the in *vitro* cellular uptake and imaging studies on mammalian cells with no significant cytotoxicity. Hybrid nanoparticles have been prepared from SPION and Ag_2S-2MPA NIRQDs by the ligand exchange method demonstrated by our group previously.[139] In this simple method, a biphasic system is prepared from mixing Ag_2S-2MPA NIRQDs in aqueous and lauric acid coated SPIONs in organic phase. Upon mixing, QDs in aqueous phase exchanged LA of SPIONs and carried the whole hybrid nanoparticle into the aqueous phase. Hybrids emitting at around 810, 875 and 910 nm were prepared with good luminescence, magnetic response and colloidal stability. Cytocompatibility of these hybrids and cell internalization were studied both in the absence and presence of magnetic field to demonstrate the effect of magnetic dragging on internalization. Confocal-fluorescence microscopy of HeLa cells incubated with hybrids showed typical cytoplasmic distribution of hybrids and effective optical imaging.

4.2 Materials and Method

4.2.1 Materials

All reagents were analytical grade or highest purity. Silver nitrate ($AgNO_3$) was purchased from Sigma-Aldrich. Sodium sulfide (Na_2S) was purchased from Alfa-Aesar. 2-Mercaptopropionic acid (2-MPA), aceticacid (CH_3COOH), sodium hydroxide (NaOH), iron(III) chloride hexahydrate ($FeCl_3.6H_2O$), iron(II) chloride tetrahydrate ($FeCl_2.4H_2O$), ammonia (26%), chloroform and 4% paraformaldehyde were purchased from Merck. Lauric acid (LA) was purchased from Fluka. LDS 798 Near-IR laser dye

was purchased from Exciton Inc. 4',6-diamidino-2-phenylindole (DAPI) was purchased from Aldrich.

4.2.2 Preparation of Ag_2S-2MPA NIRQDs

2-MPA coated Ag_2S NIRQDs were synthesized as described before and cleaned from excess materials by washing through AMICON ultrafiltration tubes (MWCO 3000 Da cut-off) with DI water.[112]

4.2.3 Preparation of Ag2S-Fe3O4 Hybrid nanoparticles

Lauric acid coated iron oxide nanoparticles were prepared as described by Acar et al.[139] Simply, aqueous suspension of LA coated SPIONs were prepared from iron salts with the action of ammonium hydroxide at 80 ^oC and extracted into chloroform as LA monolayer coated SPIONs through mixing of this aqueous solution of SPIONs with chloroform. LA coated SPION in chloroform (dark brown) and Ag_2S-2MPA NIRQD in water (brown) were mixed (equal volumes) in a round bottomed flask, sonicated briefly at room temperature and stirred at 1000 rpm overnight (Figure 4.1). Dark brown aqueous layer was separated from colorless chloroform layer in a separatory funnel. The aqueous layer which has the Ag_2S/Fe_3O_4 hybrid nanoparticles were washed through 30K cutoff Amicon-ultra centrifugal filters until no PL emission is detected in the removed water.

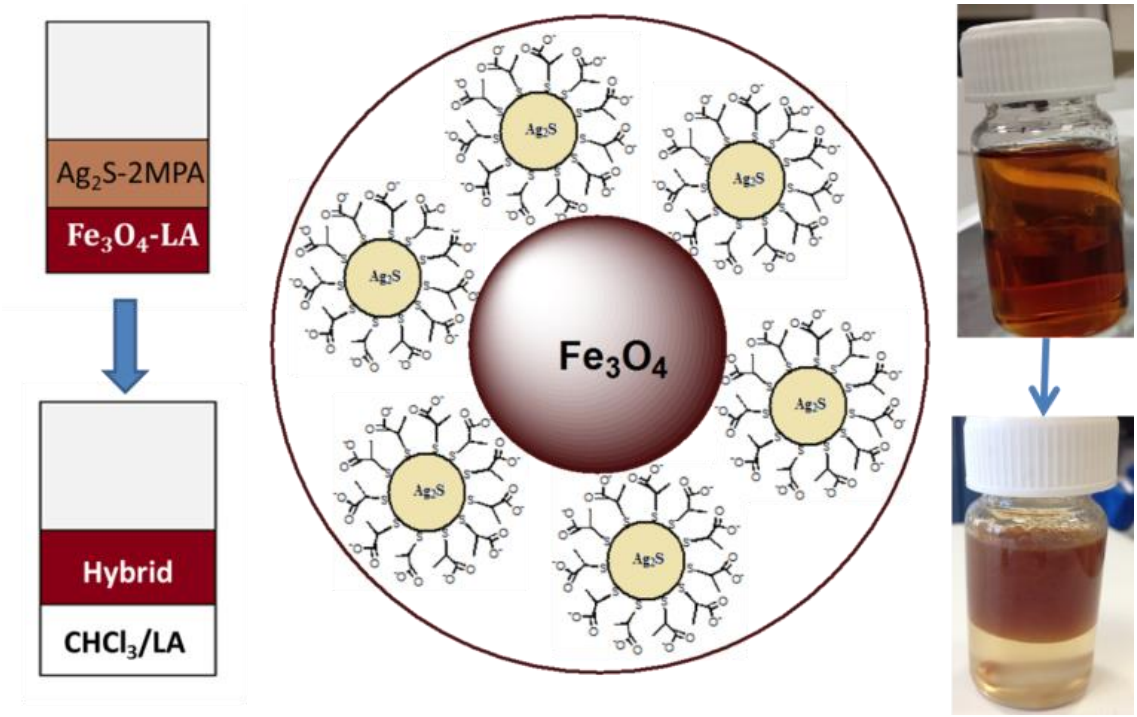

Figure 4.1 Preparation of hybrid nanoparticles by ligand exchange method.

4.2.4 Cell culture

Human cervical carcinoma (HeLa) and mouse fibroblast cells (NIH-3T3) were cultured in complete medium DMEM consisting of 10% fetal bovine serum, 1% penicillin-streptomycin antibiotic solution and 4 mM L-glutamine. Both cell lines were incubated at 37 ^{o}C under 5% CO_2 and cell detachment process was performed by Trypsin-EDTA.

4.2.5 Cell viability via MTT assay

NIH-3T3 and HeLa cell lines were cultured at a $1x10^4$ cells/well in 96-well plates in complete DMEM culture medium overnight. Then the medium was replenished and hybrid nanoparticles were added to each well at doses between 10-50 µg Ag/mL. MTT (3-(4,5-dimethylthiazol-2-yl)-2,5-diphenyltetrazolium bromide) solution at a concentration of 5 mg/mL in 1M PBS was prepared. After 24h incubation, the medium was replaced with 150 µL complete DMEM medium and 50 µL of the MTT solution

was added to each well. After 4 h incubation with MTT, medium was discarded and purple formazan product was dissolved with 200 µL DMSO:EtOH (1:1). Mitochondrial activity of viable cells reduces MTT to formazan and therefore quantity of formazan determined by absorbance at 600 nm (ELx800 Biotek Elisa reader) is proportional to the number of viable cells. Percent viability was reported as the average of five replicates with respect to absorbance average of control (cells with no nanoparticle). Statistical analysis was examined by one-way ANOVA with Tukey's multiple comparison test of the Graph Pad Prism 5 software from GraphPad Software, Inc., USA.

Cells were also incubated with hybrid nanoparticles at 25 µg Ag / mL dose for 24h under magnetic field using magnetic plate holder for 96-well plates (magnetopure-96 from Chemicell) and the MTT assay protocol was applied as described above.

Internalization of hybrid nanoparticles was quantified by the measurement of silver amount in the cell lysite using Genesis ICP-OES. For ICP analysis, cells were incubated with hybrid nanoparticles as described before in 96-well plates. After 24h incubation, medium was replaced with 200 µL de-ionized distilled water to remove un-internalized nanoparticles. 10 ml ICP-OES solutions in distilled water were prepared for each well with addition of 200 µL nitric acid and 200 µL sulfuric acid. Silver amount (µg/mL) was reported as the average of five replicates. Statistical analysis was examined by one-way ANOVA with Tukey's multiple comparison test of the Graph Pad Prism 5 software from GraphPad Software, Inc., USA.

4.2.6 Cell Imaging

100,000 HeLa cells were seeded and incubated in glass bottom dishes for18 h. 50 µg/ml Ag^+ ion containing hybrid sample was added to cells in full medium and incubated for 6 h. Also, cells were treated with DAPI (20 µl) to stain nuclei during the incubation. Cells were washed several times with PBS buffer (at pH=7.4). 4% paraformaldehyde solution was used for cell fixation.

Image acquisition was done using a home-made confocal laser scanning microscope equipped with an inverted microscope frame (Nikon TE 2000U) and a 60× (Nikon, NA=1.49) oil immersion objective.

Samples were illuminated with a 532 nm laser after reflected by a broadband 10/90 dichroic beam splitter. Emission signals were filtered by RG665 and FGL550 long pass filters and collected by Silicon APD photon counting modules.

Samples were also excited with a 420 nm laser to record both emissions from the Ag_2S QDs of the hybrid nanoparticles and DAPI in the cell nuclei. Laser output power was 7-10mW. 10/90 dichroic beam splitter was used for excitation. Two different channels were used to monitor emission from hybrid nanoparticles and DAPI, simultaneously. Silicon APD detector was used in both channels. RG665 and FL750 long pass filters, and HQ810/90 band pass filter were placed in front of the detector in the first channel for the detection of emission originating from hybrid nanoparticles. Emission of DAPI was recorded in the second channel with FL450 long pass filter and OD0.9 neutral density filter ($10^{-0.9}$ transmission) placed before the detector.

4.3 Characterization Methods

Absorbance spectra of the hybrid nanoparticles and quantum dots were taken in the range of 300-1000 nm by a Shimadzu 3600 PC UV-Vis-NIR spectrometer. Photoluminescence spectra were recorded by a homemade system consisting of a DPSS laser source working at 532 nm, a monochromator (1/8 Newport Cornerstone 130) and a silicon detector (Thorlabs PDF10A, 1.4 x 10- 15 W/Hz1/). Emission signals were filtered by 590 nm long pass filter and were collected in the range of 600-1100 nm. Malvern Zetasizer nano ZS was used for the determination of hydrodynamic size and Zeta potential of particles.

Spectro Genesis FEE Inductively Coupled Plasma Optical Emission Spectrometer (ICP OES) was used in determination of the Ag and Fe ion concentration in the samples. All the samples should be in aqueous solution in ionic form before the measurement. Thus, samples were digested with acid solutions (Concentrated HNO_3 and H_2SO_4) and diluted

to a certain volume with deionized water. Regression curves for each element were prepared at known concentrations. All analyses were done in triplicate and the mean values were reported.

Powder form of the hybrid nanoparticles were obtained after gentle removal of water using a freeze drier (Labconco). Thermo Scientific K-Alpha XPS with Al K-alpha monochromatic radiation (1486.3 eV) was used for XPS analyses. An adhesive aluminum tape was used for holding powdered samples. 400 μm x-ray spot size, 50.0 eV pass energy with 0.5 eV resolution was used. The base pressure and experimental pressure were below 3×10^{-9} mbar and about 1×10^{-7} mbar respectively. C1s peak at 285.0 eV was used as the reference.

4.4 Results and Discussion

4.4.1 Hybrid magnetic and luminescent particles (Ag_2S-2MPA/ Fe_3O_4)

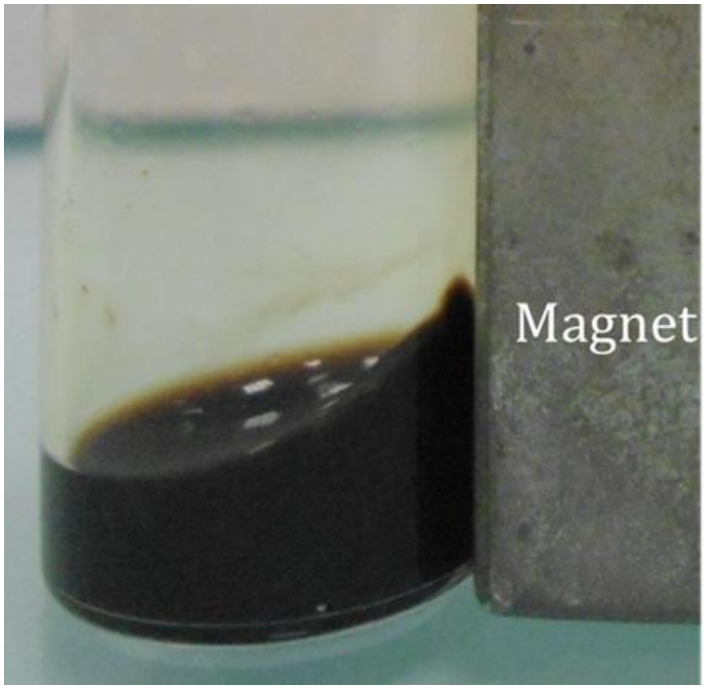

Figure 4.2 Picture of hybrid nanoparticles showing a ferrofluid behavior against an external magnet.

Hybrid nanoparticles were prepared according to the method described in reference 45 (Figure 4.1). Simply, lauric acid coating of Fe_3O_4 nanoparticles suspended in chloroform were exchanged with the Ag_2S-2MPA NIRQDs which transferred SPIONs into the aqueous phase.[139] Binding of external carboxylic acid groups of 2-MPA of Ag_2S on Fe_3O_4 surface provides hybrid structure formation. These hybrid nanoparticles have a strong dark brown/black color, respond to external magnetic field and emit in the NIR region (Figure 4.2, Figure 4.3). Absorbance and PL spectra of the hybrid nanoparticles resemble the absorbance and PL spectra of the corresponding Ag_2S-2MPA NIRQDs (Figure 4.3). There is a couple of nanometers shift in emission maxima of the hybrid material which can be expected in ligand exchange procedures. Although iron oxide does not absorb in the NIR region, hybrids luminesce less than the corresponding NIRQDs. Luminescence decreases with increasing Fe_3O_4 content. Table 4.1 shows the Ag/Fe ratio for all hybrids. H1 with Ag/Fe ratio of 14 retained about 60% of the luminescence intensity whereas others with Ag/Fe ratio less than 5 experienced larger drop in the luminescence intensity (Figure 4.3 and Figure 4.6). Main reason behind the drop in luminescence intensity is attributed to the absorbance of SPION at the excitation wavelength (532 nm) (Figure 4.4). Also, surface perturbation that may cause non-radiative coupling may play a role in such a drop in luminescence as well.

Hydrodynamic size of Ag_2S-2MPA NIRQDs is about 3.5 nm and is larger than the calculated size for the inorganic core by Brus equation, because of the thin coating material around the inorganic core. Lauric acid coated SPIONs in chloroform have about 10 nm hydrodynamic diameter (Figure 4.5). Hybrid nanoparticles composed of these two nanoparticles are about 25nm with no size selective process (Table 4.1, Figure 4.5). This highlights the ability of the preferred method in producing ultra-small hybrid nanoparticles.

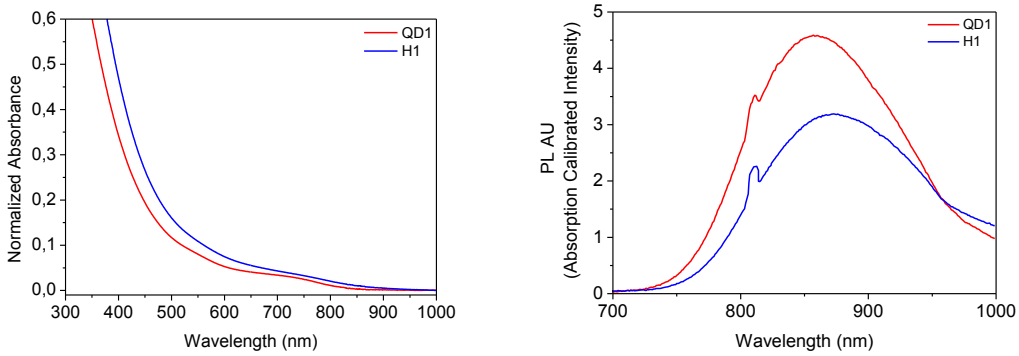

Figure 4.3 Absorbance and photoluminescence spectra (λ_{exc}=532 nm) of Hybrid nanoparticles (H1) and Ag_2S-2MPA NIRQDS (QD1).

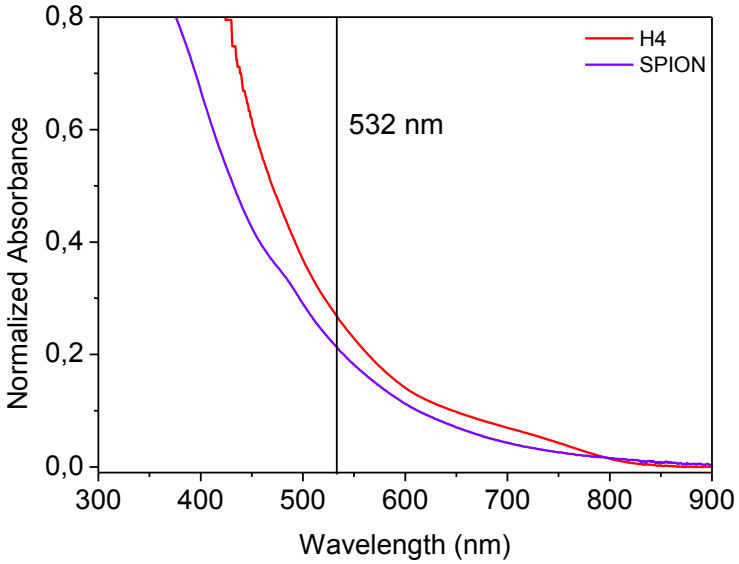

Figure 4.4 Normalized absorbance spectra of SPION and Hybrid nanoparticles.

Table 4.1 Properties of Ag_2S NIRQDs and corresponding hybrid nanoparticles.

ID	Ag_2S NIRQDs	Emission max. of Ag_2S[a] (nm)	FWHM of Ag_2S (nm)	Ag/Fe [b] (mol ratio)	Dh of Hybrids[c] (nm)	Emission max. of Hybrids[a] (nm)
H1	QD1	858	148	14	14.1	873
H2	QD2	890	150	5	123.1	-[d]
H3	QD2	890	150	3.5	42.6	912
H4	QD3*	863	165	2.2	23	876
H5	QD4	768	204	13	24.7	810

[a]Excited at 532 nm [b]Measured by ICP OES, [c]Hydrodynamic size (diameter) measured by DLS and reported as number average, [d]Could not be detected with Si detector. *QD3: Hydrodynamic size: 3.5nm, zeta potential :-38mV, quantum yield with respect to LDS 798 NIR dye:39%.

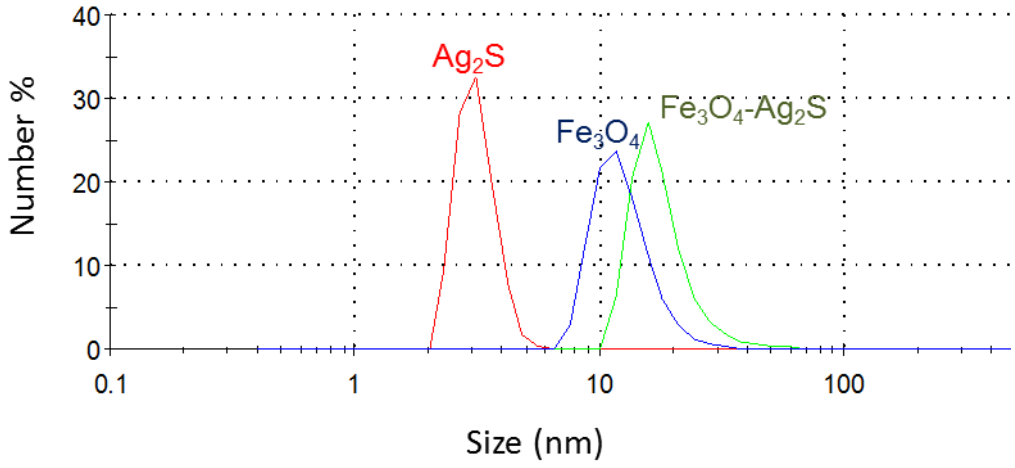

Figure 4.5 Hydrodynamic sizes of Ag_2S QDs, SPIONs and Hybrid nanoparticles (H4).

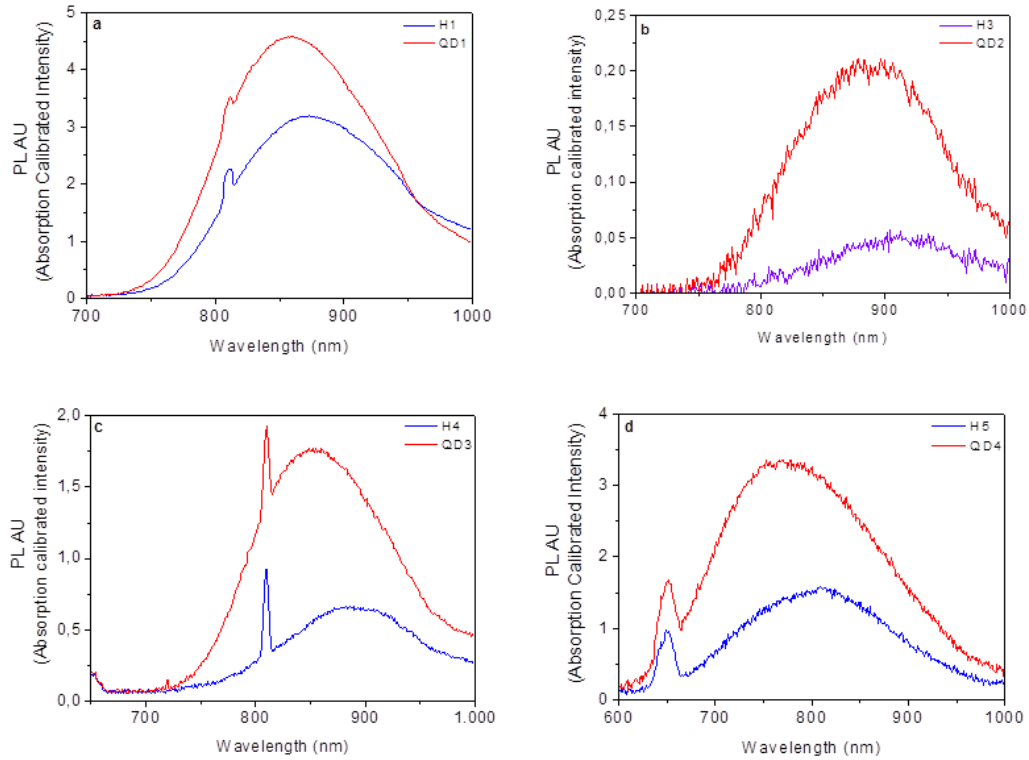

Figure 4.6 PL spectra of both Ag_2S-2MPA NIRQDs and Hybrid nanoparticles excited at 532 nm.

XPS analyses of the Hybrid nanoparticles indicated the presence of both types of particles. Signals corresponding to the binding energies (BE) of Ag 3d, Fe 2p and S 2p core level with their abundance are given in Table 4.2. Typical Fe 2p signals of SPIONs at 710 eV and 726 eV (Figure 4.7b) shifted to[90] 717 eV and 730 eV with a very low signal intensity complicating the fitting. (Figure 4.7a) Fe_3O_4 particles are surrounded by Ag_2S QDs which may be one reason for the low signal. Ag 3d core level have spin-orbit coupling pair at BEs of 367.8 eV and 373.8 eV matching well with Ag_2S (Figure 4.7c).[105, 106, 112] There are two types of sulfur based on the fittings of the signal obtained from S 2p: the one at 161 eV belongs to S in the inorganic core (Ag_2S) and the other one at 163 eV belongs to the sulfur of the coating material (2-MPA) (Figure 4.7d).[104, 112] Surface of the hybrid nanoparticles were etched through plasma.

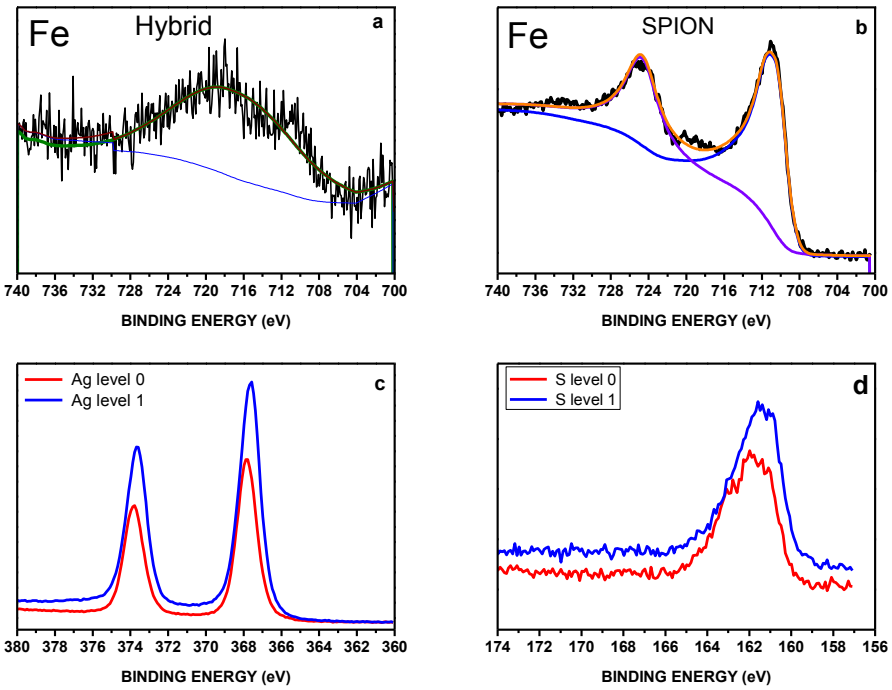

Figure 4.7 XPS spectra of Hybrid nanoparticles. a) Fe 2p region in Hybrid (H4), b) Fe 2p region in SPION, c) Ag 3d region at level 0 and level 1 (plasma etching) and d) S 2p region at level 0 and level 1.

Table 4.2 Binding Energies of the XPS signals with the compositions

	Peak	BE (eV)	FWHM	% Area
LEVEL 0				
	Ag	367.8	1.23	13.33
	S	161.1	1.27	4.76
	S	163.1	1.35	2.17
	S	162	0.96	1.81
	Fe	717	14.91	2.61
LEVEL 1				
	Ag	367.7	1.33	23.09
	S	161	1.54	8.63
	S	164.6	0.49	0.05
	S	162.6	2.15	3.08
	Fe	708.7	6.74	6.88

Intensity of the Ag 3d level increased by etching and signal intensity of S 2p of the coating material decreased with a slight shift whereas, the intensity at 161 eV increased indicating there are more Ag-S deeper in the sample. S 2p at BE of 162eV is probably originating from the Ag_2S with a different S-environment such as those closer to surface. If so, the ratio of Ag 3d to S 2p (161and 162eV) is about 2 which fits to chemical formula. Also, for the H4 Ag/Fe ratio is expected as 4.4/3 but ICP indicates much more Ag than this. However, major problem arises from the poor signal of the Fe 2p obtained for H4.

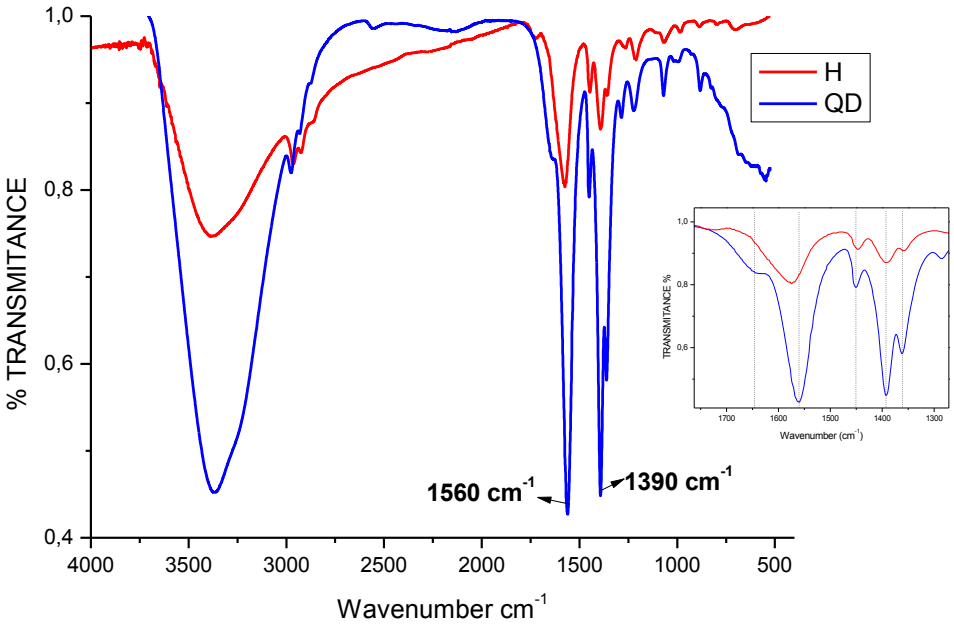

Figure 4.8 Infrared spectra of hybrid nanoparticles and Ag_2S-2MPA NIRQDs.

Infrared spectra of hybrid nanoparticles and corresponding QDs were also compared in Figure 4.8. IR spectra show the streching bands of the coating material 2-MPA. C-H asymmetric and symmetric strechings around 2900 cm^{-1} and O-H streching at 3300 cm^{-1} were seen without any shift in both spectrum.

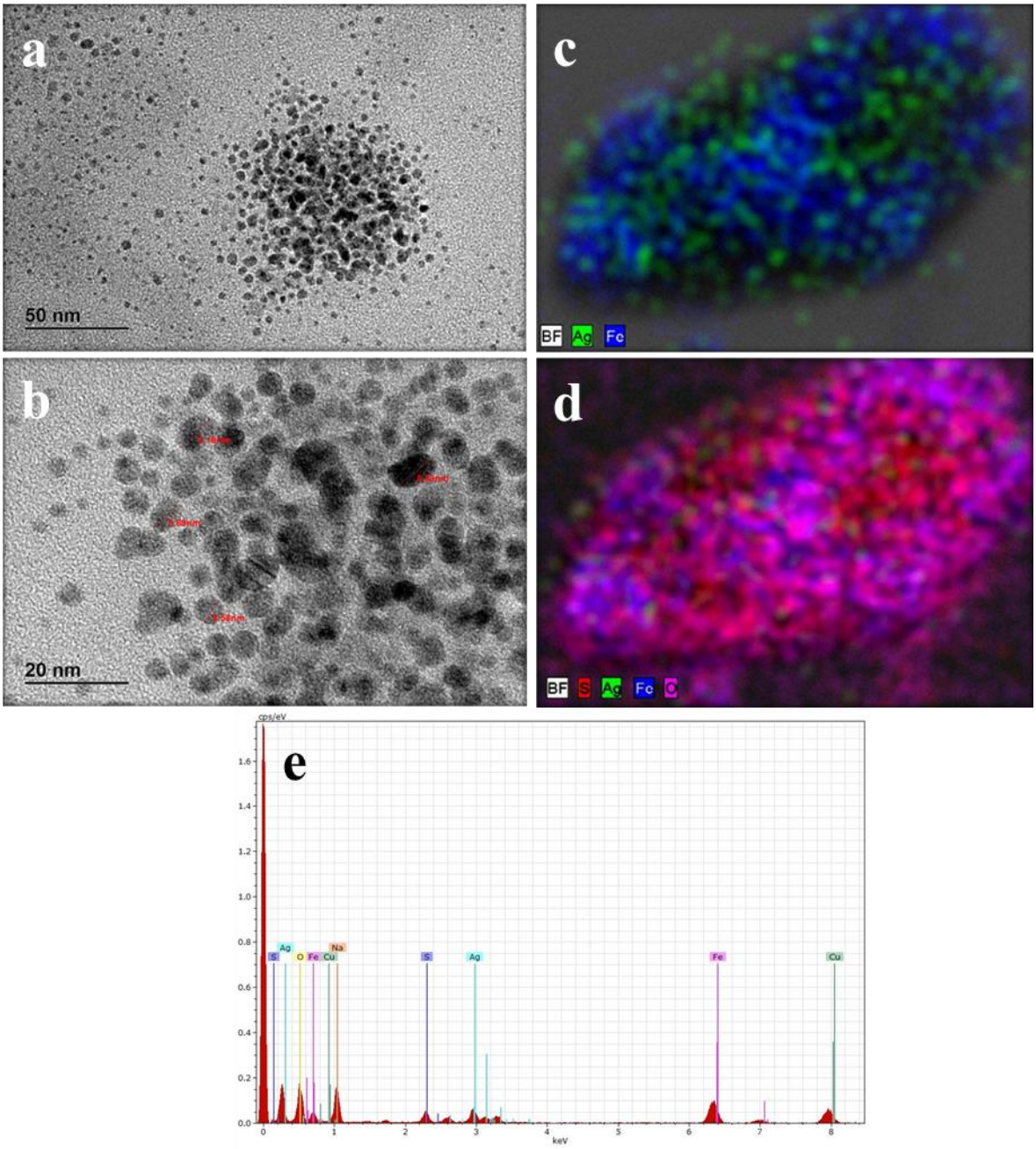

Figure 4.9 a and b) TEM images of hybrid nanoparticles at different magnification. EDX analyses of hybrid nanoparticles showing distribution of c) Ag and Fe, d) Ag, S, Fe and O in STEM images, e) EDX energy transitions for the elements between 0-8 keV.

But, there is a slight shift ($15cm^{-1}$) in symmetric C=O stretching of the carboxylate at 1550 cm^{-1} shown in the inset due to interaction with SPIONs indicating monodentate binding.

When the preparation method of these hybrids is considered, hypothetically a fine structure with SPIONs in the center and QDs around them is suggested. Yet, TEM images did not show such fine structures but rather small clusters of both particles. Such small aggregation may be due to interaction of all QDs with multiple SPIONs and vice versa since they are multifunctional particles. Also, aggregation during drying on the TEM grid may be responsible from such aggregation to a certain extent (Figure 4.9 a and b). Two different particle populations with average diameters of 5 and 8 nm can be seen in the TEM images. Two different particle domains are distinguishable indicating Ag_2S and Fe_3O_4 nanoparticles (Figure 4.10). EDX clearly indicates simultaneous presence of SPION and Ag_2S QDs within these clusters Figure 4.9 c-e. Higher concentration of S around Ag is also visible from the EDX (Figure 4.9 c). However, when O is mapped out, an overall distribution is seen all around the cluster not only due to the presence of iron oxide but because the coating molecule (2-MPA) has carboxylic acid functionality (Figure 4.9 d).

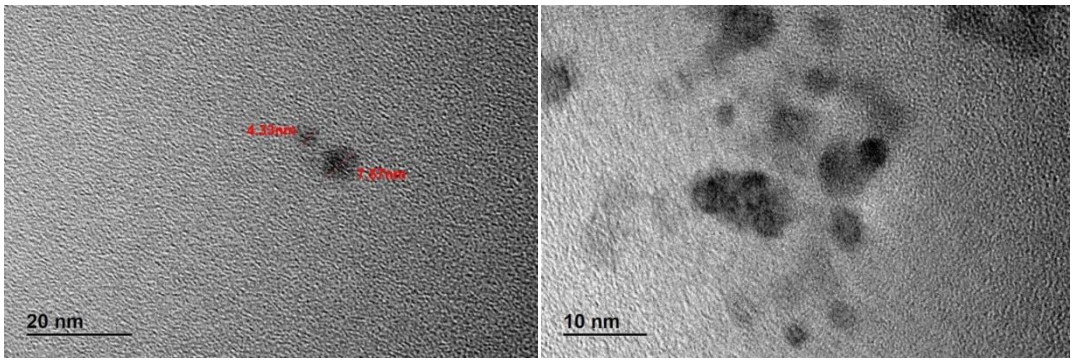

Figure 4.10 TEM images of hybrid nanoparticles indicating presence of different size particles.

4.4.2 In Vitro Studies

4.4.2.1 Cytotoxicity and Cellular Uptake Studies

Viability of HeLa and NIH-3T3 cells in contact with hybrid nanoparticles were tested in 10-50 μg Ag/ml dose range in 24h. Since each hybrid has a different SPION content, dosing could have been done in different ways such as total nanoparticle mass, but total Ag amount was used in order to be consistent with the controls which are Ag_2S QD and Ag^+ cation. As can be seen in Figure 4.11, Ag ion is toxic at all doses and at 50 μg/mL viability dropped down to 11%. QD1 which was the Ag_2S used in the formation of H1, showed no cytotoxicity. Differences in the viability values for QD1 are not significant compared to control (no nanoparticle). When H1 (made from QD1) and QD1 are compared, hybrid showed more toxicity but statistically significant result was observed at 50μg/mL indicating an influence of size and/or iron content on cytocompatibility. When only hybrids are considered, H2 and H3 showed no dose dependent toxicity. H4 and H2 showed major drop in viability only at 50 μg/ml. Overall, viability decreased in the order of QD1, H4, H1, H3-H2. This trend indicates that size of the hybrids is more influential than the Fe content of each hybrid. H1 and H4 are the smallest particles with hydrodynamic size less than 30 nm whereas the other two are larger (still less than 150nm). Total nanoparticle loading or Fe content seems to be negligible when compared with the size since H4 has the highest Fe content and has the highest nanoparticle loading at the same time, but H1 has the lowest Fe content and lowest nanoparticle loading.

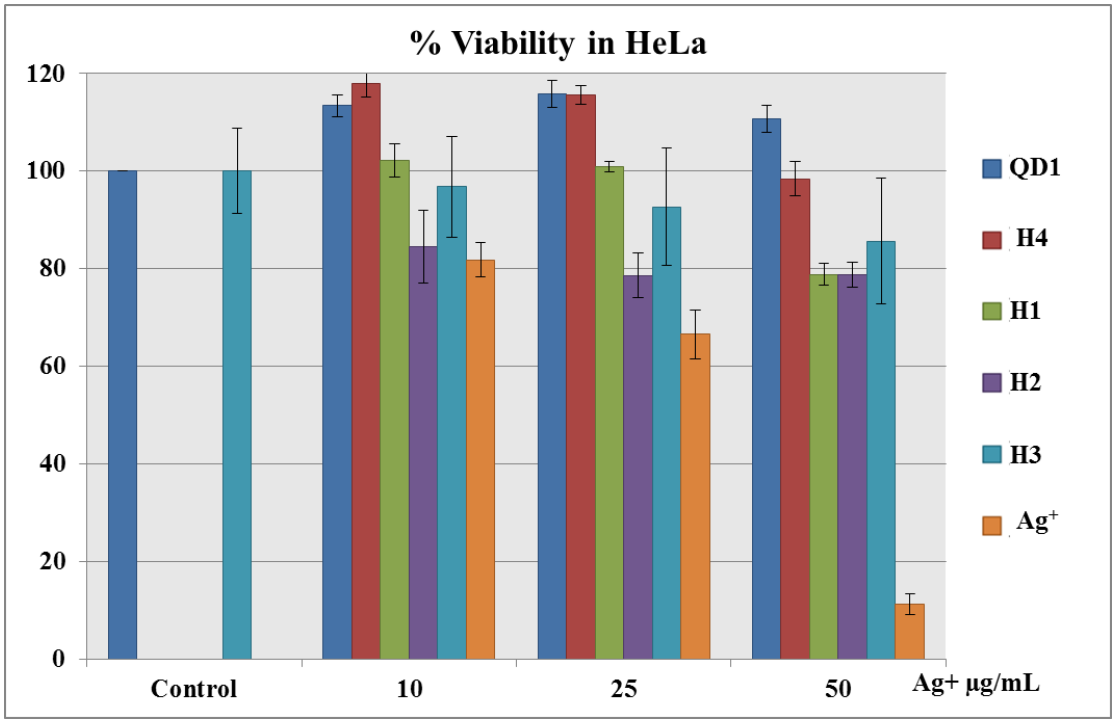

Figure 4.11 Changes in the metabolic activity of HeLa cells after 24 h exposure to Ag_2S quantum dots and Hybrids as determined by MTT Assay.

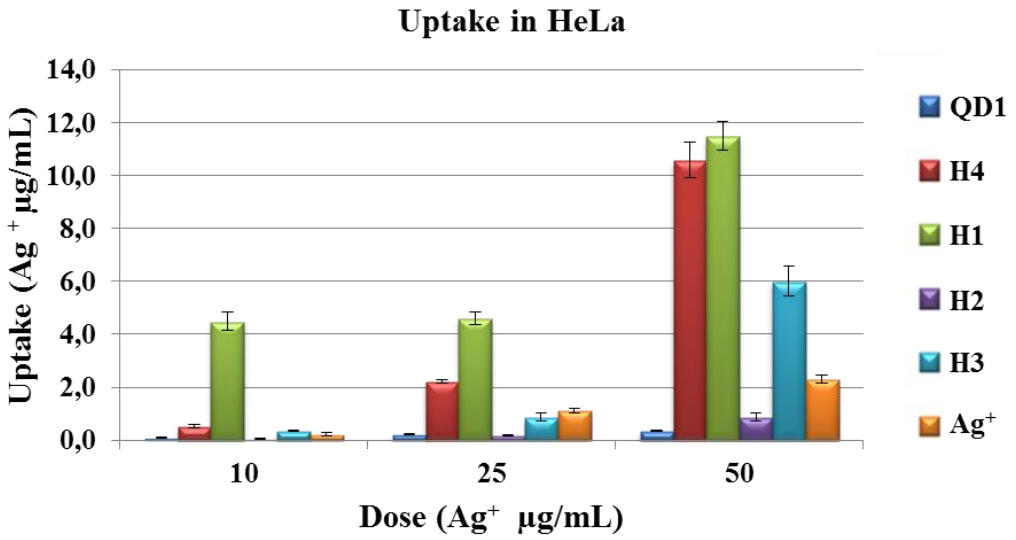

Figure 4.12 Cellular uptake of hybrid nanoparticles, Ag_2S-2MPA NIRQDs and Ag^+ determined by ICPOES for HeLa cell lines.

Correlating viability (Figure 4.11) with cell uptake of particles is important to understand the true cytocompatibility. In general, Ag concentration of the cell lystes increased with the increasing dose of nanoparticles in HeLa (Figure 4.12) with a major jump at 50 µg/ml dose. When percent uptake is considered, 45% of the incubated dose was taken up by HeLA cells at most in case of H1 at 10 µg/mL. H4 and H1, smallest particles, showed highest internalization by HeLa cells. Interpretation of this data along with the cell viability data indicates that these particles are well internalized and intrinsically cytocompatible in HeLa cells. Also, hybrid particles except H2, are internalized significantly in higher percentages than Ag ion at all doses. H3 is also internalized significantly more than silver ion at 50ug/mL, yet viability is around 86% whereas with Ag ion at the same dose dropped down to 11%.

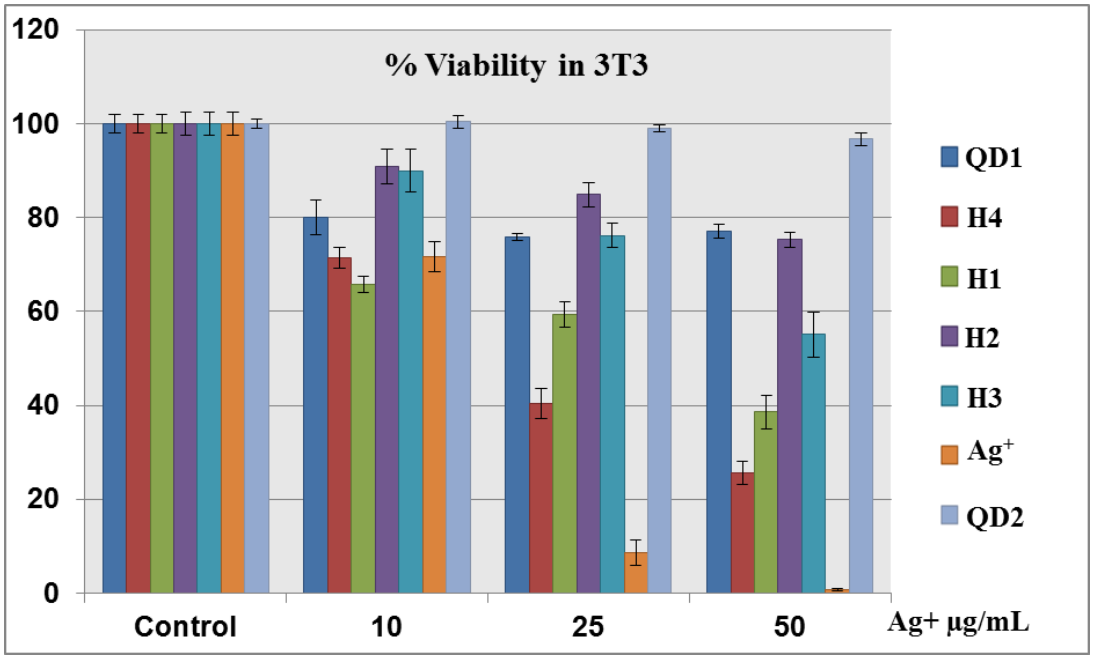

Figure 4.13 Change in the metabolic activity of NIH/3T3 mouse fibroblast cells after 24 h exposure to Ag_2S quantum dots and Hybrids as determined by XTT Assay.

Overall, despite of the higher internalization of hybrid nanoparticles compared to silver ion, their toxicity is lower, indicating stability of particles in cells and better cytocompatibility of the silver chalcogenides compared to silver ion. Another

interesting point is the extremely low level of uptake of QD1 (0.7-0.8% at all doses) compared to H1 (45-18% with the studied dose range).

Hybrid nanoparticles were more toxic to NIH-3T3 compared to HeLa. In HeLa cells, viability dropped down to ca 80% at most, yet in NIH-3T3 viability ranged between 91-26%. Just silver ion is more toxic to NIH-3T3 as well with viability falling below 10% at 25 μg/mL Ag^+. Smallest particles, H4 and H1 are the most toxic ones and toxicity increase with the dose. Viability falls below 50% at 25 μg/ml with H4 and at 50 μg/ml with H1. Largest particles, H2 and H3, are the most cytocompatible ones. H2 showed similar level of viability in the range of 90-75% similar to HeLa. H3 showed about 45% drop in viability at 50 μg/mL. H2 and H3 were made from QD2 which showed slightly better cytocompatibility than its hybrids similar to QD1 and H1. Most significant difference is between QD2 and H3 at 50 μg/mL with viability around 97% versus 55%, respectively. Overall, viability decreased in the following order: H2>H3>=QD1>H1>H4>Ag (Figure 4.13).

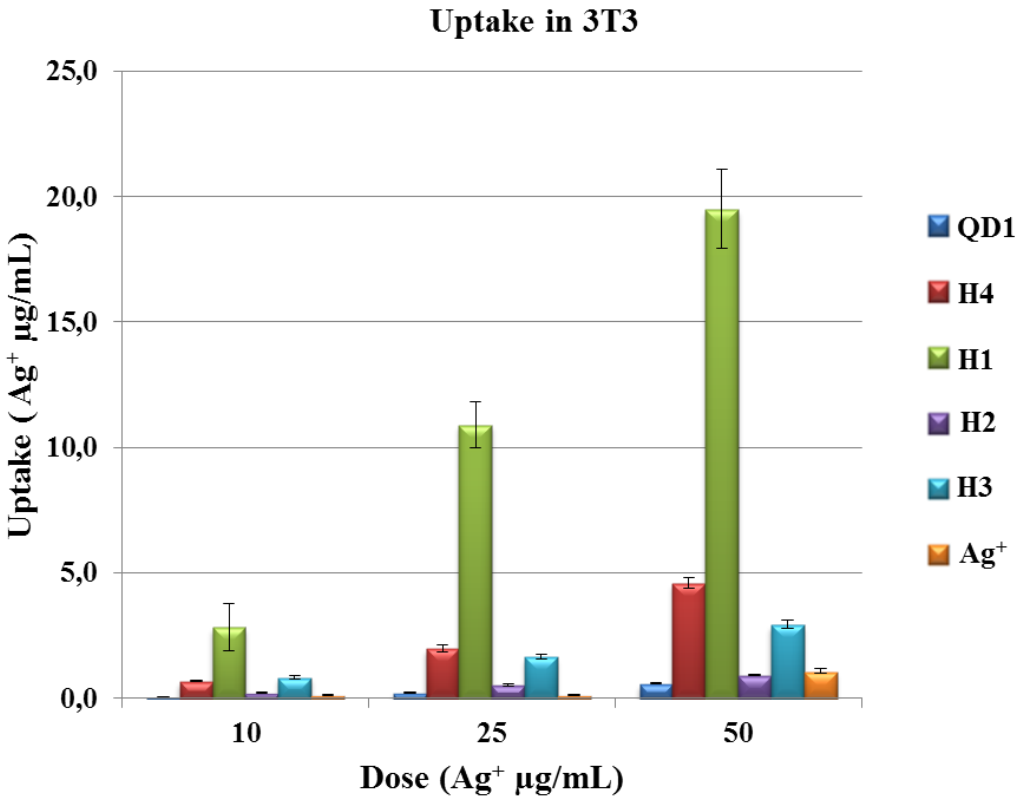

Figure 4.14 Cellular uptake of hybrid nanoparticles, Ag_2S-2MPA NIRQDs and Ag^+ determined by ICPOES for 3T3 cell lines.

Quantification of internalized particles by NIH-3T3 cells indicated decreasing uptake in the following order: H1, H4, H3, H2 (Figure 4.14). Smaller particles were taken up in higher amounts than larger particles by NIH-3T3 which is the opposite of HeLA. H1 internalized significantly more than others followed by H4. In case of H1, at the highest dose 19.5 µg Ag was found in cells compared to 10.9 µg at the middle dose in NIH-3T3. At the highest dose of H1, cells had about 11.5µg in HeLa. When viability of these two cell lines at similar internalized dose of H1 are compared, significant difference in vulnerability is seen with viability around 80% in HeLa versus 60% in NIH-3T3. H2 and H3 also internalized more by NIH-3T3 compared to HeLA. However, H4 were internalized in significantly lower amounts (similar uptake at 25

µg/mL dose in HeLa versus 50µg/ml in 3T3), but dramatically more toxic to NIH3T3 (above 100% in HeLa versus 40% in 3T3).

4.4.2.2 Magnetic Uptake

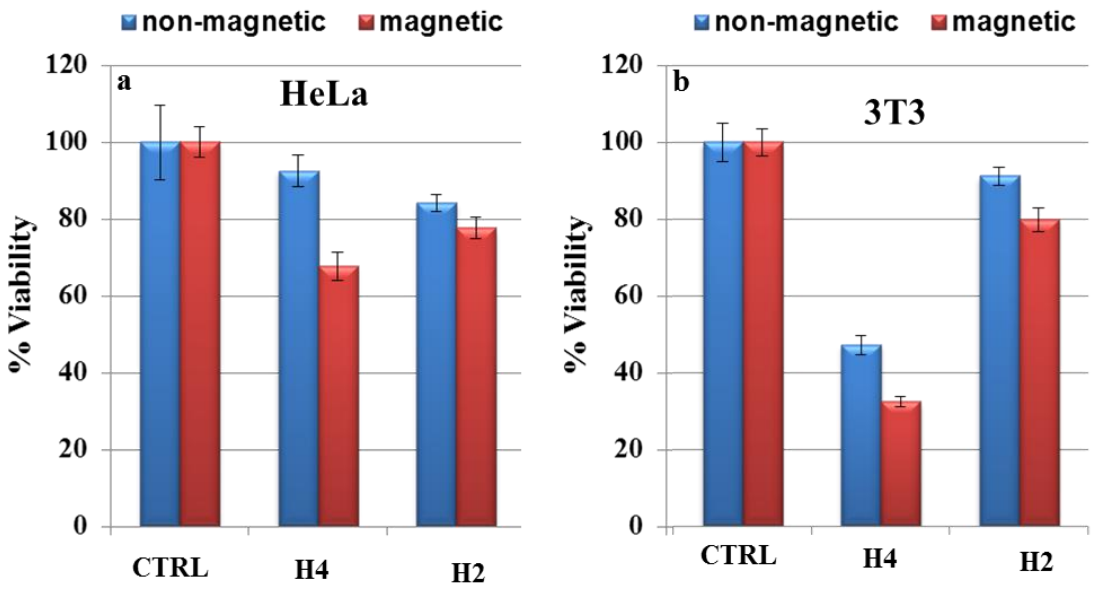

Figure 4.15 Viability of HeLa and NIH-3T3 cells treated with H4 and H2 hybrid nanoparticles at 25 µg Ag/ml for 24h in the presence or absence of external magnetic field.

Presence of the magnetic nanoparticles within the hybrid structure provides opportunity for magnetic targeting. In order to study the influence of magnetic field on cell viability H4 which showed best viability in HeLa but worst for 3T3, and H2 which showed best viability for NIH-3T3 and worst in HeLa was chosen at fixed concentration of 25 µg /ml Ag dose and incubated with HeLa and NIH/3T3 cells in the absence and presence of magnetic field for 24h. H4 showed more significant decrease in the cell viability which is reasonable since it has more SPION in the hybrid than H2 (Ag/Fe=2 versus Ag/Fe=5.1) in both cell lines (Figure 4.15). Higher SPION content provides more effective magnetic response.

4.4.2.3 In Vitro Cellular Imaging

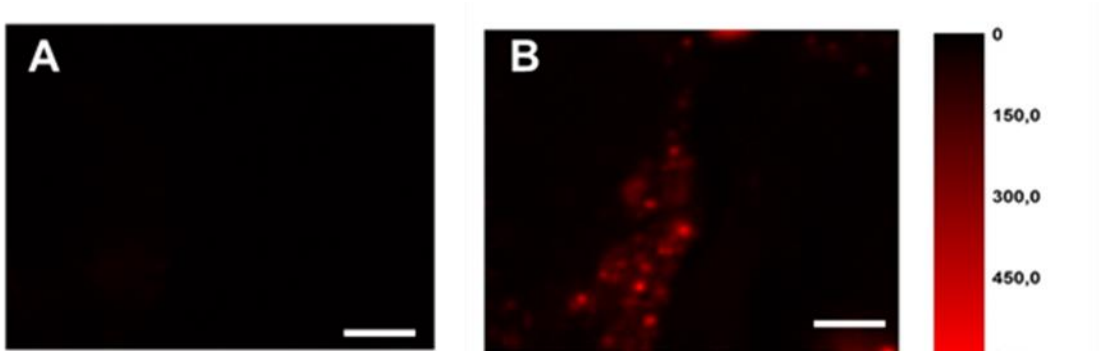

Figure 4.16 A) Autofluorescence of HeLa cells B) Florescence image of internalized hybrid nanoparticles in HeLa cells by confocal Laser Scanning Microscopy. The scale bars represent 5µm. Excitation wavelength is 532nm.

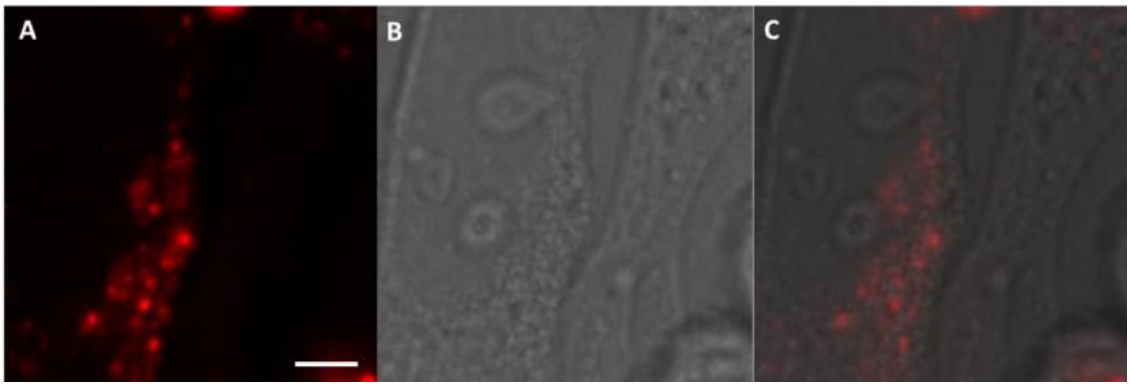

Figure 4.17 Confocal Laser Scanning micrographs of hybrid nanoparticles localized in HeLa cells (50 µg/ml hybrids incubated for 6h.) A) Fluorescence B) Transmission C) Overlay images. The scale bar represents 5µm.

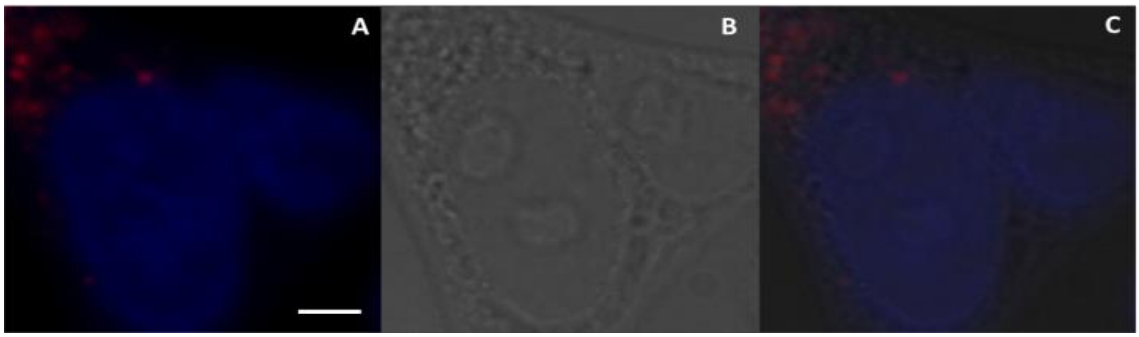

Figure 4.18 Confocal Laser Scanning micrographs of hybrid nanoparticles localized in cytoplasm of HeLa cells (50 µg/ml hybrid incubated for 6h. and nuclei was stained by DAPI A) Florescence B) Transmission C) Overlay images. The scale bar represents 5µm. Exc: 420 nm.

Hybrid nanoparticles were seeded to HeLa cells according to Ag^+ content in the hybrid. Fluorescence image can be obtained from the QD part of the hybrids. Confocal laser scanning micrographs on Figure 4.16 reveals that hybrids were successfully internalized by the HeLa cells. Autofluorescence can be observed from the non-sample treated cells but they have very low emission signals (Figure 4.16 A). Hybrid nanoparticles were monitored in the cytoplasm of the cells with high luminescence intensity (Figure 4.16 B) which completely diminishes the autofluorescence. Hybrids have cytoplasmic distribution to organelles in the cells rather than nuclei which is usual for cellular uptake (Figure 4.17).

DAPI was used to show the nucleus of a cell and to define exact position of the nanoparticles. For this reason, Fluorescence microscope set up altered. DAPI and hybrid nanoparticles have different absorbance and emission profile. Thus, appropriate excitation source (420 nm) and emission filter sets with different detector channels were used. DAPI (nucleus) and Hybrid nanoparticles (Cytoplasm) were imaged simultaneously (Figure 4.18).

4.5 Conclusions

Aqueous Ag_2S NIRQDs which has been shown as non-toxic (Chapter 2) without any shell formation or PEGylation are excellent candidates for in vitro and in vivo studies where optical imaging and drug/gene delivery is required. SPIONs which are biocompatible MRI contrast agents are also evaluated in magnetic dragging for separation or targeting and hyperthermia as well as drug delivery in the in vitro studies. Combination of the two in a nanoscale hybrid structure is very valuable for biotechnology and medicine. Therefore, Hybrid nanoparticles composed of the two were prepared by a straight forward ligand exchange method, to combine the unique properties of both in a single entity. For the hybrid formation, lauric acid coated SPIONs in chloroform and 2-MPA coated aqueous Ag2S NIRQDs were mixed. Carboxylic acid of 2-MPA replaced LA on the SPION surface and dragged SPIONs into the aqueous phase. Based on DLS and TEM analysis these hybrids are small

clusters (size less than 150nm, mostly less than 50nm) composed of multiple SPIONs and QDs. Hybrid nanoparticles emit in the NIR range (810-920 nm) having a slight red shift and decrease in PL intensity with respect to PL position and intensity of the corresponding QDs. This may be due to surface perturbation, re-absorption due to close proximity of QDs within the hybrid, absorption of photons by SPION below 800nm and absorbance of photons at the excitation wavelength by SPIONs. Yet, Hybrid nanoparticles with distinctly different emission wavelength (ca 810, 870, 910 nm), ultra-small size, colloidal stability and high luminescence intensity with ferrofluidic behavior in magnetic field were obtained. Potential as practical biomaterials was evaluated by the in vitro cytotoxicity and cellular uptake studies at doses as high as 50 μg Ag/ml in both HeLa and NIH/3T3 cell lines. Size of the hybrids was influential in cell viability and showed difference in 3T3 and HeLa cells. Small sized particles were internalized more toxic than the larger hybrid nanoparticles in NIH-3T3 cells but vice versa in HeLa. Origin of such behavior is a subject of a different study where probably internalization pathways need to be studied. Advantage of SPIONs in the hybrid composition was evaluated in magnetic targeting as well. For this purpose, cytotoxicity and cell internalization studies were performed in magnetic field generated by permanent magnets. Cell viability decreased with the particles having more Fe content due to better response to magnetic field, increasing the contact of cells with hybrid nanoparticles and therefore the cell internalization. In addition, Hybrid nanoparticles successfully used in imaging HeLa cells. A great advantage of using a NIRQD eliminating background signal in confocal laser microscopy used for optical imaging was clearly seen. Particles showed strong luminescence intensity, cytoplasmic distribution and no nuclear uptake.

Overall, in a very simple preparation method, magnetic and luminescent hybrid nanoparticles composed of SPION and Ag_2S-NIRQDs were prepared in small size regime with colloidal and optical stability, good cytocompatibility, strong luminescence and response to magnetic field which are very promising materials as theranostic nanoparticles.

Chapter 5

5 SYNTHESIS AND CHARECTERIZATION OF AQUEOUS Ag_2Te and $Ag_2Te_xS_{1-x}$ NEAR IR EMITTING QUANTUM DOTS

5.1 Introduction

In order to synthesize aqueous biocompatible silver chalcogenides emitting in the NIR window with wide emission tunability, alloy compositions were targeted in this part of the thesis work. In chapter 2, we demonstrated the development of the Ag_2S QDs emitting in the range of 750-950 nm but best particles with high PL intensity were obtained from the particles emitting 810-850 nm. Bulk Ag_2Te is in alpha phase and in monoclinic crystal structure just as Ag_2S but with a smaller band gap (Ag_2Te=0.65, Ag_2S=0.9 eV).[71] Therefore, it was thought that $Ag_2Te_xS_{1-x}$ (alloy) NIRQDs would have S and Te incorporation in to the same crystal lattice with relative ease and have emission in a broad range, at wavelengths longer than pure Ag_2S, theoretically up to 1908 nm. So, theoretically, by the incorporation of Te into Ag_2S, emission may be tuned within the whole NIR-I window (750-1000 nm) with strong luminescence intensity. In addition to this, increasing amount of Te in the $Ag_2Te_xS_{1-x}$ may allow extension of emission into NIR-II window (beyond 1100 nm) which was not our aim in this project due to the lack of instrumentation necessary for in vivo optical imaging.

This is the first report on the synthesis and characterization of aqueous Ag_2Te and $Ag_2Te_xS_{1-x}$ NIRQDs.

Cadmium chalcogenide based alloys have been reported in the literature.[100] This kind of alloys has an influence on PLQY and emission wavelengths of the particles. Chalcogen source is one of the important parameters affecting particle growth and the properties in the synthesis of chalcogenides. Therefore, in the synthesis of $Ag_2Te_xS_{1-x}$ NIRQDs, Na_2S which is a fast S-releasing source and TAA (thioacetamide) and DMSA (meso-2,3-dimercaptosuccinic acid) as slow S-releasing agents were used. As Te-source, Na_2Te and NaHTe were used. It was previously reported in our studies that DMSA can be used both as a sulfur source and a coating material in the synthesis of CdS QDs at appropriate pH-temperature combination.[34] Decomposition rate of DMSA increases with pH and the temperature. In addition, being a FDA approved heavy metal chelating agent, DMSA is important for the concept of biocompatibility.[113] The other S-source, TAA, has been widely used as fresh S-releasing agent in the CdS QD synthesis. It has also pH and temperature dependent decomposition mechanism.[140]

Strategies followed in the synthesis of Ag_2Te and $Ag_2Te_xS_{1-x}$ NIRQDs is summarized below:

- 2-MPA coated Ag_2Te NIRQDs synthesis at above 100 ^oC
  - Variables: pH, 2-MPA/Ag, Ag/Te
- $Ag_2Te_xS_{1-x}$ NIRQDs synthesis with Na_2Te/Na_2S (Simultaneous and Sequential addition of chalcogens)
  - Variables: pH and 2-MPA/Ag kept constant, Te/S
- $Ag_2Te_xS_{1-x}$ NIRQDs synthesis with Na_2Te/TAA (Simultaneous and Sequential addition of chalcogens)
  - Variables: pH and 2MPA/Ag kept constant, Te/S

- $Ag_2Te_xS_{1-x}$ NIRQDs synthesis with Na_2Te/DMSA (Simultaneous and Sequential addition of chalcogens)
  - Variables: pH and 2-MPA/Ag kept constant, Te/S

All synthesized Ag_2Te and $Ag_2Te_xS_{1-x}$ NIRQDs have emission in the range of 900-1100 nm. Two broad emission peaks are observed in the emission of all Ag_2Te and alloys. Although, variables stated above usually influence the particle size and therefore the emission wavelength, caused no significant shift in the emission peak of the alloyed particles. Origin of such behavior is the major issue attacked in this chapter. This might be due to the intrinsic optoelectronic property of Te based Silver chalcogenides, due to shape anisotropy, bimodal size distribution or due to the co-existence of Ag_2Te and Ag_2S instead of an alloy. These will be discussed in this chapter.
In vitro cell culture studies indicated that $Ag_2Te_xS_{1-x}$ NIRQDs do not poses any significant toxicity up to 200 µg/ml (Ag concentration) in HeLa cell lines indicating very good bio/cytocompatibility similar to Ag_2S NIRQDs. They were effectively used for imaging HeLa cells, demonstrating potential as optical imaging agents, first time in literature.

5.2 Materials and Methods

5.2.1 Materials

All reagents were analytical grade or highest purity. Silver nitrate ($AgNO_3$), Tellurium powder (Te), Meso-2,3- dimercaptosuccinic acid (DMSA) were purchased from Sigma-Aldrich. Sodium sulfide (Na_2S) was purchased from Alfa-Aesar. Sodium borahydride ($NaBH_4$), Sodium hydroxide (NaOH), 2-Mercaptopropionic acid (2-MPA), Thioacetamide (TAA), Ethanol and Aceticacid (CH_3COOH) were purchased from Merck. Only Milli-Q water (18.2 MOhm) was used when needed. Sodium telluride (Na_2Te) was synthesized in Advanced Inorganic Materials Research Laboratory by Mehmet Somer with a high purity. For biological applications, DMEM medium (with 4500 mg/L glucose, 4.0 mM L-glutamine, and 110 mg/L sodium pyruvate), trypsin-

EDTA, %1 penicillin-streptomycin and %10 fetal bovine serum were purchased from HyClone, USA. Thiazolyl blue tetrazolium bromide (MTT) *Biochemica* was purchased from AppliChem, Germany. Paraformaldehyde solution 4 % in PBS and UltraCruz™ 96 well plates were purchased from Santa Cruz Biotechnology, Inc., USA. Glass bottom dishes were purchased from MadTek, USA. Dimethyl sulfoxide Hybri-Max™ and phosphate buffered saline (pH 7.4) were purchased from Sigma, USA.

5.2.2 Synthesis of Ag_2X-2MPA

Typical synthesis of Ag_2X (X: S and Te) was done in a 250 ml round bottomed flask fitted to a mechanical stirrer for high stirring rate. The reaction vessel should be tightly capped by rubber septa for avoiding air leakage. Reactions were done under inert Argon (certified purity) atmosphere.

As an example, $AgNO_3$ and 2-MPA were dissolved in deoxygenated deionized water by Argon purge. pH of the mixture was brought to desired value by using Aqueous solutions of NaOH and CH_3COOH. Reaction mixture was brought to 80-90^oC. Meanwhile, Deionized (DI) water in another flask heated up to 80 ^oC and deoxygenated for the preparation Na_2Te solution. Na_2Te is very air-sensitive material stored in glove-box. The solution was freshly prepared with hot air free DI water and added to the reaction mixture by cannula to prevent air interaction instantly under vigorous mechanical stirring at 5000 rpm. Then, temperature of the reaction mixture was brought to 120 ^oC. During the reaction, samples were taken at different time points to follow the photoluminescence (PL) property. Prepared quantum dot solutions were washed with DI water using Amicon-Ultra centrifugal filters (3000 Da cut off) and stored in dark at 4 ^oC. Ag/Te/2MPA ratios of different reactions are given in table (5.1, 5.5, 5.7 and 5.10).

$$NaBH_4 + Te + H_2O \rightarrow NaHTe + H_2 + sediment$$

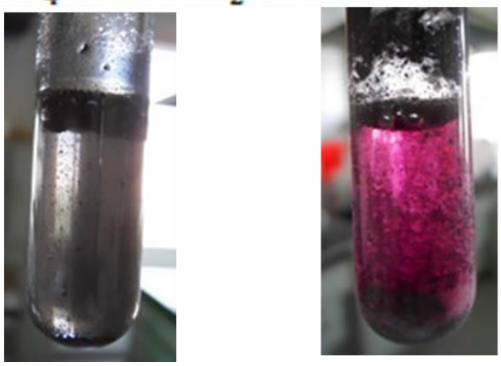

Figure 5.1 Preparation of NaHTe solution.

NaHTe was also used as a Te source in the reactions due to oxidation problem of Na_2Te. NaHTe was prepared by the reduction of Te powder with $NaBH_4$ in water. The preparation method was explained in detail in the literature.[37, 38] Reaction was completed in dark and +4 ^oC. The color of the solution turns into purple indicating the NaHTe formation (Figure 5.1).

5.2.3 In Vitro cytotoxicity studies

Cytotoxicity was evaluated by performing thiazolyl blue tetrazolium bromide (3-(4,5-dimethyl-thiazol-2yl)-2,5-diphenyltetrazolium bromide, MTT) assay on HeLa cells. Cells were cultured in 96-well culture plates ($2x10^4$ HeLa cells per plates) in DMEM medium with 10% L-glutamine,10% fetal bovine serum and 1% penicillin-streptomycin antibiotic solution and incubated at 37 ^oC in 5% CO_2 atmosphere for 24 h. QDs at the dose of 10-200 μg/ml seeded to the wells containing cells and incubated for 24h. Culture solution was removed and cells were incubated with MTT solution for 4h. Formed formazan was dissolved by DMSO:Ethanol (1:1) mixture and specific absorbance was recorded at 600 nm by ELx800 Biotek Elisa Instrument. Absorbance values of the QDs at 600nm was subtracted from the absorbance of the formazan. Experiments were repeated four times and results were reported as averages. Cell viability was evaluated with respect to reference cells. Statistical significance of the

observed differences was determined using one-way ANOVA with Tukey'smultiple comparison test of GraphPad Prism software package from GraphPad Software, Inc., USA.

5.2.4 Cell Imaging

Cell imaging was done by Nikon Eclipse Te2000-U confocal laser scanning microscope (CLSM). 50,000 HeLa cells were seeded and incubated for 18h in glass bottom dishes. Then, 2.5 µg/ml (Ag concentration) QDs was added to the culture. Cells were washed by PBS buffer after 6h incubation. 4% paraformaldehyde was used for the fixation of the cells. Images were recorded with A 60X (NA=1.49) oil immersion objective in inverted CLSM with Si detector using long pass RG665 filter and excitation at 532 nm after filtration by a broadband 10/90 dichroic beam splitter.

5.3 Characterization of Ag_2X

Absorbance spectra of the Ag_2X NIRQDs were recorded in the UV-Vis-NIR range (300-1300 nm) by a Shimadzu 3101 PC UV-Vis-NIR spectrometer. The Brus equation (chapter 1, eqn 1.1) [12, 13] was used for the particle size calculation from experimentally determined absorption onset. Photoluminescence spectra were recorded with a homemade setup in the range of 600-1500 nm. The system consists of Newport Cornerstone 130 monochromator. DPSS lasers operating at 532 nm and 605 nm were used as excitation sources. A Si and an InGaAs detectors with femtowatt sensitivity (Thorlabs PDF10A, 1.4 x 10^{-15} $W/Hz^{1/2}$, PDF10C, 7.5 x 10^{-15} $W/Hz^{1/2}$, respectively) were used for PL signal detection after filtered by a long pass filter (590 nm).

JEOL ARM 200 CFEG Cs-corrected STEM operated at 200 kV was used. EDX was done with JEOL Centurion detector with 100 mm^2 detector area for TEM analysis.A few ml of the Ag_2X-2MPA solutions were dried by freeze-drier for X-PS, X-RD and ATR-FTIR analysis. Al K-alpha radiation (1486.3 eV) was used in Thermo Scientific K-Alpha XPS for the XPS analysis of Ag_2X nanoparticles. Powdered samples on an adhesive Al tape was placed into chamber and treated with 50.0 eV pass energy. Spot

size was 400 μm. Base pressure and experimental pressure were 3×10^{-9} mbar and 1×10^{-7} mbar respectively. C1s peak at 285.0 eV was used as a reference. D8 advance Bruker instrument was used for XRD measurements. The solid sample was stacked on a glass sample holder with a double sided sticky tape and were irradiated with Cu K-α radiation (λ=1.5406 A^o). Crystal patterns were recorded between 2θ angles of 10^o and 80^o. Thermoscientific Nicolet iS10 instrument (ATR-FTIR) was used for Infrared Spectra acquisition between the wavenumber ranges of 400-4000 cm^{-1}. Hydrodynamic size and zetapotential measurements were done with the Malvern zetasizer nano ZS Instrument.

Spectro Genesis FEE Inductively Coupled Plasma Optical Emission Spectrometer (ICP OES) was used in determination of Ag^+, Te^{2-} and S^{2-} ion concentration of the NIRQD solutions. Standard solutions were used for the construction of calibration curves. QD solutions were digested by concentrated nitric acid then diluted to certain volumes by DI water before analysis. Reported values are the average of three measurements.

5.4 Results and Discussion

5.4.1 Photoluminescence measurement system

The homemade PL measurement system consists of two different lasers (532 nm and 605 nm excitation sources) and detectors; Si and an InGaAs detectors operating at different wavelength intervals. Responsivities of these detectors are given on Figure 5.2 with respect to wavelengths. Operating wavelengths of Si detector is between 500-1100 nm (Figure 5.2). But, luminescence detection above 950 nm is not reliable due to decrease in responsivity above 950 nm. On the other hand, InGaAs detector can be used in the range of 800-1600 nm. Responsivity of this detector decreases below 1000 nm.

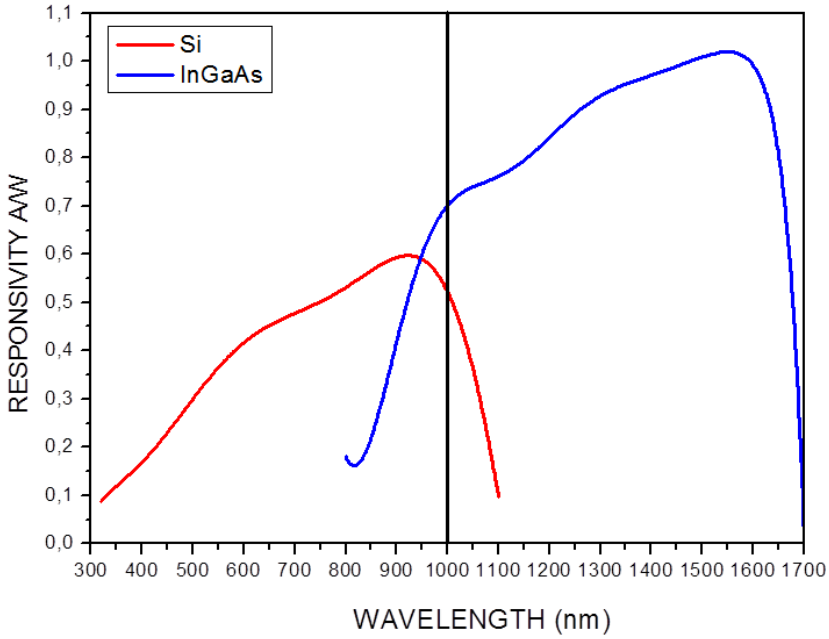

Figure 5.2 Responsivity values of Si and InGaAs detectors with respect to wavelengths

Synthesized particles have emission maximum between 900-1100 nm where the responsivity of both detectors is low. For these reason, both detectors were used in the measurements. PL spectra of a QD sample excited by 532 nm and recorded by these two detectors shown in Figure 5.3. It is difficult to overlap two spectra due to different resposivities and different intensity levels. Si detector has lower sensitivity at long wavelength side whereas; InGaAs detector has lower sensitivity at lower wavelength side. Most of the PL spectra were taken with Si detector since according to results presented in Figure 5.3 there is no much difference between the teo spectrum.

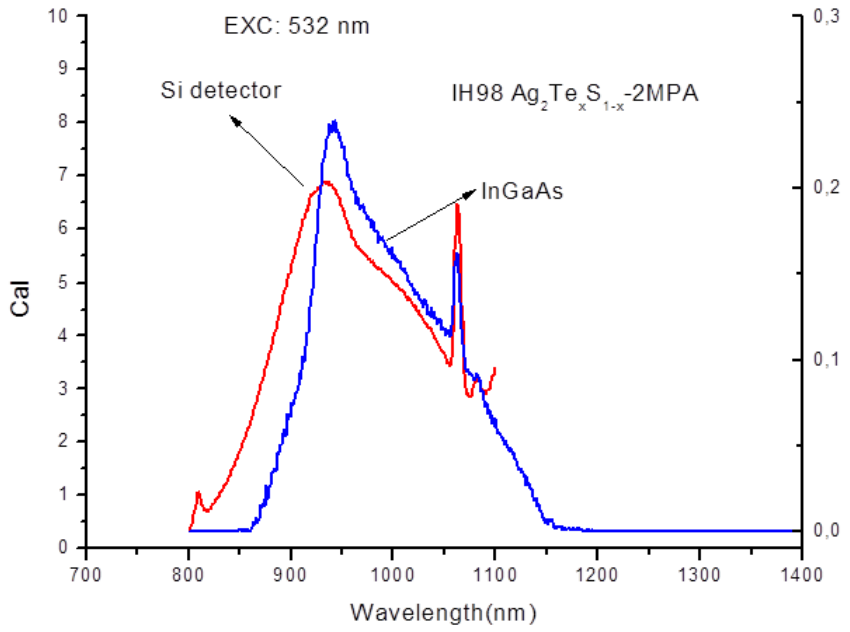

Figure 5.3 PL spectra of IH98 recorded by Si and InGaAs detectors. Excitation wavelength is 532 nm.

5.4.2 Synthesis and Characterization of 2-MPA coated Ag_2Te

Initially, Ag_2Te was synthesized with 2-MPA coating in water with the procedure optimized for Ag_2S (chapter 2) (Table 5.1, Reaction IH82).

Table 5.1 Recipe of Ag2Te-2-MPA synthesis

Reac. Code	Te (%)	pH	Te Source	Ag/Te (mol)	2MPA/Ag (mol)	Peak 1* (nm)	Peak 2* (nm)
IH82	100	7.5	Na_2Te	4	5	948	1038
IH90	100	10	Na_2Te	4	5	948	1032
IH135	100	10	NaHTe	6	5	925	1018
IH137	100	10	NaHTe	4	10	-	1042

T=120 ^{o}C, *Peak1 and Peak2 are the emission maxima of the bimodal PL spectra of the particles.

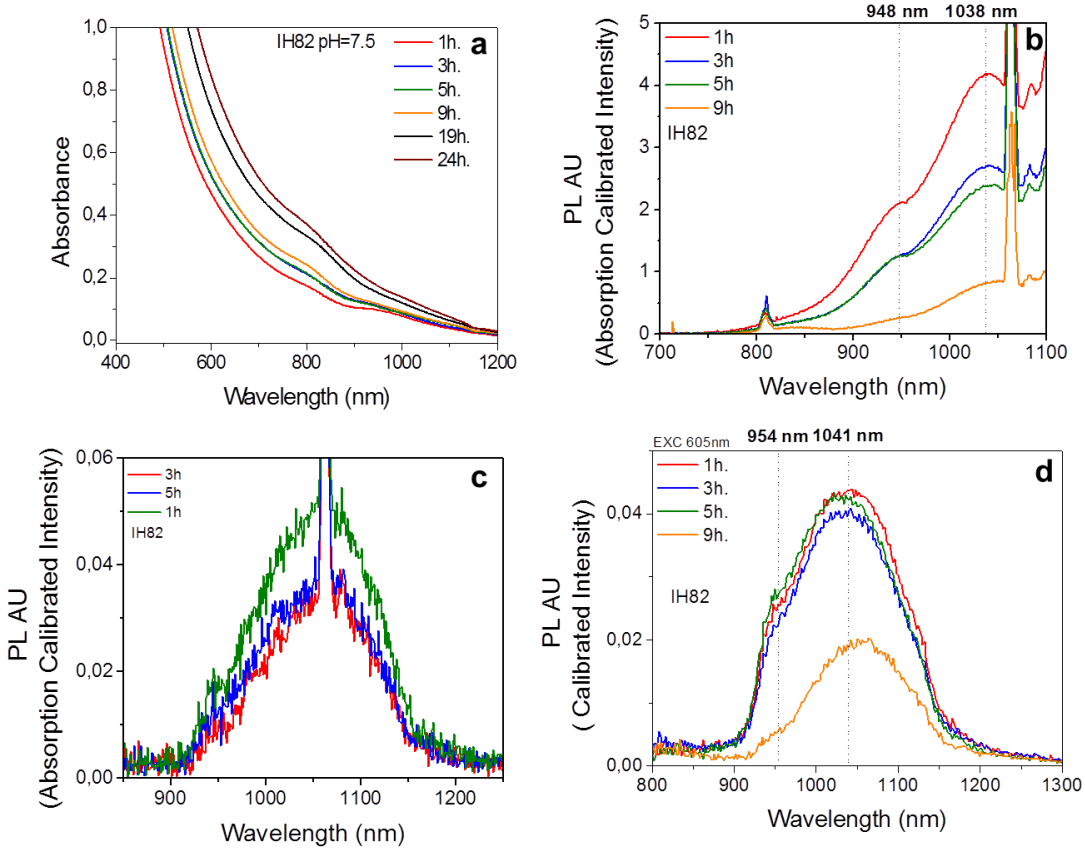

Figure 5.4 a) Absorbance and Photoluminescence spectra taken with b) Si detector (λexc:532nm) c) InGaAs detector (λexc:532nm) and d) InGaAs detector (λexc:605nm) of the reaction IH82 (samples taken at different time intervals).

Ag_2Te-2MPA NIRQDs have broad absorption in the visible region extending into NIR (Figure 5.4 a, 5.5 a, 5.6 a and 5.7 a). These particles do not have apparent excitonic peaks, which is usually a sign of monodispersity in terms of shape and size. Synthesized nanoparticles have emission in the NIR range (850-1200nm). Emission spectrum of Ag_2Te-2MPA NIRQDs has been recorded by both Si and InGaAs detectors. Photoluminescence spectra of IH82 are shown in Figure 5.4. Samples have two emission maximum around 948 (weaker) and 1038 (more intense) nm when measured with Si detector (Figure 5.4 b). Emission bands were more symmetric and emission maximum was around 1050 nm when InGaAs detector was used (Figure 5.4 c).

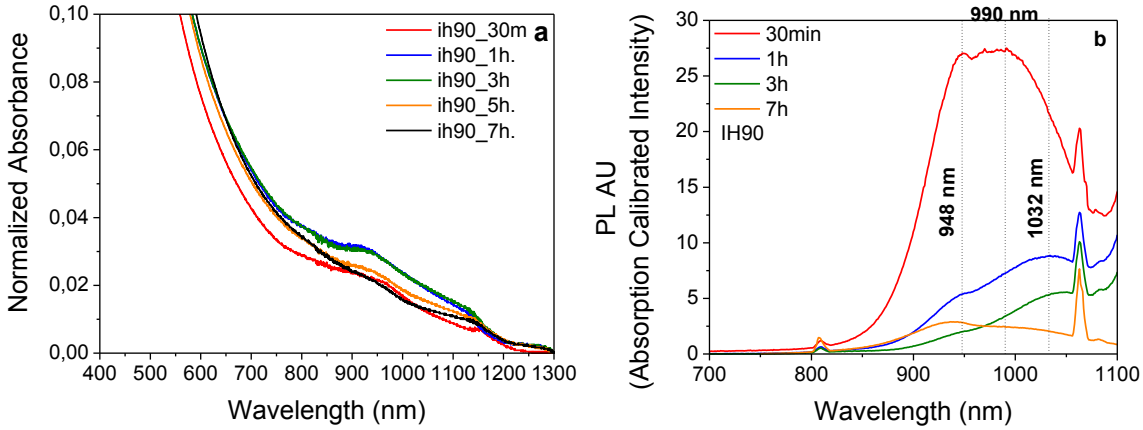

Figure 5.5 a) Absorbance and b) Photoluminescence spectra of the reaction IH90 taken with Si detector (λexc:532nm).

This might be due to the low responsivity of the InGaAs detector between 900-950 nm. Though, there is a hump in the spectra at around 950 nm beside the emission maxima (the samples were excited at 605 nm).

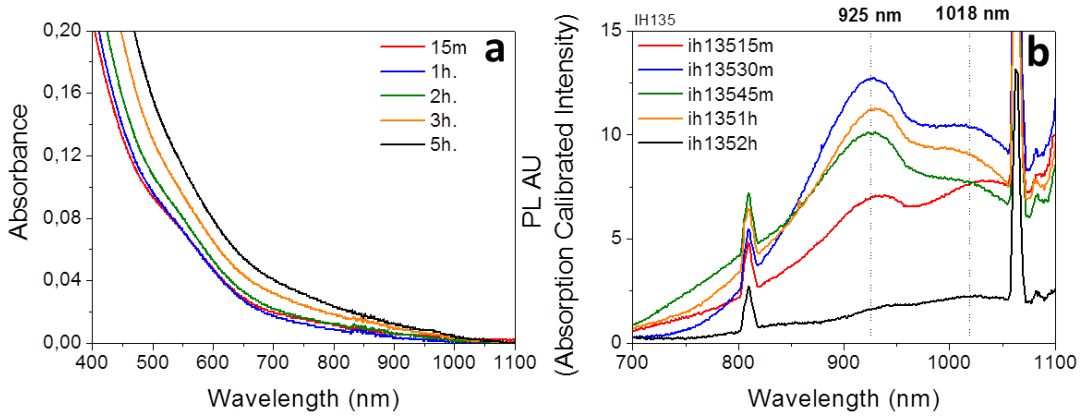

Figure 5.6 a) Absorbance and b) Photoluminescence spectra of the reaction IH135 taken with Si detector (λexc:532nm).

Looking into the absorbance and emission spectra, increasing duration of reaction did not cause a shift in the peak max but decrease in peak intensities beyond 1h. Only PL spectra taken with Si detector for the other samples will be reported in the chapter.

Samples IH82 (pH 7.5) (Figure 5.4 b) and IH90 (pH 10) (Figure 5.5 b) were compared to observe the effect of pH on emission properties. Emission profile of these two NIRQDs is similar with a blue shift of the low energy peak by 48 nm (for the sample comparison of 30m.) and a significant intensity increase at pH 10. (Figure 5.8). Looking into the changes of emission and absorption over time during the reaction, rather than a significant shift in the peak positions, a decrease in the intensity was seen from the PL spectra beyond 30min reaction time. Actually, it seems like the low energy peak is contributing less to the emission at longer reaction times, also, a slight blue shift in the low energy peak was seen after 30min.

Considering the reaction variables, Ag/Te and 2MPA/Ag are important parameters affecting the crystal size. Therefore, different Ag/Te (4,6) and 2MPA/Ag (5,10) mole ratios were studied at pH 10. Increasing coating amount and/or increasing stoichiometric off balance usually decreases the crystal size and shift the emission towards lower wavelengths in Cd-chalcogenides.[31, 32, 35]

There is a blue shift on the absorbance onsets of the samples IH135 and IH137 indicating the formation of smaller particles (Table 5.6, Figure 5.6 and 5.7). Increasing coating material amount and Ag/Te contribute this size reduction.

Ag/Te ratio was increased from 4 to 6 in IH135 but again emission with two maxima was observed in the PL spectra at 925 nm and 1025 nm. The peak at 925 nm has higher intensity with respect to 1018-1025 nm (Figure 5.6). However, double emission maxima in all spectra raise questions about particle diversity and different radiative couplings. The intensity of the 2^{nd} peak is lower for this case with respect to other two reactions.

On the other hand, IH137 coded particles which has higher amount of coating (2MPA/Ag=10) have a weak emission at 850 nm and a strong one at above 1040 nm (Figure 5.7). Crystal size growth may be seen due to decomposition of 2-MPA.

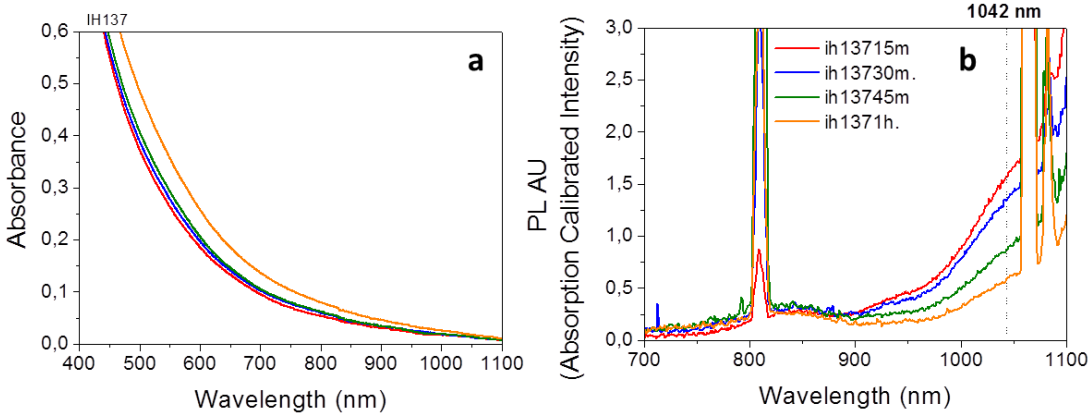

Figure 5.7 a) Absorbance and b) Photoluminescence spectra of the reaction IH137 taken with Si detector (λexc:532nm).

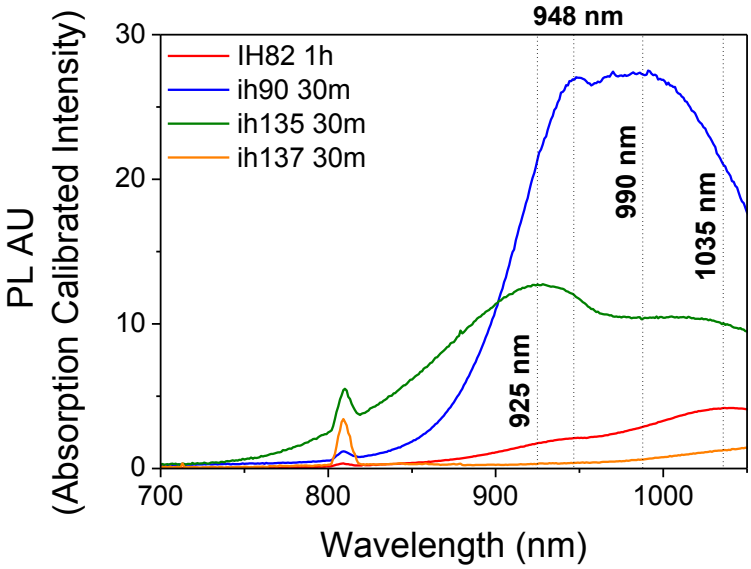

Figure 5.8 Comparison of the luminescence intensities of the samples of the four different reactions (IH82, IH90, IH135 and IH137) taken at 30m. And 1h (only for IH82).

The luminescence intensities of the Ag_2Te-2MPA NIRQDs obtained at the same time interval can be compared to evaluate emission quality. IH90 has the highest luminescence intensity, IH137 has the lowest intensity with the emission maximum

beyond 1040 nm (Figure 5.8). So, since emission max cannot be shifted much, recipe given for IH90 seems like the optimum one.

5.4.2.1 Chemical Characterization

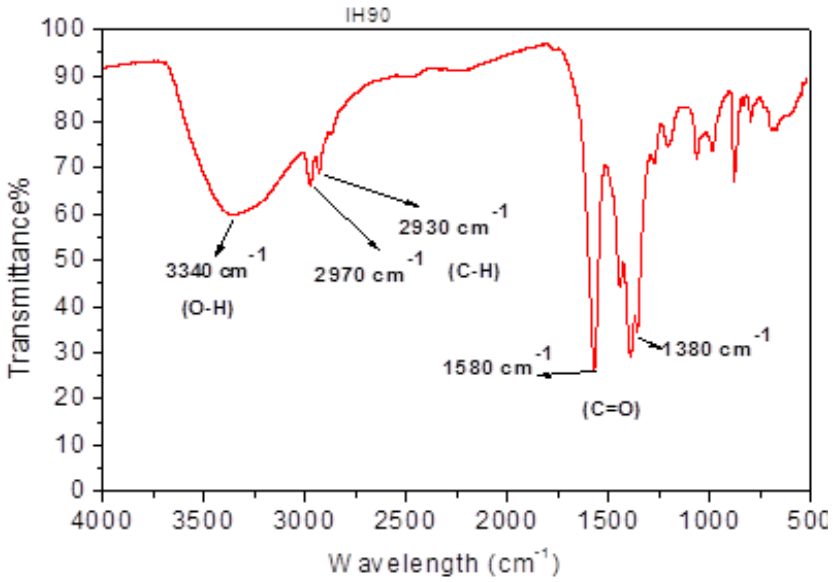

Figure 5.9 Infra-red spectrum of the IH90 codded Ag_2Te-2MPA NIRQDs.

IR spectrum of the Ag_2Te-2MPA NIRQDs demonstrates presence of the organic coating on the inorganic core. S-H band has weak and sharp stretching at around 2560 cm^{-1} and there is no S-H stretching on the spectrum indicating 2-MPA binding to the surface from the thiol group. O-H band is assigned at 3340 cm^{-1}.The other characteristic symmetric and asymmetric C-H stretchings are shown on the spectrum as 2970 cm^{-1} and 2930 cm^{-1} . Carbonyl stretching bands are also assigned accordingly (Figure 5.9).

Aqueous Ag_2S-2MPA NIRQDs were colloidally stable with a zeta-potential measurement below -30 mV due to the anionic coating (Table 5.2). Hydrodynamic sizes for both samples increase with the reaction time are also reported on Table 5.2.

Table 5.2 Hydrodynamic size and Zeta-Potential of IH90 and IH82 codded QDs

Reaction code	**D_h[a] (nm)**	**ZetaPotential(mV)**
IH90 30min.	3.92	-74.4
IH90 3h.	4.85	-78.3
IH82 1h.	3.99	-63.9
IH82 3h.	4.30	-67.5

[a] Hydrodynamic size measured by DLS.

5.4.2.2 TEM Analysis

IH90 coded particles were analyzed by TEM (Figure 5.10 a). Both spherical and semi-spherical particles co-exist together with the mean size of 2.8±1.2 nm (Figure 5.10 b). These particle sizes differ from the sizes measured by DLS due to presence and interaction of the small organic coating with water. Presence of the Ag and Te atoms were confirmed by the EDX analysis (Figure 5.10 c).

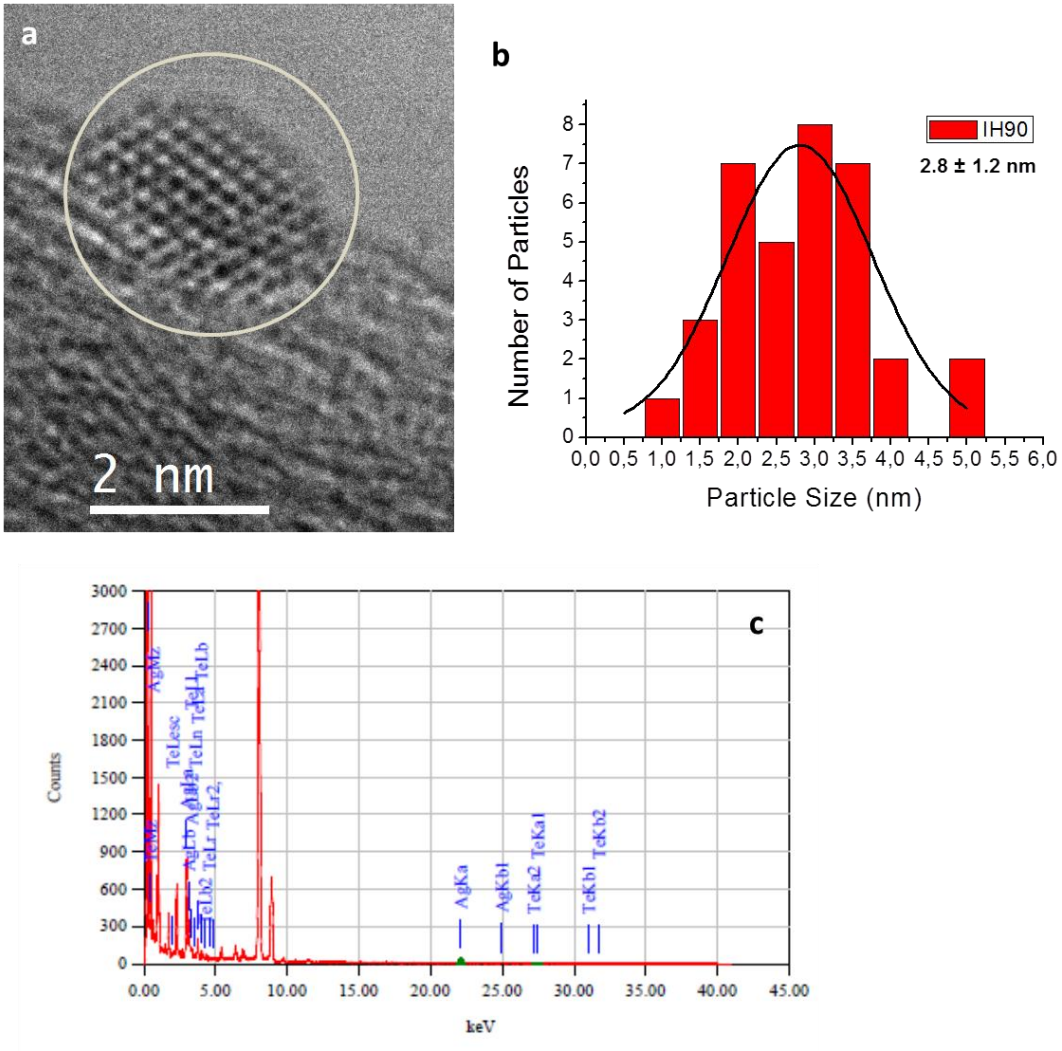

Figure 5.10 a) TEM image, b) size distribution and c) EDX analyses of the IH90 codded Ag_2S-2MPA NIRQDs.

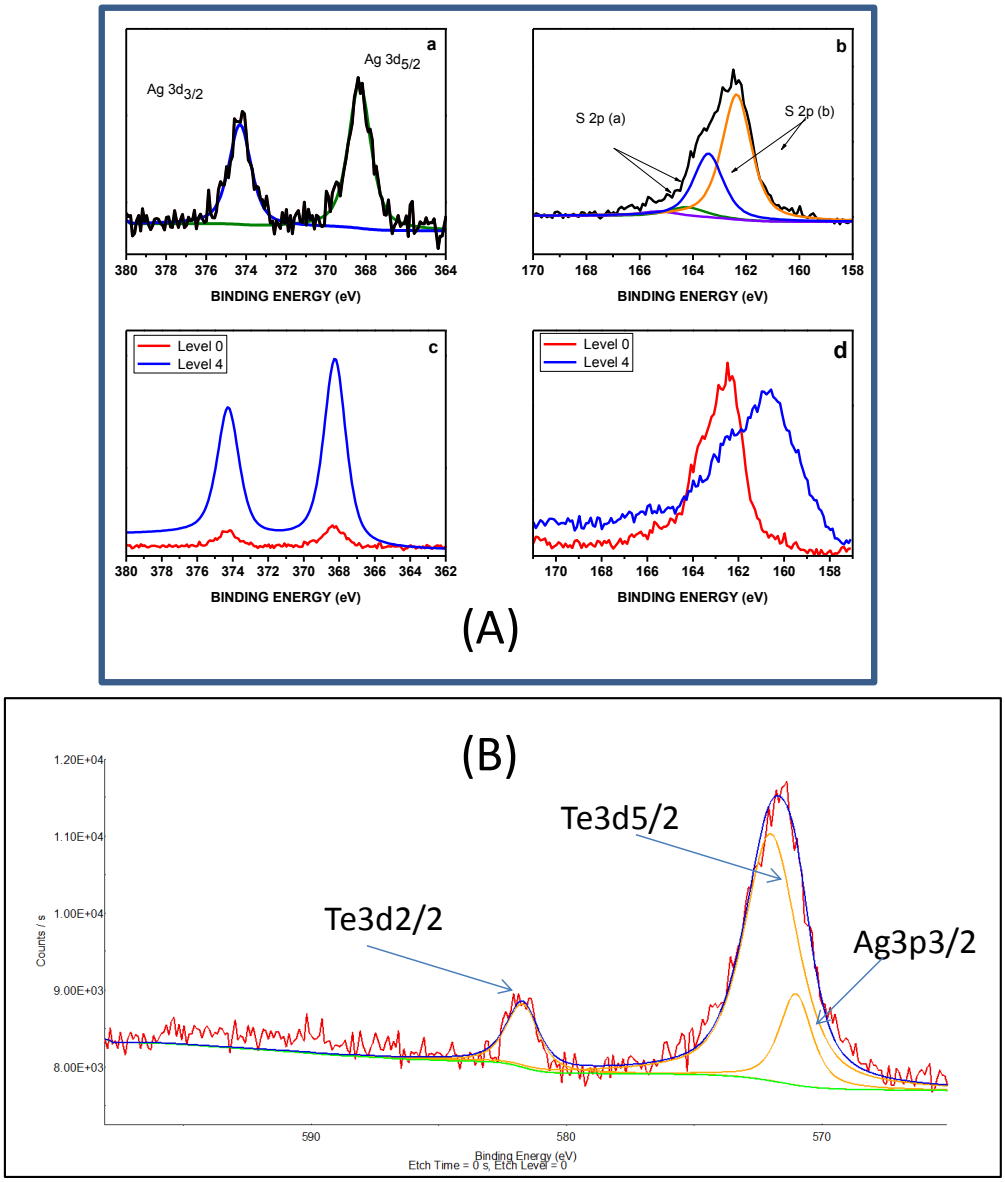

Figure 5.11 A) XPS spectra of Ag_2Te NIRQDs a) Ag 3d b) S 2p before plasma etching c) Ag 3d d) S 2p peaks before and after plasma etching. B) BE spectrum of Te atom.

5.4.2.3 XPS Analysis

IH90 coded Ag_2Te NIRQDs was analyzed by XPS. Ag $3d_{5/2}$ and $3d_{3/2}$ were fitted to their BEs 368,8 eV and 374,3 eV respectively at the core level before plasma etching (Figure 5.11 A-a). Although, one type of S (from 2-MPA) was expected, two type of S

were fitted to S 2p spectrum (Figure 5.11 A-b). S $2p_{3/2}$ coupling has BEs at 164.24 eV and 162.36 eV at level 0 and these BEs shifted to 160.19 eV and 162.36 eV after etching (level 4)(Table 5.3). It is known that S-Ag-S bond has peak around BEs 160-161 eV, thus, the peak around the 162-163 eV belongs to the S-bond between 2-MPA and QD. The S peak at around 163 eV decreased and the peak around 161 eV increased with the plasma etching (Figure 5.11 A-d). The peak of the thiol of the coating material must decrease as the inorganic core was reached by the plasma etching supports the assignment of S with higher BE to 2-MPA. However, the presence of S at 161 eV indicates that pure Ag_2Te was not synthesized and this raises a question: is it possible to have Ag_2S formation due to the decomposition of 2-MPA at the reaction conditions (120 ^oC).

Table 5.3 BEs of Ag, Te and S atoms calculated by XPS analysis.

	BE (eV)	**Amount (%)**
$Ag3d_{5/2}$	368.31	5.05
$S2p_{3/2}$	164.24	8.09
$S2p_{3/2}$	162.36	85.23
$Te3d_{3/2}$	582.87	1.64
After Plasma Etching		
$Ag3d_{5/2}$	368.24	27.69
$S2p_{3/2}$	160.19	46.44
$S2p_{3/2}$	162.36	20.71
$Te3d_{3/2}$	582.90	5.16

In order to evaluate the concentration of S and Te, area analysis was done however, Ag/(S+Te) was found as 0.53 after plasma etching (hoping to decrease the coating content significantly), which is quite different than the theoretical value of 2. An important problem has been revealed: 3d spin-orbit coupling pairs of Te, have BEs

around 583-573 eV with a 10 eV energy difference. In the XPS analysis of Ag_2Te, 573.9 eV peak of Te $3d_{5/2}$ and 573.6 eV peak of Ag $3p_{3/2}$ overlap. Therefore, the ratio of the Te peaks ($3d_{5/2}$ and $3d_{3/2}$) is not reliable (Figure 5.11 B). In the area calculation, Te peak around 583 eV was used.

5.4.2.4 ICP OES Analysis

Elemental analysis of the sample IH90 was done by ICP OES measurement. Ag, Te and S amount in moles are given in Table 5.4. Ag/Te was calculated as ca 6 which should be theoretically 2. However, excess use of thiol containing coating material (2MPA/Ag=5) in the reaction and its decomposition at elevated temperatures, are possibly responsible for such a high concentration of S in the samples. At least Ag/Te should have been found 4 but it was calculated as 5.8 by ICP, suggesting that all Te was not incorporated into the crystal. ICP could not differentiate different forms of S (from ligand versus crystal) but XPS can, and it also indicated higher content of Ag-S compared to Ag-Te in all structures including the Ag_2Te-2MPA.

Table 5.4 Ag, Te and S amounts detected in Ag_2Te-2MPA NIRQDs by ICP.

Rxn Code	Ag (mmol)	Te (mmol)	S (mmol)	Ag/Te Mol ratio	Ag/S Mol ratio
IH90	0,0177	0,00304	0,389	5,8	0,05

5.4.3 Synthesis and Characterization of $Ag_2Te_xS_{1-x}$

5.4.3.1 Investigation of Te/S ratio on particle properties

The band gap energies of the Ag_2Te and Ag_2S are 0.7 eV and 0.9 eV. Standard protocol detailed in chapter 2 was applied to Ag_2Te and $Ag_2Te_xS_{1-x}$ synthesis in this chapter. Synthesized Ag_2Te-2MPA NIRQDs showed luminescence in 900-1100 nm range. It

was hoped to be able to tune emission in the 850-1100 nm range, through formation of $Ag_2Te_xS_{1-x}$ NIRQDs.

A set of reactions with different Te/S ratios, where coating/Ag and Ag/total chalcogenide ratios, pH and temperature were kept constant, was done (Table 5.5). In a standard procedure, Na_2S and Na_2Te were added to the Ag/2MPA mixture.

Table 5.5 Formulation of $Ag_2Te_xS_{1-x}$ NIRQDs Syntheses to study the influence of S/Te ratio

Reac. Code	pH	S[a] (%)	Te[b] (%)	Method	Ag/ Chalcogenide (mol)	2MPA/ Ag (mol)	Peak 1* (nm)	Peak 2* (nm)
IH84	7.5	40	60	Mix	4	5	948	1042
IH96	10	80	20	Mix	4	5	-	1050**
IH97	10	60	40	Mix	4	5	936	1012
IH98	10	40	60	Mix	4	5	930	1044

Reaction temperature is 120 °C. [a] Na_2S and [b]Na_2Te are used as S and Te sources respectively. *Peak 1 and Peak 2 were the emission maxima of the bimodal PL spectra of the reactions. **emission was not detectable with Si detector, InGaAs detector was used in acquisition.

In order to follow crystal growth and corresponding spectral shift, samples were withdrawn from the reaction mixture and characterized as well. Table 5.6 shows the calculated crystal sizes, hydrodynamic sizes and zeta potentials of the $Ag_2Te_xS_{1-x}$ NIRQDs. All QDs possess negative surface charge, as expected. Hydrodynamic sizes measured by DLS indicate small isolated particles with average sizes between 3.8 to 4.4 nm. Crystal sizes calculated by Brus Equation (equation solved by using the parameters of Ag_2S) are between 3.5-4.8 nm. Of course with the values suitable for Ag_2S, a correct size for Ag_2Te or alloys cannot be calculated but, since composition analysis indicated greater contribution of Ag_2S, parameters of Ag_2S was used in the Brus equation. These crystal sizes should be only considered for comparison of different batches. All of $Ag_2Te_xS_{1-x}$ NIRQDs demonstrate usual bimodal emission profile observed for Ag_2Te. Initial pH study with 40% S in feed indicated that particles synthesized at pH 10 are smaller (3.6 vs 3.9 nm in 1 h reaction) and emit at shorter wavelength (930 nm) with respect to the particles synthesized at pH 7.5 (Figure 5.12 b and 5.15 b). Comparison of

the binary emission peaks can be seen in Table 5.5. This result was similar to Ag_2Te synthesized at different pH values. pH has an influence on the complex formation between Ag^+ and the coating material and the composition of this complex usually influences the crystal size. Usually, bigger clusters create high concentration spots producing bigger particles. Besides, as in case of Ag_2Te-2MPA, QD`s luminescence is stronger when synthesized at pH10 and the more intense peak is the high energy one, which may be in agreement with smaller particle size.

As can be seen in Table 5.6 from the comparison of reactions run at pH 10, as the S content of the chalcogenide precursor increased from 40 to 80%, in the first hour of the reaction crystal size increased from 3.6 to 4.3nm (IH 98 and IH96). Although particles had emission with two maxima again, this increase in the crystal size was accompanied with a red shift in peak maxima from 930 to 948 and from 1012 to 1050.

Table 5.6 Size calculation and colloidal stability of $Ag_2Te_xS_{1-x}$ NIRQDs

Reaction code:	Size [a] (nm)	Band Gap (eV)	Hydrodynamic size [b] (nm)	Zeta Potential (mV)
IH84 1h	3.8	1.1	3.90	-62.3
IH84 3h	3.8	1.1	4.37	-20.0
IH96 1h	3.5	1.2	4.31	-69.3
IH96 3h	3.6	1.2	-	-63.4
IH97 1h	3.7	1.1	3.92	-69.8
IH97 3h	4.4	1.1	3.88	-69.1
IH98 1h	3.6	1.2	3.60	-68.7
IH98 3h	3.7	1.1	4.13	-67.2

[a]Size is calculated by Brus equation. [b]Hydrodynamic size measured by DLS

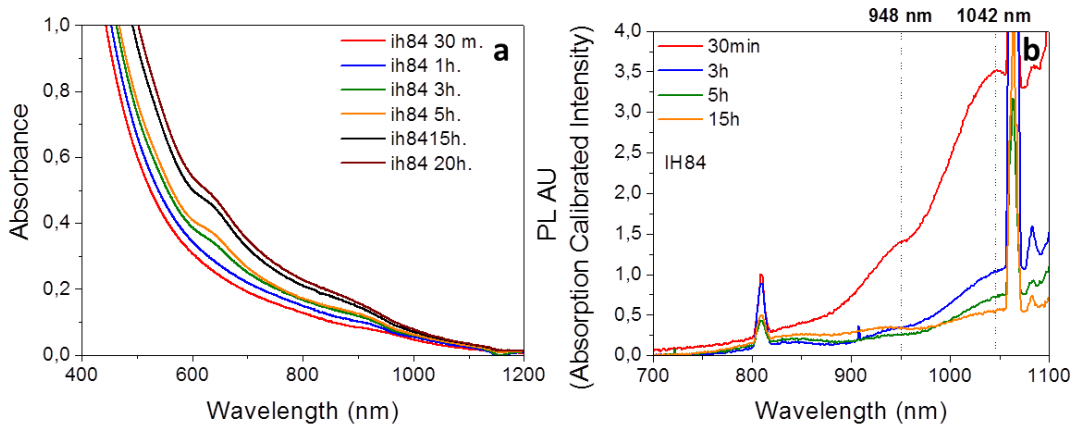

Figure 5.12 a) Absorbance and b) Photoluminescence spectra of the reaction IH84 taken with Si detector (λexc:532nm).

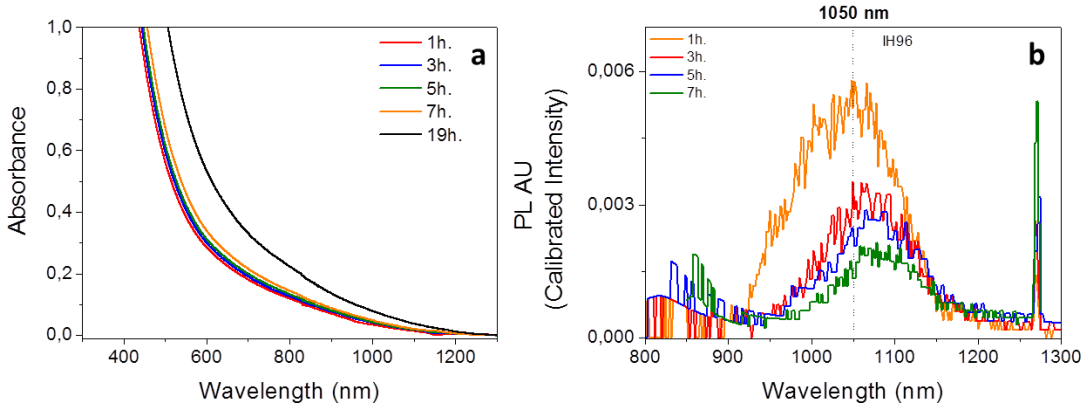

Figure 5.13 a) Absorbance and b) Photoluminescence spectra of the reaction IH96 taken with InGaAs detector (λexc:532nm).

When 60% S (IH97) is used in the feed of chalcogens, crystal size calculated was 3.92nm in 1 h and 3.88 nm in 3 h (Table 5.6) which falls between the crystal sizes of lower and higher S containing reactions IH98 and IH96 (Table 5.5 and 5.6). PL spectra of IH96 and IH97 were recorded both with Si and InGaAs detectors (Figure 5.13 b and 5.14 b-c). IH96 with 20% Te has a broad emission centered at 1050-1080 nm. IH97 with 40% Te in feed showed bimodal emission peak like Ag_2Te NIRQDs with maxima around 936 and 1012 nm. Blue shift of emission was expected since the crystal sizes were smaller with higher content of Te. However, this whole trend is quite the opposite

of common sense. Since the band gap energy of Ag_2Te is smaller, QDs with smaller band gap therefore with emission shifted towards longer wavelengths were expected with increasing Te content in feed. Yet, as Te content in feed increases, particle size decreases and emission peaks shifted to lower wavelengths. This indicates a complex structure or a difference in growth kinetics that changes the composition from the desired/expected composition. Increasing particle size with increasing S content may be due to faster kinetics of silver sulfide formation which would also make QD more S rich. Bulk Ag_2S may form with the excess S source in the lack of Te (IH96). Thus, low quality of the particles were obtained with the red shift (IH96)

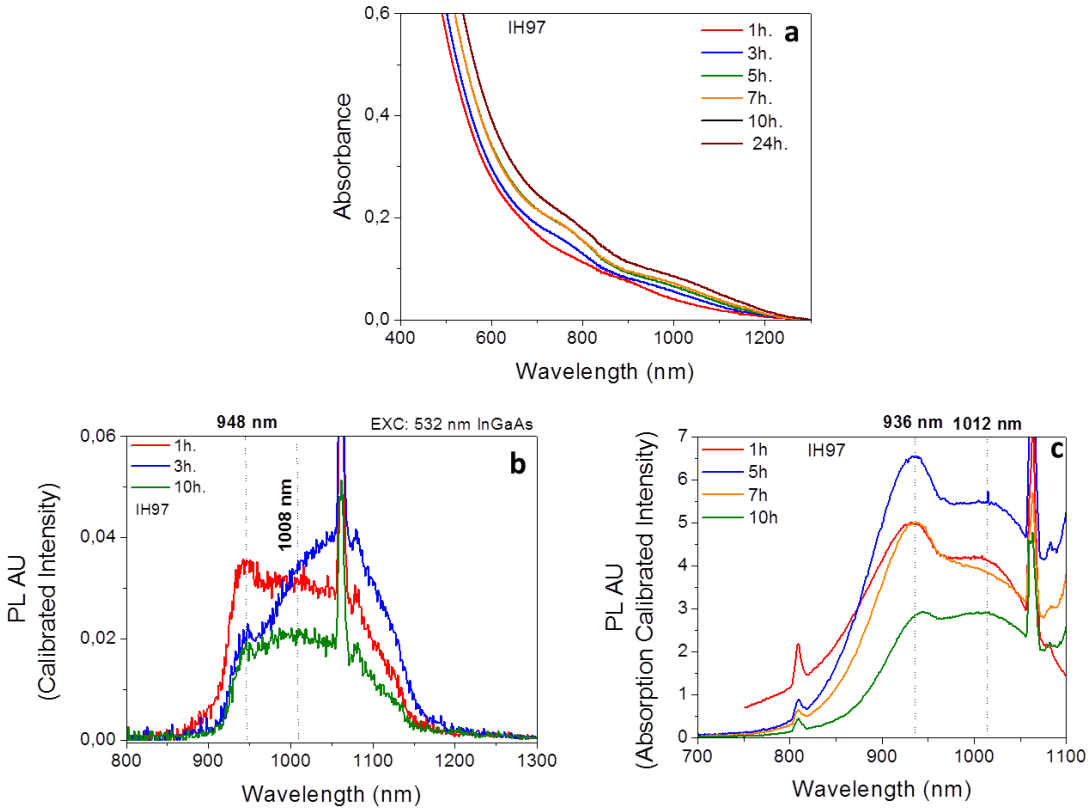

Figure 5.14 a) Absorbance and b-c Photoluminescence spectra of the reaction IH97 taken with InGaAs detector (λexc:532nm) and Si detector (λexc:532nm) respectively.

Emission obtained from IH98 with the largest Te content in feed (60%) had blue shifted emission with two peaks centered at 930 nm and 1044 nm (Figure 5.15).

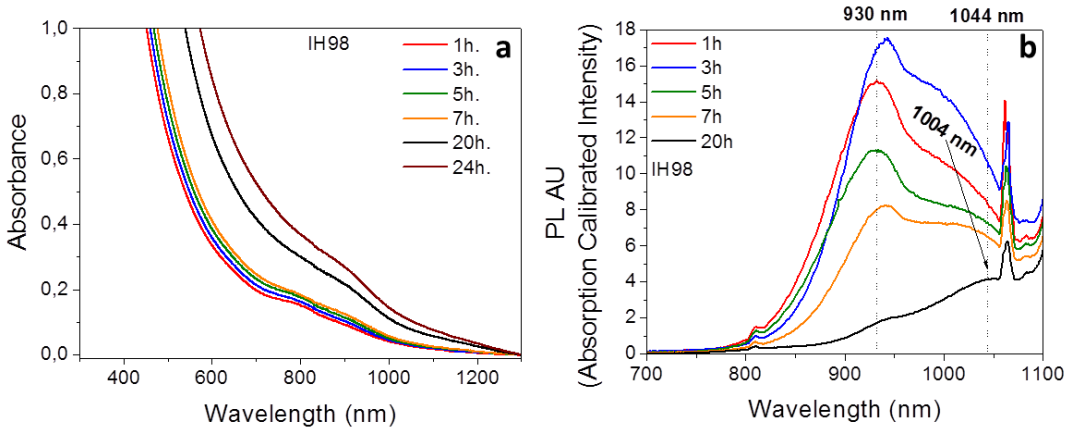

Figure 5.15 a) Absorbance and b) Photoluminescence spectra of the reaction IH98 taken with Si detector (λexc:532nm).

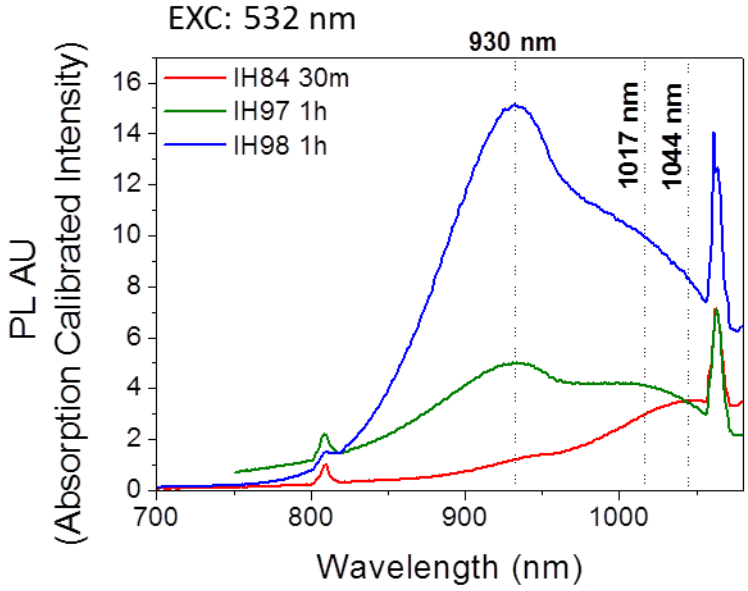

Figure 5.16 Photoluminescence intensity comparison of the samples of the different reaction.

Overall, major change in the emission peak positions occur between 80 % and 60 % S in feed which shifted the emission maxima from 1050-1080 nm to 936 and 1012 nm. Further decrease in S content to 40% shifted these peaks slightly to 930 and 1044nm. These follow the decreasing crystal size trend. Emission wavelength was slightly tuned

(peak 1 925-948 nm and peak 2 1010-1050 nm) with composition. When all alloyed QDs were compared (Figure 5.16), best luminescing particle with not much difference in emission maxima is IH98. IH96 had very low signal intensity indetectable by the Si detector therefore not included in this stacked plot.

Under the light of these results the following study is suggested:

- Determination of Te and S content of the QD
- Use of Slow S-releasing agents
- Simultaneous and sequential addition of Te and S sources

5.4.3.2 Evaluation of different Sulfur sources and Method Comparison

5.4.3.2.1 Simultaneous Addition of the Te and S sources

Table 5.7 Effect of S sources mixed with Te for the synthesis of $Ag_2Te_xS_{1-x}$ NIRQDs in simultaneous addition of chalcogens

Reac. Code	S (%)	Te (%)	S Source	Te Source	Method	Ag/ Chalc. (mol)	2MPA/ Ag (mol)	Peak 1* (nm)	Peak 2* (nm)
IH98	40	60	Na_2S	Na_2Te	Mix	4	5	930	1044
IH120	40	60	DMSA	Na_2Te	Mix	4	5	947	1014**
IH122	40	60	TAA	Na_2Te	Mix	4	5	947	1029

Reaction temperature is 120 ^oC. pH is fixed to 10 *Peak 1 and Peak 2 were the emission maxima of the bimodal PL spectra of the reactions. **blue shift on the emission maxima from 1038 nm to 10114 nm

In the section 5.4.3.1 $Ag_2Te_xS_{1-x}$ NIRQDs were synthesized with simultaneous addition of Na_2S and Na_2Te to the Ag/2MPA mixture. In order to evaluate the function of initial S content on kinetics, composition and properties, slow S^{2-} releasing agents, TAA and DMSA, were used as a S-source and results were compared with Na_2S. (Table 5.7).

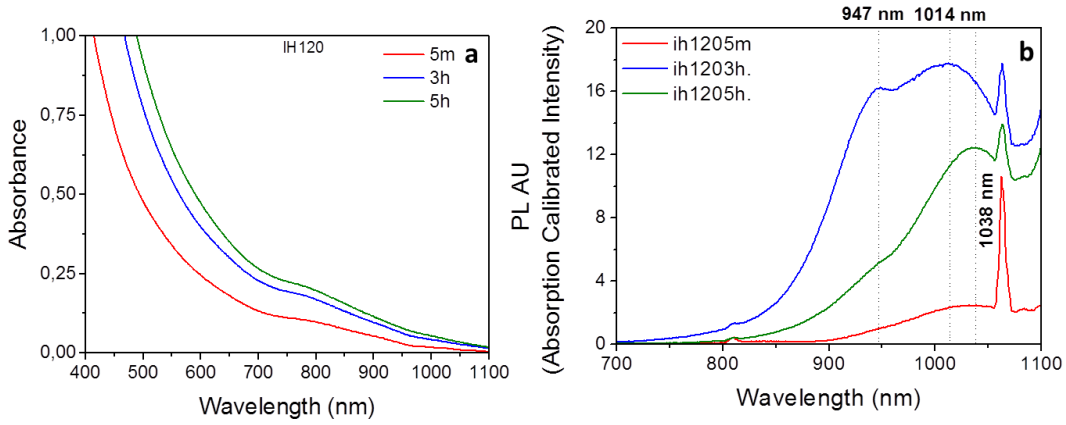

Figure 5.17 a) Absorbance and b) Photoluminescence spectra of the reaction IH120 taken with Si detector (λexc: 532nm).

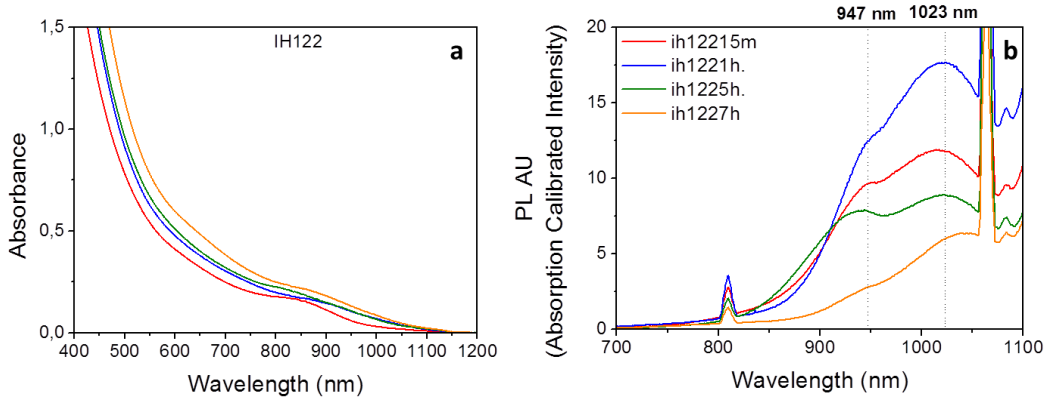

Figure 5.18 a) Absorbance and b) Photoluminescence spectra of the reaction IH122 taken by Si detector (λexc:532nm).

S/Te ratio and pH was kept constant at 40/60 and 10, respectively. Absorbance onsets in all three reactions shifted to the longer wavelength with reaction time with major shift after 15 min (Figure 5.15 a, 5.17a and 5.18a). Emission profile showed two maxima (947 and 1038 nm) again and rather than a significant shift in the wavelength a decrease in the intensity was observed at prolonged reaction times, most significant in the high energy peak (Figure 5.15 b, 5.17 b and 5.18 b). This may be due to dissolution of smaller crystals and adding on the big ones but no major shift on the low energy maxima was observed.

When all three particles are compared to evaluate the effect of S source on particle properties, it was clear that all S-sources produced particles with emission with two maxima (928 and 1035nm) but, with fast S-source (Na_2S) the most intense peak is the high energy peak, with slow S-releasing ones, the low energy peak (Figure 5.19). With slow S-releasing agents, initial number of nuclei may be fewer and grow to bigger size crystals. However, number of nucleated crystals increases with fast S release to the medium by Na_2S so it is probable to have smaller particles. Shift in emission wavelength from 928 nm to 1035 nm at the same S/Te ratio due to slow sulfur release was possible for the reactions IH98 and IH120. TAA is like DMSA but it can decompose faster to release sulfur. IH122 was prepared by TAA. Emission properties of the reaction IH122 were between the reactions IH98 and IH120. There is no dramatic difference between the absorbance spectra of three reactions as their fifth hour samples were evaluated (Figure 5.19 a). One important feature is the increasing luminescence intensity with time with DMSA possibly due to slow crystal formation and surface passivation by DMSA.

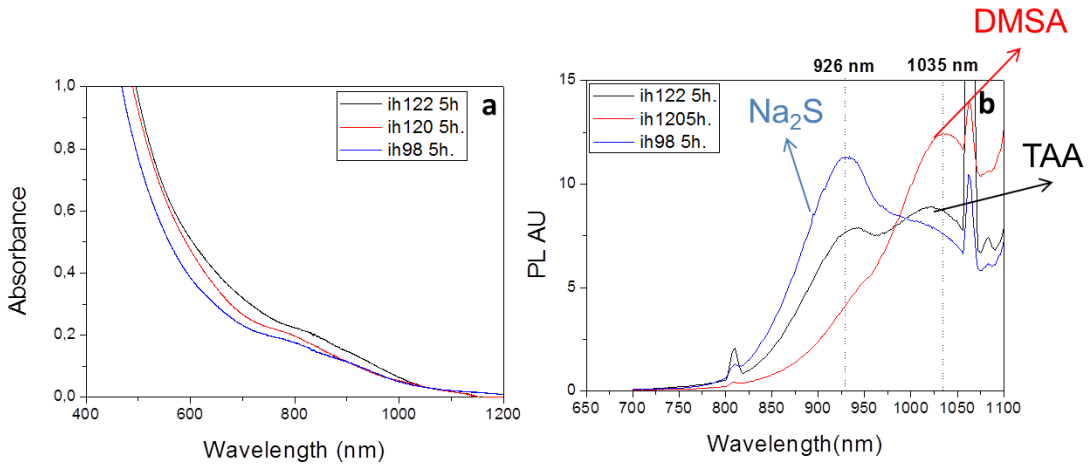

Figure 5.19 a) Absorbance and b) Photoluminescence spectra of the 5th hour of the reactions IH98, IH120 and IH122 taken by Si detector (λexc:532nm).

5.4.3.2.1.1 Chemical Characterization of particles

FTIR spectra of $Ag_2Te_xS_{1-x}$ NIRQDs prepared with DMSA and TAA are given in Figure 5.20. There is no S-H peak on the IR spectrum of $Ag_2Te_xS_{1-x}$ NIRQDs (IH122) prepared with TAA indicating thiol binding to crystal (Figure 5.20 b). However, S-H stretching was seen at around 2500 cm^{-1} in the reaction IH120 synthesized by DMSA showing the presence of thiol (Figure 5.20 a). DMSA has two thiols. One of the thiols can be present after the decomposition and may be some of the thiols are still free. Symmetric and asymmetric stretchings of C-H and C=O are seen in Figure 5.20 a and 5.20 b showing the presence of 2-MPA.

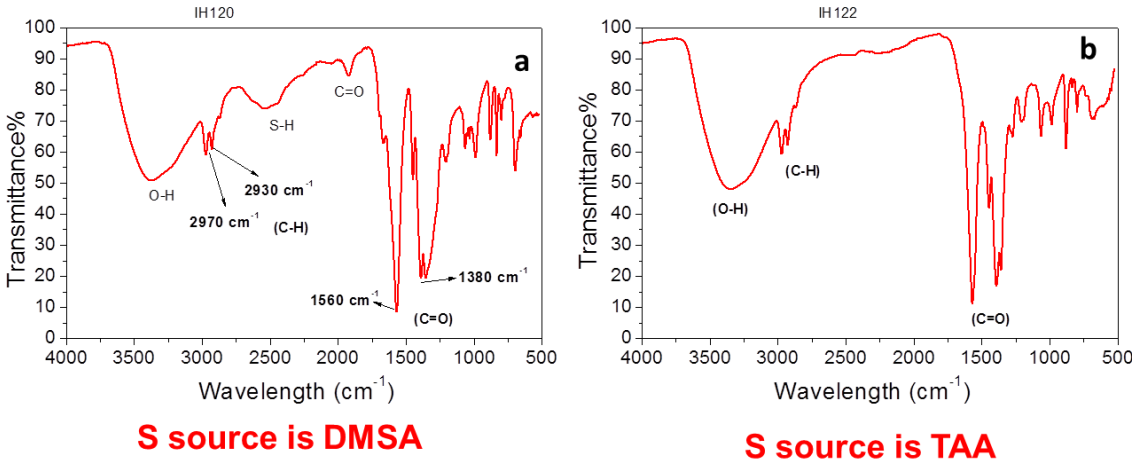

Figure 5.20 IR spectra of $Ag_2Te_xS_{1-x}$ NIRQDs obtained from reactions a) IH120 b) IH122.

5.4.3.2.1.2 XPS Analysis

XPS analyses were performed on IH98 and 120 which were synthesized with Na_2S and DMSA as S source, respectively, to calculate S/Te ratio in $Ag_2Te_xS_{1-x}$ and to possibly understand if these particles are really alloyan or somewhat a core/shell structure (Table 5.8). Samples were etched by Ar^+ plasma to detect the composition change through surface to core. Both samples showed typical Ag 3d signals at binding energy

of 367-368eV in agreement with silver chalcogenides. In both of these particles, presence of two different S is detected with 2p signal at 160.91 and 162.49 eV for IH98 and 161.32 and 163.46 eV for IH120. S-signal at lower BE correspond usually to S in the Ag_2S and at higher BE corresponds to S of the organic ligand (Chapter 2). When area of Ag, S and Te were calculated, Ag/total chalcogenide ratio came out as 1.07 and 1.48 for IH98 and IH120, respectively (Table 5.8B, C, D). Major problem here can be again the overlap of Te signal with Ag as discussed in section 5.4.2.3. Plasma etching of the samples indicated an increase in the S content coming from Ag-S but a decrease in the S content of ligand which is reasonable. Yet, S (of Ag-S)/Te ratio increases with plasma etching. Even after etching, signal for S coming from the ligand is observed at around 162-164 eV so, extent of etching is questionable. But in general, it was expected to see a compositional drift with etching as one goes from shell towards core of the particle with a possibility of Ag_2Te core and Ag_2S shell based on solubility difference ($Ksp_{Ag2S}=10X10^{-50}$, $Ksp_{Ag2Te}=10^{-54}$-10^{-64} order)[141-143] which is also based on soft and hard acid-bases chemistry.[144, 145] However, results indicate that these alloys have mostly Ag-S structure rather than Ag-Te although Te content in the feed was larger (S/Te=40/60) and possibly core is S rich. There are two things to consider here:

1. Error originating from overlapping Ag and Te signals
2. Faster kinetic of Ag-S formation compared to Ag-Te making particles S rich

For the Te and S content ICP analysis was done as a second method. For the elucidation of the second issue, sequential addition of Te and S sources were studied as will be discussed in the following section.

Table 5.8A) Reaction parameters of IH98 and IH120, BEs and ratios of Ag, Te and S atoms B) for IH98 C) for IH120 and D) compositions of IH98 and IH120 determined by XPS analyses.

A

Reac. Code	pH	S (%)	Te (%)	S Source	Te Source	Method	Ag/ Chalcogenide	2MPA/Ag
IH98	10	40	60	Na_2S	Na_2Te	Mix	4	5
IH120	10	40	60	DMSA	Na_2Te	Mix	4	5

B

IH98	Peak BE	At. %
$Ag3d_{5/2}$	367.13	34.24
$S2p_{3/2}$	160.91	29.83
$S2p_{3/2}$	162.49	33.90
$Te3d_{3/2}$	581.76	2.04
Plasma Etching		
$Ag3d_{5/2}$	367.22	41.24
$S2p_{3/2}$	160.50	39.11
$S2p_{3/2}$	162.64	17.71
$Te3d_{3/2}$	581.84	1.94

C

IH120	Peak BE	At. %
$Ag3d_{5/2}$	368.34	12.18
$S2p_{3/2}$	161.32	5.42
$S2p_{3/2}$	163.46	79.73
$Te3d_{3/2}$	573.03	2.68
Plasma Etching		
$Ag3d_{5/2}$	368.26	31.25
$S2p_{3/2}$	161.53	50.26
$S2p_{3/2}$	164.33	12.58
$Te3d_{3/2}$	572.82	5.91

D

	IH98		IH120	
	orginal	Plasma Etching	orginal	Plasma Etching
Ag/Te+$S_{(core)}$	1.07	0.82	1.48	0.55
S_{core}/Te	14.62	20.16	2.02	8.50

5.4.3.2.1.3 ICP OES results

Elemental analysis of the three reactions was done by ICP. Ag, Te and S amounts were determined in the samples (Table 5.9). In each reaction 40% S and 60% Te was used at the Ag/chalcogenide ratio of 4. Theoretically, mole ratio between the components should be $Ag_2Te_{0.6}S_{0.4.}$ The Ag/Te were found in the samples is above 10, far from the theoretical value (Table 5.9). Excess Ag and 2-MPA were used in the reactions (ratios

are tabulated on Table 5.7) with respect to chalcogenide sources. If all Ag ions consumed in the reaction with the S decomposed of coating material. Ag/Te would be 6.7 at most. Ag/S and S/Ag ratios on the Table 5.9 are not reliable since S originates both from the coating and the chalcogenide. It does not give the ratio in inorganic core. Deficiency in Te amount in the system should be investigated. Te is a softer base than S and Ag^+ is soft acid thus, affinity of Te to Ag^+ should have been more.

Table 5.9 Ag, Te and S amount in $Ag_2Te_xS_{1-x}$ NIRQDs analyzed by ICP OES

Reac. Code	Ag (mmol)	Te (mmol)	S (mmol)	Ag/Te Mole ratio	Ag/S Mole ratio	S/Ag Mole ratio
IH98	0,0123	0,00108	0,0599	11,3	0,20	4,89
IH120	0,0143	0,000901	0,0964	15,9	0,15	6,73
IH122	0,0112	0,000846	0,0793	13,3	0,14	7,06

5.4.3.2.2 Sequential addition of Te and S sources

A set of reaction was done to increase Te amount in the alloy compositions. S source was added to the reaction mixture after 1h reaction of Ag ions with telluride ions (Table 5.10). Freshly prepared NaHTe was used as a Te source instead of Na_2Te in this set of reactions due to the oxidation problem of Na_2Te.

Table 5.10 Synthesis parameters of $Ag_2Te_xS_{1-x}$ NIRQDs by Sequential addition of chalcogens

Reac. Code	S (%)	Te[a] (%)	S[b] Source	Method	Ag/ Chalcogenide (mol)	2MPA/ Ag (mol)	Peak1B[c] (nm)	Peak1A[d] (nm)	Peak 2[e] (nm)
IH132	40	60	TAA	Sequential	4	5	947	928	1034
IH133	40	60	DMSA	Sequential	4	5	939	947	1037
IH134	40	60	Na_2S	Sequential	4	5	922	944	1019

Reaction temperature is 120 °C. pH is fixed to 10 [a]NaHTe was used as a telluride source. [b]S source was added just after 1h addition of the Te. Peak 1 on the emission maxima [c]before and [d]after addition of S source. [d]Peak 2 on the emission maxima of the reactions.

There was a red shift on the absorbance onsets of the particles with respect to reaction time indicating the particle growth (Figure 5.23 a, 5.24 a and 5.25 a), this time more significant compared to simultaneous addition. PL spectra of IH132 with TAA addition after 1 h of Ag_2Te growth indicates initial intensity increase with no significant shift in peak positions of the bimodal emission profile within the first 10 min after addition of TAA, and later a drop in the intensity as usual, with a major peak being the high energy one rather than the low energy one of the initial Ag_2Te. This may indicate that as the S incorporated to the structure the band gap increase so the emission at the low wavelength increases. But this also may indicate possibility of two types of particles and/or two different emission centers, but more related to S and the other to Te. Yet, it should not be forgotten that even Ag_2Te had similar emission profile.

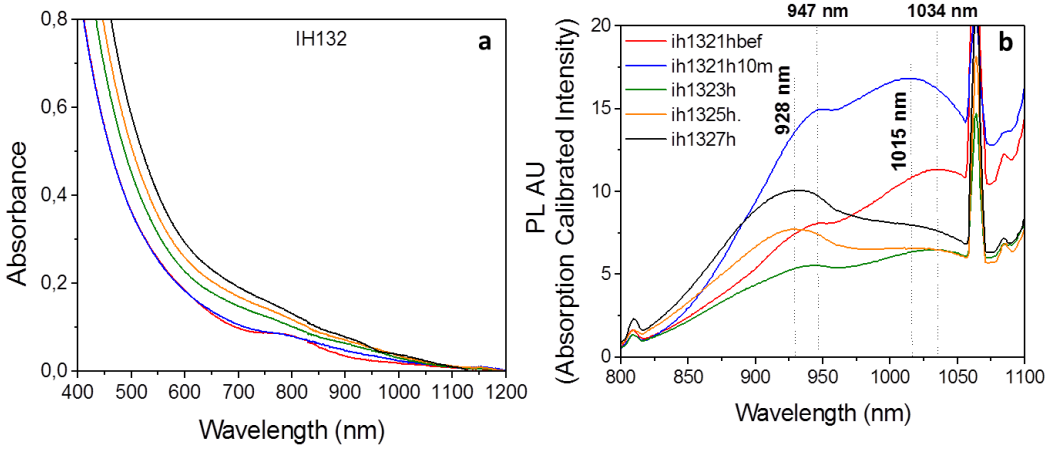

Figure 5.21 a) Absorbance and b) Photoluminescence spectra of the reaction IH132 taken with Si detector (λexc:532nm).

Size analysis of the particles by Brus equation and absorbance and PL measurements indicate the sizes of the particles are larger if synthesized with TAA (Table 5.11, Figure 5.24). As seen from the luminescence graphs for the reaction IH132 (Figure 5.21 b), emission wavelength shifted to left with decrease in PL intensity. But the emission profile has double maxima.

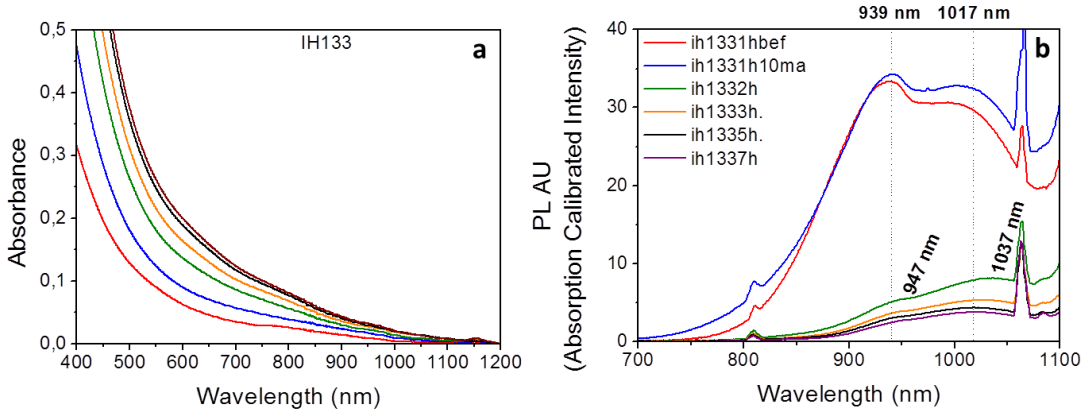

Figure 5.22 a) Absorbance and b) Photoluminescence spectra of the reaction IH133 taken with Si detector (λexc:532nm).

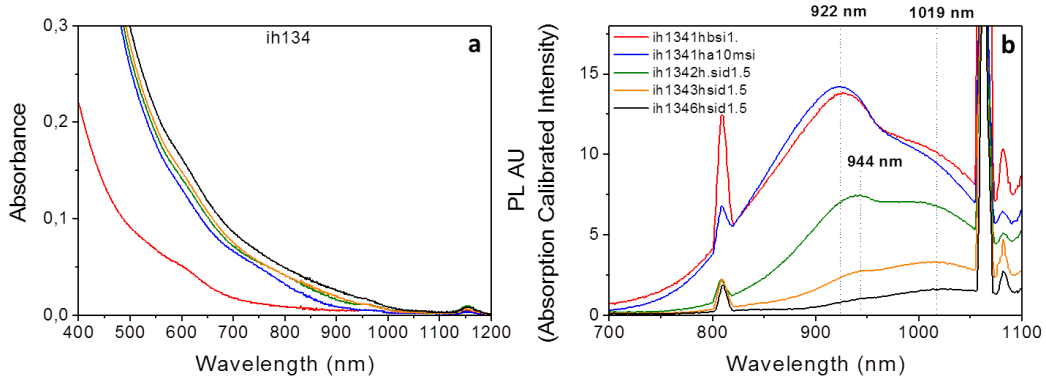

Figure 5.23 a) Absorbance and b) Photoluminescence spectra of the reaction IH134 taken with Si detector (λexc:532nm).

Table 5.11 Calculated particle sizes for $Ag_2Te_xS_{1-x}$ NIRQDs

Reaction Code	Size[a] nm	Band Gap eV
IH120 5min.	3.4	1.2
IH120 3h	3.5	1.2
IH120 5h	3.6	1.2
IH122 15 min.	3.3	1.2
IH122 1h	3.8	1.1
IH122 5h	3.8	1.1
IH132 1h bef. add.	3.3	1.2
IH132 1h 10 min.	3.6	1.2
IH132 3h	3.7	1.1
IH133 1h bef add.	3.4	1.2
IH133 1h 10 min.	3.5	1.2
IH133 3h	3.9	1.1

[a]Size is calculated by Brus equation

$Ag_2Te_xS_{1-x}$ NIRQDs (IH133) was synthesized with DMSA as well, which will release S slower than TAA and Na_2S but would also have surface adsorption characteristic. With time, absorbance onset shifted to longer wavelengths indicating particle growth (Figure 5.22). In the emission profile no significant change observed in 10 min but after 2h of reaction fallowing the addition of DMSA, a significant drop in the intensity and a small red shift was observed (Peak1 shifted from 939 nm to 947 nm, Peak2 shifted to 1017 nm to 1037 nm. Table 5.10, Figure 5.22 b). This may not be due to growth of particles rather than compositional change when the shift in absorbance onset is considered. Drop in the intensity may be due to incorporation of S and no homogenous surface and/or crystal defects as well as due to defects formed due to decomposition of the coating as well. Moreover, possibility of ligand exchange (DMSA exchanging 2MPA) on the surface may contribute to surface perturbation and increase in non-radiative

events. Lastly, fast S source, Na_2S was used in the synthesis (IH134). Dramatic red shifts were seen on both absorbance and PL spectra of the samples after Na_2S addition (Figure 5.23). The original emission maxima of the Ag_2Te were around 920 nm and 1020 nm. The contribution of the peak at 920 nm increased in intensity with reaction time accompanied by an overall decrease in PL intensity with a 20nm red shift (Peak1B and Peak1A, Table 5.10). Figure 5.24 demonstrates comparison of PL spectra of the samples taken 10 min. and 3h after the addition of the S source. To sum up, TAA and DMSA lead the formation of slightly bigger particles in early stages (Figure 5.24 a). Then, their PL intensities come to same position for all three (Figure 5.24 b, Peak1 944 nm and Peak2 1032nm). Na_2S enhances the luminescence around 940nm with possibly faster incorporation of S most visible in 10 min samples. At short reaction times DMSA produces particles with stronger emission possibly due to additional surface passivization which diminishes at longer times due to decomposition. There are no dramatic changes in the PL properties of the particles by the simultaneous and sequential addition of the chalcogenides. The first peak fixed at 940 nm in both methods whereas, second peak shifts to th elonger wavelengths by 15 nm by sequential addition.

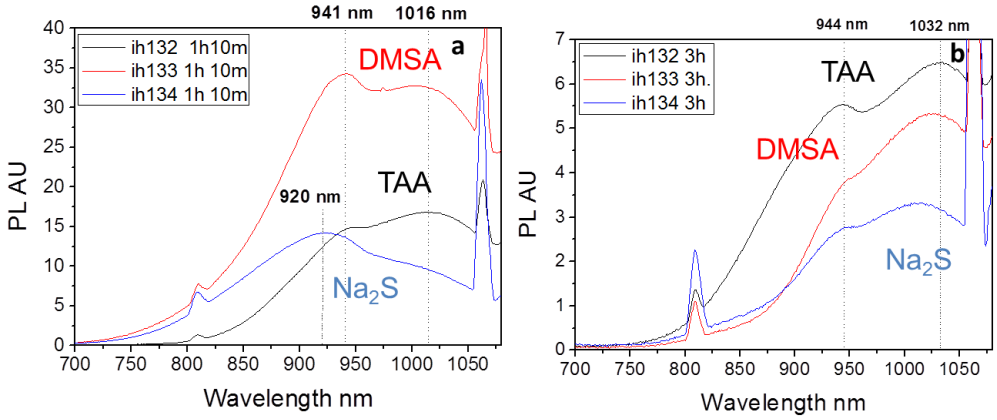

Figure 5.24 PL spectra of the samples a) 10 min. b) 3h after the addition of S source.

5.4.3.3 Long term stability of the particles

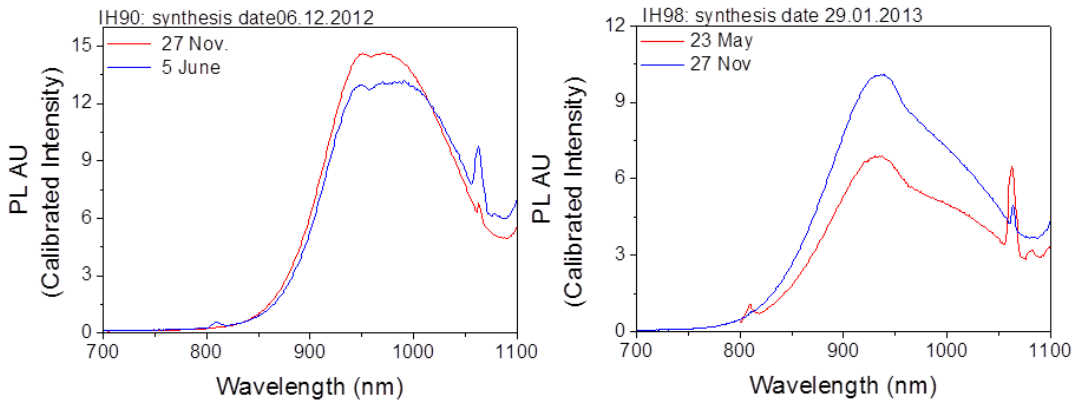

Figure 5.25 PL spectra of the IH90 and IH98 taken at different time points.

Long term stability of the particles in terms of luminescence and colloidal stability are important for the practical applications. These particles have shown both colloidal and luminescence stability over a year. PL spectra of the two different particles taken six months period were shown in Figure 5.25. There is no shift on the emission maximum for these two particles and luminescence intensities almost the same (the second PL acquisition for the sample IH98 was not power normalized, therefore, it is normal to see an intensity difference.).

5.4.4 In Vitro Studies

5.4.4.1 Cytotoxicity Evaluation

Ag_2S-2MPA NIRQDs were evaluated previously (Chapter 2) in HeLa (cancer cells) and NIH-3T3 (mouse-fibroplast healthy cells) cells. They did not show significant toxicity at extremely high doses. Similar studies were done with the Ag_2Te-2MPA (IH90 (pH=10) and IH82 (pH=7.5)) and $Ag_2Te_xS_{1-x}$-2MPA (IH97) NIRQDs (Figure 5.26, Table 5.12). In Statistical evaluations, QDs were found non-toxic to HeLa cells.

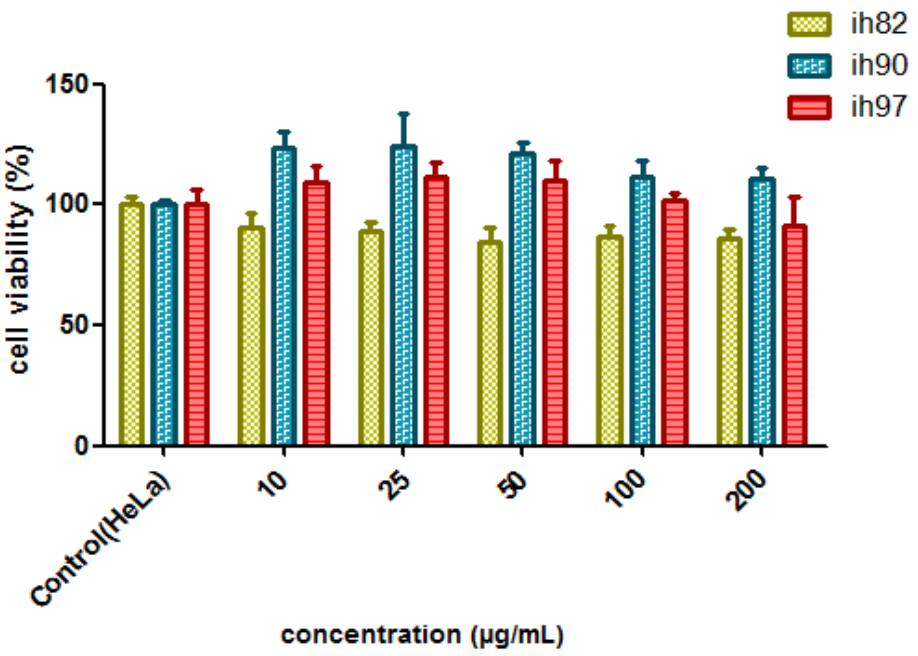

Figure 5.26 Viability of HeLa cancer cells after 24 h exposure to Ag_2Te (IH 90 and IH82) and $Ag_2Te_xS_{1-x}$ (IH 97)NIRQDs. Indicated doses are Ag concentration within the applied dose of QDs

$Ag_2Te_xS_{1-x}$ nanoparticles was expected to be cytocompatible as of Ag_2Te and Ag_2S and actually was as can be seen in Figure 5.26. The other compositions were not evaluated as these results indicate that silver chalcogenides in general are highly cytocompatible. This is the first cytotoxicity study done for the Ag_2Te and $Ag_2Te_xS_{1-x}$ NIRQDs. Possibly very low solubility of Silver chalcogenides prevents cytotoxicity of these particles.

Table 5.12 Cell viability of the HeLa cell lines exposed to QDs.

Particle Concentration (µg/mL)	0 Ctrl	10	25	50	100	200
IH82	100.0 ± 7.2	90.5 ± 11.6	88.6 ± 8.9	84.2 ± 12.3	87.1 ± 8.7	86.3 ±7.7
IH90	100.0 ± 2.8	123.2 ± 13.9	124.3 ± 26.4	121.1 ±8.9	111.2 ± 13.5	111.0 ± 8.8
IH97	100.0 ± 12.2	109.6 ± 12.6	111.7 ± 12.6	110.2 ± 15.7	101.8 ± 6.4	91.4 ± 24.4

5.4.4.2 Cellular Imaging

Biocompatible NIRQDs have been used for bio-applications especially for tagging and imaging purposes. For these reasons, cellular internalization of the Silver chalcogenides is an important property. Ag_2Te NIRQDs have been internalized and localized in cytoplasm as shown by confocal laser scanning micrographs in Figure 5.27. This was the first study that a cell line was imaged with Ag_2Te NIRQDs. Although PLQY of these materials are low with respect to Ag_2S NIRQDs, HeLa cells were successfully imaged with the punctuated distribution of the particles in the cytoplasm, indicating potential as good optical probes.

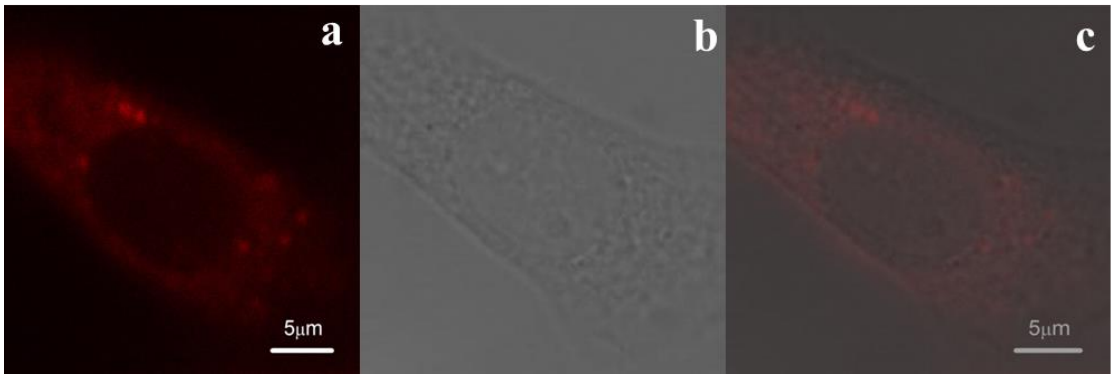

Figure 5.27 Confocal Laser Scanning Micrographs of Ag_2Te NIRQDs localized to HeLa cells a) Fluorescence b) Transmission c) overlay images. Excitation at 532 nm.

5.5 Conclusion

Aqueous Ag_2Te and $Ag_2Te_xS_{1-x}$ NIRQDs were synthesized for the first time in the literature. Luminescence, in vitro cytotoxicity and optical imaging studies were done.

2-MPA coated aqueous Ag_2Te NIRQDs have emission properties between the wavelengths 900-1200 nm which is practically a difficult range for recording emission. For this reason, both Si and InGaAs detector were used to detect luminescence of these QDs. But these two detectors enhance the PL intensity where their sensitivities are higher. Bimodal emission profile was observed in all reactions with two emission peaks. Changing the variables alter the peak intensities with shifts with respect to each

other. Emission was between 920-950 nm in peak 1 and, between 1000-1050 nm in peak 2 Overall, compared to Ag_2S; incorporation of Te shifted the luminescence towards higher wavelengths. Fast and slow sulfur release is one of the important factors affecting the PL intensities. Slow S release support the particles emitting at longer wavelengths. Different Te/S ratios were used to synthesize $Ag_2Te_xS_{1-x}$ NIRQDs to tune emission wavelengths between 850-1050 nm. Change in the band gap and compositions are controversial so it was not easy to comment on luminescence graphs.

Due to the partial decomposition of 2-MPA at the reaction temperature, both Ag_2Te and alloys are richer in terms of silver sulfide, as shown by ICP and XPS. Thereforei dramatic shifts in emission maxima was not achieved, yetdifferences upto 30nm was achieved. PL peak shifted to 1035 nm from 928 nm when the particles synthesized with DMSA instead of Na_2S.

ICP analyses also proved excess of S in all QDs with Ag/Te ratios above 6. This might be due to incorporation of S decomposed from coating material. Soft Ag ions should favor soft Te ions rather than hard S. Besides, solubility of the Ag_2Te is lower, theoretically favoring quick precipitation of Ag_2Te, but experiments did not support these theories. One possible further study may involve analysis of reaction products at the initial 15 min of the reaction to eliminate the S incorporation coming from 2MPA decomposition. A better approach in further studies may involve, organic synthesis of Ag_2Te and alloys with thiol free coatings such as oleic acid, dodecylamine or TOPO. Solid state reactions to produce pure Ag_2Te would be helpful as well to investigate the crystal structure of Ag_2Te. Te can form different crystal structures.

Only few samples were analyzed by TEM and EDX. QDs were spherical with sizes in the range of 2.5-4 nm. More comprehensive analyses have been required for the particle characterizations by TEM and EDX. Also, analysis of the lattice parameters would provide valuable information on structure.

Colloidal and photo/stability of Ag_2Te and $Ag_2Te_xS_{1-x}$ NIRQDs have been maintained over a year. They were non-toxic in HeLa cells up to high doses like 200 μg/ml. They were internalized by cells effectively and produced strong optical signal with no background, proving the potential of these particles as biocompatible optical probes.

Chapter 6

6 CONCLUSION

In the area of quantum dot based emerging technologies, utilization of NIRQDs gained a tremendous importance and reach in this field accelared within the last two-three years. Current examples target mostly biological applications and solar energy conversion. Target application of the NIRQDs developed in this thesis is medical imaging and therapy.

Emission in the NIR window is advantageous over emission in the visible region in medicine and biotechnology due to elimination of autofluorescence of the tissue and deeper penentration allowing high contrast and deep tissue imaging. Cd based NIRQDs were developed with complex alloy structures incorporating metals such as Pb and Hg and used in biological studies. However, heavy metal toxicity is a major road block in front of the clinical applications. Most of these QDs can be rendered more biocompatible with PEGylation and a second chalcogenide shell such as ZnS but, this is not enough to obtain FDA approval in many cases.

The primary aim of this thesis work is to develop highly biocompatible, colloidally and optically stable, highly luminescent quantum dots with size tunable emission in the NIR window, specifically in the NIR-I (700-1000 nm), directly in aqueous medium. For this purpose aqueous synthesis of silver chalcogenides, specifically Ag_2S and $Ag_2S_xTe_{(1-x)}$

NIRQDs were targeted due to the intrinsic biocompatibility of bulk Ag_2S. At the beginning of this thesis work there were only few reports on the synthesis and biocompatibility of silver chalcogenides, but there are more than 70 publication in the first half of 2014, showing the strong upcoming and value of these materials. First, 2-MPA coated aqueous Ag_2S NIRQDs were developed in this study. These NIRQDs were highly luminescent and cytocompatible and colloidally stable. Ag/Te and 2MPA/Ag ratios, reaction temperature (30-90^o C) and pH (7.5-10) were the studied parameters affecting the size, emission tunability, optical, chemical and physical properties of the particles. Size of the particles tuned from 2.8-3.1 nm. Ag_2S-2MPA NIRQDs have emission in the NIR-I window between 780-950 nm with PLQY between 7-14 % with respect to LDS 798 NIR dye. PLQY increased up to 39% upon aging. No significant difference in particle composition or surface corresponding to such a change could be found. This is the highest QY that has been reported in literature until now (September 2014). At the time begining of this study the highest QY reported was 2% and 13% has been just reported. One interesting point was the weak sensitivity of emission to common factors such as temperature, reaction duration and stoichiometric changes in Ag/S and coating/Ag ratios. Such factors usually are effective in tuning emission from blue to red in Cd-chalcogenides meaning in a range between 480-640 nm with a change in visible color within every 20-30 nm. Here, achieved emission wavelengths can be grouped as 785, 815, 830, 850 and 950 nm but good quality particles (with strong luminescence intensity) are those emitting around 810-850 nm. Increasing temperature from RT to 90°C increased the particle size only when high coating amounts were used and caused an emission in 950 nm however this was mainly due to the decomposition of 2-MPA at high temperatures and accompanied with a dramatic loss in luminescence intensity, probably due to loss of capping agents and defect formation. Otherwise, prolonged reaction times did not cause a shift in the emission peak despite of a slight red shift in the absorbance onset. This brings about a question about the source of emission in Ag_2S NIRQDs. Is it a band-edge emission which should be size tunable or a defect related emission which will be less sensitive to crystal size? This can be

investigated further through PL excitation and life time studies accompanied with TEM analysis for accurate size measurement of the Ag_2S crystals. Some of the data presented in Chapter 2 indicates band-edge emission. Actually, size independent luminescence of Ag_2S QDs was reported as a problem in the literature, as well.

One issue that was elucidated in the analysis of these particles is the difference between the sizes calculated by the Brus equation and by TEM. There is no data in the literature which reports such discrepancy. TEM analysis of each and every particle could not be obtained due to the lack of instrumentation. However, in a future study, Ag_2S QDs emitting both in the NIR-I and NIR-II windows can be synthesized and analyzed with TEM and measured crystal sizes should be compared with the calculated ones in order to understand if this is a problem in the small sizes of Ag_2S QDs or a general problem for all Ag_2S QDs.

Ag_2S-2MPA NIRQDs were highly cytocompatible. They showed no cytotoxicity in HeLa and MCF-7 cancer cells up to 300 μg/ml and in more vulnerable NIH/3T3 cells up to 600 μg/ml. Insolubility of Ag_2S is possibly the major reason for such a high cytocompatibility since silver ions at such high doses are cytotoxic. They were imaged by CSLM in HeLa cell lines with near no autofluoresence and strong QD emission. This was the first time that a mammalian cell was imaged by Ag_2S-2MPA NIRQDs effectively in the literature. Their high PLQY, cytocompatibility and colloidal and luminescence stability make them great candidates for in vivo applications as well.

In the third chapter, development of DMSA coated Ag_2S NIRQDs was demonstrated in an effort to obtain better size and emission tunability in Ag_2S NIRQDs with high QY at all wavelengths. DMSA is a FDA approved drug used as an antidote in heavy metal poisoning. So, it is a biocompatible material. DMSA was used both as a coating and a S-releasing agent in preparation of Ag_2S-DMSA NIRQDs. DMSA decomposes at and above pH 7.5 and 70 ^oC. Slow S-release and hence, slow particle growth, allowed production of emission tunable Ag_2S NIRQDs in a single pot reaction. Different

DMSA/Ag mol ratio, reaction pH and temperature influenced the reaction kinetics and particle properties. Ag_2S-DMSA NIRQDs emit between 730-920 nm with PLQY around 6.5% which is adequate for imaging and high compared to values reported in the literature. Use of DMSA instead of Na_2S and 2-MPA reduced particle size and shifted emission slightly to lower wavelengths with some reduction in the PLQY, but the major advantage of Ag_2S-DMSA NIRQDs is size tunability within a single pot reaction with effective PLQY. In a single reaction several Ag_2S-DMSA NIRQDs with emission maximum red shifted about 20-30nm were achieved. However, due to broad emission bands of these QDs compared to Cd_chalcogenides, effectively three or four different particles from the same pot can be used simultaneously for all practical purposes.

DMSA coated Ag_2S NIRQDs were highly cytocompatible, showed no toxicity in HeLa cell lines up to 840µg/ml. HeLa cells were successfully imaged with these QDs with no autofluoresence. Interaction of the QDs with blood components is very important for the in vivo applications. These Ag_2S QDs were demonstrated as highly hemocompatible with no significant effect on eryhrocytes, platelets, and complement system and on the intrinsic pathway of coagulation. These QDs also offer great potential as theranostics.

In chapter 4, multifunctional hybrid nanoparticles have been developed from SPIONs and Ag_2S-2MPA NIRQDs using a biphasic ligand exchange method. Method is extremely simple, reproducible, efficient and cost effective compared to alternative methods present in the literature and produce small particles (smaller than 150nm) without any size selection processes. Using different Ag_2S NIRQDs with emissions centered around 770, 860, 890nm four different hybrid nanoparticles were prepared with emission shifted to higher wavelengths by about 10-40nm and with different Ag/Fe ratios. Hybrids were colloidally and optically stable over time, responsive to external magnetic field and showed strong luminescence, yet compared to parent NIRQDs, hybrids had some loss in the luminescence intensity. Although SPIONs do not have a significant absorbance in the NIR, they do in the visible region where these

particles were excited (532nm). In addition aggregation of QDs around SPIONs may cause some re-absorption of the emitted photons causing such differences in luminescence intensity. This does not correlate well with Ag/Fe ratio, indicating no significant influence of the SPIONs actually, or with the size of the hybrid. Decrease in PL intensity might be due to the manipulation and surface perturbation of the particles caused during the ligand exchange process.

In vitro cell culture studies for the determination of cytocompatibility and cellular internalization of hybrid nanoparticles were performed on both NIH/3T3 and HeLa cells between the dose range of 10-50 μg Ag/mL in the absence and presence of magnetic field. Different sized particles were evaluated in cytotoxicity studies; size of the hybrid nanoparticles was influential on cell viabilities. Smaller particles were internalized more by the cells and showed more cytotoxicity in NIH/3T3 cells with respect to larger particles. However, it was not the case for HeLa cells. Comparison of uptake and toxicity under magnetic field compared to those performed in the absence of magnetic field indicated effectiveness of magnetic targeting with increasing Fe content of the hybrids. Internalization of particles by cells increased and therefore cytotoxicity is increased as a result of magnetic targeting of particles. Overall hybrids were more toxic compared to Ag_2S NIRQDs reported in Chapter 2 and 3. This may be due to SPIONs but also selection of the criteria for dose is an important issue. Because, dosing of Ag_2S NIRQDs were done according to Ag concentration, same was done here for the hybrids but this causes higher loading of materials to cells. Hybrid nanoparticles internalized by HeLa cells were also optically imaged using a CLSM showing a punctuated distribution of hybrids in the cytoplasm. Clear benefit of using NIR QD was seen here with the absence of autofluoresence.

Multifunctionality of these hybrid nanoparticles makes them significantly important material in medicine. They can be effectively used as a dual imaging agent as well as a

theranostic material after a more detailed dose dependent toxicity study and may b after PEGylation.

In Chapter 5, synthesis and characterization of Ag_2Te and $Ag_2Te_xS_{1-x}$ NIRQDs have been demonstrated. This was the first aqueous preparation of Ag_2Te and $Ag_2Te_xS_{1-x}$ NIRQDs reported in the literature. Considering the lower band gap of Ag_2Te, $Ag_2Te_xS_{1-x}$ composition hold great potenetial in tuning emission in the whole NIR window. 2MPA coated Ag_2Te and $Ag_2Te_xS_{1-x}$ alloys were synthesized primarily to have particles emitting in 750-1050 nm (diagnostic window for therapy) range. These QDs have bimodal emission profile with two maxima in the range of 900-1100 nm recorded with both Si and InGaAs detectors, which is at higher wavelengths than Ag_2S NIRQDs as expected. But, Te/S, fast and slow S-release and changes in the addition order of Te and S sources did not have dramatic changes in the size or emission wavelengths of the alloyed QDs. About 30-50nm shifts in the emission maxima causing emissions in 920-950 nm along with 1000-1050 nm were obtained. These QDs are colloidally stable and photostable and showed almost no toxicity up to 200 μg/ml in HeLa cell lines. These QDs were successfully internalized in cells and used as effective optical probes. Origin of the broad emission profile with two maxima was investigated. No significant shape anisotropy ,coexistence of Ag_2Te and Ag_2S QDs or bimodal distribution of particle sizes, which could explain such emission behavior, were determined. However, TEM indicated broad size distribution which may be partially responsible from such broad emission profile. A more detailed TEM analysis can be performed to detect any compositional change within the material such as a core/shell structure, due to solubility difference between Ag_2Te and Ag_2S. This was attempted with XPS, but a conclusive answer could not be obtained. The most important finding was the much faster incorporation of sulfide compared to telluride and influence of 2-MPA decomposition at high temperatures especially at extended reaction times, making the reaction and the particles significantly richer in S, even in pure Ag_2Te formulation. Although $Ag_2Te_xS_{1-x}$ synthesis were formulated with x= 20, 40, 60 resulting particles

were all richer in S as determined by XPS and ICP OES. In all formulations regardless of Te/S ratio, 2-MPA is in large excess compared to S and Te. Since reactions were performed at 120 ^oC and mostly for 3h, a significant S-release from 2-MPA can be expected producing Ag_2S mainly with few percent of Te incorporation. Although it is not a major concern of this thesis, an organic preparation method utilizing S-free capping agents can be adopted to prepare Ag_2Te and $Ag_2Te_xS_{1-x}$ QDs, to observe emission properties and ability to control composition. Also, solid state reactions of Ag and Te can be helpful to produce pure Ag_2Te and analyze the crystal structure. Although Ag_2Te and Ag_2S have same crystal structure, Ag_2Te and alloys can crystallize in different forms. [146, 147] Moreover, life-time measurements around 950 and 1050nm may be valuable to assign one peak to band edge and the other one to the defect related emissions.

Overall, in an attempt to provide size tunable synthesis of Ag_2X NIRQDs, emission tuning was best achieved with DMSA decomposition in the synthesis of Ag_2S-DMSA particles. Yet, fine tuning may be considered less important in the NIR since cameras detecting emission will not generate colorful pictures obtained CdX QDs. Different emissions can be sensed by using different emission filters, therefore is still valuable for simultaneous detection of different analytes, events, tumors etc.

6.1 Publications & Conferences

Hocaoglu, I., Asik D., Ulusoy G., Kiraz A., Servin C., Grandfils C., Jimenez I., Rossi F. and Acar Y. F.H, Development of hybrid nanoparticles composed of NIR emitting Ag_2S and superparamagnetic Fe_3O_4 as a new generation multifunctional nanomaterials. (Manuscript in Progress).

Hocaoglu, I., Demir F., Birer O., Kiraz A., Servin C., Grandfils C. and Acar Y. F.H. Emission tunable, cyto/hemocompatible, near-IR-emitting Ag_2S quantum dots by aqueous decomposition of DMSA. Nanoscale, 2014. DOI: 10.1039/C4NR02935F

Hocaoglu, I., Cizmeciyan M. N., Erdem R., Ozen C., Kurt A., Sennaroglu A. and Acar Y. F.H. Development of highly luminescent and cytocompatible near-IR-emitting aqueous Ag_2S quantum dots. Journal of Materials Chemistry, 2012. 22(29): p. 14674-14681.

Hocaoglu, I., Cizmeciyan M. N., Erdem R., Ozen C., Kurt A., Sennaroglu A. and Acar Y. F.H. Aqueous Preparation of Near Infrared Emitting Ag_2S Quantum Dots for Bioapplications, 'International Conference for Young Researchers on Advanced Materials,' Jully 1-6 2012 Singapore.

Hocaoglu, I., et al., Near IR emission properties of cytocompatible aqueous Ag2S quantum dots for biotechnology, '19th International Vacuum Congress + I. International Conference on Noscience and Nanotechnology',September 9-13, Paris-France.

Özkan-Vardar, D., Hocaoğlu, I., Yağcı Acar, H. F., Başaran, N., Comparison of the cytotoxic effects of Silver Sulfide Quantum Dots Coated with 2MPA and DMSA in V79 Cells, 3rd International Summit on Toxicology & Applied Pharmacology during October 20-22, 2014 in Chicago, USA.

Özkan-Vardar, D., Hocaoğlu, I., Yağcı Acar, H. F., Başaran, N., Effects of Silver Sulfide Quantum Dot Coated with 2MPA and DMSA Induced Cytotoxicity by Neutral Red Uptake Assay in Hela Cells, European Society of Toxicology In Vitro 2014 International Conference, June 10-13, 2014 - Egmond aan Zee, The Netherlands.

Özkan-Vardar, D., Göktaş, H. G., Hocaoğlu, I., Yağcı Acar, H. F., Başaran, N. Effects of Silver Sulfide Quantum Dot Coated with Ag2S-2MPA and DMSA) Induced Cytotoxicity by Neutral Red Uptake Assay in V79 Cells, "NANOTOX 2014, 7th International Nanotoxicology Congress, April 23-26, 2014, Antalya.

A Appendix A

A. CALCULATION OF PARTICLE SIZE FOR Ag_2S QDs BY BRUS EQUATION

A.1Band gap determination from absorption Spectra

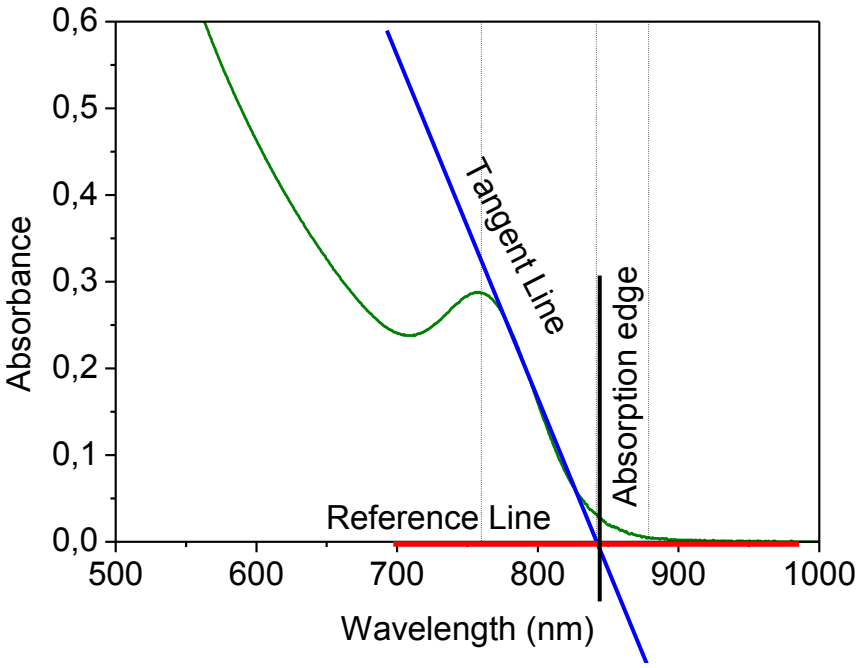

Figure A.1 Absorbance spectrum of Ag_2S NIRQDs for band gap determination.

Band gap of QDs can be determined from the absorbance spectra of QDs. Absorption edge determined from the absorbance spectrum gives the band gap of the material as shown in the Figure A1. A tangent line is drawn to the excitonic peak and also a reference line is drawn to base level where the absorption is zero. The intersection of these two lines gives the absorption edge. This edge equals to the band gap of QD. Radius of the QD can be calculated from the Brus equation using this band gap value (equation 1.1, Chapter 1).

$$Eg(QD) = Eg(Bulk) + \frac{h^2}{8R^2}\left[\frac{1}{m_e} + \frac{1}{m_h}\right] - 1.8\frac{e^2}{4\pi\varepsilon\varepsilon_0 R}$$

A.2 Matlab code for size output by Brus equation

Brus Equation can be solved by a Matlab code for particle size calculation (radius) with respect to each probable absorption edge (corresponding wavelength). Band gap energy of bulk Ag_2S is 0.9 eV. m_e (0.286 m_0) and m_h (1.096) are the respective effective electron and hole masses for Ag_2S and ε_{Ag2S}(5.95) is the dielectric constant. Calculated particle sizes are given on Table A.1 for different absorption wavelengths and corresponding band gap energies.

Matlab Code

```
clc, clear all, close all
% Variables are effective electron and hole masses
% dielectric constant and band gap energy of bulk Ag2S
Ag2Svariables=[0.286 1.096 5.95  0.9];
% mo is the mass of electron (kg)
m0=9.1095*10^-31;
% planck constant in (Js) h=6.63*10^-34;
```

```
% permittivity of vacuum in [F/m]=C*V/m
e0=8.854*10^-12;
% 1 ev = 1.6*10^-19 C
c=3.0*10^8; %speed of light
N1=651;
Lamda=linspace(340e-9,990e-9,N1);
wavelength_entered=Lamda*10^9;
display=[];
for i=1:N1
bandgap_found(i)=h*c/(Lamda(i)*1.602*10^-19);
deltaband(i)=bandgap_found(i)-Ag2Svariables(4);
z=deltaband(i);
mstar=1/(1/(Ag2Svariables(1)*m0)+1/(Ag2Svariables(2)*m0));
A=h^2/(8*mstar*10^-18*1.602*10^-19);
B=1.8*(1.602*10^-19)/(4*pi*Ag2Svariables(3)*e0*10^-9);
p=[z 0 -A];
r=roots(p);
if r(1)>r(2)
a=r(1);
else
a=r(2);
end
p1=[z B -A];
```

```
r1=roots(p1);

if r1(1)>r1(2)

a1=r1(1);

else

a1=r1(2);

end

diameter(i)=a;

diameter2(i)=a*2;

diametera1(i)=a1;

diameter2a1(i)=a1*2;

bandgap(i)= bandgap_found(i);

display=[display; wavelength_entered(i) diameter2a1(i) bandgap(i) diameter2(i)];

end

disp('  Lambda      Diameter  Bandgap')

disp([display])

figure (1)

display=[display; wavelength_entered(i) diameter2a1(i) bandgap(i) diameter2(i)];

plot(wavelength_entered, diameter2, 'r-', wavelength_entered, diameter2a1, 'b-',
'linewidth', 2)

diameter_r=diameter2';

wavelength_entered1=wavelength_entered';

bandgap_found1=bandgap_found';

deltaband1=deltaband';
```

Table A.1 Particle size of Ag_2S NIRQDs with respect to absorbance edges**.**

Wavelength (nm)	Diameter (nm)	Band Gap (eV)	Wavelength (nm)	Diameter (nm)	Band Gap (eV)
601	2,04	2,07	**630**	2,12	1,97
602	2,04	2,06	**631**	2,12	1,97
603	2,05	2,06	**632**	2,12	1,96
604	2,05	2,06	**633**	2,12	1,96
605	2,05	2,05	**634**	2,13	1,96
606	2,05	2,05	**635**	2,13	1,96
607	2,06	2,05	**636**	2,13	1,95
608	2,06	2,04	**637**	2,13	1,95
609	2,06	2,04	**638**	2,14	1,95
610	2,06	2,04	**639**	2,14	1,94
611	2,07	2,03	**640**	2,14	1,94
612	2,07	2,03	**641**	2,15	1,94
613	2,07	2,03	**642**	2,15	1,93
614	2,08	2,02	**643**	2,15	1,93
615	2,08	2,02	**644**	2,15	1,93
616	2,08	2,02	**645**	2,16	1,92
617	2,08	2,01	**646**	2,16	1,92
618	2,09	2,01	**647**	2,16	1,92
619	2,09	2,01	**648**	2,16	1,92
620	2,09	2,00	**649**	2,17	1,91
621	2,09	2,00	**650**	2,17	1,91
622	2,10	2,00	**651**	2,17	1,91
623	2,10	1,99	**652**	2,17	1,90
624	2,10	1,99	**653**	2,18	1,90
625	2,10	1,99	**654**	2,18	1,90
626	2,11	1,98	**655**	2,18	1,90
627	2,11	1,98	**656**	2,18	1,89
628	2,11	1,98	**657**	2,19	1,89
629	2,11	1,97	**658**	2,19	1,89

Wavelength (nm)	Diameter (nm)	Band Gap (eV)	Wavelength (nm)	Diameter (nm)	Band Gap (eV)
659	2,19	1,88	**690**	2,28	1,80
660	2,20	1,88	**691**	2,28	1,80
661	2,20	1,88	**692**	2,28	1,79
662	2,20	1,88	**693**	2,28	1,79
663	2,20	1,87	**694**	2,29	1,79
664	2,21	1,87	**695**	2,29	1,79
665	2,21	1,87	**696**	2,29	1,78
666	2,21	1,86	**697**	2,29	1,78
667	2,21	1,86	**698**	2,30	1,78
668	2,22	1,86	**699**	2,30	1,78
669	2,22	1,86	**700**	2,30	1,77
670	2,22	1,85	**701**	2,31	1,77
671	2,22	1,85	**702**	2,31	1,77
672	2,23	1,85	**703**	2,31	1,77
673	2,23	1,84	**704**	2,31	1,76
674	2,23	1,84	**705**	2,32	1,76
675	2,24	1,84	**706**	2,32	1,76
676	2,24	1,84	**707**	2,32	1,76
677	2,24	1,83	**708**	2,33	1,75
678	2,24	1,83	**709**	2,33	1,75
679	2,25	1,83	**710**	2,33	1,75
680	2,25	1,83	**711**	2,33	1,75
681	2,25	1,82	**712**	2,34	1,74
682	2,25	1,82	**713**	2,34	1,74
683	2,26	1,82	**714**	2,34	1,74
684	2,26	1,82	**715**	2,34	1,74
685	2,26	1,81	**716**	2,35	1,73
686	2,26	1,81	**717**	2,35	1,73
687	2,27	1,81	**718**	2,35	1,73
688	2,27	1,80	**719**	2,36	1,73
689	2,27	1,80	**720**	2,36	1,72

Wavelength (nm)	Diameter (nm)	Band Gap (eV)	Wavelength (nm)	Diameter (nm)	Band Gap (eV)
721	2,36	1,72	**752**	2,45	1,65
722	2,36	1,72	**753**	2,45	1,65
723	2,37	1,72	**754**	2,46	1,65
724	2,37	1,71	**755**	2,46	1,64
725	2,37	1,71	**756**	2,46	1,64
726	2,38	1,71	**757**	2,46	1,64
727	2,38	1,71	**758**	2,47	1,64
728	2,38	1,71	**759**	2,47	1,64
729	2,38	1,70	**760**	2,47	1,63
730	2,39	1,70	**761**	2,48	1,63
731	2,39	1,70	**762**	2,48	1,63
732	2,39	1,70	**763**	2,48	1,63
733	2,40	1,69	**764**	2,48	1,63
734	2,40	1,69	**765**	2,49	1,62
735	2,40	1,69	**766**	2,49	1,62
736	2,40	1,69	**767**	2,49	1,62
737	2,41	1,68	**768**	2,50	1,62
738	2,41	1,68	**769**	2,50	1,61
739	2,41	1,68	**770**	2,50	1,61
740	2,42	1,68	**771**	2,51	1,61
741	2,42	1,68	**772**	2,51	1,61
742	2,42	1,67	**773**	2,51	1,61
743	2,42	1,67	**774**	2,51	1,60
744	2,43	1,67	**775**	2,52	1,60
745	2,43	1,67	**776**	2,52	1,60
746	2,43	1,66	**777**	2,52	1,60
747	2,44	1,66	**778**	2,53	1,60
748	2,44	1,66	**779**	2,53	1,59
749	2,44	1,66	**780**	2,53	1,59
750	2,44	1,66	**781**	2,53	1,59
751	2,45	1,65	**782**	2,54	1,59

Wavelength (nm)	Diameter (nm)	Band Gap (eV)	Wavelength (nm)	Diameter (nm)	Band Gap (eV)
783	2,54	1,59	**814**	2,64	1,53
784	2,54	1,58	**815**	2,64	1,52
785	2,55	1,58	**816**	2,64	1,52
786	2,55	1,58	**817**	2,65	1,52
787	2,55	1,58	**818**	2,65	1,52
788	2,56	1,58	**819**	2,65	1,52
789	2,56	1,57	**820**	2,65	1,51
790	2,56	1,57	**821**	2,66	1,51
791	2,57	1,57	**822**	2,66	1,51
792	2,57	1,57	**823**	2,66	1,51
793	2,57	1,57	**824**	2,67	1,51
794	2,57	1,56	**825**	2,67	1,50
795	2,58	1,56	**826**	2,67	1,50
796	2,58	1,56	**827**	2,68	1,50
797	2,58	1,56	**828**	2,68	1,50
798	2,59	1,56	**829**	2,68	1,50
799	2,59	1,55	**830**	2,69	1,50
800	2,59	1,55	**831**	2,69	1,49
801	2,60	1,55	**832**	2,69	1,49
802	2,60	1,55	**833**	2,70	1,49
803	2,60	1,55	**834**	2,70	1,49
804	2,60	1,54	**835**	2,70	1,49
805	2,61	1,54	**836**	2,71	1,49
806	2,61	1,54	**837**	2,71	1,48
807	2,61	1,54	**838**	2,71	1,48
808	2,62	1,54	**839**	2,72	1,48
809	2,62	1,53	**840**	2,72	1,48
810	2,62	1,53	**841**	2,72	1,48
811	2,63	1,53	**842**	2,72	1,47
812	2,63	1,53	**843**	2,73	1,47
813	2,63	1,53	**844**	2,73	1,47

Wavelength (nm)	Diameter (nm)	Band Gap (eV)	Wavelength (nm)	Diameter (nm)	Band Gap (eV)
845	2,73	1,47	**876**	2,84	1,42
846	2,74	1,47	**877**	2,84	1,42
847	2,74	1,47	**878**	2,85	1,41
848	2,74	1,46	**879**	2,85	1,41
849	2,75	1,46	**880**	2,85	1,41
850	2,75	1,46	**881**	2,86	1,41
851	2,75	1,46	**882**	2,86	1,41
852	2,76	1,46	**883**	2,86	1,41
853	2,76	1,46	**884**	2,87	1,40
854	2,76	1,45	**885**	2,87	1,40
855	2,77	1,45	**886**	2,87	1,40
856	2,77	1,45	**887**	2,88	1,40
857	2,77	1,45	**888**	2,88	1,40
858	2,78	1,45	**889**	2,88	1,40
859	2,78	1,45	**890**	2,89	1,40
860	2,78	1,44	**891**	2,89	1,39
861	2,79	1,44	**892**	2,89	1,39
862	2,79	1,44	**893**	2,90	1,39
863	2,79	1,44	**894**	2,90	1,39
864	2,80	1,44	**895**	2,90	1,39
865	2,80	1,44	**896**	2,91	1,39
866	2,80	1,43	**897**	2,91	1,38
867	2,81	1,43	**898**	2,92	1,38
868	2,81	1,43	**899**	2,92	1,38
869	2,81	1,43	**900**	2,92	1,38
870	2,82	1,43	**901**	2,93	1,38
871	2,82	1,43	**902**	2,93	1,38
872	2,82	1,42	**903**	2,93	1,37
873	2,83	1,42	**904**	2,94	1,37
874	2,83	1,42	**905**	2,94	1,37
875	2,83	1,42	**906**	2,94	1,37

Wavelength (nm)	Diameter (nm)	Band Gap (eV)	Wavelength (nm)	Diameter (nm)	Band Gap (eV)
907	2,95	1,37	**938**	3,06	1,32
908	2,95	1,37	**939**	3,07	1,32
909	2,95	1,37	**940**	3,07	1,32
910	2,96	1,36	**941**	3,07	1,32
911	2,96	1,36	**942**	3,08	1,32
912	2,97	1,36	**943**	3,08	1,32
913	2,97	1,36	**944**	3,09	1,32
914	2,97	1,36	**945**	3,09	1,31
915	2,98	1,36	**946**	3,09	1,31
916	2,98	1,36	**947**	3,10	1,31
917	2,98	1,35	**948**	3,10	1,31
918	2,99	1,35	**949**	3,10	1,31
919	2,99	1,35	**950**	3,11	1,31
920	2,99	1,35	**951**	3,11	1,31
921	3,00	1,35	**952**	3,12	1,30
922	3,00	1,35	**953**	3,12	1,30
923	3,01	1,35	**954**	3,12	1,30
924	3,01	1,34	**955**	3,13	1,30
925	3,01	1,34	**956**	3,13	1,30
926	3,02	1,34	**957**	3,14	1,30
927	3,02	1,34	**958**	3,14	1,30
928	3,02	1,34	**959**	3,14	1,29
929	3,03	1,34	**960**	3,15	1,29
930	3,03	1,34	**961**	3,15	1,29
931	3,04	1,33	**962**	3,16	1,29
932	3,04	1,33	**963**	3,16	1,29
933	3,04	1,33	**964**	3,16	1,29
934	3,05	1,33	**965**	3,17	1,29
935	3,05	1,33	**966**	3,17	1,29
936	3,05	1,33	**967**	3,18	1,28
937	3,06	1,33	**968**	3,18	1,28

Wavelength (nm)	**Diameter (nm)**	**Band Gap (eV)**	**Wavelength (nm)**	**Diameter (nm)**	**Band Gap (eV)**
969	3,18	1,28	**980**	3,23	1,27
970	3,19	1,28	**981**	3,23	1,27
971	3,19	1,28	**982**	3,24	1,26
972	3,20	1,28	**983**	3,24	1,26
973	3,20	1,28	**984**	3,25	1,26
974	3,20	1,27	**985**	3,25	1,26
975	3,21	1,27	**986**	3,25	1,26
976	3,21	1,27	**987**	3,26	1,26
977	3,22	1,27	**988**	3,26	1,26
978	3,22	1,27	**989**	3,27	1,26
979	3,23	1,27	**990**	3,27	1,25

BIBLIOGRAPHY

1. Rogers, B., J. Adams, and S. Pennathur, *Nanotechnology: understanding small systems*2008: CRC Press.
2. Murray, C.B., D.J. Norris, and M.G. Bawendi, *Synthesis and characterization of nearly monodisperse CdE (E = sulfur, selenium, tellurium) semiconductor nanocrystallites.* Journal of the American Chemical Society, 1993. **115**(19): p. 8706-8715.
3. Dabbousi, B.O., et al., *(CdSe)ZnS Core−Shell Quantum Dots: Synthesis and Characterization of a Size Series of Highly Luminescent Nanocrystallites.* The Journal of Physical Chemistry B, 1997. **101**(46): p. 9463-9475.
4. Peng, Z.A. and X. Peng, *Nearly Monodisperse and Shape-Controlled CdSe Nanocrystals via Alternative Routes: Nucleation and Growth.* Journal of the American Chemical Society, 2002. **124**(13): p. 3343-3353.
5. Li, H., W.Y. Shih, and W.-H. Shih, *Highly Photoluminescent and Stable Aqueous ZnS Quantum Dots.* Industrial & Engineering Chemistry Research, 2009. **49**(2): p. 578-582.
6. Xie, R., D. Battaglia, and X. Peng, *Colloidal InP Nanocrystals as Efficient Emitters Covering Blue to Near-Infrared.* Journal of the American Chemical Society, 2007. **129**(50): p. 15432-15433.
7. Battaglia, D. and X. Peng, *Formation of High Quality InP and InAs Nanocrystals in a Noncoordinating Solvent.* Nano Letters, 2002. **2**(9): p. 1027-1030.
8. Ellingson, R.J., et al., *Highly Efficient Multiple Exciton Generation in Colloidal PbSe and PbS Quantum Dots.* Nano Letters, 2005. **5**(5): p. 865-871.
9. Bakueva, L., et al., *PbS Quantum Dots with Stable Efficient Luminescence in the Near-IR Spectral Range.* Advanced Materials, 2004. **16**(11): p. 926-929.
10. Pietryga, J.M., et al., *Pushing the Band Gap Envelope: Mid-Infrared Emitting Colloidal PbSe Quantum Dots.* Journal of the American Chemical Society, 2004. **126**(38): p. 11752-11753.
11. Pan, Y., et al., *Size controlled synthesis of monodisperse PbTe quantum dots: using oleylamine as the capping ligand.* Journal of Materials Chemistry, 2012. **22**(44): p. 23593-23601.
12. Brus, L.E., *Electron--electron and electron-hole interactions in small semiconductor crystallites: The size dependence of the lowest excited electronic state.* The Journal of Chemical Physics, 1984. **80**(9): p. 4403-4409.
13. Brus, L., *Electronic wave functions in semiconductor clusters: experiment and theory.* The Journal of Physical Chemistry, 1986. **90**(12): p. 2555-2560.
14. Mansur, H.S., *Quantum dots and nanocomposites.* Wiley Interdisciplinary Reviews: Nanomedicine and Nanobiotechnology, 2010. **2**(2): p. 113-129.

15. Bockelmann, U., *Exciton relaxation and radiative recombination in semiconductor quantum dots.* Physical Review B, 1993. **48**(23): p. 17637-17640.
16. Klimov, V.I., et al., *Electron and hole relaxation pathways in semiconductor quantum dots.* Physical Review B, 1999. **60**(19): p. 13740-13749.
17. Thi Thuy, P., T. Thi Kim Chi, and N. Quang Liem, *Temperature-dependent photoluminescence study of InP/ZnS quantum dots.* Advances in Natural Sciences: Nanoscience and Nanotechnology, 2011. **2**(2): p. 025001.
18. Fournier-Bidoz, S., et al., *Facile and Rapid One-Step Mass Preparation of Quantum-Dot Barcodes.* Angewandte Chemie International Edition, 2008. **47**(30): p. 5577-5581.
19. Russ Algar, W., M. Massey, and U.J. Krull, *The application of quantum dots, gold nanoparticles and molecular switches to optical nucleic-acid diagnostics.* TrAC Trends in Analytical Chemistry, 2009. **28**(3): p. 292-306.
20. Rizvi, S.B., et al., *Semiconductor quantum dots as fluorescent probes for in vitro and in vivo bio-molecular and cellular imaging*. 20102010.
21. Hines, M.A. and P. Guyot-Sionnest, *Synthesis and Characterization of Strongly Luminescing ZnS-Capped CdSe Nanocrystals.* The Journal of Physical Chemistry, 1996. **100**(2): p. 468-471.
22. Peng, Z.A. and X. Peng, *Formation of High-Quality CdTe, CdSe, and CdS Nanocrystals Using CdO as Precursor.* Journal of the American Chemical Society, 2000. **123**(1): p. 183-184.
23. Hines, M.A. and P. Guyot-Sionnest, *Bright UV-Blue Luminescent Colloidal ZnSe Nanocrystals.* The Journal of Physical Chemistry B, 1998. **102**(19): p. 3655-3657.
24. Bailey, R.E. and S. Nie, *Alloyed Semiconductor Quantum Dots: Tuning the Optical Properties without Changing the Particle Size.* Journal of the American Chemical Society, 2003. **125**(23): p. 7100-7106.
25. Medintz, I.L., et al., *Quantum dot bioconjugates for imaging, labelling and sensing.* Nat Mater, 2005. **4**(6): p. 435-446.
26. Pinaud, F., et al., *Bioactivation and Cell Targeting of Semiconductor CdSe/ZnS Nanocrystals with Phytochelatin-Related Peptides.* Journal of the American Chemical Society, 2004. **126**(19): p. 6115-6123.
27. Kumar, H., et al., *Stable and luminescent wurtzite CdS, ZnS and CdS/ZnS core/shell quantum dots.* Applied Physics A, 2014: p. 1-10.
28. Parak, W.J., et al., *Conjugation of DNA to Silanized Colloidal Semiconductor Nanocrystalline Quantum Dots.* Chemistry of Materials, 2002. **14**(5): p. 2113-2119.
29. Torchynska, T. and Y. Vorobiev, *Semiconductor II-VI Quantum Dots with Interface States and Their Biomedical Applications*. Advanced Biomedical Engineering2011.
30. Hui Li, W.Y.S., Wei-Heng Shih*, *Synthesis and Characterization of Aqueous Carboxyl-Capped CdS Quantum Dots*

for Bioapplications. Ind. Eng. Chem. Res. , 2007. **46**: p. 2013-2019.
31. Acar, H.Y., et al., *Emergence of 2MPA as an Effective Coating for Highly Stable and Luminescent Quantum Dots.* The Journal of Physical Chemistry C, 2009. **113**(23): p. 10005-10012.
32. Celebi, S., et al., *Synthesis and Characterization of Poly(acrylic acid) Stabilized Cadmium Sulfide Quantum Dots.* The Journal of Physical Chemistry B, 2007. **111**(44): p. 12668-12675.
33. Ozturk, S.S., F. Selcuk, and H.Y. Acar, *Development of Color Tunable Aqueous CdS-Cysteine Quantum Dots with Improved Efficiency and Investigation of Cytotoxicity.* Journal of Nanoscience and Nanotechnology, 2010. **10**(4): p. 2479-2488.
34. Sevinc, E., et al., *Meso-2,3-dimercaptosuccinic acid: from heavy metal chelation to CdS quantum dots.* Journal of Materials Chemistry, 2012. **22**(11): p. 5137-5144.
35. Guo-Xi, L., et al., *Preparation and bioapplication of high-quality, water-soluble, biocompatible, and near-infrared-emitting CdSeTe alloyed quantum dots.* Nanotechnology, 2009. **20**(41): p. 415103.
36. Zhai, C., et al., *One-Pot Synthesis of Biocompatible CdSe/CdS Quantum Dots and Their Applications as Fluorescent Biological Labels.* Nanoscale Res Lett, 2011. **6**(1): p. 31.
37. Tian, J., et al., *Controllable synthesis and cell-imaging studies on CdTe quantum dots together capped by glutathione and thioglycolic acid.* Journal of Colloid and Interface Science, 2009. **336**(2): p. 504-509.
38. Zhang, H., et al., *The Influence of Carboxyl Groups on the Photoluminescence of Mercaptocarboxylic Acid-Stabilized CdTe Nanoparticles.* The Journal of Physical Chemistry B, 2002. **107**(1): p. 8-13.
39. Korgel, B.A. and H.G. Monbouquette, *Quantum Confinement Effects Enable Photocatalyzed Nitrate Reduction at Neutral pH Using CdS Nanocrystals.* The Journal of Physical Chemistry B, 1997. **101**(25): p. 5010-5017.
40. Sun, Y.H., et al., *Photostability and pH sensitivity of CdSe/ZnSe/ZnS quantum dots in living cells.* Nanotechnology, 2006. **17**(17): p. 4469.
41. Biju, V., et al., *Bioconjugated quantum dots for cancer research: Present status, prospects and remaining issues.* Biotechnology Advances, 2010. **28**(2): p. 199-213.
42. Azzazy, H.M.E., M.M.H. Mansour, and S.C. Kazmierczak, *From diagnostics to therapy: Prospects of quantum dots.* Clinical Biochemistry, 2007. **40**(13–14): p. 917-927.
43. Lin, C.-A.J., et al., *Bioanalytics and biolabeling with semiconductor nanoparticles (quantum dots).* Journal of Materials Chemistry, 2007. **17**(14): p. 1343-1346.
44. Ghoroghchian, P.P., M.J. Therien, and D.A. Hammer, *In vivo fluorescence imaging: a personal perspective.* Wiley Interdisciplinary Reviews: Nanomedicine and Nanobiotechnology, 2009. **1**(2): p. 156-167.

45. Michalet, X., et al., *Quantum Dots for Live Cells, in Vivo Imaging, and Diagnostics.* Science, 2005. **307**(5709): p. 538-544.
46. Gur, I., et al., *Air-Stable All-Inorganic Nanocrystal Solar Cells Processed from Solution.* Science, 2005. **310**(5747): p. 462-465.
47. Kongkanand, A., et al., *Quantum Dot Solar Cells. Tuning Photoresponse through Size and Shape Control of CdSe−TiO2 Architecture.* Journal of the American Chemical Society, 2008. **130**(12): p. 4007-4015.
48. Colvin, V.L., M.C. Schlamp, and A.P. Alivisatos, *Light-emitting diodes made from cadmium selenide nanocrystals and a semiconducting polymer.* Nature, 1994. **370**(6488): p. 354-357.
49. Kamat, P.V., *Quantum Dot Solar Cells. The Next Big Thing in Photovoltaics.* The Journal of Physical Chemistry Letters, 2013. **4**(6): p. 908-918.
50. Klimov, V.I., et al., *Optical Gain and Stimulated Emission in Nanocrystal Quantum Dots.* Science, 2000. **290**(5490): p. 314-317.
51. Wu, X., et al., *Immunofluorescent labeling of cancer marker Her2 and other cellular targets with semiconductor quantum dots.* Nat Biotech, 2003. **21**(1): p. 41-46.
52. Aswathy, R., et al., *Near-infrared quantum dots for deep tissue imaging.* Analytical and Bioanalytical Chemistry, 2010. **397**(4): p. 1417-1435.
53. Tetyana, T. and V. Yuri, *Semiconductor II-VI Quantum Dots with Interface States and Their Biomedical Applications*, 2011.
54. Xie, R., et al., *InAs/InP/ZnSe core/shell/shell quantum dots as near-infrared emitters: Bright, narrow-band, non-cadmium containing, and biocompatible.* Nano Research, 2008. **1**(6): p. 457-464.
55. Li, L., et al., *Highly Luminescent CuInS2/ZnS Core/Shell Nanocrystals: Cadmium-Free Quantum Dots for In Vivo Imaging.* Chemistry of Materials, 2009. **21**(12): p. 2422-2429.
56. Allen, P.M. and M.G. Bawendi, *Ternary I−III−VI Quantum Dots Luminescent in the Red to Near-Infrared.* Journal of the American Chemical Society, 2008. **130**(29): p. 9240-9241.
57. Guchhait, A., A.K. Rath, and A.J. Pal, *To make polymer: Quantum dot hybrid solar cells NIR-active by increasing diameter of PbSnanoparticles.* Solar Energy Materials and Solar Cells, 2011. **95**(2): p. 651-656.
58. Jiang, W., et al., *Assessing Near-Infrared Quantum Dots for Deep Tissue, Organ, and Animal Imaging Applications.* Journal of Laboratory Automation, 2008. **13**: p. 6-12.
59. Altınoğlu, E.İ. and J.H. Adair, *Near infrared imaging with nanoparticles.* Wiley Interdisciplinary Reviews: Nanomedicine and Nanobiotechnology, 2010. **2**(5): p. 461-477.
60. Sharma, P., et al., *Nanoparticles for bioimaging.* Advances in Colloid and Interface Science, 2006. **123–126**(0): p. 471-485.
61. Taik Lim, Y., et al., *Selection of Quantum Dot Wavelengths for Biomedical Assays and Imaging.* Molecular Imaging, 2003. **2**(1): p. 50-64.

62. John V, F., *In vivo near-infrared fluorescence imaging.* Current Opinion in Chemical Biology, 2003. **7**(5): p. 626-634.
63. Lim, Y.T., et al., *Selection of quantum dot wavelengths for biomedical assays and imaging.* Molecular imaging, 2003. **2**(1): p. 50-64.
64. Chen, H.Y., et al., *Characterization of CdHgTe/CdS QDs for Near Infrared Fluorescence Imaging of Spinal Column in a Mouse Model.* Photochemistry and Photobiology, 2011. **87**(1): p. 72-81.
65. Blackman, B., D. Battaglia, and X. Peng, *Bright and Water-Soluble Near IR-Emitting CdSe/CdTe/ZnSe Type-II/Type-I Nanocrystals, Tuning the Efficiency and Stability by Growth.* Chemistry of Materials, 2008. **20**(15): p. 4847-4853.
66. Morgan, N.Y., et al., *Real time in vivo non-invasive optical imaging using near-infrared fluorescent quantum dots1.* Academic Radiology, 2005. **12**(3): p. 313-323.
67. Kim, S., et al., *Near-infrared fluorescent type II quantum dots for sentinel lymph node mapping.* Nat Biotech, 2004. **22**(1): p. 93-97.
68. Ding, H., et al., *Non-invasive tumor detection in small animals using novel functional Pluronic nanomicelles conjugated with anti-mesothelin antibody.* Nanoscale, 2011. **3**(4): p. 1813-1822.
69. Du, Y., et al., *Near-Infrared Photoluminescent Ag2S Quantum Dots from a Single Source Precursor.* Journal of the American Chemical Society, 2010. **132**(5): p. 1470-1471.
70. Hirsch, M.P., *Toxicity of silver sulfide-spiked sediments to the freshwater amphipod (Hyalella azteca).* Environmental Toxicology and Chemistry, 1998. **17**(4): p. 601-604.
71. Madelung, O., *Semiconductors: Data Handbook*, 2004, Springer: Verlag Berlin Heidelberg Newyork. p. 1528.
72. Ehrlich, S.H., *Spectroscopic Studies of AgBr with Quantum-Sized nanoclusters of Iodiede, Silver and Silver Sulfides.* Journal of Imaging Science and Technology, 1993. **37**(1): p. 73-91.
73. Gu, Y.-P., et al., *Ultrasmall Near-Infrared Ag2Se Quantum Dots with Tunable Fluorescence for in Vivo Imaging.* Journal of the American Chemical Society, 2011. **134**(1): p. 79-82.
74. Jiang, P., et al., *Emission-Tunable Near-Infrared Ag2S Quantum Dots.* Chemistry of Materials, 2011. **24**(1): p. 3-5.
75. Yarema, M., et al., *Infrared Emitting and Photoconducting Colloidal Silver Chalcogenide Nanocrystal Quantum Dots from a Silylamide-Promoted Synthesis.* ACS Nano, 2011. **5**(5): p. 3758-3765.
76. Jiang, P., et al., *Water-soluble Ag2S quantum dots for near-infrared fluorescence imaging in vivo.* Biomaterials, 2012. **33**(20): p. 5130-5135.
77. Selvan, S.T., T.T. Tan, and J.Y. Ying, *Robust, Non-Cytotoxic, Silica-Coated CdSe Quantum Dots with Efficient Photoluminescence.* Advanced Materials, 2005. **17**(13): p. 1620-1625.

78. Martínez-Castañón, G.A., et al., *Characterization of silver sulfide nanoparticles synthesized by a simple precipitation method.* Materials Letters, 2005. **59**(4): p. 529-534.
79. Remya, K.P., T. Udayabhaskararao, and T. Pradeep, *Low-Temperature Thermal Dissociation of Ag Quantum Clusters in Solution and Formation of Monodisperse Ag2S Nanoparticles.* The Journal of Physical Chemistry C, 2012. **116**(49): p. 26019-26026.
80. Zhao, Y. and Z. Song, *Phase transfer-based synthesis of highly stable, biocompatible and the second near-infrared-emitting silver sulfide quantum dots.* Materials Letters, 2014. **126**(0): p. 78-80.
81. Gui, R., et al., *Water-soluble multidentate polymers compactly coating Ag2S quantum dots with minimized hydrodynamic size and bright emission tunable from red to second near-infrared region.* Nanoscale, 2014. **6**(10): p. 5467-5473.
82. Hua-Yan, Y., et al., *One-pot synthesis of water-dispersible Ag 2 S quantum dots with bright fluorescent emission in the second near-infrared window.* Nanotechnology, 2013. **24**(5): p. 055706.
83. Tan, L., A. Wan, and H. Li, *Synthesis of near-Infrared Quantum Dots in Cultured Cancer Cells.* ACS Applied Materials & Interfaces, 2013. **6**(1): p. 18-23.
84. Chen, G., et al., *Tracking of Transplanted Human Mesenchymal Stem Cells in Living Mice using Near-Infrared Ag2S Quantum Dots.* Advanced Functional Materials, 2014. **24**(17): p. 2481-2488.
85. Zhang, Y., et al., *Ag2S Quantum Dot: A Bright and Biocompatible Fluorescent Nanoprobe in the Second Near-Infrared Window.* ACS Nano, 2012. **6**(5): p. 3695-3702.
86. Shokrollahi, H., *Contrast agents for MRI.* Materials Science and Engineering: C, 2013. **33**(8): p. 4485-4497.
87. Gupta, A.K. and M. Gupta, *Synthesis and surface engineering of iron oxide nanoparticles for biomedical applications.* Biomaterials, 2005. **26**(18): p. 3995-4021.
88. Lacroix, L.M., et al., *New generation of magnetic and luminescent nanoparticles for in vivo real-time imaging.* Interface Focus, 2013. **3**(3).
89. Chan, W.C.W., et al., *Luminescent quantum dots for multiplexed biological detection and imaging.* Current Opinion in Biotechnology, 2002. **13**(1): p. 40-46.
90. Maleki, H., et al., *Size-controlled synthesis of superparamagnetic iron oxide nanoparticles and their surface coating by gold for biomedical applications.* Journal of Magnetism and Magnetic Materials, 2012. **324**(23): p. 3997-4005.
91. Abdukayum, A., et al., *Gadolinium Complexes Functionalized Persistent Luminescent Nanoparticles as a Multimodal Probe for Near-Infrared Luminescence and Magnetic Resonance Imaging in Vivo.* Analytical Chemistry, 2014. **86**(9): p. 4096-4101.

92. Yi, D.K., et al., *Silica-Coated Nanocomposites of Magnetic Nanoparticles and Quantum Dots.* Journal of the American Chemical Society, 2005. **127**(14): p. 4990-4991.
93. Gaponik, N., et al., *Luminescent Polymer Microcapsules Addressable by a Magnetic Field.* Langmuir, 2004. **20**(4): p. 1449-1452.
94. Gu, H., et al., *Facile One-Pot Synthesis of Bifunctional Heterodimers of Nanoparticles: A Conjugate of Quantum Dot and Magnetic Nanoparticles.* Journal of the American Chemical Society, 2004. **126**(18): p. 5664-5665.
95. Liu, X., et al., *Generalized and Facile Synthesis of Fe3O4/MS (M = Zn, Cd, Hg, Pb, Co, and Ni) Nanocomposites.* The Journal of Physical Chemistry C, 2008. **112**(33): p. 12728-12735.
96. Corr, S., Y. Rakovich, and Y. Gun'ko, *Multifunctional Magnetic-fluorescent Nanocomposites for Biomedical Applications.* Nanoscale Research Letters, 2008. **3**(3): p. 87-104.
97. Shen, J.-M., et al., *Luminescent/Magnetic Hybrid Nanoparticles with Folate-Conjugated Peptide Composites for Tumor-Targeted Drug Delivery.* Bioconjugate Chemistry, 2012. **23**(5): p. 1010-1021.
98. Wang, H., et al., *Magnetic iron oxide-fluorescent carbon dots integrated nanoparticles for dual-modal imaging, near-infrared light-responsive drug carrier and photothermal therapy.* Biomaterials Science, 2014. **2**(6): p. 915-923.
99. Wang, X., et al., *Preparation of hybrid fluorescent–magnetic nanoparticles for application to cellular imaging by self-assembly.* Colloids and Surfaces A: Physicochemical and Engineering Aspects, 2011. **392**(1): p. 103-109.
100. Jiang, W., et al., *Optimizing the Synthesis of Red- to Near-IR-Emitting CdS-Capped CdTexSe1-x Alloyed Quantum Dots for Biomedical Imaging.* Chemistry of Materials, 2006. **18**(20): p. 4845-4854.
101. Yong, K.-T., et al., *Synthesis of ternary CuInS2/ZnS quantum dot bioconjugates and their applications for targeted cancer bioimaging.* Integrative Biology, 2010. **2**(2-3): p. 121-129.
102. Sahu, A., et al., *Facile Synthesis of Silver Chalcogenide (Ag2E; E = Se, S, Te) Semiconductor Nanocrystals.* Journal of the American Chemical Society, 2011. **133**(17): p. 6509-6512.
103. *A Guide to Recording Fluorescence Quantum Yields* 2012; Available from: http://www.horiba.com/fileadmin/uploads/Scientific/Documents/Fluorescence/quantumyieldstrad.pdf.
104. Rui, C., et al., *Silver sulfide nanoparticle assembly obtained by reacting an assembled silver nanoparticle template with hydrogen sulfide gas.* Nanotechnology, 2008. **19**(45): p. 455604.
105. Orléans, R.B.C. 2012; Available from: http://www.lasurface.com/database/elementxps.php.
106. *Handbook of The Elements and Native Oxides*. 1999; Available from: http://www.xpsdata.com/XI_BE_Lookup_table.pdf.

107. Scudiero, D.A., et al., *Evaluation of a soluble tetrazolium/formazan assay for cell growth and drug sensitivity in culture using human and other tumor cell lines.* Cancer Res, 1988. **48**(17): p. 4827-33.
108. Suresh, A.K., et al., *Monodispersed biocompatible silver sulfide nanoparticles: facile extracellular biosynthesis using the gamma-proteobacterium, Shewanella oneidensis.* Acta Biomater, 2011. **7**(12): p. 4253-8.
109. Choi, O., et al., *Role of sulfide and ligand strength in controlling nanosilver toxicity.* Water Research, 2009. **43**(7): p. 1879-1886.
110. Blaser, S.A., et al., *Estimation of cumulative aquatic exposure and risk due to silver: Contribution of nano-functionalized plastics and textiles.* Science of The Total Environment, 2008. **390**(2–3): p. 396-409.
111. Xing, R., S. Liu, and S. Tian, *Microwave-assisted hydrothermal synthesis of biocompatible silver sulfide nanoworms* Journal of Nanoparticle Research, 2011(13): p. 4847-4854.
112. Hocaoglu, I., et al., *Development of highly luminescent and cytocompatible near-IR-emitting aqueous Ag2S quantum dots.* Journal of Materials Chemistry, 2012. **22**(29): p. 14674-14681.
113. Yantasee, W., et al., *Direct detection of Pb in urine and Cd, Pb, Cu, and Ag in natural waters using electrochemical sensors immobilized with DMSA functionalized magnetic nanoparticles.* Analyst, 2008. **133**(3): p. 348-355.
114. Graziano, J.H., et al., *Controlled study of meso-2,3-dimercaptosuccinic acid for the management of childhood lead intoxication.* The Journal of Pediatrics, 1992. **120**(1): p. 133-139.
115. Durgadas, C.V., K. Sreenivasan, and C.P. Sharma, *Bright blue emitting CuSe/ZnS/silica core/shell/shell quantum dots and their biocompatibility.* Biomaterials, 2012. **33**(27): p. 6420-6429.
116. Painuly, D., A. Bhatt, and V.K. Krishnan, *Physicochemical and in vitro biocompatibility evaluation of water-soluble CdSe/ZnS core/shell.* Journal of Biomaterials Applications, 2014. **28**(8): p. 1125-1137.
117. Durgadas, C.V., C.P. Sharma, and K. Sreenivasan, *Fluorescent and superparamagnetic hybrid quantum clusters for magnetic separation and imaging of cancer cells from blood.* Nanoscale, 2011. **3**(11): p. 4780-4787.
118. *Standard X-Ray Diffraction Patterns*. Vol. 10. 1960: Natl. Bur. Stand. (U.S.), Circ. 539. 51.
119. Zhang, Y., et al., *Controlled Synthesis of Ag2S Quantum Dots and Experimental Determination of the Exciton Bohr Radius.* The Journal of Physical Chemistry C, 2014. **118**(9): p. 4918-4923.
120. Grandfils, C., et al., *Optimization and application of electrophoretic mobility analysis of human red blood cells to study their in vitro stability, interaction with polycations and proteolytic enzymes.* Journal of Biomedical Materials Research Part A, 2008. **84A**(2): p. 535-544.
121. Radomski, A., et al., *Nanoparticle-induced platelet aggregation and vascular thrombosis.* British Journal of Pharmacology, 2005. **146**(6): p. 882-893.

122. Paul M Knopf, D.S.R., Si-Han Hai, Julie McMurry, William Martin and Anne S De Groot, *Novel function of complement C3d as an autologous helper T-cell target.* Immunol Cell Biol, 2008. **86**(3): p. 4.
123. Gorbet, M.B. and M.V. Sefton, *Biomaterial-associated thrombosis: roles of coagulation factors, complement, platelets and leukocytes.* Biomaterials, 2004. **25**(26): p. 5681-5703.
124. Cerda-Cristerna, B.I., et al., *Hemocompatibility assessment of poly(2-dimethylamino ethylmethacrylate) (PDMAEMA)-based polymers.* Journal of Controlled Release, 2011. **153**(3): p. 269-277.
125. Singh, A. and S.K. Sahoo, *Magnetic nanoparticles: a novel platform for cancer theranostics.* Drug Discovery Today, (0).
126. Hasan Hussein-Al-Ali, S., et al., *Arginine–chitosan- and arginine– polyethylene glycol-conjugated superparamagnetic nanoparticles : Preparation, cytotoxicity and controlled-release.* Journal of Biomaterials Applications, 2014.
127. Cohen, Y. and S.Y. Shoushan, *Magnetic nanoparticles-based diagnostics and theranostics.* Current Opinion in Biotechnology, 2013. **24**(4): p. 672-681.
128. Rosen, J.E., et al., *Iron oxide nanoparticles for targeted cancer imaging and diagnostics.* Nanomedicine: Nanotechnology, Biology and Medicine, 2012. **8**(3): p. 275-290.
129. Jain, T.K., et al., *Magnetic nanoparticles with dual functional properties: Drug delivery and magnetic resonance imaging.* Biomaterials, 2008. **29**(29): p. 4012-4021.
130. Gao, J., et al., *In Vivo Tumor-Targeted Fluorescence Imaging Using Near-Infrared Non-Cadmium Quantum Dots.* Bioconjugate Chemistry, 2010. **21**(4): p. 604-609.
131. Robel, I., et al., *Quantum Dot Solar Cells. Harvesting Light Energy with CdSe Nanocrystals Molecularly Linked to Mesoscopic TiO2 Films.* Journal of the American Chemical Society, 2006. **128**(7): p. 2385-2393.
132. Rizvi, S.B., et al., *Semiconductor quantum dots as fluorescent probes for in vitro and in vivo bio-molecular and cellular imaging.* Nano Reviews; Vol 1 (2010) incl Supplements, 2010.
133. Gerion, D., et al., *Synthesis and Properties of Biocompatible Water-Soluble Silica-Coated CdSe/ZnS Semiconductor Quantum Dots†.* The Journal of Physical Chemistry B, 2001. **105**(37): p. 8861-8871.
134. Derfus, A.M., W.C.W. Chan, and S.N. Bhatia, *Probing the Cytotoxicity of Semiconductor Quantum Dots.* Nano Letters, 2003. **4**(1): p. 11-18.
135. Selvan, S.T., et al., *Synthesis of Silica-Coated Semiconductor and Magnetic Quantum Dots and Their Use in the Imaging of Live Cells.* Angewandte Chemie, 2007. **119**(14): p. 2500-2504.
136. Cai, W., et al., *Peptide-Labeled Near-Infrared Quantum Dots for Imaging Tumor Vasculature in Living Subjects.* Nano Letters, 2006. **6**(4): p. 669-676.

137. Chen, H., et al., *Synthesis of Brightly PEGylated Luminescent Magnetic Upconversion Nanophosphors for Deep Tissue and Dual MRI Imaging.* Small, 2014. **10**(1): p. 160-168.
138. Won, N., et al., *Imaging Depths of Near-Infrared Quantum Dots in First and Second Optical Windows.* Molecular Imaging, 2012. **11**(4): p. 338-352.
139. Kas, R., et al., *A Universal Method for the Preparation of Magnetic and Luminescent Hybrid Nanoparticles.* The Journal of Physical Chemistry C, 2010. **114**(17): p. 7758-7766.
140. Liu, Y.-F., et al., *Synthesis of Highly Stable CdTe/CdS Quantum Dots with Biocompatibility.* European Journal of Inorganic Chemistry, 2010. **2010**(10): p. 1501-1506.
141. Yarema, M., et al., *Infrared Emitting and Photoconducting Colloidal Silver Chalcogenide Nanocrystal Quantum Dots from a Silylamide-Promoted Synthesis.* Acs Nano, 2011. **5**(5): p. 3758-3765.
142. Lokhande, C.D. and K.M. Gadave, *A simple chemical method for conversion of CdS into Ag2S and CdSe into Ag2Se.* Materials Chemistry and Physics, 1993. **36**(1–2): p. 119-123.
143. Moon, G.D., et al., *Chemical Transformations in Ultrathin Chalcogenide Nanowires.* ACS Nano, 2010. **4**(4): p. 2307-2319.
144. Ho, T.-L., *Hard soft acids bases (HSAB) principle and organic chemistry.* Chemical Reviews, 1975. **75**(1): p. 1-20.
145. Pearson, R.G., *Hard and Soft Acids and Bases.* Journal of the American Chemical Society, 1963. **85**(22): p. 3533-3539.
146. Mikus, H. and H.J. Deiseroth, *Ag12Te6S: A Contribution to Open Problems in the Crystal Chemistry of Complex Non-Metallic Filled Frank-Kasper Phases.* Zeitschrift für anorganische und allgemeine Chemie, 2005. **631**(6-7): p. 1233-1236.
147. Pertlik, F., *Crystal structure of Ag2TeS3 and Na(Na1−x Ag x)TeS3 (x≈0.5) and the geometry of Te(IV)S3 polyhedra.* Monatshefte für Chemie / Chemical Monthly, 1997. **128**(2): p. 157-163.

VITA

İbrahim Hocaoğlu was born in Kadıköy in İstanbul, Turkey in 1983. He completed Lafarge Aslan Çimento Technical High School from the department of Chemistry (Kocaeli) in 2000. He received his B.S. degree from the Department of Chemistry, Bilkent University (Ankara) in 2007. In 2007, he started his MBA degree in Social Sciences department at Gebze Institute of High Technology. He completed his military service (Tekirdağ) in 2008. He received his MBA degree from the department of Bussiness and Administrations, Gebze Institute of High Technology (Kocaeli) in 2010. In 2010, He started Ph.D. programme in the department of Material Science and Engineering, Koç University (İstanbul).